UNIVERSITÀ DEGLI STUDI DI TRIESTE

XXX CICLO DEL DOTTORATO DI RICERCA IN FISICA

GROWTH OF TWO-DIMENSIONAL MATERIALS AND INVESTIGATION OF THEIR STRUCTURAL AND ELECTRONIC PROPERTIES

Settore scientifico-disciplinare: FIS/03

DOTTORANDO
HARSH VARDHAN BANA

COORDINATORE
PROF. LIVIO LANCERI

SUPERVISORE DI TESI
PROF. ALESSANDRO BARALDI

Co-SUPERVISORE DI TESI
Dr. SILVANO LIZZIT

ANNO ACCADEMICO 2016/2017

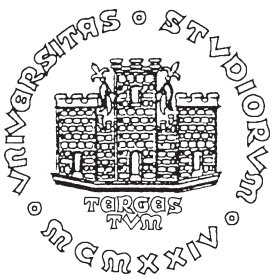

UNIVERSITY OF TRIESTE

Department of Physics

Graduate School in Physics, Cycle XXX

PhD Thesis

Growth of two-dimensional materials and investigation of their structural and electronic properties.

Supervisor:
Prof. Alessandro Baraldi

Candidate:
Harsh Vardhan Bana

Cosupervisor:
Dr. Silvano Lizzit

Academic Year 2016-2017

माँ

Abstract

The advent of graphene has had a phenomenal impact on the scientific community, resulting in the opening of a novel research field that focused on the properties of 2D materials. Apart from graphene, transition metal dichalcogenides (TMDCs) were among the first materials to be isolated in single layer (SL) form, exhibiting outstanding electrical and optical properties. In recent years the interest of the scientific community on TMDCs has rapidly grown and has been motivated by the possibility to use them in highly performing and energy efficient transistors with an aggressive scaling of the dimensions. In addition, also exotic physical phenomena related to single layer TMDCs like the spin and valley-Hall effect are being actively investigated for the production of electronic devices whose working principle goes beyond the standard charge based devices. However, such applications require SL with large area and low density of defects and although various approaches have been implemented to produce 2D TMDCs, they lacked the control over uniformity, thickness and size of the 2D film.

In this thesis, we focused on the experimental investigation of the 2D materials, particularly TMDCs, epitaxially grown on different metal substrates. We explored the nucleation process to identify the optimal conditions for the growth of 2D layers by studying the adsorption of the chemical species on the metal substrates by means of a combination of different in-situ spectroscopy techniques. This allowed us to synthesize large area TMDCs layers with a single orientation, thus reducing the presence of grain boundaries and leading to the growth of better quality layers. In addition to this we also investigated the electronic structure close to the Fermi level to gain more insight into these 2D materials.

In the first part, the physical vapour deposition growth of SL TMDCs on different transition metal substrates is discussed, with the aim of investigating the effect of the adsorbate-substrate interaction and the substrate symmetry on the electronic and structural properties of the epitaxially grown 2D layers of TMDCs. We developed a new synthesis method for the growth of SL MoS_2 on Au(111) that resulted in extended layer with single domain orientation, that is without the presence of mirror domains. This latter point has also been confirmed by the measurement of complete out-of plane spin polarisation of the valence bands near **K** and **-K** point of the surface Brillouin zone of MoS_2. Furthermore, we also investigated the properties of WS_2 on Au(111) that is one of most promising TMDCs for spin and valleytronic applications due to its large splitting of the spin degeneracy in the valence band. By carefully tuning the growth parameters while following the same method developed for MoS_2, we successfully produced high quality SL WS_2/Au(111) with a single orientation that led to the observation of moirè-induced mini gaps in the electronic band structure and the quantification of electron-phonon coupling strength, thus deriving useful information for electronic device applications.

We have subsequently adapted the new synthesis method also for the

growth of SL MoS_2 on both Ag(111) and Ag(110) substrates. The use of Ag as a substrate is also attractive in the perspective of the realization of good contacts in field effect transistor (FET) devices. In fact, the continue miniaturization of FETs demands for low intrinsic contact resistance between the active part of the FET and the contacts that interface it with external components in order to mantain high device performances. MoS_2/Ag(111) has been predicted to have much smaller Schottky barrier height than MoS_2/Au(111) therefore expected to result in lowering of the contact resistance. We demonstrate the high quality of the grown layers but with the presence of equal proportions of two mirror domain orientations.

In the end, in order to shed light on the formation of silicene on Ir(111), the Si-based 2D material analogous to graphene, the adsorption of Si on Ir(111) up to more than one monolayer Si coverage is presented. The comparison between the experimental results and DFT calculations indicate towards the instability of Si/Ir(111) interface, thus implying the formation of Si-Ir alloys, rather than the growth of a silicene layer.

Contents

CHAPTER 1

Introduction

Understanding the properties of materials has been at the core of scientific breakthroughs, throughout the evolution of human society. For example, Rasa-Ratna-Samuccaya, a thirteenth century A.D. text, authored by Vāgabhatācārya, speaks about the preparation and properties of drugs of mineral origin. [1] The Sanskrit text also throws light on the state of expertise in the field of mineral extraction, purification and on alloys displaying various properties. From the discovery of fire in the prehistoric period to the semiconductor based supercomputers of the modern era, it is quite clear that the history of our civilization has unfolded hand in hand with material science. This syncretic discipline hybridizing solid-state physics and chemistry, is vital for the developments in science and technology. In the talk titled "Plenty of Room at the Bottom" presented to the American Physical Society in Pasadena in December 1959, Richard P. Feynman explored the technological possibilities through material manipulation at the atomic level. Indeed, most of the pressing scientific problems that we face today are due to the limits of the materials available and with the emergence of nanotechnology, the ability to control the dimensional scales of materials has become highly demanding. Consequently, by following Moore's law [1] [2], the semiconductor industry has been able to manage long-term planning and to set targets for research and development. However, a shortfall to Moore's law is expected as the efficiency of silicon transistors is predicted to fail below 5-nanometer gate lengths

[1] Moore's Law is the observation made in 1965 by Gordon Moore that the number of transistors per square inch on integrated circuits had doubled every year since the integrated circuit was invented. Moore predicted that this trend would continue for the foreseeable future.

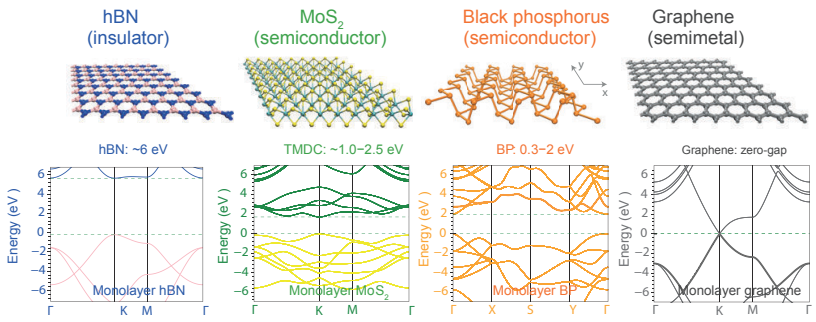

Figure 1.1: The atomic structures of some 2D materials along with their respective electronic band structure. Adapted from ref. Xia *et. al* [5]

because of severe short channel effects and difficulties with heat dissipation. [2] This advocates for the necessity of finding new strategies to gain processing speed within compact integrated circuits in the years to come.

An interesting field of materials science that deals with the phenomena at surfaces and interfaces has been around effectively for over hundred years, although the first use of the term 'surface science' dates back to the early sixties of the twentieth century. In the more recent years, the field of surface science has benefited from the developments in vacuum technology and high speed analytical capabilities of computers. Such improvements have extended the possibility to study the physical mechanisms governing the properties of materials at molecular and atomic scale, allowing the scientific community to move beyond the study of three dimensional (3D) bulk systems, towards the two dimensional (2D) materials counterpart. 2D materials are crystalline single layer of atoms that do not need to be supported by a substrate to exist and can be isolated as free-standing layers. The high surface-to-volume ratio and quantum confinement effects are responsible for the remarkable modifications of the electronic and the optical properties of the materials when reduced to the two dimensional scale. [3, 4]

Graphene is the most studied 2D material for its fundamental properties as well as potential applications. It is a one-atom-thick crystal composed of sp^2 hybridized carbon atoms arranged in a honeycomb lattice which shows extraordinary strength as well as unprecedented flexibility. [6] With the highest elastic constants ever measured in any material, graphene can be stretched for up to 20% without breaking. It shows linear π-band dispersion at the Fermi energy at the K-point of the Brillouin zone [7] thus showing extremely high carrier mobility and thermal conductivity at room temperature. [8] Electrons in

[2]The International Technology Roadmap for Semiconductors (Semiconductor Industry Association, 2011). http://www.itrs.net/Links/2011ITRS/Home2011.html

the vicinity of the Dirac points behave as relativistic quasi-particles with zero effective mass which, when coupled with the application of a strong magnetic field, gives rise to the unconventional quantum Hall effect. [9] The high surface to volume ratio allows chemical modification and functionlization of graphene making it possible to appropriately tune its properties. Together with its unique properties and high stability under ambient conditions, graphene is a suitable material for a lot of different applications such as spintronics [10], molecular sensing [11], and flexible electronic devices. [12]

Single layer hexagonal Boron Nitride (hBN) is another important member of the 2D materials family. Isostructural to graphene, hBN is a layered material with alternating boron and nitrogen atoms arranged in a sp^2 hybridized honeycomb lattice. [13] With an energy band gap of 5.9 eV [14], hBN is an insulator and displays high chemical and thermal stability. As a result hBN is an apt material to be used as a dielectric substrate for various electronic devices, capable to play an important role in arranging different materials in nanoscale heterostructures. [15] Moreover, it has been observed that the carrier mobility and homogeneity of graphene grown on hBN is about an order of magnitude higher than that of graphene on SiO_2. [16] Black phosphorus (BP) has been recently synthesized in single layer form known as Phosphorene. [17] Each phosphorus atom in single layer phosphorene is coordinated to three phosphorus atoms in sp^3 hybridization giving rise to a crystal structure with a puckered honeycomb lattice. Phosphorene is a semiconductor with a sizable direct band gap that evolves with the applied strain and the number of layers, making it an appealing material for the development of photonic and optoelectronic devices. Besides the above mentioned examples, there are several other elemental 2D materials such as stanene [18], germanene [19] and silicene [20], that are attracting the attention of the scientific community. 2D transition metal oxides (TMOs), like Al_2O_3, ZrO_2, TiO_2, HfO_2 and Ta_2O_5 are interesting for their potential use as high κ dielectric materials. These TMOs show diverse physical and chemical properties that could be useful for a wide range of potential applications such as catalysts, sensors, piezoelectric devices and superconductors. [21]

Another highly attractive ensemble of 2D materials is constituted by transition metal dichalcogenides (TMDCs). TMDCs represent a large family of crystalline materials showing distinct structures and properties. They consist of compounds with general formula MX_2, where a layer of transition metal atoms (M = Mo, W, Re, Nb, V) is sandwiched between two layers of chalcogen atoms (X = S, Se, Te). In the 3D bulk configuration these layers are stacked on top of each other coupled by weak van der Waals (vdW) forces. Owing to the ability of these vdW coupled stacked layers to slide past one another MoS_2, one of the most studied members of TMDCs, has been used as dry lubricant for a long time. The properties of these materials depend strongly on the structural arrangement as well as the constituent elements. Depending on the coordination and oxidation state of the metal atom, bulk TMDCs can be metallic, like NbS_2 and VS_2, semiconducting like MoS_2 and

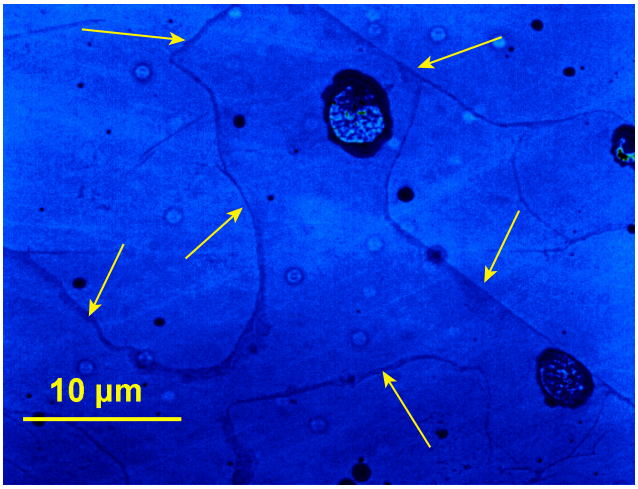

Figure 1.2: An optical microscope image of CVD grown MoS_2 on SiO_2 substrate showing different grains of single layer MoS_2. The inhomogeneity due to defects close to the grain boundaries (indicated with arrows) can be easily noticed. The contrast is enhanced for better identification of the details in the presented image. This sample was prepared from MoO_3 and S powder precursors, in a furnace, by following the procedure mentioned in [24].

WS_2 or insulating like HfS_2. The transition from the 3D bulk to the 2D counterpart leads to the emergence of new exotic properties of these materials. For instance MoS_2 exhibits a transition from an indirect band gap (E_g = 1.29 eV) in its bulk form to a direct band gap (E_g = 1.90 eV) in the monolayer form as a consequence of quantum confinement. They also present high on/off ratio and high carrier mobility. [22] As a result group-VI TMDCs like MoS_2 and WS_2 are gaining attention as channel material for field-effect transistors. The presence of direct band gap in the visible range coupled with the high absorbance coefficient and efficient electron-hole pair generation during photo-excitation, qualifies these materials to be used for the production of highly sensitive photo-transistors in the optoelectronic integrated circuits, light sensors, and biomedical imaging. [23]

The advancement in research activity has already shown a phenomenal development in the production of 2D TMDCs suitable for applications. Various approaches have been implemented to produce 2D TMDCs. Mechanical exfoliation produces 2D crystals that show significant mechanical strength and flexibility [25] but lacks the control over uniformity, thickness and size of the 2D film. Therefore it cannot be used for large scale device fabrication. [26] Similarly, liquid exfoliation using organic solvents [27], and by intercalation of lithium ions using an electrochemical set-up [28] result in uncontrolled and inhomogeneous products. Other techniques such as dip

coating in metal salt solutions followed by annealing [29], thermolysis of compounds containing transition metal (M) and chalcogen (X) atoms [30], and solid phase sulphurization of thin films of transition metals [31] have also been used to produce 2D TMDCs with poor quality and limited reproducibility. Chemical vapor deposition (CVD) is a promising approach towards large scale production of 2D TMDCs, through either direct processing of the metal and the chalcogen [31] atoms, or from metal oxides and chalcogen precursors. [32–34] Although CVD grown 2D TMDCs extend up to a lateral dimension of tens of micrometer, they also show coexistence of single and multilayer islands together with randomly oriented grains, thus presenting a number of defects such as grain boundaries and chalcogen atom vacancies (figure 1.2). [34] The presence of such defects greatly deteriorates the optical and electrical properties of TMDCs, thus leading to underperforming fabricated devices.

The understanding of the growth process is undeniably the most important step towards the large-scale synthesis of continuous high-quality single or few-layers of TMDCs. It is therefore important to explore the nucleation process and subsequent growth of the two dimensional layers. The aspects driving the crystal assembling following the adsorption of the chemical species, metal-chalcogen bonding and eventual desorption need to be investigated in detail.

The topics discussed in this thesis are focused on the experimental investigation of two dimensional materials, particularly of single layers of transition metal dichalcogenides epitaxially grown on different metal substrates. My research activity aims at opening up new paths for the synthesis of large area TMDCs layers by combining in-situ spectroscopies with chemical and surface sensitivity, capable to explore crystal and electronic structure providing fundamental information during interface assembling while regulating the growth parameters.

In chapter 3, the Physical Vapour Deposition (PVD) growth of single layer (SL) MoS_2 on Au(111) is going to be discussed. I will show how the availability of cutting-edge surface science techniques helped us to study the growth dynamics of MoS_2, in terms of the different species that evolve during the growth process. This understanding allowed us to formulate a new procedure leading to the direct growth SL MoS_2. Besides the improved quality of the layer, the most important aspect of the new growth is that the layer had just one single orientation. The single orientation character of the layer resulted in the complete out-of plane spin polarization of the bands near **K** and **-K** points of the surface Brillouin zone of MoS_2. As a result, this procedure was then extended to the study of other TMDCs.

In chapter 4, I will discuss the growth of single orientation SL WS_2 on Au(111), performed by carefully tuning the growth parameters. The high quality of the grown layer was also reflected in the electronic band structure measurements, showing significantly sharper bands than previously reported values, that allowed the quantification of many body effects such as the branch-dependent electron-phonon coupling strength.

MoS_2 growth on other high symmetry surfaces, in particular Ag(111), will be examined in chapter 5. This surface is characteristic for the stronger interaction with the MoS_2 overlayer with respect to Au(111). Although the growth resulted in the presence of mirror domains, a high structural order was observed and the layer showed a continuous growth extended over step edges of the Ag substrate. Moreover, the core level spectra indicated towards a substrate induced semiconductor to metal transition of the grown MoS_2 monolayer.

In chapter 6, the growth of SL MoS_2 on an highly anisotropic surface such as Ag(110) will be presented. This study was aimed at exploring the possibility of growing MoS_2, which is three-fold symmetric, on a substrate with a two-fold symmetry and to investigate the effects of the different substrate geometry on the electronic and structural properties of the layer. An ordered MoS_2 monolayer was obtained with coexistence of an equal amount of twin domains as dictated by the symmetry of the substrate.

Finally, in chapter 7, the adsorption of Si on Ir(111) will be presented. The purpose of this study was to shed light on the formation of silicene, the Si-based 2D material analogous to graphene. On the basis of the experimental results, supported by DFT calculations we found that the Si/Ir(111) interface is not stable and leads to the formation of Si-Ir alloys, rather than the growth of a silicene layer.

References

[1] Biswa, A. K. Rasa-Ratna-Samuccaya and Mineral processing state-of-art in the 13th century A.D. India. *Indian Journal of History of Science* **1987**, *22*, 29–46.

[2] Moore, G. E. Cramming more components onto integrated circuits. *Electronics* **1965**, *38*, 114–117.

[3] Chhowalla, M.; Jena, D.; Zhang, H. Two-dimensional semiconductors for transistors. *Nature Reviews Materials* **2016**, *1*, 16052, 1–15.

[4] Schaibley, J. R.; Yu, H.; Clark, G.; Rivera, P.; Ross, J. S.; Seyler, K. L.; Yao, W.; Xu, X. Valleytronics in 2D materials. *Nature Reviews Materials* **2016**, *1*, 16055, 1–15.

[5] Xia, F.; Wang, H.; Xiao, D.; Dubey, M.; Ramasubramaniam, A. Two-dimensional material nanophotonics. *Nature Photonics* **2014**, *8*, 899–907.

[6] Lee, C.; Wei, X.; Kysar, J. W.; Hone, J. Measurement of the Elastic Properties and Intrinsic Strength of Monolayer Graphene. *Science* **2008**, *321*, 385–388.

[7] Novoselov, K. S.; Geim, A. K.; Morozov, S. V.; Jiang, D.; Katsnelson, M. I.; Grigorieva, I. V.; Dubonos, S. V.; Firsov, A. A. Two-dimensional gas of massless Dirac fermions in graphene. *Nature* **2005**, *438*, 197–200.

[8] Mayorov, A. S.; Gorbachev, R. V.; Morozov, S. V.; Britnell, L.; Jalil, R.; Ponomarenko, L. A.; Blake, P.; Novoselov, K. S.; Watanabe, K.; Taniguchi, T.; Geim, A. K. Micrometer-Scale Ballistic Transport in Encapsulated Graphene at Room Temperature. *Nano Letters* **2011**, *11*, 2396–2399.

[9] Goerbig, M. O. Electronic properties of graphene in a strong magnetic field. *Reviews of Modern Physocs* **2011**, *83*, 1193–1243.

[10] Han, W.; Kawakami, R. K.; Gmitra, M.; Fabian, J. Graphene spintronics. *Nature Nanotechnology* **2014**, *9*, 794–807.

[11] Schedin, F.; Geim, A. K.; Morozov, S. V.; Hill, E. W.; Blake, P.; Katsnelson, M. I.; Novoselov, K. S. Detection of individual gas molecules adsorbed on graphene. *Nature Materials* **2007**, *6*, 652–655.

[12] Kim, K. S.; Zhao, Y.; Jang, H.; Lee, S. Y.; Kim, J. M.; Kim, K. S.; Ahn, J.-H.; Kim, P.; Choi, J.-Y.; Hong, B. H. Large-scale pattern growth of graphene films for stretchable transparent electrodes. *Nature* **2009**, *457*, 706–710.

[13] Paffett, M.; Simonson, R.; Papin, P.; Paine, R. Borazine adsorption and decomposition at Pt(111) and Ru(001) surfaces. *Surface Science* **1990**, *232*, 286 – 296.

[14] Watanabe, K.; Taniguchi, T.; Kanda, H. Direct-bandgap properties and evidence for ultraviolet lasing of hexagonal boron nitride single crystal. *Nature Materials* **2004**, *3*, 404–409.

[15] Corso, M.; Auwärter, W.; Muntwiler, M.; Tamai, A.; Greber, T.; Osterwalder, J. Boron Nitride Nanomesh. *Science* **2004**, *303*, 217–220.

[16] Dean, C.; Young, A.; Meric, I.; Lee, C.; Wang, L.; Sorgenfrei, S.; Watanabe, K.; Taniguchi, T.; Kim, P.; Shepard, K.; Hone, J. Boron nitride substrates for high-quality graphene electronics. *Nature Nanotechnology* **2010**, *5*, 722–726.

[17] Castellanos-Gomez, A. Black Phosphorus: Narrow Gap, Wide Applications. *The Journal of Physical Chemistry Letters* **2015**, *6*, 4280–4291.

[18] Zhu, F.-F.; Chen, W.-J.; Xu, Y.; Gao, C.-L.; Guan, D.-D.; Liu, C.-H.; Qian, D.; Zhang, S.-C.; Jia, J.-F. Epitaxial growth of two-dimensional stanene. *Nature Materials* **2015**, *14*, 1020–1025.

[19] Dávila, M. E.; Xian, L.; Cahangirov, S.; Rubio, A.; Lay, G. L. Germanene: a novel two-dimensional germanium allotrope akin to graphene and silicene. *New Journal of Physics* **2014**, *16*, 095002, 1–10.

[20] Vogt, P.; De Padova, P.; Quaresima, C.; Avila, J.; Frantzeskakis, E.; Asensio, M. C.; Resta, A.; Ealet, B.; Le Lay, G. Silicene: Compelling Experimental Evidence for Graphenelike Two-Dimensional Silicon. *Physical Review Letters* **2012**, *108*, 155501, 1–5.

[21] Sun, Z.; Liao, T.; Dou, Y.; Hwang, S. M.; Park, M.-S.; Jiang, L.; Kim, J. H.; Dou, S. X. Generalized self-assembly of scalable two-dimensional transition metal oxide nanosheets. *Nature Communications* **2014**, *5*, 3813, 1–9.

[22] Radisavljevic, B.; Radenovic, A.; Brivio, J.; Giacometti, V.; Kis, A. Single-layer MoS_2 transistors. *Nature Nanotechnology* **2011**, *6*, 147–150.

[23] Lopez-Sanchez, O.; Lembke, D.; Kayci, M.; Radenovic, A.; Kis, A. Ultrasensitive photodetectors based on monolayer MoS_2. *Nature Nanotechnology* **2013**, *8*, 497–501.

[24] Wang, S.; Rong, Y.; Fan, Y.; Pacios, M.; Bhaskaran, H.; He, K.; Warner, J. H. Shape Evolution of Monolayer MoS_2 Crystals Grown by Chemical Vapor Deposition. *Chemistry of Materials* **2014**, *26*, 6371–6379.

[25] Bertolazzi, S.; Krasnozhon, D.; Kis, A. Nonvolatile Memory Cells Based on MoS_2/Graphene Heterostructures. *ACS Nano* **2013**, *7*, 3246–3252.

[26] Kolobov, A. V.; Tominaga, J. *Two-Dimensional Transition-Metal Dichalcogenides*; Springer International Publishing: Cham, 2016; pp 79–107.

[27] Coleman, J. N. et al. Two-Dimensional Nanosheets Produced by Liquid Exfoliation of Layered Materials. *Science* **2011**, *331*, 568–571.

[28] Zeng, Z.; Yin, Z.; Huang, X.; Li, H.; He, Q.; Lu, G.; Boey, F.; Zhang, H. Single-Layer Semiconducting Nanosheets: High-Yield Preparation and Device Fabrication. *Angewandte Chemie International Edition* **2011**, *50*, 11093–11097.

[29] Liu, K.-K.; Zhang, W.; Lee, Y.-H.; Lin, Y.-C.; Chang, M.-T.; Su, C.-Y.; Chang, C.-S.; Li, H.; Shi, Y.; Zhang, H.; Lai, C.-S.; Li, L.-J. Growth of Large-Area and Highly Crystalline MoS_2 Thin Layers on Insulating Substrates. *Nano Letters* **2012**, *12*, 1538–1544.

[30] Altavilla, C.; Sarno, M.; Ciambelli, P. A Novel Wet Chemistry Approach for the Synthesis of Hybrid 2D Free-Floating Single or Multilayer Nanosheets of MS_2@oleylamine (M=Mo, W). *Chemistry of Materials* **2011**, *23*, 3879–3885.

[31] Zhan, Y.; Liu, Z.; Najmaei, S.; Ajayan, P. M.; Lou, J. Large-Area Vapor-Phase Growth and Characterization of MoS_2 Atomic Layers on a SiO_2 Substrate. *Small* **2012**, *8*, 966–971.

[32] Lee, Y.-H.; Zhang, X.-Q.; Zhang, W.; Chang, M.-T.; Lin, C.-T.; Chang, K.-D.; Yu, Y.-C.; Wang, J. T.-W.; Chang, C.-S.; Li, L.-J.; Lin, T.-W. Synthesis of Large-Area MoS_2 Atomic Layers with Chemical Vapor Deposition. *Advanced Materials* **2012**, *24*, 2320–2325.

[33] Najmaei, S.; Liu, Z.; Zhou, W.; Zou, X.; Shi, G.; Lei, S.; Yakobson, B. I.; Idrobo, J.-C.; Ajayan, P. M.; Lou, J. Vapour phase growth and grain boundary structure of molybdenum disulphide atomic layers. *Nature Materials* **2013**, *12*, 754–759.

[34] van der Zande, A. M.; Huang, P. Y.; Chenet, D. A.; Berkelbach, T. C.; You, Y.; Lee, G.-H.; Heinz, T. F.; Reichman, D. R.; Muller, D. A.; Hone, J. C. Grains and grain boundaries in highly crystalline monolayer molybdenum disulphide. *Nature Materials* **2013**, *12*, 554–561.

CHAPTER 2

Experimental setup, techniques and data analysis

The experiments discussed in this work were performed mostly at the SuperESCA beamline of the Elettra synchrotron radiation facility in Trieste (Italy). Elettra is a third generation light source that covers a spectral range spanning from infrared to hard X-rays and provides light for different experimental techniques that include spectroscopy, microscopy, diffraction, scattering and lithography. The synchrotron radiation is produced by bunches of relativistic electrons accelerated on a curved trajectory. As a result a highly collimated beam of photons is emitted in the tangential direction. [1, 2] The electron bunches are initially produced by a linear accelerator and supplied to the electron storage ring via a booster ring that provides electrons at full energy in order to maintain the machine operations in a top-up mode by maintaining constant current during the runtime. In the storage ring kept at base pressure of $\sim 10^{-9}$ mbar, the bending magnets are used to keep the electrons in the orbit and produce a very broad band spectrum. Other magnetic devices such as quadrupoles and sextupoles are used to control the trajectory of the electrons, and the radio-frequency cavities reintegrate the energy lost by the electrons as emitted radiation. High brilliance X-rays are generated by insertion devices that are integrated at the straight sections of the storage ring. The undulators, consisting of two periodic arrays of magnets, force the incoming electrons to follow a wiggling trajectory and emit radiation. The synchrotron offers many advantages over conventional X-ray sources, such as the high brilliance, defined as the photon flux per unit time per unit solid angle and unit solid area for photons falling within a bandwidth of 0.1% of central frequency: it is 10 billion times higher than other conventional X-rays sources. Another fundamental advantage is the energy tunability that makes

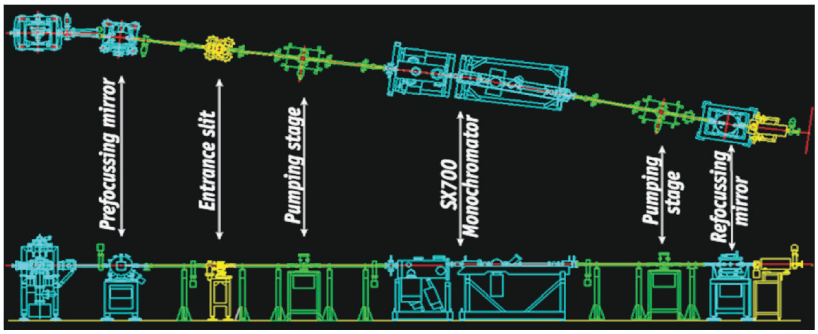

Figure 2.1: Schematic drawing of the SuperESCA beamline at Elettra

wide range of photon energy available to users. Contrarily the photon energy of a conventional sources is fixed and depends on the anode material used. It is also possible to exploit higher degree of polarization while utilizing synchrotron radiation.

2.1 SuperESCA beamline at Elettra

SuperESCA was the first beamline to operate at Elettra [3] and it is optimized for photoelectron spectroscopy measurements with soft X-rays (0.09-2.5 keV). Horizontally polarized X-rays are generated from a two sections 46 mm period undulator with 98 periods. The photon energy range spans from 90 eV up to 1800 eV (depending also on the electron energy of the storage ring). The energy of the incoming photons is varied by changing the undulator gap value from 13.5 to 40 mm. The X-ray beam produced by the undulator is pre-focused in the sagittal plane onto the entrance slit of the monochromator (a SX700 plane grating monochromator (PGM)), then monochromatized and finally re-focused into the center of the experimental chamber by an ellipsoidal refocusing mirror. Schematic drawing of the SuperESCA beamline is shown in figure 2.1. The beamline end station (as shown in figure 2.2) consists of two ultra-high vacuum (UHV) chambers (with a base pressure of 10^{-10}-10^{-11} mbar) used for sample preparations and spectroscopy measurements. It is vital for photoelectron spectroscopy experiments to realize such a low pressure. The mean free paths of atoms, molecules and ions depends on the residual pressure, as shown below,

$$\lambda = \frac{k_B T}{\sqrt{2} P \sigma} \tag{2.1}$$

where k_B is the Boltzmann constant, T is the temperature and σ being the effective cross section in the classical theory for scattering. In order to keep the mean free path of the emitted photoelectrons large enough to allow them

to reach the analyzer without being scattered by the residual gas molecules, the pressure in the measurement chamber has to maintained below 10^{-5} mbar. UHV is also important to prepare and maintain the atomically clean surface (free from contaminants), in order to allow the measurements on a well defined system. The flux of molecules impinging the surface is given by the Hertz-Knudsen formula [4] (Equation 2.2),

$$\Phi = \frac{P}{\sqrt{2mk_BT}} \tag{2.2}$$

where P is the gas pressure, m is the molecular mass and T is the gas temperature. Assuming the sticking probability of the contaminants to be 1, it can be deduced that if the background pressure is $\sim 10^{-6}$ mbar than the surface would be completely covered by the contaminants in just a few seconds. Thus in order to maintain the sample surface clean for a significant amount of time to perform the experiments, the base pressure has to be maintained in the 10^{-10} mbar pressure range. For this reason, a stainless steel chamber with efficient pumping system is used and a bake out procedure is carried out for water desorption from the inner wall of the chamber. The two UHV chambers of SuperESCA are placed one on top of the other and are separated by a gate valve, as shown in figure 2.2.

The upper chamber chamber is dedicated to the preparation of the samples and is equipped with a sputter gun (ion beam energy 0.1-3 keV) for sample cleaning, a plasma source, a gas line and several feed-through ports for evaporators. This chamber is also connected with a fast entry lock system that makes it possible to change sample without breaking the UHV conditions. The experimental chamber at the bottom is made up of μ-metal, a particular Ni-Fe alloy with a high magnetic permeability, in order to screen stray magnetic fields that might effect the electrons trajectory. This chamber is equipped with a Low Energy Electron Diffraction (LEED) setup, a monochromatized electron gun, a mass spectrometer, a gas inlet system, and an electron energy analyzer. The evaporators are placed inside the experimental chamber for performing the in-situ growth and measurements.

Two different manipulators were used to move the sample from the preparation to the main chamber and for performing the experiments. The first is a modified CTPO manipulator (from VG) with 5 degrees of freedom that allows to move 3 translational (x, y, z) and 2 rotational (θ, ϕ) axes. With the availability of its fully motorized rotational movements, this manipulator is specifically designed for X-ray Photoelectron Diffraction (XPD) experiments, where the photoemission intensity is measured as a function of the emission angle. The other manipulator is a liquid He cryostat with four degrees of freedom (x, y, z, θ) and a possibility to vary sample temperature in the range 20-1600 K, though the movements are manually controlled. The photoelectrons are collected by the SPECS GmbH PHOIBOS electron energy analyzer with a mean radius of 150 mm. The analyzer has a hemispherical geometry with two concentric electrodes of different radii (R_1 and R_2). The

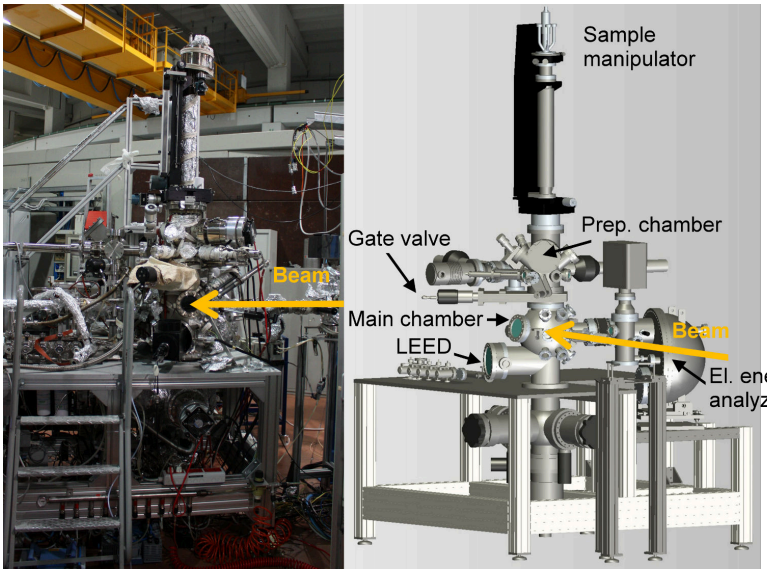

Figure 2.2: Experimental end station of the SuperESCA beamline at Elettra.

incoming electrons are linearly dispersed at the exit slit where the detector is mounted (depending on their kinetic energy). The potential difference between the electrodes that is required in order to allow the photoelecton with a given kinetic energy E_0 to reach the exit slit is as follows,

$$V_2 - V_1 = V_0 \left(\frac{R_2}{R_1} - \frac{R_1}{R_2} \right) \tag{2.3}$$

E_0 is also known as Pass Energy, where $E_0 = eV_0$. Only electrons with kinetic energy E_0 will follow an orbit with radius $R_0 = (R_1 + R_2)/2$, that will allow them to reach the exit slit and be measured. The total energy resolution of the instrument depends on the eventual divergence of the electron beam (represented by an angular offset α from the normal to the entrance slit), on the selected pass energy and on the geometrical parameters of the analyzer given by,

$$\Delta E = E_0 \left(\frac{w}{2R_0} + \frac{\alpha^2}{4} \right) \tag{2.4}$$

where w is the average width of the entrance and exit slits. It is clear from Eq. 2.4 that the energy resolution can be improved either by increasing R_0 or by decreasing E_0. While the radius of the analyzer is limited by technical constraints, the electron transmission is damped while reducing the pass energy (E_0). Thus, a choice has to be made between higher resolution and count rate in order to obtain a spectrum with good signal to noise ratio. Moreover, in order to measure a photoemission spectrum with a constant resolution throughout

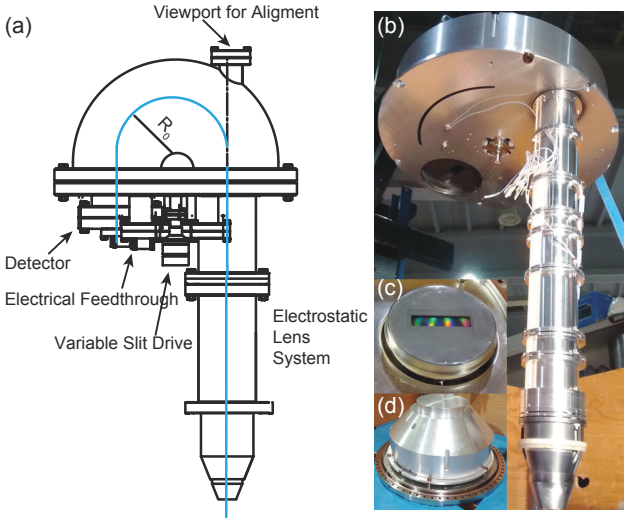

Figure 2.3: (a) Schematic drawing of a hemispherical electron analyzer (path followed by photoelectrons is shown in blue stroke) and (b) Photograph of the analyzer exposing the electrostatic lenses, the top side of the detector showing the microchannel plates (c), and the exposed outer hemisphere of the electron energy analyzer (d).

the whole energy range, the entire photoemission spectrum is recorded at a fixed value of the pass energy (E_0). A major role in this achievement is played by the system of electrostatic lenses placed before the entrance slit which is performing two very important functions. Firstly, it collects the electrons from a solid angle (as large as possible) and then focuses them into the entrance slit. Secondly, it decelerates the incoming photoelectrons to the required value of kinetic energy given by the fixed pass energy (E_0). The analyzer of SuperESCA is equipped with a home-made photoelectron delay-line detector, developed at Elettra-Sincrotrone Trieste. [5] The photoelectrons are collected by two microchannel plates (MCPs) placed in chevron configuration acting as electron multipliers. When the electron cloud from the MCPs stage impinges on the detector, it generates two signals that travel in opposite directions towards the two ends of the delay line. The outputs are then amplified, discriminated and processed by a time to digital converter, which measures the delay time between the two signals and converts it into a spatial information on the position of the incident electron cloud, giving access to the energetic distribution along the analyzer dispersive direction of the exit slit.

The analyzer can be operated in two possible working configurations, i.e. scanning (*sweep*) mode and fixed (*snapshot*) mode. In the scanning mode, the voltages of the two hemispheres V_1 and V_2 (and therefore the pass energy (E_0)) are kept constant while sweeping the voltage applied to the electrostatic lenses. In this way each channel counts electrons with the selected kinetic

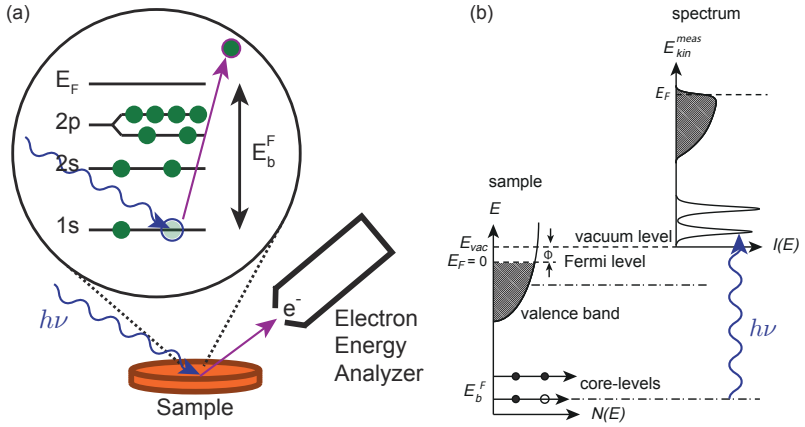

Figure 2.4: (a) The photoelectric effect. An electron is removed from a core level following excitation through a photon with energy $h\nu$. (b) Schematic representation of the energies involved in photoelectron spectroscopy.

energy for an interval equal to the selected time window. While operating in the fixed mode the acquisition time can be drastically reduced. This procedure exploits the relation between the energy of the electron and its position on the detector. If the energy range covered by the detector is wide enough and if the number of available channels is sufficiently high to clearly resolve the photoemission features, it is possible to acquire a detector image and obtain the photoemission spectrum in one single shot. This allows not only to monitor in real-time chemical reactions occurring at solid surfaces but also to prevent sample contamination due to residual gas during time consuming measurements that require the acquisition of thousands spectra, as in the case of the XPD measurements discussed in more detail in the sections 2.3.

2.2 Chemical analysis - X-ray photoelectron spectroscopy

When a photon with sufficient energy interacts with matter, it can remove an electron from an atomic orbital or an electronic band, promoting it above the vacuum level with a certain kinetic energy, as shown in figure 2.4. This phenomenon is called photoelectric effect. Photoelectron spectroscopy is based on this effect that was explained by Albert Einstein in 1905, for which he was awarded the Nobel Prize in Physics in 1921. The photoemission from solids can be described as three step process. [6] Sequentially, electron excitation due to absorption of radiation, followed by the propagation of photoelectron to the surface and their subsequent escape into the vacuum. For this event to take place, the energy of the incoming photon (photon transfers its energy

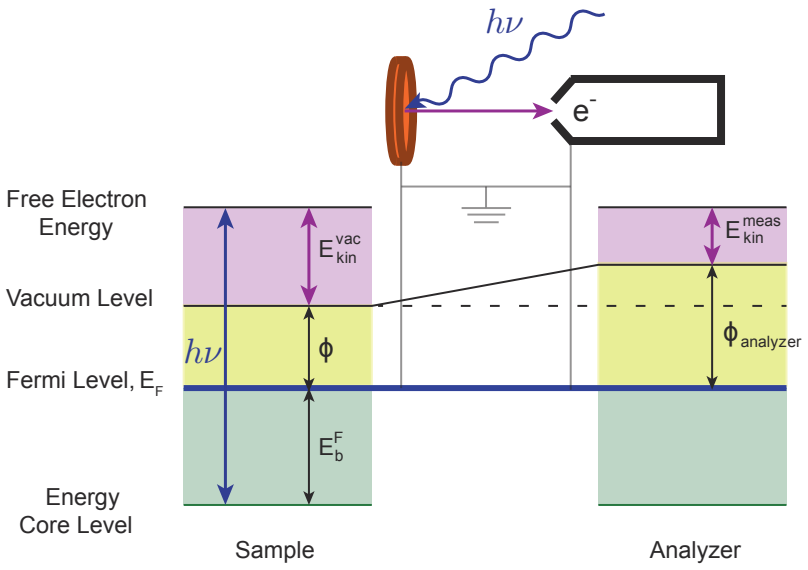

Figure 2.5: Energy level diagram for a XPS experiment.

completely to the solid) must be higher than the binding energy of the electrons in the solid state plus the work function of the solid and the number of the event is proportional to the intensity of the radiation. Following the energy conservation law within the one-electron approximation, we can write

$$E_{kin}^{vac} = h\nu - E_b^F - \phi \tag{2.5}$$

where (E_{kin}^{vac}) is the kinetic energy, $h\nu$ is the photon energy, E_b^F is the binding energy referenced to the Fermi level (E_F) and ϕ is the specific work function of the material. This was used by K. Siegbahn (Nobel Prize for Physics, 1981), who developed the Electron Spectroscopy for Chemical Analysis (ESCA) technique, [7] popularly known as X-ray Photoelectron Spectroscopy (XPS), as an analytical tool to study the composition and the chemical state of sample surface. From equation 2.5, it is possible to estimate E_b^F experimentally, if the other quantities are known. In the most general configuration of the XPS experimental arrangement, both the sample and the analyzer are grounded together, so that their respective Fermi levels align (figure 2.5) leading to a potential difference between the sample's and the analyzer's vacuum levels. Upon reaching the analyzer the photoelectron feels the difference in work function (with respect to the sample work function) and its kinetic energy gets modified. Thus, using the kinetic energy of the photoelectron inside the analyzer, E_{kin}^{meas}, the equation 2.5 can be re-written as

$$E_b^F = h\nu - E_{kin}^{meas} - \phi_{analyzer} \tag{2.6}$$

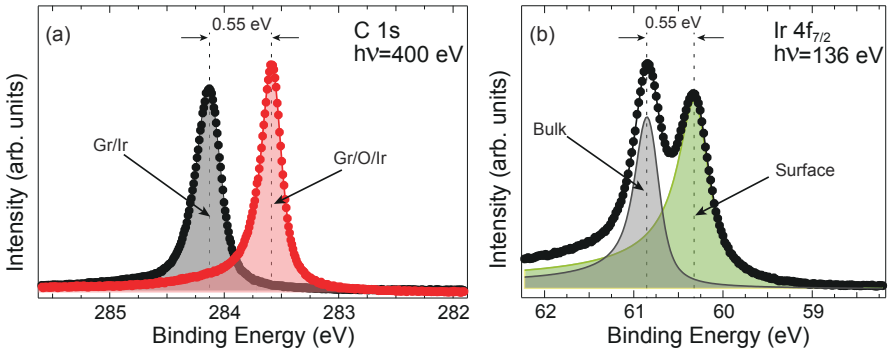

Figure 2.6: High resolution XPS spectra exhibiting chemical sensitivity by the means of binding energy shifts. (a) C 1s core level for graphene grown on Ir(111) substrate (in grey) is shifted to 0.55 eV lower binding energy when 0.66 monolayer of oxygen is intercalated below graphene (in red) as a result of p-doping. (b) Surface-core level shift displayed by the Ir $4f_{7/2}$ core level spectrum discriminates between the atoms belonging to the crystal bulk (in grey) and the surface layer of the Ir(111) surface.

where the work function of the electron energy analyzer $\phi_{analyzer}$ is a known value. It is therefore enough to know the photon energy and using the analyzer's work function one can easily calculate the binding energy of a photoelectron just by measuring its kinetic energy, although, while measuring little shifts in binding energy, small errors could effect the accuracy of the measurements. It is therefore necessary, to also acquire a energy distribution curve around the Fermi level for each core level spectrum, in order to carry out a direct calibration for each measurement. Since E_b^F is characteristic for each element and the value in a solid or in a molecule is similar to the one of the free atom, XPS can be used for chemical identification. The formation of a chemical bond or a change in the oxidation state affects the charge density and distribution, which is also perceived by the core electrons and, as a consequence, the core level binding energy is slightly altered. A particular form of chemical shift, Surface Core Level Shift (SCLS), originates as consequence of different coordination of the surface atoms with respect to the bulk in a solid. The SCLS is extremely useful while performing studies of the reactivity at surfaces (see figure 2.6(b)), as it permits to obtain information on what is happening to the sample surface atoms, for example during a chemical reaction. Chemical sensitivity is one of the most striking features of the XPS technique. With the remarkable development in the field of electron energy analyzers and X-ray sources, it is also possible to determine the chemical shift (see figure 2.6(a)), due to the presence of atoms or molecules in different structural and/or chemical environments. In addition to this, it is possible to distinguish among chemically non-equivalent atoms within a molecule or, considering photoemission from a solid, to discriminate between suface and bulk atoms. [9]

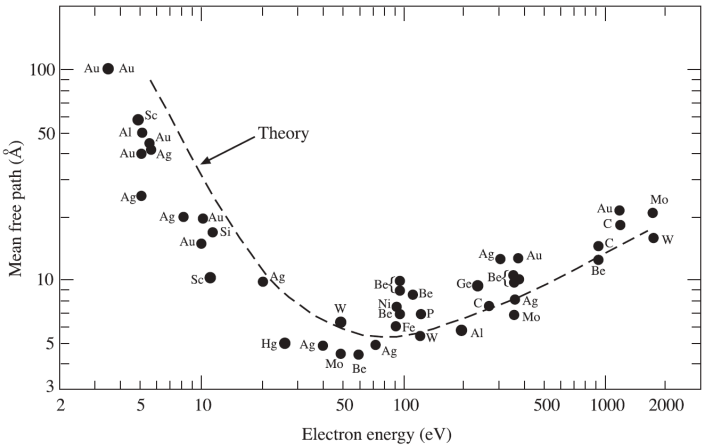

Figure 2.7: Universal curve of the electron IMFP as a function of the electron kinetic energy. [8]

Furthermore, one of the most characteristic properties of photoemission spectroscopy is its surface sensitivity, given by the inelastic mean free path (IMFP) of the electrons, i.e. the average distance that an electron can travel before losing energy. The IMPF as a function of the electron kinetic energy (Fig.2.1), is represented by the universal curve, that shows a minimum for the kinetic energies between 50 and 100 eV. Generally, the IMFP is less than 10 Å for energy ranging from 20 to 500 eV, which means that only photoelectrons emitted from the first few layers of the material can escape into the vacuum and be detected. This makes XPS an exceptional technique to study thin films, surfaces and interfaces.

Quantum mechanically the photoemission process can be described by as the transition of an electron in initial (ground) state defined by wave function ψ_i and energy E_i, to a final state ψ_f with energy E_f by the absorption of radiation. The time-dependent Schrödinger equation is given by

$$\hat{H}\psi(t) = \iota\hbar\frac{\partial\psi(t)}{\partial t} \tag{2.7}$$

for the electron wave function

$$\psi(t) = \sum_n c_n\psi_n e^{\iota\frac{E_n}{\hbar}t} \tag{2.8}$$

and the Hamiltonian operator of the form

$$\hat{H} = H_0 = -\frac{\hbar^2}{2m_e}\nabla^2 + U(r) \tag{2.9}$$

with ∇^2 being the Laplacian and $U(r)$ the potential energy of the electron before the perturbation takes effect. With the onset of perturbation, the Hamiltonian

is then modified to account for the perturbation of the form $U(t)$

$$\hat{H} = H_0 + U(t) \tag{2.10}$$

By applying equation 2.10 to equation 2.7 within the one-electron approximation, we obtain the transition probability P_{if} that is defined as the probability that a transition from an initial state i to a final state f will take place.A better understanding is possible while working with transition probability per unit time ($W_{if} = P_{if}/t$), that also solves the problem of $P_{if} \to \infty$ as $t \to \infty$,

$$W_{if} = \frac{2\pi}{\hbar} \left|\langle \Psi_f | \, U \, | \Psi_i \rangle\right|^2 \delta(E_f - E_i + h\nu) \tag{2.11}$$

where $\langle \Psi_f | \, U \, | \Psi_i \rangle$ is the matrix element that describes the perturbation of the form U action on initial state ψ_i and bringing the system in to final state given by ψ_f. The equation 2.11 is known as Fermi golden rule and describes the transition rate for excitation from initial state to final under the effect of induced perturbation. The $\delta(E_f - E_i + h\nu)$ term corresponds to the energy conservation during the photoelectric process. Mathematically, the electromagnetic perturbation (absorption of a photon) is of the form

$$U = -\frac{i\hbar e}{2mc} \nabla \cdot \mathbf{A} - \frac{i\hbar e}{mc} \mathbf{A} \cdot \nabla + \frac{e^2}{2mc^2} \left|A\right|^2 - e\phi \tag{2.12}$$

where $\mathbf{A}$ and ϕ are the vector and scalar potential respectively. Assuming

$$\nabla \cdot \mathbf{A} = 0 \qquad \text{and} \qquad \phi = 0 \tag{2.13}$$

and that the week field leads to $\left|A\right|^2 \cong 0$ and also defining a momentum operator $\mathbf{p} = -i\hbar\nabla$, we can rewrite the transition rate defined in Eq. 2.11 as,

$$W_{if} = \frac{2\pi}{\hbar} \left|\langle \Psi_f | \, \mathbf{A} \cdot \mathbf{p} \, | \Psi_i \rangle\right|^2 \delta(E_f - E_i + h\nu) \tag{2.14}$$

The quantitative analysis of the photoemission spectra makes use of the dependence of the photoemission intensity on the photoioniztion cross-section, σ, that describes the transition probability per unit time of exciting a system from an inital state Ψ_i to a final state Ψ_f by absorbing a photon with energy $h\nu$.

The photoemission cross-section is a scalar quantity given by

$$\sigma_{fi} = \frac{4\pi^2 e^2}{3\hbar c} \omega \left| \, \langle \Psi_f | \, \hat{\mathbf{r}} \, | \Psi_i \rangle \, \right|^2 \tag{2.15}$$

where $\hat{\mathbf{r}}$ is the position operator. As the cross-section is characterized by the radial part of the wave function, the photoemission cross section depends on the different atomic levels defined by the quantum numbers n and l. However, it

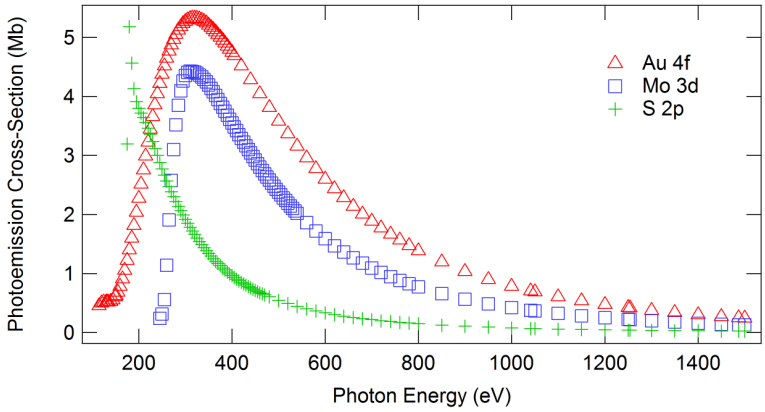

Figure 2.8: Photoemission cross-section for Au $4f$, Mo $3d$ and S $2p$ core levels as a function of the energy of the incident photons ($h\nu$).

is not dependent on the chemical environment of the atoms and so it is feasible to make use of the calculated atomic cross-sections. [10]

The variation of the photoemission cross-section depending on photon energy for some of the core levels investigated in this work is shown in figure 2.8. This modulation of the cross-section highlights the advantage of synchrotron radiation facility (tunability of photon energy) that allows the possibility to select an appropriate photon energy in order to maximize the sensitivity to a specific core level.

2.3 Structural determination - X-ray photoelectron diffraction

A proper understanding of local structures is an important parameter, in order to unfold the mechanism governing the growth of materials on the surface, to conceptualize the physical and chemical interaction between the adsorbate and the substrate, and to characterize the unique processes aided by the atomically clean surfaces. The structural information also provides the basis for the understanding of the electronic properties of novel materials.

X-ray Photoelectron Diffraction (XPD) is a powerful surface sensitive technique to study local geometry of surfaces and adsorbates. Following the excitation due to the incoming photon, the photoemitted electron from the core level of an atom on the surface can reach the analyzer directly or it can be elastically scattered by the atoms surrounding the emitter, as shown in figure 2.9. The coherent interference between the directly emitted photoelectron wave and the scattered photoelectron waves will induce modulations in the photoemission intensity detected by the analyzer. These

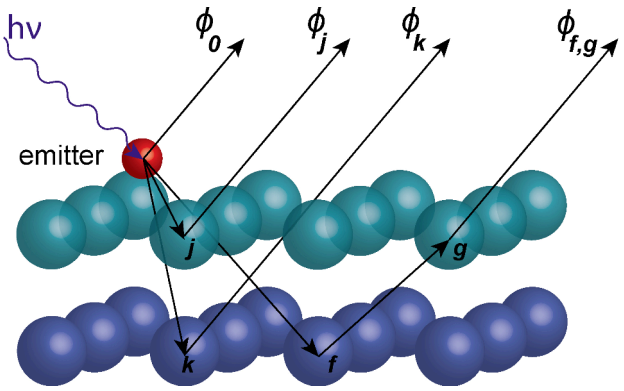

Figure 2.9: Sketch of the photoelectron diffraction process.

modulations, that depend on the kinetic energy of the emitted photoelectron and the emission direction, are an imprint of the scattering factor and the pathlength difference and provide precise information about the local structural geometry around the emitter atom. Therefore, by circumventing the requirements for a long range order as is needed in the case of low energy electron diffraction (LEED), the XPD technique acting as a probe of local structure allows the study of materials that are difficult to arrange in extended ordered structures. An important feature of this technique is that it is element specific, since the core level binding energies are characteristic of the chemical identity of the emitter atom. Thus XPD can be used to study the structure around different elements in the same layer independently and to classify distinct structures in complex materials. In a simplified approach, the photoelectron diffraction process can be described using the single scattering approximation, accordingly

$$|\psi_f\rangle = \phi_0 + \sum_j \phi_j(\mathbf{r}_j \rightarrow \mathbf{k}) \tag{2.16}$$

where ϕ_0 is the emitted plane wave, while ϕ_j is the wave singly scattered at $\mathbf{r}_j$ and emerging along the $\mathbf{k}$ direction. The photoemission intensity can therefore be expressed as,

$$\begin{aligned} I(\mathbf{k}) \propto \Big| & \hat{\boldsymbol{\epsilon}} \cdot \hat{\mathbf{k}} e^{-L/\Lambda_e} + \\ & + \sum_j \frac{\hat{\boldsymbol{\epsilon}} \cdot \hat{\mathbf{r}}_j}{r_j} |f_j(\theta_j)| W_j e^{-L_j/\Lambda_e} e^{i[kr_j(1-\cos\theta_j)+\varphi_j(\theta_j)]} \Big|^2 \end{aligned} \tag{2.17}$$

where the term $\hat{\boldsymbol{\epsilon}} \cdot \hat{\mathbf{k}}$ is associated with the directly emitted wave, whereas the sum is extended to all spherical photoelecton wavefront of the scattered

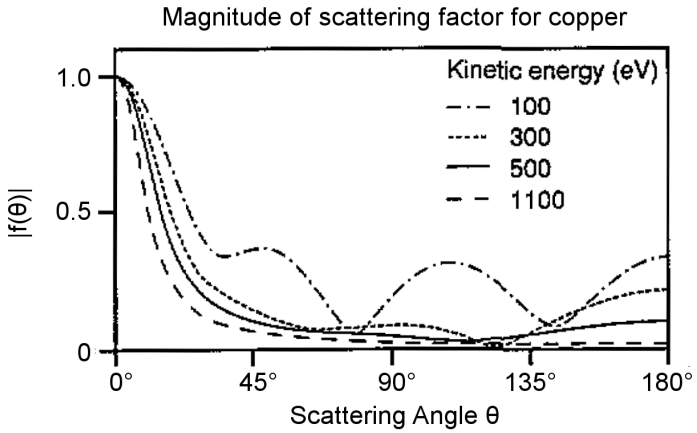

Figure 2.10: The scattering factor, $f(\theta)$, for a copper atom as a function of the scattering angle and for different electron kinetic energies.

electrons by an atom located at $\mathbf{r}_j$ with an amplitude given by $|f_j(\theta_j)|$. The inelastic scattering is taken into account by the exponential terms given by e^{-L/Λ_e} and e^{-L_j/Λ_e}, with $L(L_j)$ being the total path length of the photoelectron. Vibrational effects, that can attenuate the modulations registered in XPD experiment, are included through the Debye-Waller factor W_j. Also, the phase shift φ_j of each spherical wave is determined by the scattering process and the path difference $kr_j(1-\cos\theta_j)$ between the incident and scattered waves. The atomic scattering cross section of an electron and its dependence on the kinetic energy and the scattering direction is another important parameter that influences the XPD experiments. The scattering at atom j is governed by the scattering factor $f_j(k,\theta_j)$, a complex number, given by

$$f_j(k,\theta_j) = |f_j(k,\theta_j)|e^{i\chi_j(\theta_j)} \tag{2.18}$$

where the imaginary part $\chi_j(\theta_j)$ accounts for the scattering phase shift, while the magnitude determines the scattering intensity.

A general behavior of the magnitude of the scattering factor, $f(\theta)$, as a function of scattering angle, at different electron energies, is shown in figure 2.10 for a Cu atom. [11] An intense peak is present for the scattering angle, $\theta = 0°$, and gets sharper with increasing electron kinetic energy. This is known as the forward scattering effect, which is useful in determining the interatomic bond directions at crystal surfaces. Apart from the intense peak, the high energy forward scattering event involves very small scattering phase shift. In these conditions the interference between the direct and the scattered waves is always constructive. For example, as depicted in figure 2.11, when the scatterer is placed between the emitter and the analyzer the photoemission intensity is enhanced as a result of constructive interference between the

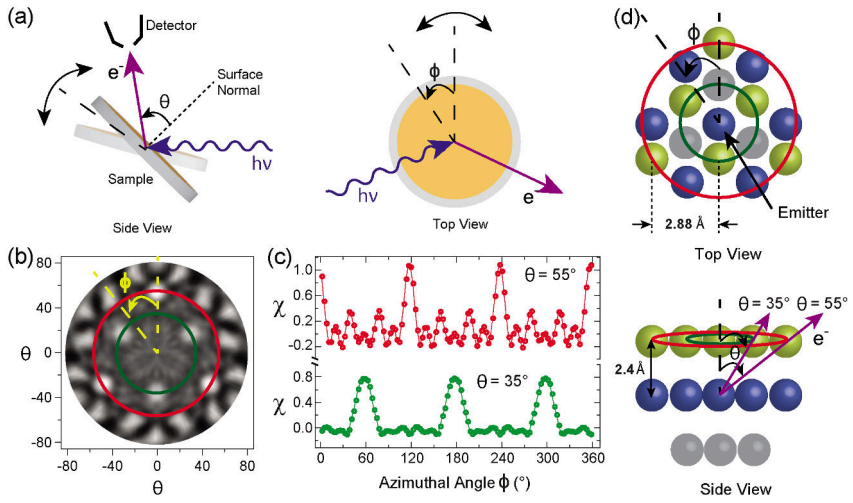

Figure 2.11: (a) Schematic diagram showing details of the sample movement while acquiring the photoemission diffraction data at SuperESCA beamline. (b) The stereographic projection of the XPD pattern simulation for Au 4f core level of the Au(111) sample performed using EDAC package [12] at 1000 eV kinetic energy is shown depicting the forward scattering condition. (c) Intensity modulation function for the azimuthal angle ϕ scan corresponding to the polar angle cuts ($\theta = 35^\circ$ (green) and $\theta = 55^\circ$ (red)) on the XPD pattern. (d) Au(111) crystal lattice structure with parameters taken from reference [13], used for simulating the XPD pattern in (b), showing calculated bond angle directions based on parameters mentioned in reference, between the top surface layer and the second layer that corresponds to the maxima in the modulation function and satisfies the forward scattering condition.

directly emitted and the scattered wave. Another feature of the scattering factor is the backscattering. At $\theta = 180^\circ$ (figure 2.10) is enhanced when the photoelectron kinetic energy is low, thus making it suitable to study the adsorbate atom geometry on the surface by utilising the photoelectrons elastically scattered by the atoms behind the emitter atom. Thus XPD experiments can be performed either by constraining the kinetic energy and varying the emission angle or by constraining the emission geometry and spanning the photon energy to vary the photoemission kinetic energy. The photoelectron diffraction experiments performed at the SuperESCA beamline and discussed in this thesis were performed following the former methodology: while keeping the photoelectron kinetic energy constant, the 5-degree of freedom manipulator (x, y, z, θ, ϕ) allowed sequential movements along the polar angle θ (angle between the emitted photoelectron and the normal to the surface) and azimuthal angle ϕ, as shown in figure 2.11 (a). The angular resolution of the experiments presented in this thesis was better than $\pm\ 2^\circ$.

For more detailed interpretation and understanding of the diffraction

patterns, it is important to include multiple scattering effects in the diffraction pattern simulations. In this regards, one of the most popular methods to perform multiple scattering calculations is based on the separable representation of the Green's function matrix, first developed by Rehr and Albers. [14] Thus, the theoretical calculations can be compared to the experimental diffraction patterns in order to extract detailed information about the short-range structure around the emitting atom. All the theoretical simulations that are presented in this thesis have been performed using the Electron Diffraction in Atomic Clusters (EDAC) package. [12] The working principle of this code is based on the implementation of an atomic cluster and the use of multiple scattering theory to model the XPD pattern for a specific electron kinetic energy. Furthermore, the simulated patterns are compared with the experimental data utilizing procedure discussed in the data analysis part of this chapter.[1]

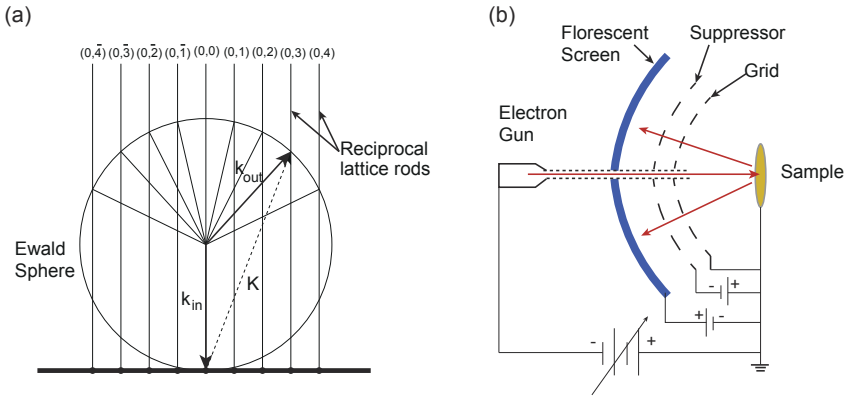

Figure 2.12: (a) Ewald construction for 2D surfaces in 3D space. Modulus of the incoming electron wave vector k_{in} gives the radius of the sphere, while the reciprocal lattice points for the 2D surface forms the rods perpendicular to the surface. The Laue condition for diffraction is fulfilled by the intersection of the Ewald sphere with the reciprocal lattice rods which gives the direction of the scattered beam. (b) Schematic diagram of a LEED apparatus. The incoming and the scattered electron directions are marked with red arrows.

[1]For further details on the EDAC code the reader is referred to the reference manual available online at http://garciadeabajos-group.icfo.es/widgets/edac/manual/edac.html

2.4 Surface long range order - Low energy electron diffraction

Low Energy Electron Diffraction (LEED) is one of the most commonly used surface science technique that is capable of determining long range order of solid surfaces. Davisson and Germer, while studying the reflection of electrons from a nickel surface in the year 1927, [15] discovered that the electrons (in the energy range 5 - 500 eV) interacted with the crystal target producing diffraction patterns and provided an experimental basis to the concept of wave-particle duality. Already after its discovery, low energy electron diffraction came to be recognized for its potential in determining surface structures. Following the development in vacuum technology, simple experimentation procedure and reduced cost of the instrument have resulted to its spread to almost every surface science laboratory. The analysis of the spot positions yields information on the size, symmetry and rotational alignment of the adsorbate unit cell with respect to the substrate unit cell, while the study of spot intensity with respect to the electron beam energy provides structural information upon comparison with theoretical simulations. One of the most striking features of LEED is its surface sensitivity: the electrons in a typical LEED experiment have an energy of 40 eV to 400 eV, as the incoming electrons interact with the atoms of the target, they could penetrate into the solid for only a few angstroms following the 'universal curve' of the inelastic mean free path shown in figure 2.7. Thus, the diffraction spots usually carry information about the top few layers ($\sim$ 10 Å) of the material under study.

Following the de Broglie's hypothesis of the wave nature of the electron, in the single scattering approximation (kinematic theory), where the electrons impinging on a well-ordered crystal surface are elastically scattered only once, the electron beam is represented by a plane wave with wavelength λ,

$$\lambda = \frac{h}{\sqrt{2mE}} \tag{2.19}$$

where E is the energy of the incoming electron. The most convenient way of describing the interactions between the incoming electron beam and the scatterers on the surface is considering the reciprocal space. For the incoming electron with the wave vector $\mathbf{k_{in}}$ and the scattered wave vector $\mathbf{k_{out}}$, the condition for constructive interference is given by the Laue condition as,

$$\mathbf{k_{in}} - \mathbf{k_{out}} = \mathbf{K} \in G \tag{2.20}$$

where $\mathbf{K}$ is the scattering wave vector and G is the reciprocal lattice. For an ideal 2D atomic arrangement, there are no diffraction conditions in the direction perpendicular to the surface to be fulfilled. Consequentially, the reciprocal lattice for a surface can be visualized as a 2D lattice with rods extending perpendicular from each lattice point. The rods can be pictured as regions

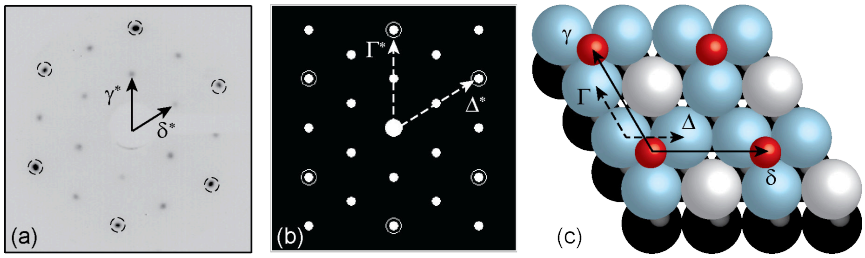

Figure 2.13: Experimental LEED pattern of p(2×2) structure for oxygen adsorbed on Ir(111) surface acquired at 96 eV kinetic energy (a) and the LEEDpat [16] simulation for the same structure showing the reciprocal lattice vectors for oxygen and Ir lattices respectively, where the principle (1×1) Ir spots are encircled. (c) Ball model showing real space lattice vectors for p(2×2) oxygen (red balls) on Ir(111) surface. The real space lattice vectors $\mathbf{\Gamma}$ and $\mathbf{\Delta}$ (for example as shown for Ir lattice in (c)) are related to the reciprocal lattice vectros as $\mathbf{\Gamma}^* = \frac{2\pi(\mathbf{\Delta}\times\hat{\mathbf{n}})}{|\mathbf{\Gamma}\times\mathbf{\Delta}|}$.

where the reciprocal lattice points are infinitely dense. In this way the equation 2.20 can be rewritten as,

$$\mathbf{k}_{\mathbf{in}}^{||} - \mathbf{k}_{\mathbf{out}}^{||} = \mathbf{K} \in G \tag{2.21}$$

where $\mathbf{k}_{\mathbf{in}}^{||}$ and $\mathbf{k}_{\mathbf{out}}^{||}$ are the components of the incident and the scattered wave vectors parallel to the surface. This condition can be visualized through the geometric construction of the Ewald sphere, whose radius depends on the modulus of the **k**-vector of the incident electrons as shown in figure 2.12. The points of intersection between the lines represented by the rods for the reciprocal lattice and the Ewald sphere satisfies the Laue condition for diffraction (Eq. 2.21) and determines the direction of the scattered beam as the elastic scattering is considered, i.e. $|\mathbf{k}_{\mathbf{in}}^{||}| = |\mathbf{k}_{\mathbf{out}}^{||}|$.

The sketch of a typical LEED apparatus is shown in figure 2.12(b). The monochromatic electron beam is focused with the electron gun towards the sample with direction normal to the sample surface. The backscattered electrons are subjected to pass through a grid, in common ground with the sample, which allows the electrons to move in a field-free region. Subsequently, the electrons are exposed to a suppressor grid (at a potential slightly lower than the electron kinetic energy) which clears the inelastically scattered electrons and finally the electrons are accelerated towards the fluorescent screen where they form the diffraction pattern to be recorded by a CCD camera. The full width at half maxima (FWHM) of the diffraction spots is inversely proportional to the average domain size. Thus, the larger the crystal domains on the surface, the sharper are the diffraction spots. The instrumental resolution is also limited by the electron beam angular divergence and its energy spread.

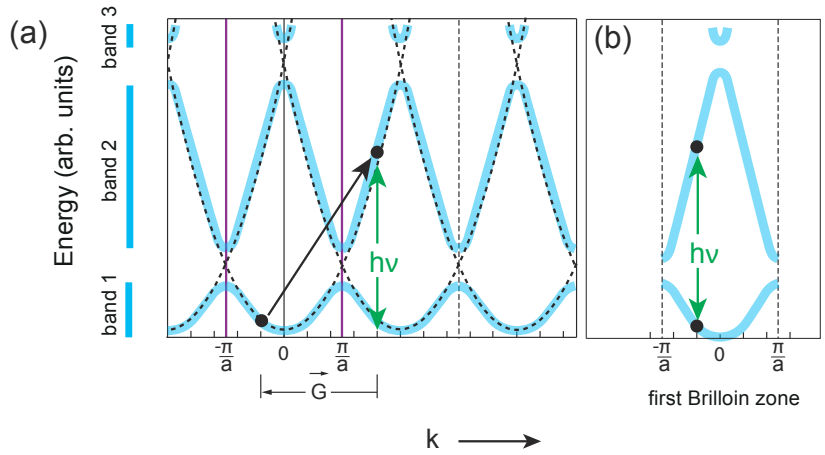

Figure 2.14: (a) The electronic band structure of a one dimensional atomic chain with a lattice constant a shows the dispersion of the form given by equation 2.25. The dashed lines shows the repetitive parabolas centered at $k = 0, \pm\frac{2\pi}{a}$ show the band dispersion in the absence of the periodic potential $U(\mathbf{r})$, while the solid lines shows the splitting of the bands in the vicinity of the brillouin zone boundary ($\pm\frac{\pi}{a}$) due to the non-vanishing fourier coefficients ($U_{\mathbf{G}}$). For a nearly free electron in a constant potential, the energy and momentum can be simultaneously conserved by adding a reciprocal lattice vector $\mathbf{G}$. A similar picture is shown in the reduced zone scheme in (b). The images are adapted from ref. [17].

2.5 Electronic structure - Angle-resolved photoemission spectroscopy

Angle-resolved phototemission spectroscopy (ARPES) is one of the most widely used techniques to study the electronic band structure of solids. As most of the properties of solids (such as structure, conductivity, superconductivity, magnetism and so on) are directly related to the valence band electrons, ARPES is one of the most important probes to obtain information on the band dispersion.

The electronic structure of solids can be understood on the basis of a simple model consisting of a one-electron approximation within a potential due to the ions and other electrons. For this case the Schrödinger equation can be written as

$$\hat{H}\psi(\mathbf{r}) = E\psi(\mathbf{r}) = \frac{-\hbar^2}{2m_e}\nabla^2\psi(\mathbf{r}) + U(\mathbf{r})\psi(\mathbf{r}) \tag{2.22}$$

where $U(\mathbf{r}) = U((\mathbf{r}) + (\mathbf{R})) = \sum_{(\mathbf{G})} U_{\mathbf{G}} e^{i\mathbf{G}\cdot\mathbf{r}}$ is the lattice periodic potential. The solution of the equation 2.22 are given by the Bloch theorem and the corresponding electrons are expressed as Bloch waves given by the wave function

$$\psi_{\mathbf{k}}(\mathbf{r}) = u_{\mathbf{k}}(\mathbf{r}) e^{i\mathbf{k}\cdot\mathbf{r}} \tag{2.23}$$

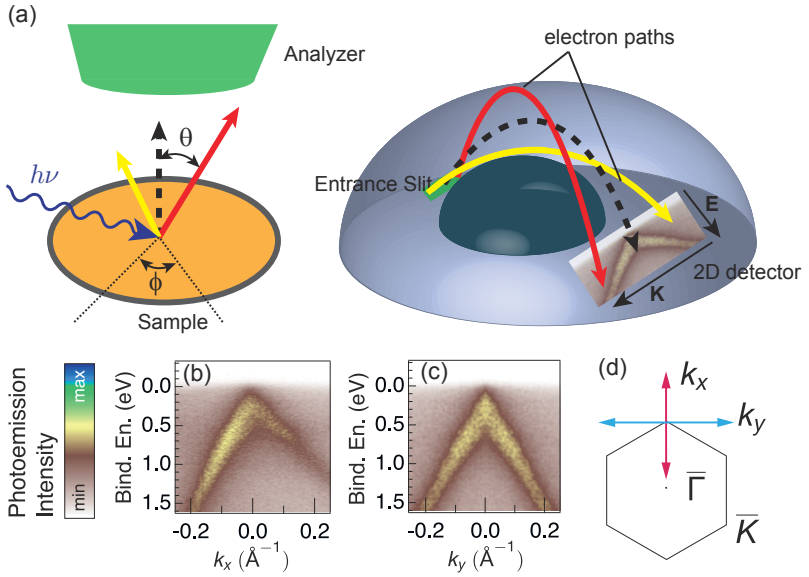

Figure 2.15: (a) Schemetic diagram of the 2D detector used in ARPES measurements showing the different trajectories followed by the photoelectrons with distinct kinetic energy and emission direction. The band structure of lifted graphene (via oxygen intercalation) on Ni(111) at photon energy of 34 eV, showing the details of Dirac cone at/near $\bar{K}$ point of the graphene brillouin zone corresponding to (d), in the (b) $\bar{\Gamma}\bar{K}$ direction and (c) direction perpendicular to $\bar{\Gamma}\bar{K}$. Band dispersion images adapted from ref. [18].

with lattice periodic function $u_{\mathbf{k}}$. Where the wave function ($\psi_{\mathbf{k}}(\mathbf{r}) = \psi_{\mathbf{k}+\mathbf{G}}(\mathbf{r})$) is given by reciprocal lattice vector $\mathbf{G}$. As a result the energy is also conserved when propagated along $\mathbf{G}$

$$E_{\mathbf{k}} = E_{\mathbf{k}+\mathbf{G}} \tag{2.24}$$

A simple picture of electronic band dispersion in the k-space for a one dimensional periodic lattice with periodicity a is shown in figure 2.14 (a) and (b). The parabolic bands (centered at $k = 0$ and $k = \pm\frac{2\pi}{a}$) are represented as the solution of Schrödinger equation for a particle in a potential well given by energy eigenvalues

$$E_{\mathbf{k}} = \frac{\hbar^2|\mathbf{k}|^2}{2m_e} \tag{2.25}$$

where the dashed line represents the bands in the presence of a lattice potential $U(\mathbf{r}) \sim 0$ and presents the motion of nearly free electrons (similar to those in metals). However depending upon the lattice potential $U(\mathbf{r}) \neq 0$ the bands split at the Brillouin zone boundaries as shown by the dark stroke lines (similar to those in semiconductors and insulators).

It is clear that in order to map the electronic band dispersion the information on the binding energy (E_b) and the corresponding wave vector ($\mathbf{k}$) of the electrons must be recorded. The information about the binding energy comes from the energy conservation in photoemission process also described in equation 2.6. However, obtaining the information about the wave vector ($\mathbf{k}$) is a complex issue due to the fact that only the translational symmetry parallel to the surface is upheld and the symmetry perpendicular to surface is broken. As a result when the photoemitted electron leaves the surface the $k_{\parallel}$ component of the wave vector $\mathbf{k}$ is conserved while the $k_{\perp}$ is not. Anyhow, in our case, related to the study of band structures of 2D materials, in the absence of translational symmetry perpendicular to the surface, we can ignore $k_{\perp}$ and explore the band dispersion ($E(\mathbf{k}\parallel)$) by measuring $k_{\parallel}$ as

$$k_{\parallel} = |\mathbf{k}| sin(\theta) = \frac{\sqrt{2m_e}}{\hbar}\sqrt{E_{kin}^{meas}} sin(\theta) \tag{2.26}$$

and we get all the information about the band structure of 2D materials in a given direction. While performing ARPES measurements the photoemitted electrons from the valence band are recorded as a function of emission direction (represented by polar angle θ and azimuthal angle ϕ) and kinetic energy by using a two-dimensional detector. As shown in the figure 2.15 (a), the photoemitted electrons (red, yellow and dashed black, also the arrow length is a representation of the magnitude of kinetic energy of the photoelectron) that enter the hemispherical analyzer through the entrance slit are dispersed in energy and direction of emission given by the angle θ between the direction of emission and the surface normal (dashed black line). The 2D detector at the end of the analyzer acquires, simultaneously, the position and the energy of the impinging photoelectron. The band dispersion of 2D materials is usually shown via a plot of photoemission intensity as a function of binding energy and the wave vector in a given direction of the brillouin zone. Angle-resolved photoemission spectroscopy measurements [18] on the oxygen intercalated graphene grown on Ni(111) crystal, showing the Dirac cone [19] in the $\bar{\Gamma} - \bar{K}$ direction and the direction perpendicular to the $\bar{\Gamma} - \bar{K}$ direction are shown in figure 2.15 (b) and (c). The respective directions are shown in the marked brillouin zone in figure 2.15 (c).

2.5.1 ARPES measurements at SGM-3 beamline of ASTRID2

The ARPES measurements reported in this work were performed at the SGM-3 beamline located at the synchrotron radiation source ASTRID2 in Aarhus Denmark. [20] This beamline is optimized for valence band photoemission measurements, with a photon energy range of 12-150 eV. The radiation is produced by an undulator, then monochromatized and finally focused onto the sample. The end station consists of two different UHV

chambers: the preparation chamber and the main chamber, where measurements are performed. The two chambers are separated by a gate valve, and are placed side-by-side. Every chamber has its own manipulator. In the preparation chamber, the manipulator is placed horizontally and allow the transfer of the sample to the main chamber. While the six degrees of freedom (x, y, z, θ, ϕ and *tilt*) manipulator in the main chamber is placed vertically on the top flange and allows sample cooling to 30 K using liquid helium. The electron detection system consists of SPECS Phoibos 150 mm hemispherical energy analyzer equipped with a 2D-CCD detector with energy and angular resolution better than 30 meV and 0.2°, respectively.

2.5.2 Spin polarized ARPES measurements at APE beamline of Elettra

The Spin Polarized ARPES measurements reported in this work were performed at the APE Beamline [21] that consists of two spectroscopy end-stations connected to two distinct beamlines: the low energy beamline (APE-LE) that operates within the 8-120 eV photon energy range devoted to high resolution ARPES, and the high energy beamline (APE-HE) that exploits a 150-1600 eV photon energy range. APE-LE hosts VG-Scienta DA30 electron energy analyzer and two very low energy electron diffraction (VLEED) spin polarimeters that operates in deflection mode and allows for detailed k-space mapping at fixed sample geometry (fixed angle). The total measured energy resolution (analyzer, temperature, photons) is $\sim$ 6 meV (at 30 eV photon energy), while the angular resolution is less than 0.2°. Photons with selected polarization are emitted by two non-collinear Apple II type insertion devices. Both end stations are equipped with liquid He cryostats.

2.6 Real space imaging - Scanning tunneling microscopy

The Scanning Tunneling Microscopy (STM) is used for imaging surfaces at atomic level. It was invented by Rohrer and Binning in 1981 at IBM Zurich, [22] for which they were later awarded the 1986 Nobel prize in Physics. Ever since its discovery, the instrument has come a long way, and the extent of STM studies is continuously growing. Apart from basic surface topography, STM (being capable of mapping both occupied and unoccupied states) is being used for chemical identification, atomic manipulation [23] and to study the ground state, vibrational [24] as well as magnetic properties. [25] A basic STM setup as shown in figure 2.16 consists of a sharp probe tip which is attached to a piezoelectric motor. The piezo-motor consists of three mutually perpendicular piezoelectric transducers for the three transversal axes (x, y, z). The contraction/expansion of these piezoelectric transducers, upon the application of a voltage, allows the precise movement of the probe tip on the sample surface. As the tip scans

very close to the surface, STM utilizes the quantum mechanical phenomenon of 'Tunneling' through a barrier. The tunneling current (upon the application of bias voltage across the sample and the probe tip) is recorded for the raster scan and the contour images are produced that represent the electronic density of states (DoS) of the surface. In a way, it is also a drawback of STM that it requires a conducting samples in order to allow the tunneling to take place. One way to acquire the STM images is to measure the tunneling current while rastering the sample with the tip separation kept constant. This is however not so common in practice as the sample surface might have some artifact or the adsorbate species that might crash with the tip. Thus, a more usual procedure is followed by keeping the tunneling current constant by changing the distance between the tip and the sample through a feedback loop. In this way, the image is displayed by registering the voltage provided to the piezoelectric motor.

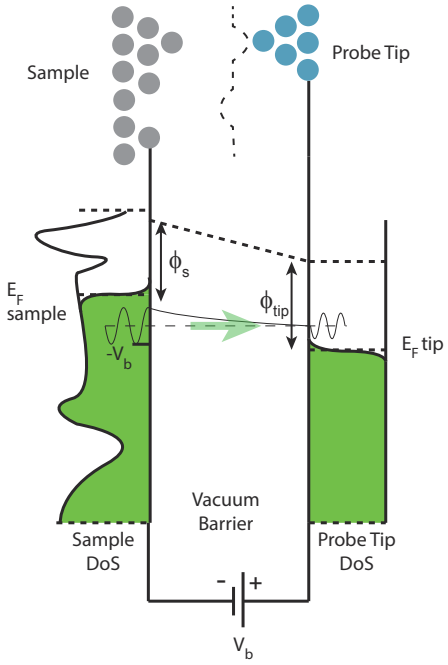

Figure 2.16: Illustration of the energy level scheme for a common STM experimental setup. When the bias voltage V_b is applied, the electrons from the sample surface tunnel through the vacuum barrier into the probe tip.

The basic concept of STM can be understood on the basis of one-dimensional potential barrier between the sample and the tip, giving rise to a tunneling process while ignoring the losses due to sample-tip interactions. For an electron with energy E_i in the initial state ψ_i, an exponential decaying solution for the electron wave function while tunneling in the barrier of height $\phi > E_i$ and

length d is given by

$$\psi_d = \psi_i e^{-\kappa d} \qquad \text{where} \qquad \kappa = \frac{\sqrt{2m(\phi - E_i)}}{\hbar} \tag{2.27}$$

where κ is the decay constant and the probability of finding an electron after the barrier of the width d is

$$w_d = |\psi_d|^2 = |\psi_i|^2 e^{-2\kappa d} \tag{2.28}$$

As shown in figure 2.16, while performing STM measurements a small bias voltage V_b is applied across the sample and the tip so that the presence of the electric field leads to the tunneling of electrons, resulting in the tunneling current I_t. The height of the barrier can roughly be approximated as the average work function of sample (ϕ_s) and tip (ϕ_{tip}) given by

$$\phi_b = \frac{(\phi_s + \phi_{tip})}{2} \tag{2.29}$$

for a rectangular barrier. Although there will be some tilt at the top of the barrier, which can be ignored, as the tilt will be due to the applied bias voltage of the order ~ 100 meV, much less than the height of the barrier i.e. roughly several eV. As shown in the figure 2.16, when the negative bias ($-V_b$) is applied to the sample, it raises the Fermi level of the sample with respect to the Fermi level of the probe tip. In this way the occupied states of the sample can be mapped. Contrarily, with the application of positive bias to the sample the unoccupied states can be mapped. For the applied bias voltage $|-V_b| << \phi_b$, the inverse decay length for the tunneling tunneling electrons can be rewritten as

$$\kappa = \frac{\sqrt{2m\phi_b}}{\hbar} \tag{2.30}$$

The tunneling current I_t, that is dependent on the tunneling probability, can be described as

$$I_t = \sum_{E_b = E_F - V_b}^{E_F} |\psi_b|^2 e^{-2\kappa d} \tag{2.31}$$

Substituting the definition of local density of states,

$$\rho(E) = \frac{1}{\epsilon} \sum_{E_b = E - \epsilon}^{E} |\psi_b|^2, \quad \text{for a sufficiently small energy range} \quad \epsilon \to 0 \tag{2.32}$$

in equation 2.31 and assuming a point-like tip, we get

$$I_t \propto V_b \rho_{sample}(E_F) e^{-2\kappa d} \tag{2.33}$$

thus suggesting that the tunneling current is proportional to the local density of states of the sample at the Fermi energy. Furthermore, the exponential decay

relation of the I_t with the distance between the sample and the probe tip d, gives the high sensitivity of the STM towards the vertical resolution, in the direction perpendicular to the surface. However, in practice the probe tip is highly unlikely to be point-like. In such cases the lateral resolution is preserved if the distance between the sample and the tip ($d << R$), where R is the radius of the probe tip, assuming that the tip is spherically terminated. In that case, a slight shift in the lateral separation (Δx) will result in the error in the vertical separation,

$$\Delta d = \frac{\Delta x}{2R} \tag{2.34}$$

which will ultimately result in a steep decrement of I_t. Thus the lateral separation given by the current column with the radius $\frac{\Delta x}{2}$ gives the lateral resolution of the STM setup.

The STM measurements presented in this work were carried out on the CoSMoS end station, which is placed at the branch line of the SuperESCA beamline at Elettra. The images were acquired by a SPECS STM 150 Aarhus instrument equipped with a W tip. STM images were analysed by means of the open-source software Gwyddion. [26]

2.7 Data analysis

2.7.1 Core level photoemission lineshape

In order to perform quantitative chemical analysis with XPS, a theoretical model that describes the photoemission spectrum is needed to fit the data. A commonly used model is the Doniach-Šunjić semi-empirical formalism [27] convoluted with a Gaussian. One of the three contributions in describing the photoemission lineshape arises from the finite core-hole life time, which can be accounted for by the Lorentzian distribution as,

$$I_{Lor}(E_{kin}) = \frac{I_0}{\pi} \frac{\Gamma/2}{(E_{kin} - E_0)^2 + (\Gamma/2)^2}, \tag{2.35}$$

where Γ is the full width at half maximum (FWHM) and E_0 is the position of the adiabatic peak for the maximum intensity I_0. Another contribution to the spectral line shape can be understood on the basis of experimental energy resolution, the inelastic scattering caused by exciting or absorbing phonons, and the inhomogeneous broadening. While the energy resolution is limited by the finite monochromaticity of the x-ray radiation and the limited resolving power of the analyzer, the vibrational broadening accounts for the excitation of low energy vibrational modes and the unresolved binding energy components are reciprocated in the form of inhomogeneous broadening. The resulting Gaussian function takes the form,

$$I_{Gaus} = I_0 \exp\left(-\frac{(E_{kin} - E_0)^2}{2\sigma^2}\right), \tag{2.36}$$

where σ is the Full Width at Half Maximum (FWHM).

In order to take into account the inelastic tail due to excitation of electron-hole pairs at the Fermi level, the Doniach-Šunjić function presents an asymmetry parameter α also known as the Anderson singularity index as follows,

$$I_{DS}(E_{kin}) = I_0 \frac{\Gamma_E(1-\alpha)}{[(E_{kin}-E_0)^2 + (\Gamma/2)^2]^{(1-\alpha)/2}} \zeta(E_{kin}), \tag{2.37}$$

where Euler gamma function

$$\zeta(E_{kin}) = \cos\left[\frac{\pi\alpha}{2} + (1-\alpha)\arctan\left(\frac{E_{kin}-E_0}{\Gamma/2}\right)\right] \tag{2.38}$$

The Doniach-Šunjić profile of the form mentioned above was used to analyze the XPS spectra presented in this thesis. All the binding energies presented in this work are referenced to the Fermi level of the substrate measured in the same experimental conditions. Moreover, the spectra were corrected for the linear background already accounted in the fitting procedure, apart from some cases where it was necessary to include a Shirley background, [28] that is, a semi empirical function proportional to the peak integral, which effectively describes a step-like behavior in the background due to inelastic losses.

2.7.2 Multiple scattering simulation for photoelectron diffraction

The X-ray photoelectron diffraction experiments discussed in this thesis were compared with multiple scattering simulations performed using the program package for Electron Diffraction in Atomic Clusters (EDAC), [12] for unfolding the details in order to learn about the structural geometries of the samples under study.

While performing the acquisition of core level spectra of an element on the sample surface (at a fixed photon energy in order to keep the photoelectron kinetic energy constant), a large number of spectra were measured for different polar (θ) and azimuthal (ϕ) angles settings. Each XPD pattern was measured over a wide azimuthal sector (ranging roughly from $-80°$ to $80°$), from normal (θ=0°) to grazing emission (θ=70°), as shown in the sketch of Figure 2.11. The modulation function χ, (spanning over different azimuthal angles) was obtained for each polar emission angle θ from the peak intensity I(θ, ϕ) (area under the photoemission spectral curve), resulting from the fit of each individual spectrum, as

$$\chi = \frac{I(\theta,\phi) - I_0(\theta)}{I_0(\theta)} \tag{2.39}$$

where $I_0(\theta)$ is the average intensity for each azimuthal scan. The modulation function χ in this experimental geometry defines the intensity modulation as a function of θ and ϕ.

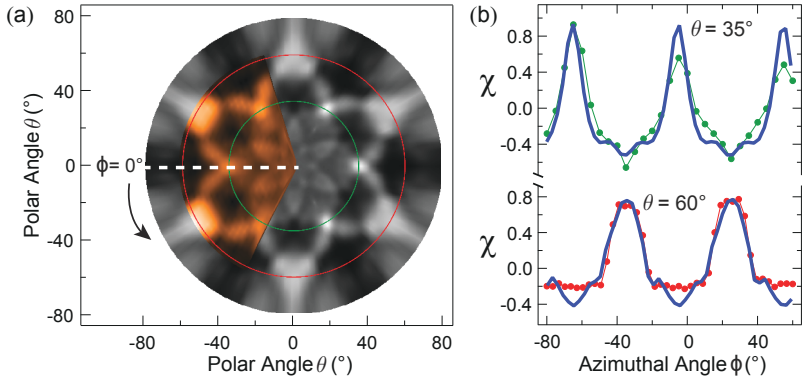

Figure 2.17: (a) XPD images for C 1s core level for graphene on Ir(111) measured at 400 eV photon energy. The experimental data (in gold) was acquired over an azimuthal sector of $-80^\circ \leq \phi \leq 60^\circ$ from normal emission ($\theta = 0^\circ$) to grazing emission ($\theta = 60^\circ$). The experimental data was compared with the simulation (in grey) yielding a very good R-factor of 0.1. (b) The intensity modulation functions for the experimental date (line with dots) are compared with the modulation function for the simulated data (thick blue lines) for the polar angle cuts at $\theta = 60^\circ$ and $\theta = 35^\circ$ as shown on the XPD image in (a).

In order to obtain the quantitative information about the sample structure, the experimental XPD results were compared with the multiple scattering simulations performed using the EDAC package. The best agreement between the simulations and the experimental results was obtained by minimizing the Reliability Factor (R). [29] The R-factor is defined as,

$$R = \frac{\sum_i (\chi_{exp,i} - \chi_{sim,i})^2}{\sum_i (\chi^2{}_{exp,i} + \chi^2{}_{sim,i})} \tag{2.40}$$

where $\chi_{sim,i}$ and $\chi_{exp,i}$ are the calculated and the experimental modulation functions for each data point i.

References

[1] Iwanenko, D.; Pomeranchuk, I. On the Maximal Energy Attainable in a Betatron. *Physical Review* **1944**, *65*, 343–343.

[2] Schwinger, J. On the Classical Radiation of Accelerated Electrons. *Physical Review* **1949**, *75*, 1912–1925.

[3] Abrami, A.; Barnaba, M.; Battistello, L.; Bianco, A.; Brena, B.; Cautero, G.; Chen, Q. H.; Cocco, D.; Comelli, G.; Contrino, S.; DeBona, F.; Di Fonzo, S.; Fava, C.; Finetti, P.; Furlan, P.; Galimberti, A.; Gambitta, A.; Giuressi, D.; Godnig, R.; Jark, W.; Lizzit, S.; Mazzolini, F.; Melpignano, P.; Olivi, L.; Paolucci, G.; Pugliese, R.; Qian, S. N.; Rosei, R.; Sandrin, G.; Savoia, A.; Sergo, R.; Sostero, G.; Tommasini, R.; Tudor, M.; Vivoda, D.; Wei, F. Q.; Zanini, F. Super ESCA: First beamline operating at ELETTRA. *Review of Scientific Instruments* **1995**, *66*, 1618–1620.

[4] Pizzini, S.; Sacchi, M. Modern techniques of surface science, 2nd edition. By D. P. Woodruff and T. A. Delchar, Cambridge University Press, Cambridge 1994. *Chemical Vapor Deposition* **1995**, *1*, 32–33.

[5] Cautero, G.; Sergo, R.; Stebel, L.; Lacovig, P.; Pittana, P.; Predonzani, M.; Carrato, S. A two-dimensional detector for pump-and-probe and time resolved experiments. *Nuclear Instruments and Methods in Physics Research, Section A: Accelerators, Spectrometers, Detectors and Associated Equipment* **2008**, *595*, 447–459.

[6] Woodruff, D.; Delchar, T. *Modern techniques of surface science.*, 2nd ed.; Cambridge University Press, 1994.

[7] Siegbahn, K. Electron spectroscopy for atoms, molecules, and condensed matter. *Science* **1982**, *217*, 111–121.

[8] Seah, M. P.; Dench, W. A. Quantitative electron spectroscopy of surfaces: A standard data base for electron inelastic mean free paths in solids. *Surface and Interface Analysis* **1979**, *1*, 2–11.

[9] Mårtensson, N.; Nilsson, A. On the origin of core-level binding energy shifts. *Journal of Electron Spectroscopy and Related Phenomena* **1995**, *75*, 209 – 223.

[10] Yeh, J.; Lindau, I. Atomic subshell photoionization cross sections and asymmetry parameters: $1 \leq Z \leq 103$. *Atomic Data and Nuclear Data Tables* **1985**, *32*, 1 – 155.

[11] Woodruff, D. P.; Bradshaw, A. M. Adsorbate structure determination on surfaces using photoelectron diffraction. *Reports on Progress in Physics* **1994**, *57*, 1029–1080.

[12] García de Abajo, F. J.; Van Hove, M. A.; Fadley, C. S. Multiple scattering of electrons in solids and molecules: A cluster-model approach. *Physical Review B* **2001**, *63*, 075404, 1–16.

[13] Li, J.; Abruña, H. D. Phases of Underpotentially Deposited Hg on Au(111)-An in Situ Surface X-ray Diffraction Study. *The Journal of Physical Chemistry B* **1997**, *101*, 2907–2916.

[14] Rehr, J. J.; Albers, R. C. Scattering-matrix formulation of curved-wave multiple-scattering theory: Application to x-ray-absorption fine structure. *Physical Review B* **1990**, *41*, 8139–8149.

[15] Davisson, C.; Germer, L. H. Diffraction of Electrons by a Crystal of Nickel. *Physical Review* **1927**, *30*, 705–740.

[16] utility by K.E. Hermann (FHI),; (HKBU), M. V. H. *LEEDpat*; 2014; Vol. Version 4.2.

[17] Hofmann, P. *Solid State Physics: An Introduction*, 1st ed.; John Wiley & Sons Inc., 2011.

[18] Bignardi, L.; Lacovig, P.; Dalmiglio, M. M.; Orlando, F.; Ghafari, A.; Petaccia, L.; Baraldi, A.; Larciprete, R.; Lizzit, S. Key role of rotated domains in oxygen intercalation at graphene on Ni(111). *2D Materials* **2017**, *4*, 025106, 1–11.

[19] Pesin, D.; MacDonald, A. H. Spintronics and pseudospintronics in graphene and topological insulators. *Nature Materials* **2012**, *11*, 409–416.

[20] Hoffmann, S. V.; Søndergaard, C.; Schultz, C.; Li, Z.; Hofmann, P. An undulator-based spherical grating monochromator beamline for angle-resolved photoemission spectroscopy. *Nuclear Instruments and Methods in Physics Research A* **2004**, *523*, 441–453.

[21] Bigi, C.; Das, P. K.; Benedetti, D.; Salvador, F.; Krizmancic, D.; Sergo, R.; Martin, A.; Panaccione, G.; Rossi, G.; Fujii, J.; Vobornik, I. Very efficient spin polarization analysis (VESPA): new exchange scattering-based setup for spin-resolved ARPES at APE-NFFA beamline at Elettra. *Journal of Synchrotron Radiation* **2017**, *24*, 750–756.

[22] Binnig, G.; Rohrer, H.; Gerber, C.; Weibel, E. Tunneling through a controllable vacuum gap. *Applied Physics Letters* **1982**, *40*, 178–180.

[23] Meyer, G.; Bartels, L.; Rieder, K.-H. Atom manipulation with the scanning tunneling microscope: nanostructuring and femtochemistry. *Superlattices and Microstructures* **1999**, *25*, 463–471.

[24] Stipe, B. C.; Rezaei, M.; Ho, W. Inducing and viewing the rotational motion of a single molecule. *Science* **1998**, *279*, 1907–1909.

[25] Heinrich, A. J.; Gupta, J. A.; Lutz, C. P.; Eigler, D. M. Single-Atom Spin-Flip Spectroscopy. *Science* **2004**, *306*, 466–469.

[26] David, N.; Petr, K. Gwyddion: an open-source software for SPM data analysis. 2011.

[27] Doniach, M., S.; Sunjic Many-Electron Singularity in X-ray Photoemission and X-ray Line Spectra from Metals. *Journal of Physical Chemistry* **1970**, *3*, 285–291.

[28] Shirley, D. A. High-Resolution X-Ray Photoemission Spectrum of the Valence Bands of Gold. *Physical Review B* **1972**, *5*, 4709–4714.

[29] Dippel, R.; Weiss, K.; Schindler, K.; Gardner, P.; Fritzsche, V.; Bradshaw, A.; Asensio, M.; Hu, X.; Woodruff, D.; González-Elipe, A. A photoelectron diffraction study of the structure of PF_3 adsorbed on Ni(111). *Chemical Physics Letters* **1992**, *199*, 625 – 630.

CHAPTER 3

Synthesis of single-orientation high-quality molybdenum disulfide monolayers on Au(111) showing complete spin polarization

The progress in the field of graphene research, in the last decade, and the development of techniques related to the study of layered materials have catalyzed the growth in the research related to 2D TMDCs. As already pointed out in the introduction, the 2D TMDCs are one of the most attractive class of materials that exhibit unique properties, significant for fundamental studies pertaining novel physical phenomena and for the application in next generation devices. Following the first determination of their structure by Dickinson and Pauling in the year 1923 [1], around 40 layered structures of TMDCs were identified in the late sixties of the twentieth century. [2] The properties of TMDCs strongly depend on the structural arrangement of the material, the most common of which are trigonal prismatic (1H) and octahedral (1T) phase, as shown in figure 3.1.

One of the most studied members of TMDCs family is molybdenum disulphide (MoS_2) which consists of a hexagonal 2D structure of covalently bonded 'S-Mo-S' layers. [3, 4] For a long time, bulk MoS_2 has been used as a dry lubricant [5] and as heterogeneous catalyst. [6] Low dimensional MoS_2 has attracted a lot of interest due to its distinctive properties. The naturally occurring trigonal prismatic (1H) phase, as shown in figure 3.1, is also the thermodynamically stable structural phase for 2D MoS_2 with the lattice parameter for a free standing single layer $\alpha \sim 3.15$ Å. [7] As a result of the quantum confinement, MoS_2 shows a transition from indirect band gap (~ 1.2 eV [8]) in the semiconducting bulk state, to a direct band gap ($\sim$

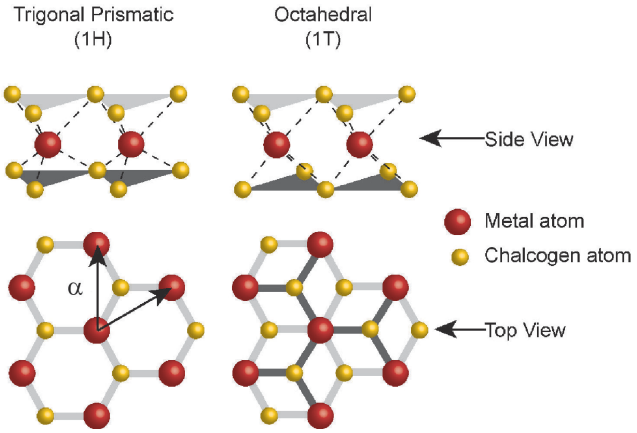

Figure 3.1: Ball diagram showing two structural phases most commonly displayed by layered TMDCs. The lattice parameter (α) is also illustrated. Ball model color code: red (Mo) and yellow (S)

1.8 eV [9, 10]) in the monolayer form. This, coupled with the structural stability makes SL MoS_2 an excellent choice as a channel material for next generation electronic devices, such as transistors [11], diodes [12] and memristors. [13, 14] Moreover, the presence of the band gap in the visible region and a strong photovoltaic response [15, 16] of 2D MoS_2 is also attracting interest towards nanoscale photovoltaics.

Furthermore, novel two-dimensional materials that exploit the valley [17–19] and spin degrees [20, 21] of freedom are attracting the interest of the scientific community as they form the basis of future electronic devices. In this framework, 2D TMDCs, and in particular the 1H phase group VI TMDCs like MoS_2, are promising candidates for such applications. The valence band maximum (VBM) for SL MoS_2 is present at the high-symmetry **K** point of the Brillouin zone and is constituted mainly by the d-orbitals of the Mo atoms. [22, 23] The lack of inversion symmetry (in the single layer form) and the the strong spin-orbit coupling of the heavy transition metal (Mo) leads to Zeeman-like spin splitting [24] ($\sim$ 145 meV [25]) of the valence band. Moreover, the time-reversal symmetry dictates the reversal of spin character of the spin-splitted bands at inequivalent valleys. This is schematically illustrated in figure 3.2 that shows the unit cell and electronic structure of SL MoS_2 mirror domains, highlighting the spin-reversal in the valence band maxima near **K** and -**K**. Such a coupling of spin and valley degree, opens the possibility of conceptualizing new spintronic and valleytronic devices. However, the realization of such devices based on the valley Hall effect (see figure 3.3) requires a distinction between the **K** and -**K** points of the Brillouin zone (i.e. a single domain orientation), as a simultaneous presence of the twin domains would result in averaging and the loss of the spin and valley polarization, preventing the observation of the valley Hall effect.

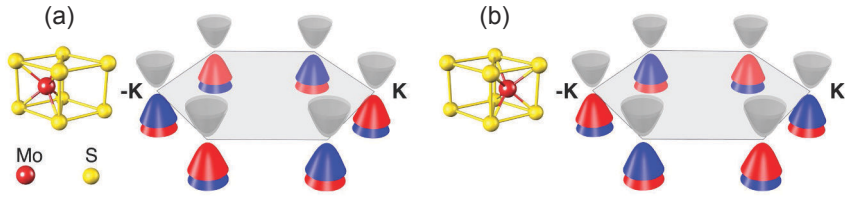

Figure 3.2: Structure, Brillouin zone and schematic band structure for two mirror domain orientations of SL MoS_2. The colors of the split valence band maximum (blue/red) refer to the different spin orientation of these states.

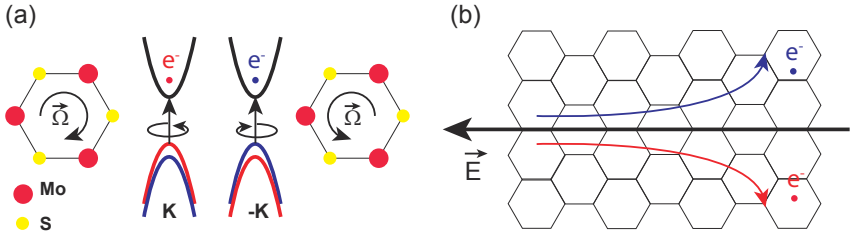

Figure 3.3: (a) Schematics of the valley-dependent Berry curvatures $\vec{\Omega}$, showing the clockwise and the anti-clockwise hopping motion of the electron belonging to **K** and **-K**. (b) Schematic of a valley Hall effect (VHE), where electrons belonging to the different valley are separated and move in the opposite directions, under the effect of an applied electric field $\vec{E}$. Adapted from Mak *et. al* ref. [19].

In addition to this, the growth of large area and high quality SL MoS_2 is imperative for the utilization of its potential in device assembly. Various approaches attempting to obtain monolayer MoS_2 have resulted in variable quality and reproducibility of the grown samples. One of the most widely used growth methods is CVD, leading to the growth of SL MoS_2 triangular islands tens of micrometres in size. [26] However, the CVD grown layers show the presence of surface defects such as grain boundaries and atomic vacancies, degrading the aforementioned properties of MoS_2 and limiting the efficiency of fabricated devices. [27] Recently, it has been shown that the epitaxial growth of monolayer MoS_2 can be achieved using PVD, by repeated cycles of Mo evaporation in H_2S environment on the Au(111) surface at room temperature, followed by high temperature annealing. [28] This method led to the growth of clean and extended nano-islands that allowed the measurement of the electronic band structure of SL MoS_2 [25], though showing the coexistence of differently oriented domains. [29]

The PVD growth of MoS_2 is exploited in this chapter, with the aim of understanding the mechanisms driving the growth of MoS_2 and of optimizing the parameters to grow high quality single layers. In the first part, using in-situ fast-XPS, we highlight the processes involved in the transition from the pre-sulfided Mo clusters on Au(111) to SL MoS_2. This will be followed by the formulation of a new high temperature growth (HTG) method, leading to the growth of high quality SL MoS_2 by properly controlling the synthesis conditions. High-resolution XPS, LEED and STM were used to characterize the chemical and structural properties of the grown layers. XPD measurements showed that, while the room temperature deposition followed by high temperature (Temperature Programmed Growth, TPG) annealing gives rise to the formation of two domains with opposite orientation, a MoS_2 monolayer with single orientation is obtained by following the HTG procedure. Furthermore, the spin polarization measurements showed that the singly oriented HTG MoS_2 presents a complete spin polarization of the bands near **K** and **-K** points of the surface Brillouin zone of MoS_2.

3.1 Experiments and methods

The growth of SL MoS_2 was performed at the SuperESCA beamline of Elettra, [30] together with the XPS and XPD measurements. The atomically clean Au(111) surface was prepared by repeated cycles of Ar^+ sputtering followed by annealing up to 920 K for 10 min at 1 Ks^{-1} heating and cooling rate. The sample cleanliness was checked with XPS in the O 1s, C 1s as well as the Au $4f_{7/2}$ core level regions. No contaminants were detected within the detection limit of the technique (< 0.01 ML) and the clean Au $4f_{7/2}$ spectrum showed the SCLS of 330 meV, in agreement with the previous findings. [31] The surface long-range order was verified by acquiring LEED images that showed the spots of the herringbone reconstruction of the freshly prepared sample.

Molybdenum atoms were deposited from a home-built evaporator (consisting of a Mo filament heated through direct current) while H_2S, which acted as the source of sulfur with a nominal purity of 99.8%, was dosed through a leak valve.

The careful tuning of the growth parameters was obtained by following in real time the evolution of the MoS_2 layer during the growth by means of fast-XPS of the Mo 3d and S 2p core levels measured simultaneously at photon energy of 360 eV. In order to do this, the Mo evaporator was mounted in front of the sample and H_2S was introduced in the main chamber during the measurements. After deposition, high resolution XPS and LEED were used to characterize the MoS_2 monolayers. For the high-resolution XPS measurements presented in this chapter, the energy resolution was better than 50 meV. XPD measurements with photon energy corresponding to photoelectron kinetic energy of 108 eV ($h\nu = 270$ eV) for topmost sulfur, 130 eV ($h\nu = 360$ eV) for molybdenum and 397 eV ($h\nu = 560$ eV) for bottommost sulfur in the covalently bonded 'S-Mo-S' layers of MoS_2 were performed in order to achieve backward (low kinetic energy) and forward (high kinetic energy) scattering conditions. The experimental XPD results were compared with multiple scattering simulations performed using the EDAC program package. [32] The ARPES data were taken at the SGM-3 beamline of the synchrotron radiation facility ASTRID2 in Aarhus. [33] The energy and angular resolution were better than 30 meV and 0.2°, respectively. The sample temperature was ≈ 30 K during the ARPES measurements. Spin-resolved ARPES measurements were taken at the APE beamline of Elettra, [34] equipped with a VG-Scienta DA30 analyser and two very low energy electron diffraction (VLEED) spin polarimeters. The energy and angular resolution were better than 50 meV and 0.75°, respectively. The measurements were performed at 80 K. Scanning Tunneling Microscopy (STM) measurements were carried out on the CoSMoS facility at Elettra. The images were acquired at room temperature with a SPECS STM 150 Aarhus instrument. The samples were transferred in air from the preparation chamber of the SuperESCA beamline to the SGM-3 and APE beamlines and the STM chamber of CoSMoS, where they were subsequently annealed up to ca. 800 K for 30 min to remove adsorbed impurities. This was possible due to the stability of this system in air, as already observed in [29].

3.2 Transition of sulfided Mo clusters to MoS_2

The PVD growth of MoS_2 on Au(111) was followed by means of real time fast-XPS, with the aim of understanding the transient species, to uncover the growth kinetics and to identify the optimum parameters for the growth of single layer MoS_2. Following an already established TPG procedure, [28] the growth was performed by depositing atomic Mo on the sample at room temperature in H_2S background pressure of ca. 2×10^{-6} mbar followed by post annealing at 0.5 Ks^{-1} from room temperature (RT) to 823 K for 40 minutes. In order to increase the coverage of the grown layer, this procedure was repeated 7 times by

depositing Mo for 5 minutes (for each subsequent deposition step) on top of the previous layer, similar to the procedure adopted by Sorensen *et al.* [28] The Mo deposition rate was measured by means of a quartz microbalance and amounted to $\sim 2.2 \times 10^{-2}$ ML/minute, where a monolayer (ML) is defined as the surface atomic density of the Au(111) surface, corresponding to 1.39×10^{15} atoms/cm^2.

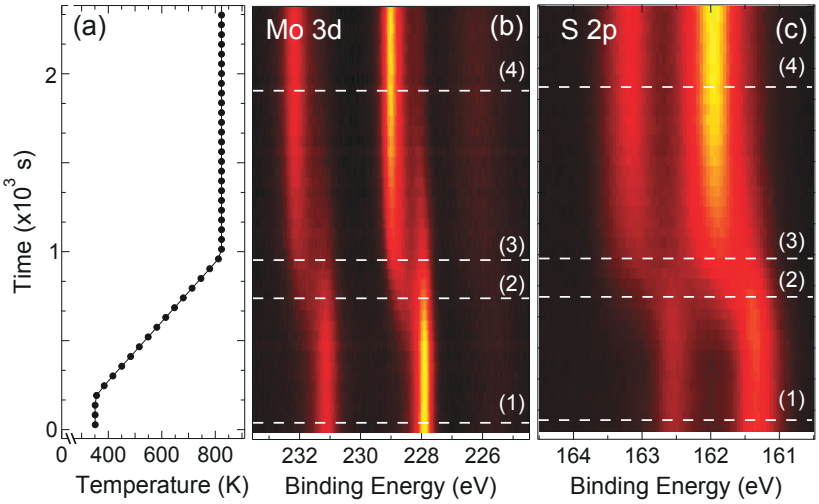

Figure 3.4: (a) Temperature evolution, (b) fast-XPS intensity plot for Mo 3d and (c) S 2p core level spectra acquired simultaneously while annealing after the first depositing at room temperature. The measurements were performed at 360 eV photon energy.

In figure 3.4, the 2D intensity plots corresponding to the real-time XPS spectra acquired at 360 eV photon energy, measured simultaneously for the Mo 3d and S 2p core levels, show the evolution of the core level spectra corresponding to the different chemical species present on the surface. Each spectrum was measured in ∼10 s. Following the first Mo deposition in H_2S at room temperature, the Mo $3d_{5/2}$ (figure 3.4 (b)) and S $2p_{3/2}$ (figure 3.4 (c)) grow initially at 228.05 eV and 161.41 eV, respectively. Upon annealing to 823 K, they shift gradually towards the binding energy (BE) characteristic of single layer MoS_2 on Au(111) (Mo $3d_{5/2}$ = 229.19 eV and S $2p_{3/2}$ = 162.15 eV). [28, 35] From the temperature rate profile (figure 3.4 (a)), it can be seen that the transition starts around 500 K and continues with the increasing temperature until the sulfided clusters convert into single layer MoS_2 islands at 823 K. Further annealing to 873 K shows no change in the BE positions for both Mo 3d and S 2p.

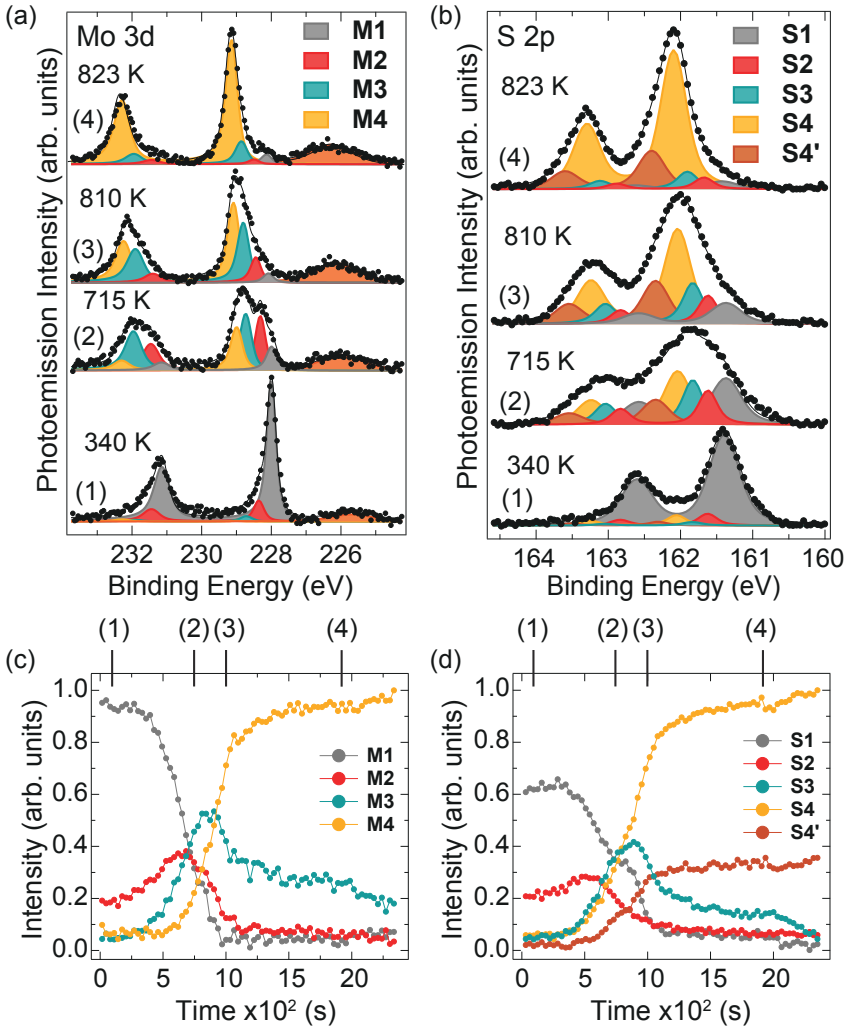

Figure 3.5: Fast-XPS spectra for (a) Mo 3d and (b) S 2p core level for some selected temperature marked in the intensity plots in figure 3.4, together with the spectral contribution of different components resulting from peak fit analysis. The evolution of these components while annealing in H_2S is shown in (c) and (d) for the Mo 3d and S 2p core level, respectively.

Figure 3.5 (a) and (b) show the deconvolution of the spectra with different components at various stages of the annealing process for Mo 3d and S 2p core level spectra, respectively. The identification of these components and the determination of their spectral line shape was achieved by fitting the high-resolution spectra that will be discussed later in this chapter. Based on the findings in [36, 37], these components can be attributed to the MoS_x stoichiometry given by different degree of Mo sulfidation of the 2D Mo-S clusters. Indeed, Baker *et al.* [36] have shown that the value of the stoichiometric coefficient x depends linearly on the Mo 3d BE shift with respect to the BE of MoS_2. The intensity profile, figure 3.5 (c) and (d), shows the evolution of the different components in Mo 3d and S 2p core levels, respectively. At the beginning, the Mo 3d core level presents two peaks $M1$ (grey) at 228.05 eV (-1.14 eV with respect to the BE of MoS_2) and $M2$ (red) at 228.35 eV (-0.84 eV with respect to the BE of MoS_2) corresponding to $x = 0.97 \pm 0.1$ and $x = 1.24 \pm 0.1$, respectively, in accordance with the values reported in [36]. The presence of these sulfided components at the beginning is the result of Mo deposition performed in H_2S environment that leads to pre-sulfidation of Mo and prevents it from alloying with Au. [28] Similarly, the S 2p core level also presents two components: $S1$ (grey) at 161.41 eV and $S2$ (red) at 161.66 eV. These pre-sulfided species decline in intensity with the increase of sample temperature, thereby aiding to the growth of components at higher BE. When the temperature reaches 500 K, $M3$ (blue) starts growing at 228.8 eV in Mo 3d core level as a result of increased sulfidation. $M3$ is complemented by the growth of $S3$ (blue) component at 161.91 eV BE in the S 2p core level. The intensity of $M3$ and $S3$ increase up to 750 K and then continue to decline as the annealing proceeds. From the BE shift calculation, [36, 37] these components can be attributed to the under-coordinated and incompletely sulfided Mo-S species, of the form MoS_x ($x = 1.6 \pm 0.1$). The growth of incompletely sulfided peaks is followed by other components growing at even higher BE, corresponding to the basal plane of MoS_2 [28, 35]; $M4$ (yellow) at 229.19 eV in Mo 3d core level is accompanied by $S4$ (yellow) at 162.15 eV in S 2p core level spectra. Although most of the conversion has already taken place by the time that the sample reaches 823 K, both $M4$ and $S4$ continue to grow at the expenses of the peaks at lower BE as the sample temperature is kept at 823 K for other 20 minutes. This progression is in agreement with the sulfidation of $M3$ that leads to the stoichiometric rearrangement from MoS_x ($x = 1.6 \pm 0.1$) to MoS_2.

The components belonging to MoS_2, $M4$ and $S4$, appear already at 500 K, suggesting the presence of MoS_2 nano-crystallites already at this temperature. It has been reported in literature that in the early stage of growth on Au(111), the MoS_2 nano-islands have a higher affinity towards Mo terminated edges [4] that results in Mo 3d core level shifted components at 400 meV lower BE than that of the basal plane component. [35] This corresponds to the $M3$ peak that is more intense in the beginning of the transformation, with respect to the corresponding component in the S 2p core level ($S3$), as it also includes the contribution of Mo atoms at the nano-island edges. It is also important to

highlight that in addition to $S4$, another component $S4'$ (brown) appears at 162.41 eV in the S 2p core level and shows a quite similar growth trend of $S4$. The nature of this component will be discussed in more detail in the following sections.

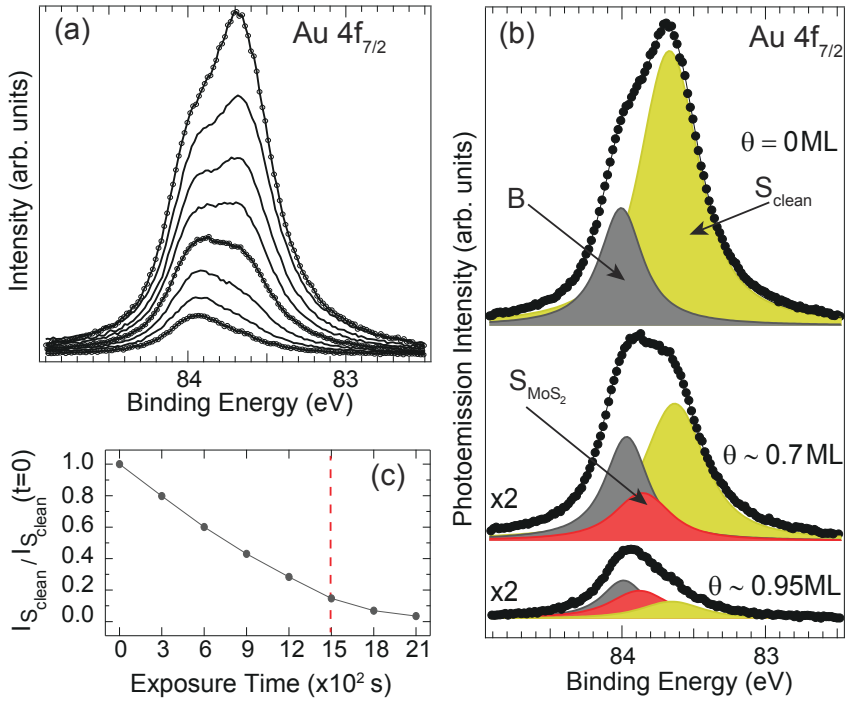

Figure 3.6: (a) Au $4f_{7/2}$ core level XPS spectra for different MoS_2 growth stages, the highlighted spectra are complimentary to those displayed in (b). (b) Au $4f_{7/2}$ core level XPS spectra of clean Au(111) surface, after MoS_2 growth with coverage of 0.7 ML and 0.95 ML at 136 eV photon energy, together with the spectral contributions resulting from peak fit analysis. (c) Intensity of surface peak with the increasing Mo amounts, dashed line (red) marks the coverage of MoS_2 ca. 0.8 ML.

3.3 Characterization of TPG grown single layer MoS_2

After the TPG growth was completed, the sample was cooled down to room temperature and the high-resolution XPS spectra were measured in order to identify the different chemical species present on the surface. In figure 3.6, we

report the Au $4f_{7/2}$ core level spectra for the clean Au(111) sample together with the spectra measured at different MoS_2 coverage, while the Doniach-Šunjić [38] line shape parameters (convoluted with Gaussian) used for the analysis of the Au $4f_{7/2}$ spectrum are presented in table 3.1. The deconvolution of the spectrum for the clean Au (figure 3.6 (b)) presents two components due to differently coordinated bulk (B) at 84.0 eV and surface (S_{clean}) atoms at 83.67 eV. The resulting surface core level shift (which is the BE shift between the core levels of the surface and bulk atoms) of 330 meV is in close agreement with previous studies.[39, 40] The Au(111) surface presents the herringbone reconstruction, which results in the compression of the lattice parameter in one of the three $< \bar{1}10 >$ directions. [41] The SCLS of 330 meV is attributed to the reconstructed surface. It has been shown in literature [29] that the growth of MoS_2 ad-layer results in the lifting of the herringbone reconstruction. Indeed, in our XPS measurements, the growth of the MoS_2 layer is complemented by the appearance of a new component (S_{MoS_2}) at 83.89 eV that continues to grow at the expenses of the S_{clean} peak, as the MoS_2 coverage increases.Therefore, this peak can be attributed to the Au surface atoms that feel the variation in the local atomic environment due to the interactions with the MoS_2 layer on top, [42, 43] resulting in the SCLS of 110 meV. The nature of these interactions will be discussed in more detail in the following sections. It has been reported in literature that the growth of SL MoS_2 on Au(111) proceeds through the formation of 2D nano-islands, even in the early stages of growth. Accordingly, the extension of the MoS_2 layer on the Au surface (following the subsequent deposition steps) is reflected in the decrease (increase) of the S_{clean} (S_{MoS_2}) peak. Therefore, assuming a negligible contribution from the incompletely sulfided species on the surface, the MoS_2 coverage θ_{MoS_2} was calculated from the decrement of the intensity of the Au surface component $I_{S_{clean}}$ after the growth of MoS_2 for successive TPG cycles as,

$$\theta_{MoS_2} = 1 - \frac{I_{S_{clean}}(t)}{I_{S_{clean}}(t=0)} \tag{3.1}$$

where t is the exposure time and the MoS_2 coverage is expressed in monolayer (ML). From here on 1 ML is referred to one complete layer of MoS_2 on Au(111) which, considering the lattice parameter of MoS_2 (0.315 nm), results in a Mo surface density of 1.15×10^{15} atoms/cm^2.

In figure 3.6 (c), the intensity of the Au surface peak is shown as a function of Mo deposition cycles for the different TPG growth performed one after the other, in order to increase the coverage. For the first 4 deposition cycles (coverage $\sim$ 0.7 ML), the linear behavior of the decrement of the intensity is in agreement with continuous lateral growth of MoS_2 nano-islands on top of the Au surface. On the other hand, the linear behavior is not observed for coverage higher than 0.8 ML, marked with the dashed red line. This can be attributed to the decrease in the MoS_2 growth rate due to the desorption, at high temperature, of Mo atoms adsorbed on top of the previously formed MoS_2 layer, or could be due to the formation of MoS_2 bi-layer, as already observed

in [29], even though, in our Mo 3d spectra we did not observe any additional component that might correspond to the Mo atoms of the MoS_2 bi-layer.

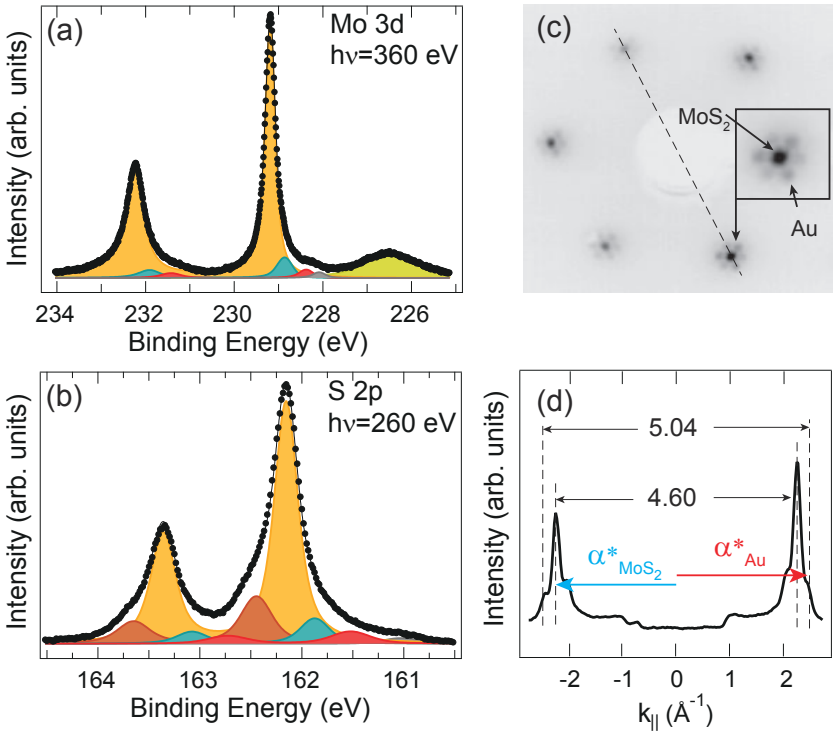

Figure 3.7: Mo 3d (a) and S 2p (b) core level spectra taken at 360 eV and 260 eV photon energy respectively, together with the spectral contributions resulting from peak-fit analysis for a MoS_2 coverage $\theta \sim 0.6$ ML. (c) LEED pattern measured at 117 eV. (d) Intensity line profile along the dashed line in (c), indicating the reciprocal lattice vectors corresponding to MoS_2 ($\alpha^*_{MoS_2}$) and Au surface (α^*_{Au}) unit cell.

Figure 3.7 (a) and (b) show the high-resolution XPS spectra of Mo 3d and S 2p core levels, respectively, acquired for the MoS_2 coverage of 0.6 ML where, as outlined earlier, double layer formation has not yet started. The deconvolution of the Mo 3d core level spectra acquired at 360 eV photon energy shows an intense peak (yellow) at 229.19 eV BE together with its spin-orbit splitted component at 232.33 eV. The position of this peak is well-matched with the one observed experimentally [28] and predicted theoretically [35] for the basal plane component for single layer MoS_2 on Au(111). Similarly, the deconvolution of the S 2p core level spectra obtained at 260 eV photon energy also presents an intense peak $S4$ (yellow) at 162.15 eV belonging to the basal

Au $4f_{7/2}$ ($h\nu$=136 eV)	L(eV)	α	G(eV)	SCLS(eV)
Bulk (B)	0.31	0.02	0.09	0.0
Surface (S_{clean})	0.37	0.02	0.23	-0.33
S_{MoS_2}	0.37	0.02	0.23	-0.11

Table 3.1: Doniach-Šunjić line shape parameters for different components in Au $4f_{7/2}$ spectrum acquired at 136 eV photon energy. L is the Lorentzian width, α is the asymmetry parameter and G is the Gaussian width.

plane atoms of the MoS_2 layer, together with the spin-orbit splitted component at 163.35 eV. For both Mo 3d and S 2p core level spectra, the main peak is accompanied by various components at lower BE, corresponding to the different degree of sulfidation of the Mo-S species [36, 37], as explained in the previous paragraph. These extra species degrade the quality of the prepared sample as they did not transform into MoS_2, even after prolonged annealing in H_2S (see section 3.2). In figure 3.7 (a), the peak at 226.49 eV (green) is the S 2s core level.

Mo 3d ($h\nu$=360 eV)	L(eV)	α	G(eV)	BE(eV)
$3d_{5/2}$	0.20	0.05	0.14	229.19
$3d_{3/2}$	0.43	0.05	0.14	232.33
S 2p ($h\nu$=260 eV)	L(eV)	α	G(eV)	BE(eV)
$2p_{3/2}$ $S4$	0.18	0.03	0.16	162.15
$2p_{3/2}$ $S4'$	0.23	0.02	0.21	162.44
$2p_{1/2}$ $S4$	0.18	0.03	0.16	163.35
$2p_{1/2}$ $S4'$	0.23	0.02	0.21	163.64

Table 3.2: Line shape parameters for different components for Mo 3d and S 2p spectra acquired at 360 eV and 260 eV photon energy, respectively, for the TPG sample. L is the Lorentzian width, α is the asymmetry parameter and G is the Gaussian width.

Interestingly, the S $2p_{3/2}$ core level presents an additional component ($S4'$) at 162.44 eV BE. This component is shifted towards higher BE from the main peak ($S4$), as opposed to the incompletely sulfided species that are present at lower BE, as seen in section 3.2. Bruix *et al.* [35] found that the S 2p core level of the S terminated island edges lies in the BE region of $S4'$. However, it is unlikely that $S4'$ belongs to these atoms because this peak shows a growth trend similar to that of the main $S4$ peak, instead of decreasing as a function of the dimensions of the MoS_2 islands. Theoretical calculations [44] have predicted that the bottom S atom has a 2p electron BE shift comparable to the one we measured for $S4'$ with respect to $S4$.

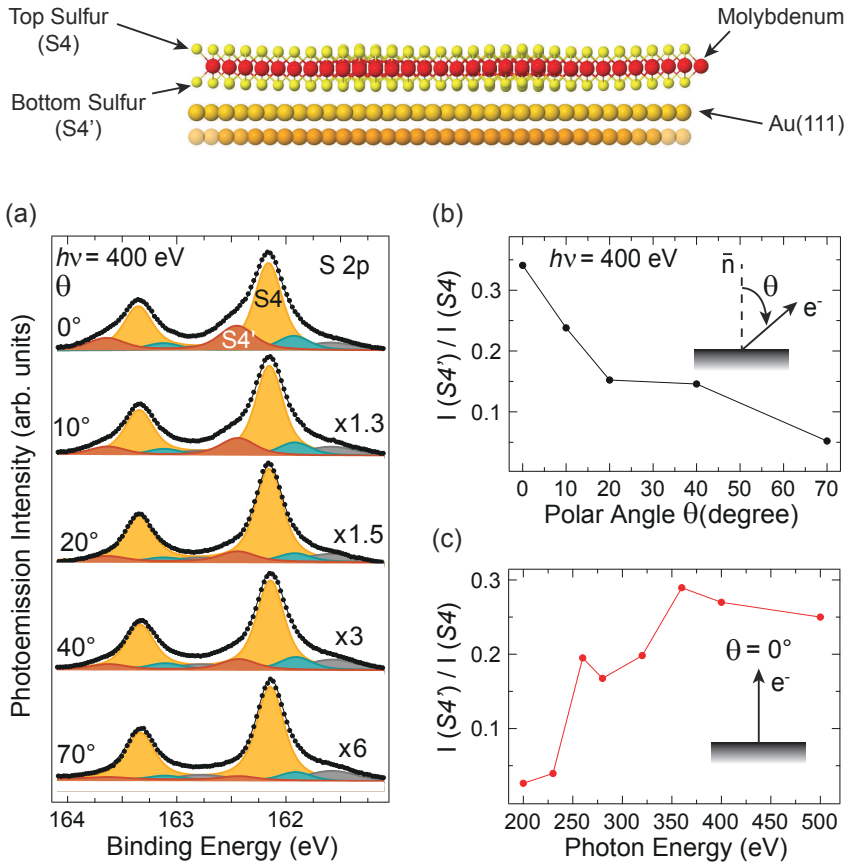

Figure 3.8: (a) Polar scan of the S 2p core level acquired at photon energy of 400 eV, together with the spectral contributions resulting from peak-fit analysis for TPG grown MoS_2 ($\theta \sim 0.6$ ML). (b) Ratio between the intensity of *S4'* and *S4* components at different polar angles θ resulting from the analysis of (a). (c) Variation in the relative intensity of *S4'* with respect to *S4* at normal emission ($\theta = 0°$) for spectra collected by varying the photon energy from 200 eV to 500 eV, corresponding to a kinetic energy variation from ca. 38 eV to ca. 338 eV.

In order to further elucidate the nature of these components, we performed a polar scan (figure 3.8 (a)) measuring the S 2p core level, by varying the polar emission angle from normal emission to 70° off normal, at 400 eV photon energy. Figure 3.8 (b) shows the relative intensity of the *S4'* with respect to *S4* component at different emission angles. As a consequence of the variation in the probing depth, the intensity of *S4'* shows a continuous decrease while moving from bulk sensitive (at normal emission) to surface sensitive (off-normal emission) measurements, thus suggesting that the component at higher BE (*S4'*) originates from the bottom layer S atoms. The modulation of the relative intensity of the two components, for the S 2p spectra acquired at different photon energy is shown in figure 3.8 (c). The increase in the IMFP while moving from low to high photon energy results in an enhanced signal from *S4'* component, implying that the signal is coming from the S layer underneath. A more detailed characterization of these components will be presented in the following section.

Figure 3.7 (c) shows the LEED pattern for the TPG grown single layer MoS_2. Sharp diffraction pattern with main spots (corresponding to the MoS_2 reciprocal lattice) surrounded by moiré satellite due to small lattice mismatch between Au (lattice constant; $\alpha_{Au} \sim 0.288\,nm$) and MoS_2 lattice ($\alpha_{MoS_2} \sim 0.315\,nm$), shows the presence of a long range order of the grown layer. By comparing the reciprocal lattice vectors, indicated in the intensity line profile shown in figure 3.7 (d), corresponding to MoS_2 ($\alpha^*_{MoS_2}$) and Au surface (α^*_{Au}) unit cell (figure 3.7 (d)), we obtain a moiré periodicity of 3.31±0.1 nm, in close agreement with previous studies. [29]

3.4 Direct growth of high quality singly oriented MoS_2 monolayers

The TPG growth method explained so far, leads to the formation of MoS_2 together with other unwanted species, a sign of the low quality of the final layer. Indeed, it was already observed by means of STM in Ref. [28, 46] that the extension of the MoS_2 islands remained below 50 nm and showed the presence of structural defects such as domain boundaries, forming when two islands with different orientation join together. [29] Thus, in order to improve the quality of the MoS_2 layer we searched for an alternative growth method by depositing Mo in H_2S atmosphere directly at high temperature, hereafter this method is called High Temperature Growth (HTG). This choice is based on the fact that the mobility of the Mo atoms on the Au surface increases at high temperature and this is an important parameter to be considered which allows the formation of higher quality layers. This has been observed also for the growth of graphene on different metal substrates [47, 48], as well as for h-BN. [49] On the other hand, it is of utmost importance to pay attention to the maximum temperature that can be reached, which may result in sulfur desorption from the MoS_2 layer, leading to the formation of S vacancies. Indeed, we observed that the optimum

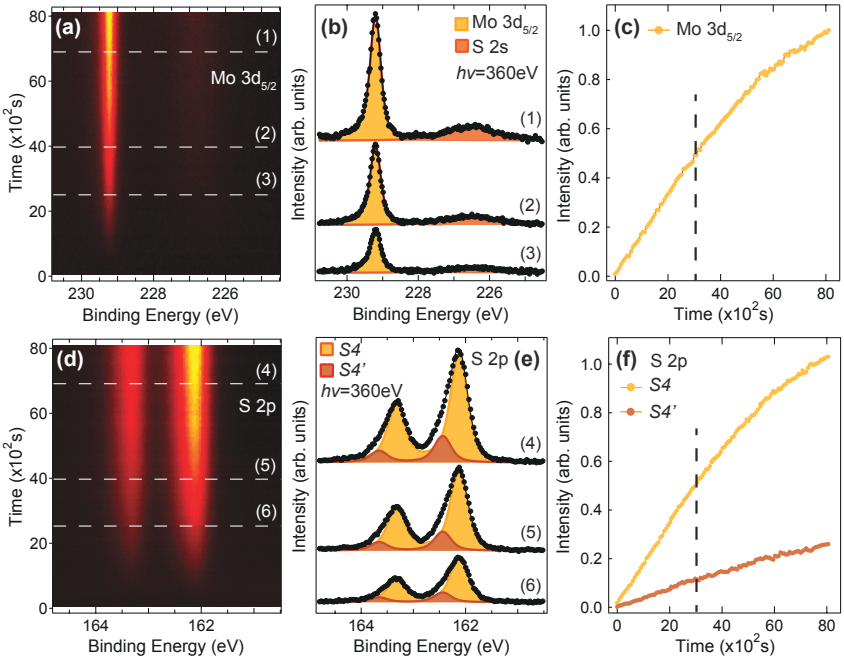

Figure 3.9: Fast-XPS during MoS_2 growth. The final coverage is 0.6 ML. (a) and (d) show the intensity plot of the sequence of fast-XPS spectra of Mo 3d and S 2p core levels, respectively, acquired simultaneously at 360 eV photon energy. (b) Mo 3d and (e) S 2p core level spectra together with the spectral contributions resulting from the peak fit analysis acquired at different stages of the growth, as indicated by the dashed lines in (a) and (d), respectively. (c) and (f) display the photoemission intensities obtained from the fit of the fast-XPS spectra, showing the evolution of the Mo $3d_{5/2}$ and S $2p_{3/2}$ for $S4$ (yellow) and $S4'$ (brown) layer sulfur atoms.

range for the growth of MoS_2 on Au with TPG is between 823 and 873 K. We also observed that higher temperatures lead to the decrease of the S 2p intensity, owing to the desulfidation of the MoS_2 layer. Therefore, the deposition of Mo was performed while keeping the Au(111) sample at 823 K.

In order to find the best parameters for the HTG growth we used the same strategy adopted for the TPG, i.e. we followed the MoS_2 growth with fast-XPS by measuring the S 2p and Mo 3d core levels. This allowed us to carefully tune the Mo deposition rate in accordance with the maximum H_2S background pressure of 2×10^{-6} mbar, to observe just the development of the Mo 3d and S 2p peaks of MoS_2, thus avoiding the growth of extra components observed with TPG, not converting into MoS_2. One of the problems of the HTG could be the formation of Mo-Au alloys at the high temperature used for the growth, if the proper combination of Mo deposition rate and H_2S pressure is not attained. [50] Indeed, the Mo $3d_{5/2}$ component, due to metallic Mo or Mo-Au alloy showed up at BE $\sim$ 228 eV, [51] when the Mo rate was too high. Therefore, the growth of these peaks was essentially avoided by significantly reducing the Mo deposition rate with respect to that used for TPG, amounting to ca. 5×10^{-3} ML/minute (where a monolayer (ML) is referred to the surface atomic density of Au(111)).

The intensity plot for the sequence of fast-XPS spectra of Mo 3d and S 2p core levels (figure 3.9 (a) and (d)) shows the increase of the peaks at the BE corresponding to SL MoS_2 [28] from the beginning of the growth. Moreover, the spectra for the HTG method do not present extra components (apart from the ones belonging to SL MoS_2) at the different stages of the growth, as shown in figure 3.9 (b) and (e), as opposed to the TPG method described in section 3.2 which produces also partially sulfided Mo-S species. The spectral line profiles (figure 3.9 (c) and (f)) obtained from the peak fit analysis show how the MoS_2 growth proceeds up to the final coverage of MoS_2 of 0.6 ML. From these graphs it can be seen that the MoS_2 growth rate is constant up to a coverage of $\sim$ 0.3 ML (marked with dashed lines), then it starts to decrease. This means that not all the Mo atoms react to form MoS_2 when the surface coverage increases because of the desorption, at high temperature, of the Mo atoms impinging on the already formed MoS_2 layer.

Figure 3.10 (a) and (b) show the high-resolution XPS measurements of the Mo 3d and S 2p core levels, respectively. The line shape parameters used to fit the spectra are presented in table 3.3. Similarly to the results obtained in the case of TPG growth, the Mo $3d_{5/2}$ core level (figure 3.10 (a)) shows the presence of a main peak (yellow) at 229.19 eV BE corresponding to the SL MoS_2. [28] Also, the S $2p_{3/2}$ core level shows the same behavior, with two components at 162.15 eV ($S4$) and 162.44 eV BE ($S4'$). Most importantly, the absence of extra components belonging to the differently sulfided MoS_x species ($0.9 \leq x \leq 1.6$), that were present in the case of TPG, reflect a better quality of the sample prepared by following the HTG method.

The structural properties of the MoS_2 layer were characterized by STM and LEED measurements whose results are shown in figure 3.10 (c) and (d),

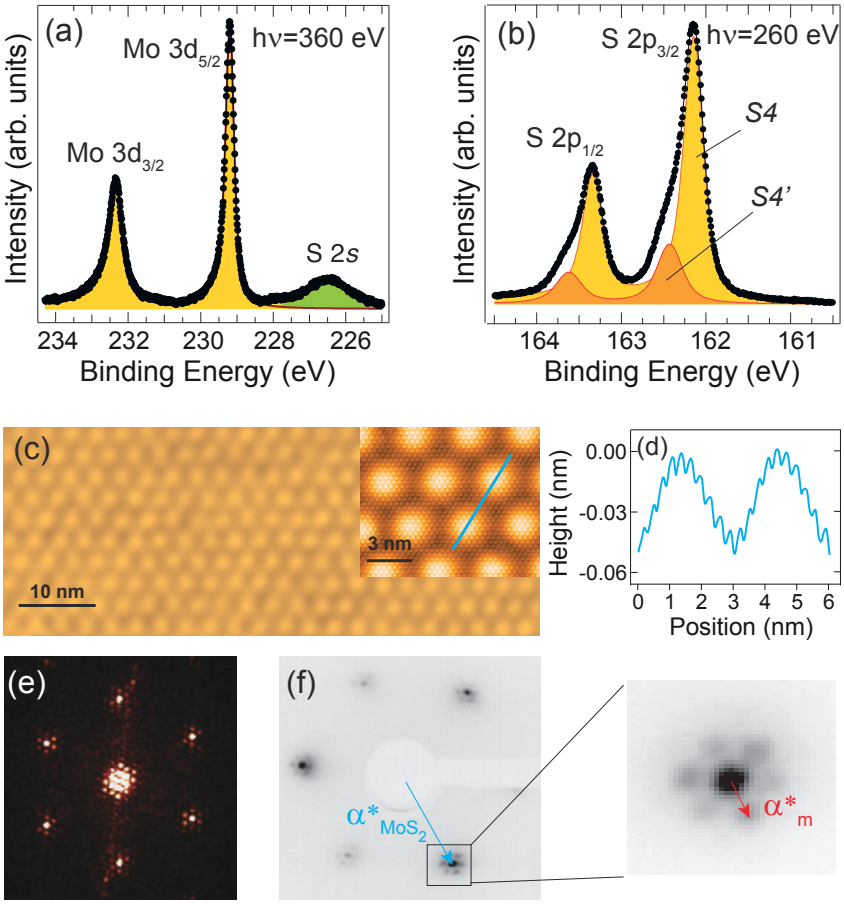

Figure 3.10: (a) Mo 3d and (b) S 2p core level spectra taken at hν=360 eV and hν=260 eV, respectively, with the resulting fit (line) and the fitted components (solid areas). (c) STM image (Tunneling parameters: V_B = 0.525 V, I_T = 0.54 nA for the main image. V_B = 0.525 V, I_T = 0.89 nA for the inset) showing the large scale moiré and the local atomic structure. (d) Line-scan along the indicated blue line on the STM image in the inset in (c) showing the moiré periodicity and the corrugation of the MoS_2 layer. (e) 2D fast Fourier transform (FFT) of the STM image in the insert in (c). (f) LEED pattern (electron kinetic energy E = 185 eV), with the magnified image indicating the reciprocal lattice vectors corresponding to MoS_2 ($\alpha^*_{MoS_2}$) and moiré (α^*_m) unit cell.

Mo 3d ($h\nu$=360 eV)	L(eV)	α	G(eV)	BE(eV)
$3d_{5/2}$	0.2	0.06	0.14	229.19
$3d_{3/2}$	0.43	0.06	0.14	232.33
S 2p ($h\nu$=260 eV)	L(eV)	α	G(eV)	BE(eV)
$2p_{3/2}$ $S4$	0.18	0.05	0.16	162.15
$2p_{3/2}$ $S4'$	0.23	0.02	0.21	162.44
$2p_{1/2}$ $S4$	0.18	0.05	0.16	163.35
$2p_{1/2}$ $S4'$	0.23	0.02	0.21	163.64

Table 3.3: Line shape parameters for Mo 3d and S 2p spectra acquired at 360 eV and 260 eV photon energy, respectively, for the HTG sample. L is the Lorentzian width, α is the asymmetry parameter and G is the Gaussian width.

respectively. The 70 nm×30 nm STM topographic image shows a large scale moiré pattern due to the lattice mismatch between the adsorbate layer and the Au substrate. The periodic modulation in the local density of states (due to the lattice mismatch giving rise to the formation of moiré superstructure) results in the bright protrusions, visible in the STM image. The domain size observed here, is considerably larger than that reported for the TPG grown samples. [28, 29] The atomically-resolved STM topograph (figure 3.10 (c): inset), shows the S atoms of the topmost layer of MoS_2 within the moiré superlattice. From the line profile corresponding to the marked blue line (figure 3.10 (d)), we estimate the moiré periodicity that amounted to 3.15±0.03 nm, indicating the formation of a moiré superlattice corresponding to 10×10 MoS_2 unit cells over 11×11 Au(111) unit cells. In addition to that, the out-of plane corrugation of $\sim$ 0.4 Å can also be calculated from the line profile scan. However, it should be noticed that the measurements of the out-of plane distances contain contributions from topographic and electronic effects, since the STM measures the local density of states and not the real topography. Therefore, the value of out-of plane corrugation has to be taken with care. The moiré corrugation of epitaxially grown 2D layer has been observed also for other 2D materials on top of metal surfaces such as graphene on various substrates [52, 53] or h-BN. [54, 55] STM allowed us to measure the in-plane S-S interatomic distance of 3.15±0.3 Å, corresponding to the lattice constant of the MoS_2 layer. The LEED pattern of the HTG sample (figure 3.10 (f)) shows the main diffraction spots surrounded by moiré satellites, resulting in the moiré periodicity of 3.2 ± 0.1 nm, in agreement with the STM measurements. Moreover, the MoS_2 crystallographic axes are aligned with those of the Au substrate. A noticeable difference with respect to TPG is the relative intensity of the spots that will be discussed later. The satellite spots are consistent with the moiré pattern observed by STM, and are clearly visible in the Fourier transform of the STM image (figure 3.10 (c)), which highlights that this pattern extends over a large area probed by LEED.

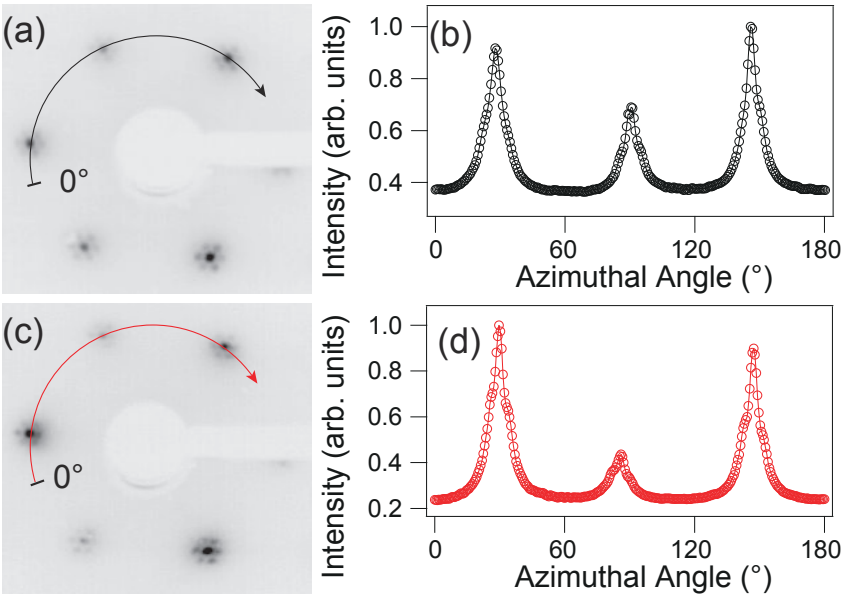

Figure 3.11: (a) LEED image at 117 eV and (b) the spot intensity profile along the marked arc in (a) for the TPG grown SL MoS_2. (c) LEED image at 117 eV and (d) the spot intensity profile along the marked arc in (c) for the HTG grown SL MoS_2.

3.4.1 Structure and orientation of TPG and HTG grown MoS_2

Figure 3.11 (a) and (c) show the LEED pattern acquired at 117 eV for the SL MoS_2 prepared by following the TPG and HTG procedure, respectively. It can be observed that both images show a three-fold symmetric pattern, as expected from the MoS_2 layer, whose symmetry is indeed three-fold, as shown in figure 3.1, as well as from the underlying Au(111) substrate. However, the spot profile analysis (figure 3.11 (b) and (d)), corresponding to the marked cuts along the MoS_2 spots reveals that the intensity of the central peak in the line profile is lower in the case of the HTG with respect to the TPG grown sample. In other words, the LEED pattern of the HTG grown sample shows a more pronounced three-fold symmetry. This points towards a preference for one of the two possible mirror orientations, aligned with the Au substrate for the HTG grown MoS_2, as the mixture of the two orientations in equal proportion should lead to a six-fold symmetric pattern, if the contribution from the substrate is not taken into account. The presence of two anti-parallel domains of MoS_2 on Au(111) surface have also been reported for similar PVD grown system by Grønborg *et al*. [29], and also for other growth methods on different substrates such as c-sapphire [56] and SiO_2. [57]

In order to characterize the local structure of the MoS_2 layer and to get further insight into the orientation of the MoS_2 domains grown with the HTG and TPG methods, we performed XPD measurements and compared them with multiple scattering simulations. While performing XPD measurements, more than 1000 spectra were measured over a wide azimuthal sector of 160°, from normal (0°) to grazing emission (70°). Each of these spectra were fitted and the intensity, i.e. the area under the photoemission line, was extracted for the spectral components belonging to MoS_2. The experimental XPD patterns (colored) of the Mo 3d core level acquired at 360 eV photon energy (photoelectron kinetic energy of 130 eV) for the HTG and TPG grown layer are shown together with the EDAC simulated patterns (at the same kinetic energy, in grey) in figure 3.12 (c) and (d), respectively. To construct the geometrical structure of MoS_2 for performing the simulations, we assumed the orthogonal prismatic (1H phase) structure with the lattice constant of 3.15 Å and the interlayer distance (distance between the planes of S and Mo atoms in 'S-Mo-S' structure of MoS_2) of 1.62 Å as reported in literature. [58, 59] Also, the simulations were performed for a freestanding MoS_2 layer without the Au(111) substrate. Due to the lack of a specific local adsorption configuration of MoS_2 with respect to the substrate, as evident from the moiré pattern, the overall influence of the substrate on the diffraction patterns of the MoS_2 layer can be neglected. Figure 3.12 (a) and (b) show the XPD simulations corresponding to the two mirror orientations (i.e. orientation 1 and orientation 2, sketched on top), resulting in 180° rotated three-fold symmetric patterns. In order to quantify the contribution of mirror domains in the as grown layers, the simulated diffraction patterns of the two orientations were mixed with different concentrations and

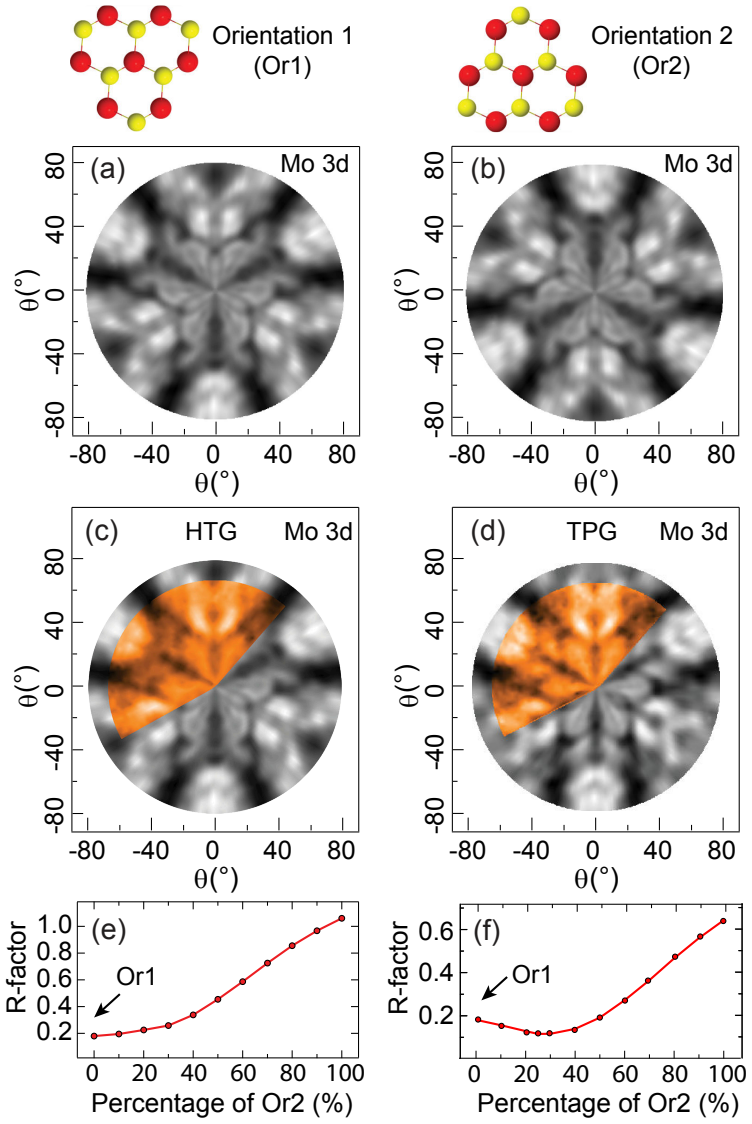

Figure 3.12: (a) and (b) Multiple scattering simulations of Mo 3d core level at 130 eV photoelectron kinetic energy, corresponding to the two orientations shown on top. (c) and (d) Mo 3d XPD patterns (colored) at 360 eV photon energy (130 eV kinetic energy) for the HTG and TPG grown MoS_2, respectively, with simulations (grey) for the best agreement given by R-factor minimization. (e) and (f) R-factor analysis corresponding to different intermixing of domains for the HTG and TPG preparation, respectively. Ball model color code: red (Mo) and yellow (S)

compared with the experimental data by means of R-factor (see section 2.7.2 in chapter 2). The total simulated intensity I_{tot} is,

$$I_{tot} = aInt_{Or1} + bInt_{Or2} \qquad (b = 1 - a) \tag{3.2}$$

where, Int_{Or1} and Int_{Or2} are the contributions to the total simulated patterns from the orientation 1 and 2, respectively, as shown in figure 3.12 and a and b are the fractions of the orientation 1 and orientation 2, respectively, included in the simulations.

The R-factor analysis for the HTG grown layer, in figure 3.12 (e), shows the best agreement for the simulation corresponding to orientation 1. Indeed with the addition of the mirror domain orientation the agreement is worsened, as seen from the trend of the R-factor. This clearly shows that the HTG grown MoS_2 layer presents just one single orientation. On the other hand, for the TPG grown layer, the R-factor analysis (figure 3.12 (f)) shows the coexistence of mirror domains with 75% of domains corresponding to orientation 1 and the remaining 25% to orientation 2.

Having determined that the HTG growth method leads to a single orientation, we used the HTG grown sample to further characterize the local structure of MoS_2. In order to do this, the experimental Mo 3d XPD pattern (figure 3.13 (a)) was compared with different simulations performed by changing the lattice parameter and the Mo-S interlayer distance of the model structure. From the R-factor analysis we obtained the best agreement for the 1H phase structure (ball model in figure 3.13) of SL MoS_2 with a lattice constant of 3.17±0.04 Å (figure 3.13 (b)) and an interlayer distance of 1.59±0.03 Å (figure 3.13 (c)), in very good agreement with the values reported in literature [58, 59] and used in the study of the orientation of the MoS_2 domains. These structural parameters were then used to analyze the XPD measurements of the S 2p core level. The measurements were performed at different photon energy, resulting in a different kinetic energy of the S 2p photoemitted electrons. The XPD measurements for the bottom layer S atoms were performed at high kinetic energy of the photoelectrons, to satisfy the forward scattering condition from the Mo and S atoms above. Similarly, low kinetic energy was used to satisfy backward scattering condition for the XPD measurements for the top layer S atoms. In figure 3.13 (d) and (e), the XPD patterns for the $S4'$ component of figure 3.10 (b) acquired at 560 eV photon energy (KE $\sim$ 397 eV) and the $S4$ component acquired at 270 eV photon energy (KE $\sim$ 108 eV) are shown together with the simulated patterns for the bottom and top S layer, respectively. Apart from a clear three-fold symmetry, the XPD patterns from both $S4'$ (R-factor = 0.15) as well as $S4$ (R-factor = 0.25), show a very good agreement as quantified by the R-factor, confirming the assignment of the peaks in S 2p core level spectra to bottom and top S layer atoms for the 1H phase structure of SL MoS_2.

However, the higher R-factor in the analysis of the XPD pattern for the $S4$ component assigned to the top S, shown in figure 3.13 (e), calls for attention.

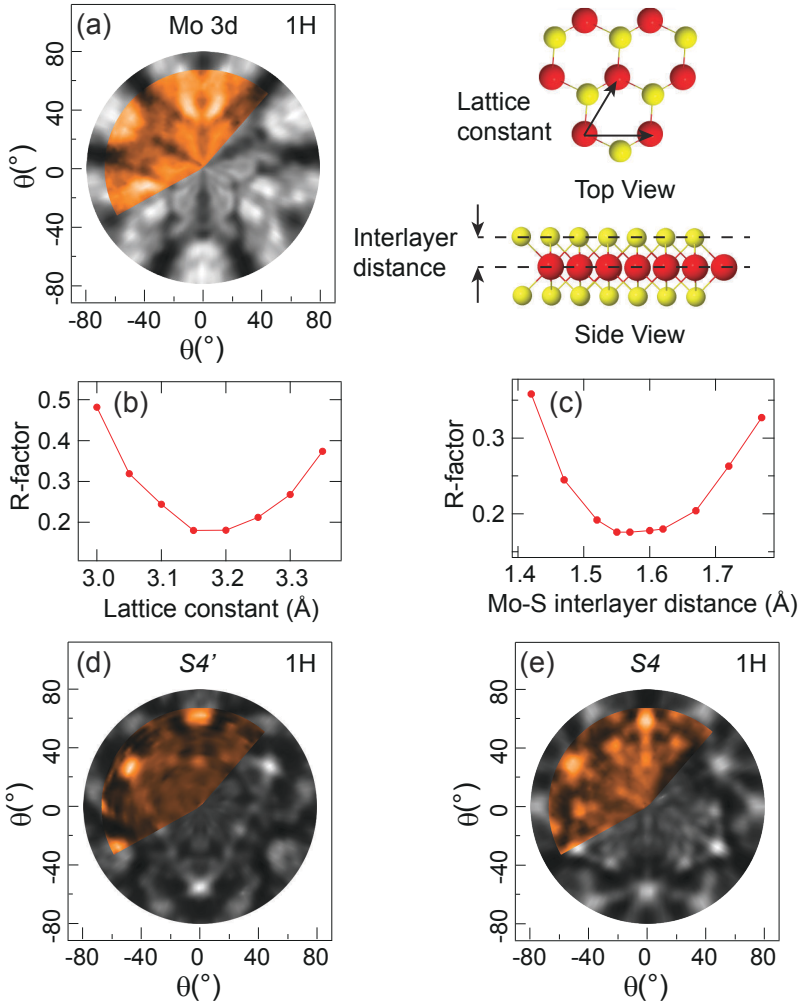

Figure 3.13: (a) Mo 3d XPD pattern obtained at 360 eV photon energy (KE = 130 eV) used to determine the local structure of MoS_2 layer, together with the ball model of the identified 1H phase structure of the grown layer, indicating the lattice parameter and the interlayer distance. R-factor analysis for the determination of (b) the lattice constant and (c) the interlayer distance of HTG grown SL MoS_2. (d) and (e) S 2p XPD patterns (color) for the $S4'$ component (162.44 eV BE, $\sim$ 397 eV KE) and the $S4$ component (162.15 eV BE, $\sim$ 108 eV KE), respectively, with multiple scattering simulations (grey) performed with structure determined before for the bottom S and top S, respectively. Ball model color code: red (Mo) and yellow (S).

Indeed, it turns out that the R-factor has a minimum when contributions to the simulated XPD pattern from top as well as bottom S components are included (see figure 3.14 (a) and (b)). In order to ascertain the contribution of bottom S in the XPD pattern of the $S4$ component at 162.15 eV BE (figure 3.10 (b)), the simulations for the S 2p intensity of top and bottom S (both at 108 eV KE) were intermixed in different proportions and the total simulated intensity was compared with the experimental XPD pattern of figure 3.13 (e). R-factor analysis, in figure 3.14 (b), shows a minimum value (0.17) when 40% of the intensity from bottom S is included in the simulation, indicating that the $S4$ component, shown in figure 3.10 (b), is not only due to the topmost S layer but also due to 40% of the bottom one. Moreover, to further support this observation, we performed a complementary analysis which demonstrates that the XPD pattern acquired at 560 eV photon energy (KE $\sim$ 397 eV) for $S4$ presents features corresponding to those shown by $S4'$, which belongs to the bottom layer S atoms. Figure 3.14 (d) shows the behavior of the R-factor obtained by comparing the simulated top S 2p XPD pattern with the experimental data obtained by subtracting to the intensity of the $S4$ component a given percentage of the intensity of the $S4'$ component, showing the best agreement with a percentage of 80%. Figure 3.14 (c) shows the comparison between simulated (grey) and experimental data (color) obtained by subtracting the aforementioned percentage of $S4'$ intensity from $S4$. Previous studies for graphene (GR) grown on different transition metal substrates have shown that, depending upon the strength of the interactions between the substrate and the GR ad-layer, the C 1s core level shows different components belonging to the strongly and weakly interacting C atoms. [60–62] Based on this, our observations suggest that the bottom layer S atoms in the 'S-Mo-S' sandwich structure of MoS_2/Au(111) can also be classified into populations of S atoms differently interacting with the Au substrate. Consequently, the S atoms that interact strongly with the substrate present a component shifted to higher BE ($S4'$, brown), while the weakly interacting S atoms show a peak (blue) at the same BE of the component belonging to top layer S atoms (yellow), as shown in the S 2p core level spectrum in figure 3.14 (e). The bottom S layer is therefore divided into about 60% of the S atoms that are strongly interacting and 40% that are weakly interacting with the Au(111) substrate. The corresponding S 2p core level can be then considered as the sum of the two contributions as shown by the spectrum with red markers in figure 3.14 (e). Moreover, the intensity of the bottom S component (red markers) is calculated to be 38% of the top S component (yellow), as a result of the attenuation of the signal from the Mo and S layers on top.

In order to determine the orientation of the Au(111) substrate, needed to identify the relative orientation of the MoS_2 ad-layer, we performed XPD measurements of the Au $4f_{7/2}$ core level for the clean sample. Figure 3.15 (a) and (b) show the XPD patterns corresponding to the bulk (B) and clean surface (S_{clean}) components (colored), respectively, measured at 200 eV photon energy (photoelectron KE $\sim$ 115 eV). The XPD pattern of the bulk component

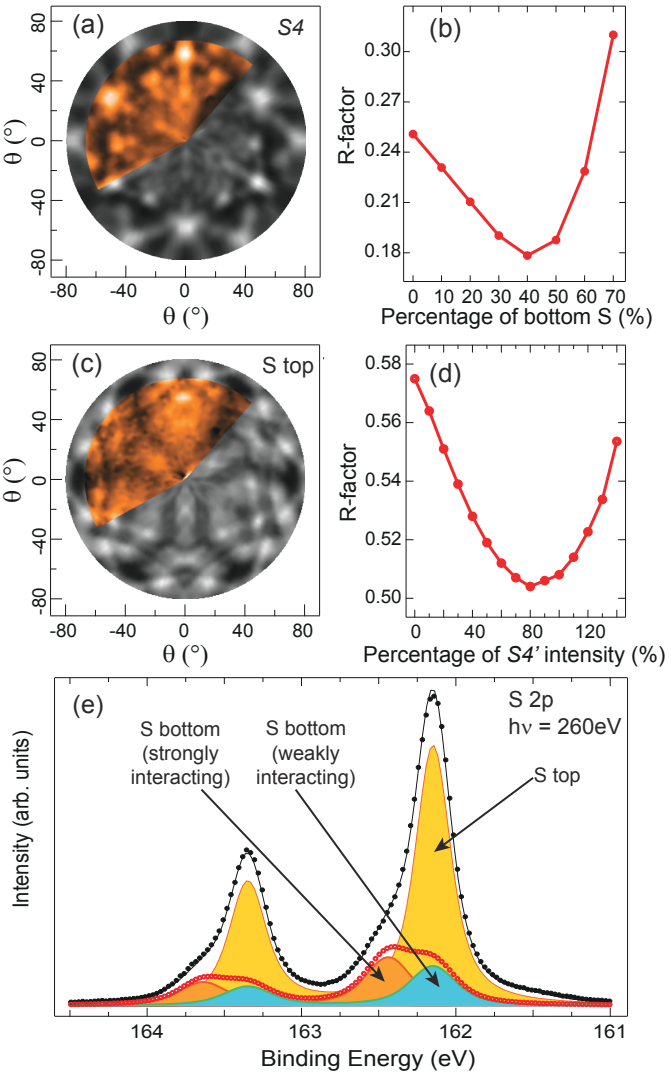

Figure 3.14: (a) S 2p XPD pattern (color) for the $S4$ component measured at 270 eV photon energy (108 eV KE) with simulation (grey) including 40% contribution of intensity from bottom layer S. (b) R-factor analysis for the determination of bottom layer S contribution in the XPD pattern of $S4$ in (a). (c) S 2p XPD pattern (color) for the $S4$ component measured at 560 eV photon energy (397 eV KE) with 80% of the intensity of $S4'$ XPD removed from the data, in comparison with the simulation (grey) for the top layer S (397 eV KE). (d) R-factor analysis for the determination of $S4'$ contribution in $S4$ XPD in (c). (e) S 2p core level spectra acquired at 260 eV photon energy, indicating different spectral components.

shows the expected three-fold symmetry of the fcc crystal stacking, while the herringbone reconstruction presents an almost six-fold symmetry of the pattern from the Au 4f surface component. The herringbone reconstruction was simulated by compressing the surface unit cell in the $< \bar{1}10 >$ direction by 4.5%, averaging over the three 60° rotated domains, while three layers below the surface were considered as the bulk. The experimental data show a good agreement (R-factor = 0.33 eV) with the simulations and the resulting orientation of gold substrate was identified as shown in figure 3.15 (d). It is also important to highlight that the agreement between experiment and simulation for the Au 4f surface peak is not excellent because the simulations were performed for a flat layer, while in reality the Au surface is corrugated with a large unit cell and many non-equivalent atoms.

The 10×10 MoS_2 superstructure on 11×11 Au unit cell for the two mirror domain orientations of MoS_2 on Au, are shown in figure 3.16. Theoretical calculations by A. Bruix *et al.* [44] showed that the most favorable configuration for small 2D MoS_2 clusters on Au(111) is with the S atoms in *atop* position. These small 2D clusters are likely to be the seeds for the further growth of MoS_2 . With the S atoms in *atop* position, the Mo atoms can go in the three-fold fcc or *hcp* position, as shown in figure 3.16 (a) and (b), respectively. Our XPD results show that, in the case of the HTG, the MoS_2 layer assumes one single orientation which corresponds to the one of figure 3.16 (a), with the local configuration of S *atop* and Mo in threefold fcc site. In the case of TPG 25% of the MoS_2 domains assume the opposite orientation, i.e. locally with S *atop* and Mo in the *hcp* site.

3.4.2 ARPES and complete spin polarization in HTG grown MoS_2

Once the presence of a single domain orientation was confirmed by analyzing the geometric structure of the layer through XPD measurements, we performed ARPES measurements on the HTG MoS_2 (coverage $\sim$ 0.6 ML) in order to obtain information about its electronic structure. Figure 3.17 (a), shows the dispersion of the MoS_2 bands measured by ARPES at the SGM-3 beamline of ASTRID2. [33] The valence band maxima (1.39 eV BE) at **K** point of the surface Brillouin zone of MoS_2 is clearly visible, as well as, the spin-orbit splitting (144 meV) of the state, in close agreement with literature. [25, 29] We did not observe any detectable contributions from a second layer, as this would give rise to a second band near **Γ** point, as shown in 3.17 (b) for a sample with higher MoS_2 coverage, in agreement with literature. [63, 64] It is also important to note that the simultaneous presence of mirror domains, as observed by Grønborg *et al.* [29], is not detectable in the band structure obtained from ARPES, at least in a non-spin resolved experiment. On the other hand, the presence of many small domains would result in defects such as domain boundaries, leading to the scattering induced spectral broadening of the bands. Although, the band dispersion shown in figure 3.17 (a) is similar

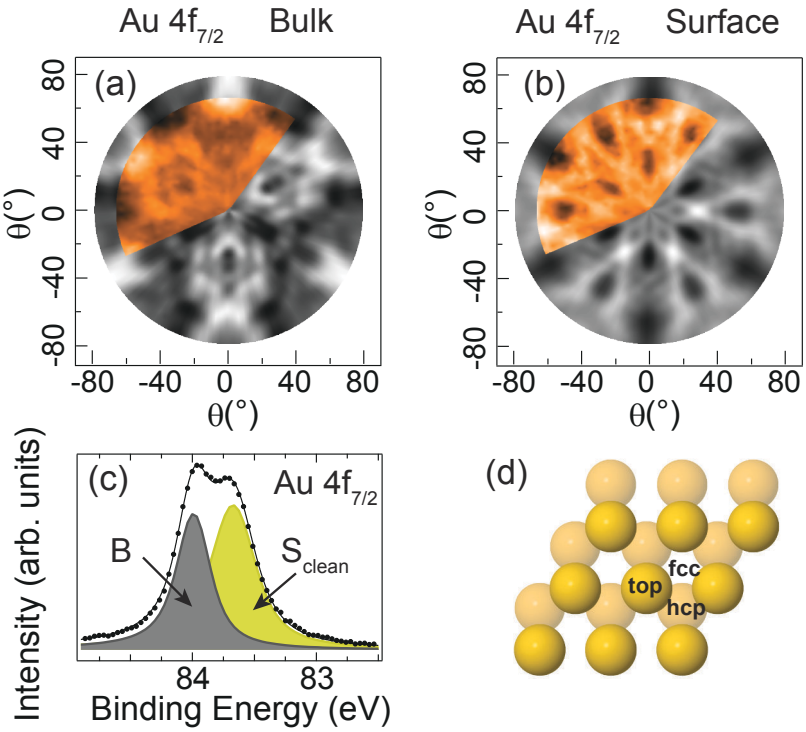

Figure 3.15: Au $4f_{7/2}$ XPD patterns acquired at $\sim$ 115 eV photoelectron KE for (a) Bulk (R-factor = 0.33) and (b) Surface (R-factor = 0.33) components. The experimental patterns (colored) are compared with multiple scattering simulations (grey) and the orientation of the Au(111) crystal is identified as shown in (d). (c) Au $4f_{7/2}$ XPS spectrum acquired of the clean Au(111) sample at 200 eV photon energy, showing the bulk (B) and clean surface (S_{clean}) components.

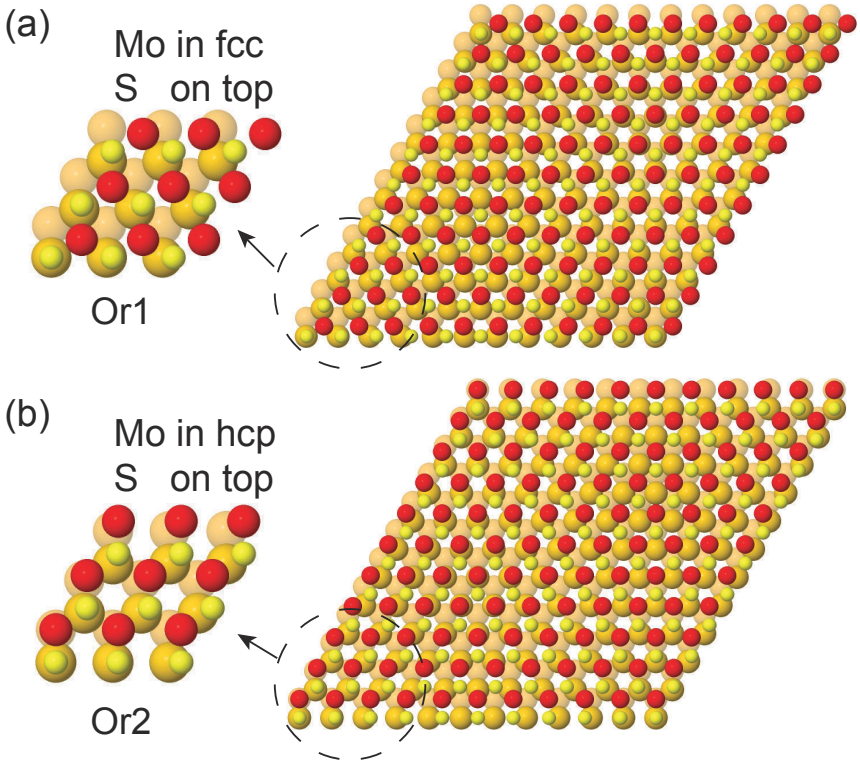

Figure 3.16: 10×10-MoS_2/11×11-Au(111) superstructure. For S adsorbed *atop* position, insets on the left show the adsorption configuration of bonding regions (a) Mo in *fcc* and (B) Mo in *hcp* sites. Ball color code: red (Mo), yellow (S), orange (Au surface layer) and amber (Au second layer).

to previous findings for this system [25, 65], the linewidth of the states near **K** point is substantially smaller (51 and 70 meV for the upper and lower band instead of 164 and 117 meV measured in [25]), indicating a higher quality of the layer grown by following the HTG procedure.

As mentioned earlier, the single orientation character of the layer allows to distinguish between the **K** and $-\mathbf{K}$ points of the reciprocal lattice of MoS_2. In order to do this we performed spin-resolved ARPES at the APE beamline of Elettra [34] to measure the spin polarization of the states near **K** and $-\mathbf{K}$ and to show that the spin polarization is reversed, when moving from one point to the other. The measured spin-resolved energy distribution curves (EDCs) near **K** and $-\mathbf{K}$ are shown in figure 3.17 (c). The spin polarization P_i was determined from these EDCs as

$$P_i = \frac{I_i^{\uparrow} - I_i^{\downarrow}}{S(I_i^{\uparrow} + I_i^{\downarrow})}, \tag{3.3}$$

where $i = x, y, z$ denotes the spin quantization axis in the reference frame of the detection and $S = 0.3$ is the Sherman function of the detector, also known as the analyzing power for Mott scattering from single free-atoms. [66] $I_i^{\uparrow,\downarrow}$ were corrected by a relative efficiency calibration and fitted with Voigt function (figure 3.17 (c)). The background contribution consisting of spin-unpolarized tails of lower-lying Au states was taken into account for the calculated P_i spectra (figure 3.17 (d)). Quantitative spin polarization magnitudes were determined from the area ratio of the fitted peaks and P_i were transformed into the sample's reference frame by applying an Euler's rotation matrix. As a result of this analysis, we obtain the spin polarization of 86±14 % with opposite orientation for the **K** and $-\mathbf{K}$ points of the reciprocal space, as shown in figure 3.17 (d). The high degree of the measured spin polarization further confirms the single-orientation character of the SL MoS_2 grown with the HTG procedure because the presence of a mixture of mirror domains would cause a decrease of the spin polarization. This effect was observed also for SL $MoSe_2$ grown on bilayer graphene. [67]

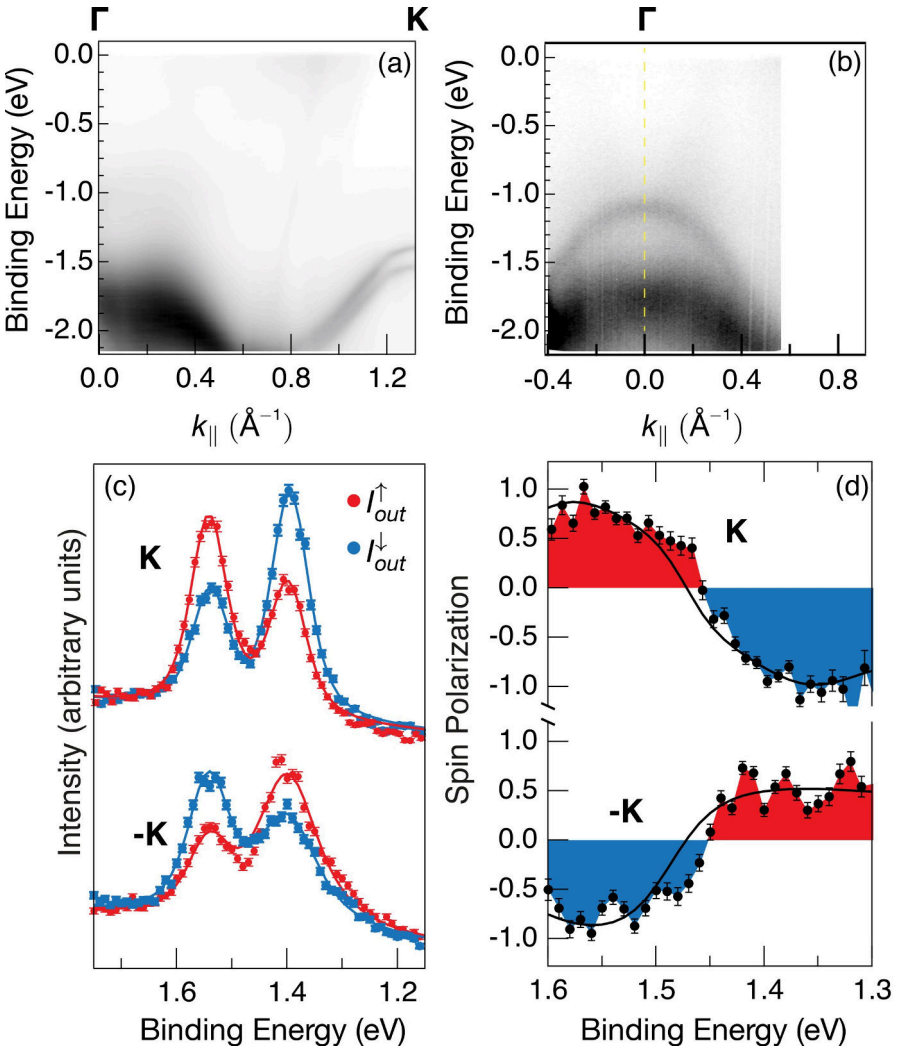

Figure 3.17: Angle-resolved photoemission intensity (hν = 25 eV) along the **Γ**-**K** direction of SL MoS_2 Brillouin zone for 0.6 ML of HTG grown MoS_2. (b) For a different sample with higher coverage of MoS_2, angle-resolved photoemission intensity (hν = 25 eV) close to **Γ** point (indicated with a dashed line) showing an extra band due to the presence of bi-layer MoS_2. (c) Out-of plane spin-resolved energy distribution curves at **K** and −**K** points (hν = 30 eV) for 0.6 ML of MoS_2. Red and blue colors mark spin-up and spin-down signals, respectively. Raw data is shown without a correction for the spin-sensitivity (Sherman function) of the detector. Solid lines are Voigt fittings to the experimental data marked with circles. (d) Background-subtracted out-of plane spin polarization at **K** and −**K** points. Solid lines mark the spin polarization calculated from the fits, taking the Sherman function into account.

3.5 Conclusions

A multi-method experimental approach was employed to study the growth of SL MoS_2 on Au(111) substrate. First, by following a method already reported in literature, [28] we used fast-XPS to study the transformation of pre-sulfided 2D Mo-S clusters to SL MoS_2, while annealing in H_2S background pressure, the so called temperature programmed growth (TPG). High-resolution XPS of Mo 3d and S 2p core levels show the presence of incompletely sulfided Mo-S compounds of the type MoS_x ($x < 2$) [36, 37], that do not convert to MoS_2 even after prolonged annealing in H_2S, besides the spectral components belonging to MoS_2. Thereafter, following the growth in real time by fast-XPS, to carefully tune the growth parameters, we developed a new procedure that consisted of Mo deposition at 823 K in H_2S pressure, leading to the direct growth of SL MoS_2. This results in a superior quality of the layer, as the high-resolution XPS of Mo 3d and S 2p core level do not show any contribution from unwanted species, similar to those present in the case of TPG. The higher quality of the MoS_2 layer is further demonstrated by the sharp spots in LEED and STM measurements that show domains with much larger size than previously reported for similar system. [28, 29]

The S 2p core level shows the presence of two components belonging to the top and the bottom layer S atoms in the 'S-Mo-S' structure of MoS_2. The shift of bottom layer S component to higher BE provides the spectroscopic evidence of the interactions with the Au substrate, as previously predicted by theory. [42] Such interactions are also observed from the SCLS of the Au $4f_{7/2}$ spectra, where an extra component appears with the growth of MoS_2 and increases at the expanses of the Au clean surface peak.

The most important aspect of the HTG growth is that the resulting MoS_2 layer presents just one single orientation, as evident from the XPD results analyzed with the multiple scattering simulations. [32] On the contrary, the TPG produces a layer that shows the coexistence of mixed domains with 180° rotated orientations in 75:25 fraction. Moreover, the HTG grown SL MoS_2 results in much smaller linewidth of the bands near **K** point, than previously reported values [25], and results in a complete out-of plane spin polarization, as a result of high crystalline nature and the single domain orientation of the HTG grown layer.

References

[1] Dickinson, R. G.; Pauling, L. The crystal structure of molybdenite. *Journal of the American Chemical Society* **1923**, *45*, 1466–1471.

[2] Wilson, J.; Yoffe, A. The transition metal dichalcogenides discussion and interpretation of the observed optical, electrical and structural properties. *Advances in Physics* **1969**, *18*, 193–335.

[3] Helveg, S.; Lauritsen, J. V.; Lægsgaard, E.; Stensgaard, I.; Nørskov, J. K.; Clausen, B. S.; Topsøe, H.; Besenbacher, F. Atomic-Scale Structure of Single-Layer MoS_2 Nanoclusters. *Physical Review Letters* **2000**, *84*, 951–954.

[4] Lauritsen, J. V.; Kibsgaard, J.; Helveg, S.; Topsøe, H.; Clausen, B. S.; Lægsgaard, E.; Besenbacher, F. Size-dependent structure of MoS_2 nanocrystals. *Nature Nanotechnology* **2007**, *2*, 53–58.

[5] Tenne, R. Inorganic nanotubes and fullerene-like nanoparticles. *Nature Nanotechnology* **2006**, *1*, 103–111.

[6] Clausen, H. T. B. S.; Massoth, E. E. Hydrotreating Catalysis Science and Technology. *Springer Verlag: Berlin-Heidelberg* **1996**, *11*.

[7] Young, P. A. Lattice parameter measurements on molybdenum disulphide. *Journal of Physics D: Applied Physics* **1968**, *1*, 936, 1–5.

[8] Kam, K. K.; Parkinson, B. A. Detailed photocurrent spectroscopy of the semiconducting group VIB transition metal dichalcogenides. *The Journal of Physical Chemistry* **1982**, *86*, 463–467.

[9] Mak, K. F.; Lee, C.; Hone, J.; Shan, J.; Heinz, T. F. Atomically Thin MoS_2: A New Direct-Gap Semiconductor. *Physical Review Letters* **2010**, *105*, 136805, 1–4.

[10] Kuc, A.; Zibouche, N.; Heine, T. Influence of quantum confinement on the electronic structure of the transition metal sulfide TS_2. *Physical Review B* **2011**, *83*, 245213, 1–4.

[11] Radisavljevic, B.; Radenovic, A.; Brivio, J.; Giacometti, V.; Kis, A. Single-layer MoS_2 transistors. *Nature Nanotechnology* **2011**, *6*, 147–150.

[12] Lin, Y.-C.; Ghosh, R. K.; Addou, R.; Lu, N.; Eichfeld, S. M.; Zhu, H.; Li, M.-Y.; Peng, X.; Kim, M. J.; Li, L.-J.; Wallace, R. M.; Datta, S.; Robinson, J. A. Atomically thin resonant tunnel diodes built from synthetic van der Waals heterostructures. *Nature Communications* **2015**, *6*, 7311, 1–6.

[13] Sangwan, V. K.; Jariwala, D.; Kim, I. S.; Chen, K.-S.; Marks, T. J.; Lauhon, L. J.; Hersam, M. C. Gate-tunable memristive phenomena mediated by grain boundaries in single-layer MoS_2. *Nature Nanotechnology* **2015**, *10*, 403–406.

[14] Bertolazzi, S.; Krasnozhon, D.; Kis, A. Nonvolatile Memory Cells Based on MoS_2/Graphene Heterostructures. *ACS Nano* **2013**, *7*, 3246–3252.

[15] Bernardi, M.; Palummo, M.; Grossman, J. C. Extraordinary Sunlight Absorption and One Nanometer Thick Photovoltaics Using Two-Dimensional Monolayer Materials. *Nano Letters* **2013**, *13*, 3664–3670.

[16] Gutiérrez, H. R.; Perea-López, N.; Elías, A. L.; Berkdemir, A.; Wang, B.; Lv, R.; López-Urías, F.; Crespi, V. H.; Terrones, H.; Terrones, M. Extraordinary Room-Temperature Photoluminescence in Triangular WS_2 Monolayers. *Nano Letters* **2013**, *13*, 3447–3454.

[17] Mak, K. F.; He, K.; Shan, J.; Heinz, T. F. Control of valley polarization in monolayer MoS_2 by optical helicity. *Nature Nanotechnology* **2012**, *7*, 494–498.

[18] Zeng, H.; Dai, J.; Yao, W.; Xiao, D.; Cui, X. Valley polarization in MoS_2 monolayers by optical pumping. *Nature Nanotechnology* **2012**, *7*, 490–493.

[19] Mak, K. F.; McGill, K. L.; Park, J.; McEuen, P. L. The valley Hall effect in MoS_2 transistors. *Science* **2014**, *344*, 1489–1492.

[20] Xiao, D.; Liu, G.-B.; Feng, W.; Xu, X.; Yao, W. Coupled Spin and Valley Physics in Monolayers of MoS_2 and Other Group-VI Dichalcogenides. *Physical Review Letters* **2012**, *108*, 196802, 1–5.

[21] Xu, X.; Yao, W.; Xiao, D.; Heinz, T. F. Spin and pseudospins in layered transition metal dichalcogenides. *Nature Physics* **2014**, *10*, 343–350.

[22] Zhu, Z. Y.; Cheng, Y. C.; Schwingenschlögl, U. Giant spin-orbit-induced spin splitting in two-dimensional transition-metal dichalcogenide semiconductors. *Physical Review B* **2011**, *84*, 153402, 1–5.

[23] Cappelluti, E.; Roldán, R.; Silva-Guillén, J. A.; Ordejón, P.; Guinea, F. Tight-binding model and direct-gap/indirect-gap transition in single-layer and multilayer MoS_2. *Physical Review B* **2013**, *88*, 075409, 1–18.

[24] Yuan, H.; Bahramy, M. S.; Morimoto, K.; Wu, S.; Nomura, K.; Yang, B.-J.; Shimotani, H.; Suzuki, R.; Toh, M.; Kloc, C.; Xu, X.; Arita, R.; Nagaosa, N.; Iwasa, Y. Zeeman-type spin splitting controlled by an electric field. *Nature Physics* **2013**, *9*, 563–569.

[25] Miwa, J. A.; Ulstrup, S.; Sørensen, S. G.; Dendzik, M.; Čabo, A. G.; Bianchi, M.; Lauritsen, J. V.; Hofmann, P. Electronic Structure of Epitaxial Single-Layer MoS_2. *Physical Review Letters* **2015**, *114*, 046802, 1–5.

[26] van der Zande, A. M.; Huang, P. Y.; Chenet, D. A.; Berkelbach, T. C.; You, Y.; Lee, G.-H.; Heinz, T. F.; Reichman, D. R.; Muller, D. A.; Hone, J. C. Grains and grain boundaries in highly crystalline monolayer molybdenum disulphide. *Nature Materials* **2013**, *12*, 554–561.

[27] Schmidt, H.; Wang, S.; Chu, L.; Toh, M.; Kumar, R.; Zhao, W.; Castro Neto, A. H.; Martin, J.; Adam, S.; Özyilmaz, B.; Eda, G. Transport Properties of Monolayer MoS_2 Grown by Chemical Vapor Deposition. *Nano Letters* **2014**, *14*, 1909–1913.

[28] Sorensen, S. G.; Füchtbauer, H. G.; Tuxen, A. K.; Walton, A. S.; Lauritsen, J. V. Structure and Electronic Properties of In Situ Synthesized Single-Layer MoS_2 on a Gold Surface. *ACS Nano* **2014**, *8*, 6788–6796.

[29] Grønborg, S. S.; Ulstrup, S.; Bianchi, M.; Dendzik, M.; Sanders, C. E.; Lauritsen, J. V.; Hofmann, P.; Miwa, J. A. Synthesis of Epitaxial Single-Layer MoS_2 on Au(111). *Langmuir* **2015**, *31*, 9700–9706.

[30] Abrami, A.; Barnaba, M.; Battistello, L.; Bianco, A.; Brena, B.; Cautero, G.; Chen, Q. H.; Cocco, D.; Comelli, G.; Contrino, S.; DeBona, F.; Di Fonzo, S.; Fava, C.; Finetti, P.; Furlan, P.; Galimberti, A.; Gambitta, A.; Giuressi, D.; Godnig, R.; Jark, W.; Lizzit, S.; Mazzolini, F.; Melpignano, P.; Olivi, L.; Paolucci, G.; Pugliese, R.; Qian, S. N.; Rosei, R.; Sandrin, G.; Savoia, A.; Sergo, R.; Sostero, G.; Tommasini, R.; Tudor, M.; Vivoda, D.; Wei, F. Q.; Zanini, F. Super ESCA: First beamline operating at ELETTRA. *Review of Scientific Instruments* **1995**, *66*, 1618–1620.

[31] Jia, J.; Bendounan, A.; Kotresh, H. M. N.; Chaouchi, K.; Sirotti, F.; Sampath, S.; Esaulov, V. A. Selenium Adsorption on Au(111) and Ag(111) Surfaces: Adsorbed Selenium and Selenide Films. *The Journal of Physical Chemistry C* **2013**, *117*, 9835–9842.

[32] García de Abajo, F. J.; Van Hove, M. A.; Fadley, C. S. Multiple scattering of electrons in solids and molecules: A cluster-model approach. *Physical Review B* **2001**, *63*, 075404, 1–16.

[33] Hoffmann, S. V.; Søndergaard, C.; Schultz, C.; Li, Z.; Hofmann, P. An undulator-based spherical grating monochromator beamline for angle-resolved photoemission spectroscopy. *Nuclear Instruments and Methods in Physics Research A* **2004**, *523*, 441–453.

[34] Bigi, C.; Das, P. K.; Benedetti, D.; Salvador, F.; Krizmancic, D.; Sergo, R.; Martin, A.; Panaccione, G.; Rossi, G.; Fujii, J.; Vobornik, I. Very efficient

spin polarization analysis (VESPA): new exchange scattering-based setup for spin-resolved ARPES at APE-NFFA beamline at Elettra. *Journal of Synchrotron Radiation* **2017**, *24*, 750–756.

[35] Bruix, A.; Füchtbauer, H. G.; Tuxen, A. K.; Walton, A. S.; Andersen, M.; Porsgaard, S.; Besenbacher, F.; Hammer, B.; Lauritsen, J. V. In Situ Detection of Active Edge Sites in Single-Layer MoS_2 Catalysts. *ACS Nano* **2015**, *9*, 9322–9330.

[36] Baker, M.; Gilmore, R.; Lenardi, C.; Gissler, W. XPS investigation of preferential sputtering of S from MoS_2 and determination of MoS_x stoichiometry from Mo and S peak positions. *Applied Surface Science* **1999**, *150*, 255 – 262.

[37] Lince, J. R.; Carre, D. J.; Fleischauer, P. D. Effects of argon-ion bombardment on the basal plane surface of molybdenum disulfide. *Langmuir* **1986**, *2*, 805–808.

[38] Doniach, S.; Šunjić, M. Many-Electron Singularity in X-ray Photoemission and X-ray Line Spectra from Metals. *Journal of Physical Chemistry: Solid State* **1970**, *3*, 285–291.

[39] Dendzik, M.; Michiardi, M.; Sanders, C.; Bianchi, M.; Miwa, J. A.; Grønborg, S. S.; Lauritsen, J. V.; Bruix, A.; Hammer, B.; Hofmann, P. Growth and electronic structure of epitaxial single-layer WS_2 on Au(111). *Physical Review B* **2015**, *92*, 245442, 1–7.

[40] Klyushin, A. Y.; Rocha, T. C. R.; Havecker, M.; Knop-Gericke, A.; Schlögl, R. A near ambient pressure XPS study of Au oxidation. *Physical Chemistry Chemical Physics* **2014**, *16*, 7881–7886.

[41] Narasimhan, S.; Vanderbilt, D. Elastic stress domains and the herringbone reconstruction on Au(111). *Physical Review Letters* **1992**, *69*, 1564–1567.

[42] Bollinger, M. V.; Jacobsen, K. W.; Nørskov, J. K. Atomic and electronic structure of MoS_2 nanoparticles. *Physical Review B* **2003**, *67*, 085410, 1–17.

[43] Tsai, C.; Abild-Pedersen, F.; Nørskov, J. K. Tuning the MoS_2 Edge-Site Activity for Hydrogen Evolution via Support Interactions. *Nano Letters* **2014**, *14*, 1381–1387.

[44] Bruix, A.; Lauritsen, J. V.; Hammer, B. Effects of particle size and edge structure on the electronic structure, spectroscopic features, and chemical properties of Au(111)-supported MoS_2 nanoparticles. *Faraday Discussions* **2016**, *188*, 323–343.

[45] Weber, T.; Muijsers, J.; Niemantsverdriet, J. Structure of amorphous MoS_3. *Journal of Physical Chemistry* **1995**, *99*, 9194–9200.

[46] Lauritsen, J. V.; Kibsgaard, J.; Helveg, S.; Topsøe, H.; Clausen, B. S.; Lægsgaard, E.; Besenbacher, F. Size-dependent structure of MoS_2 nanocrystals. *Nature Nanotechnology* **2007**, *2*, 53–58.

[47] Batzill, M. The surface science of graphene: Metal interfaces, CVD synthesis, nanoribbons, chemical modifications, and defects. *Surface Science Reports* **2012**, *67*, 83 – 115.

[48] Bignardi, L.; Lacovig, P.; Dalmiglio, M. M.; Orlando, F.; Ghafari, A.; Petaccia, L.; Baraldi, A.; Larciprete, R.; Lizzit, S. Key role of rotated domains in oxygen intercalation at graphene on Ni(111). *2D Materials* **2017**, *4*, 025106, 1–11.

[49] Orlando, F.; Lacovig, P.; Omiciuolo, L.; Apostol, N. G.; Larciprete, R.; Baraldi, A.; Lizzit, S. Epitaxial Growth of a Single-Domain Hexagonal Boron Nitride Monolayer. *ACS Nano* **2014**, *8*, 12063–12070.

[50] Christensen, A.; Ruban, A. V.; Stoltze, P.; Jacobsen, K. W.; Skriver, H. L.; Nørskov, J. K.; Besenbacher, F. Phase diagrams for surface alloys. *Physical Review B* **1997**, *56*, 5822–5834.

[51] Song, Z.; Cai, T.; Chang, Z.; Liu, G.; Rodriguez, J. A.; Hrbek, J. Molecular Level Study of the Formation and the Spread of MoO_3 on Au(111) by Scanning Tunneling Microscopy and X-ray Photoelectron Spectroscopy. *Journal of the American Chemical Society* **2003**, *125*, 8059–8066.

[52] Martin-Recio, A.; Romero-Muniz, C.; Martinez-Galera, A. J.; Pou, P.; Perez, R.; Gomez-Rodriguez, J. M. Tug-of-war between corrugation and binding energy: revealing the formation of multiple moire patterns on a strongly interacting graphene-metal system. *Nanoscale* **2015**, *7*, 11300–11309.

[53] Grånás, E.; Knudsen, J.; Schröder, U. A.; Gerber, T.; Busse, C.; Arman, M. A.; Schulte, K.; Andersen, J. N.; Michely, T. Oxygen Intercalation under Graphene on Ir(111): Energetics, Kinetics, and the Role of Graphene Edges. *ACS Nano* **2012**, *6*, 9951–9963.

[54] Vinogradov, N. A.; Zakharov, A. A.; Ng, M. L.; Mikkelsen, A.; Lundgren, E.; Mårtensson, N.; Preobrajenski, A. B. One-Dimensional Corrugation of the h-BN Monolayer on Fe(110). *Langmuir* **2012**, *28*, 1775–1781.

[55] Schwarz, M.; Riss, A.; Garnica, M.; Ducke, J.; Deimel, P. S.; Duncan, D. A.; Thakur, P. K.; Lee, T.-L.; Seitsonen, A. P.; Barth, J. V.; Allegretti, F.; Auwärter, W. Corrugation in the Weakly Interacting Hexagonal-BN/Cu(111) System: Structure Determination by Combining Noncontact Atomic Force Microscopy and X-ray Standing Waves. *ACS Nano* **2017**, *11*, 9151–9161.

[56] Dumcenco, D.; Ovchinnikov, D.; Marinov, K.; Lazić, P.; Gibertini, M.; Marzari, N.; Sanchez, O. L.; Kung, Y.-C.; Krasnozhon, D.; Chen, M.-W.; Bertolazzi, S.; Gillet, P.; i Morral, A. F.; Radenovic, A.; Kis, A. Large-Area Epitaxial Monolayer MoS_2. *ACS Nano* **2015**, *9*, 4611–4620.

[57] Zhou, W.; Zou, X.; Najmaei, S.; Liu, Z.; Shi, Y.; Kong, J.; Lou, J.; Ajayan, P. M.; Yakobson, B. I.; Idrobo, J.-C. Intrinsic Structural Defects in Monolayer Molybdenum Disulfide. *Nano Letters* **2013**, *13*, 2615–2622.

[58] Winer, W. Molybdenum disulfide as a lubricant: A review of the fundamental knowledge. *Wear* **1967**, *10*, 422 – 452.

[59] Holinski, R.; Gänsheimer, J. A study of the lubricating mechanism of molybdenum disulfide. *Wear* **1972**, *19*, 329 – 342.

[60] Preobrajenski, A. B.; Ng, M. L.; Vinogradov, A. S.; Mårtensson, N. Controlling graphene corrugation on lattice-mismatched substrates. *Physical Review B* **2008**, *78*, 073401, 1–4.

[61] Alfè, D.; Pozzo, M.; Miniussi, E.; Günther, S.; Lacovig, P.; Lizzit, S.; Larciprete, R.; Burgos, B. S.; Menteş, T. O.; Locatelli, A.; Baraldi, A. Fine tuning of graphene-metal adhesion by surface alloying. *Scientific Reports* **2013**, *3*, 2430, 1–6.

[62] Miniussi, E.; Pozzo, M.; Baraldi, A.; Vesselli, E.; Zhan, R. R.; Comelli, G.; Menteş, T. O.; Niño, M. A.; Locatelli, A.; Lizzit, S.; Alfè, D. Thermal Stability of Corrugated Epitaxial Graphene Grown on Re(0001). *Physical Review Letters* **2011**, *106*, 216101, 1–4.

[63] Zhang, Y.; Chang, T.-R.; Zhou, B.; Cui, Y.-T.; Yan, H.; Liu, Z.; Schmitt, F.; Lee, J.; Moore, R.; Chen, Y.; Lin, H.; Jeng, H.-T.; Mo, S.-K.; Hussain, Z.; Bansil, A.; Shen, Z.-X. Direct observation of the transition from indirect to direct bandgap in atomically thin epitaxial $MoSe_2$. *Nature Nanotechnology* **2014**, *9*, 111–115.

[64] Miwa, J. A.; Dendzik, M.; Grønborg, S. S.; Bianchi, M.; Lauritsen, J. V.; Hofmann, P.; Ulstrup, S. Van der Waals Epitaxy of Two-Dimensional MoS_2–Graphene Heterostructures in Ultrahigh Vacuum. *ACS Nano* **2015**, *9*, 6502–6510.

[65] Bruix, A.; Miwa, J. A.; Hauptmann, N.; Wegner, D.; Ulstrup, S.; Grønborg, S. S.; Sanders, C. E.; Dendzik, M.; Čabo, A. G.; Bianchi, M.; Lauritsen, J. V.; Khajetoorians, A. A.; Hammer, B.; Hofmann, P. Single-layer MoS_2 on Au(111): Band gap renormalization and substrate interaction. *Physical Review B* **2016**, *93*, 165422, 1–10.

[66] Sherman, N. Coulomb Scattering of Relativistic Electrons by Point Nuclei. *Physical Review* **1956**, *103*, 1601–1607.

[67] Mo, S.-K.; Hwang, C.; Zhang, Y.; Fanciulli, M.; Muff, S.; Hugo Dil, J.; Shen, Z.-X.; Hussain, Z. Spin-resolved photoemission study of epitaxially grown $MoSe_2$ and WSe_2 thin films. *Journal of Physics: Condensed Matter* **2016**, *28*, 454001, 1–7.

CHAPTER 4

Synthesis of single layer tungsten disulfide on Au(111) with single orientation.

Another material of the TMDC family that is suitable for the realization of ultrathin electronic devices is tungsten disulfide (WS_2). It has been demonstrated by means of optical measurements that SL WS_2 exhibits a direct band gap $\sim$ 2 eV. [1] The fundamental properties of SL WS_2 are very similar to those of MoS_2 and can therefore be used in the same range of technological applications. On the other hand, as the spin-orbit coupling SOC is proportional to the fourth power of atomic number Z (SOC $\propto Z^4$), a much stronger overall effect on the valence band splitting is expected for WS_2 than in the case of Mo based analogue. Indeed, previous studies [2, 3] have shown that the spin splitting at the valence band of SL WS_2 ($\sim$ 420 meV) is almost three times stronger than for MoS_2 ($\sim$ 145 meV [4]). Moreover, the strong spin-splitting of bands can give rise to increased band curvature near the top of the valence band, resulting in a reduced effective mass. Indeed, SL WS_2 is predicted to be the best choice as transistor channel material among the TMDCs family, due to its low effective hole mass that allows for high hole mobility values. [5, 6] Consequently, SL WS_2 based devices are more suited for technological applications, as the strong splitting would result in increased stability of the aforementioned properties, even at room temperature. However, a single domain orientation of the layer is important in order to differentiate between the two valleys (as shown in the chapter 3 for SL MoS_2), leading to the realization of spintronic and valleytronic devices. [7]

In this chapter, we present the synthesis of high quality singly oriented WS_2 monolayers obtained by optimizing the HTG procedure, already used to obtain singly oriented MoS_2 presented in chapter 3. The careful tuning of

the growth parameters was achieved again by following the deposition in real time by means of in-situ fast-XPS, that allowed us to avoid the formation of incompletely sulfided and metallic clusters. The layer was characterized by high-resolution XPS and LEED, that confirmed a long range order and high quality of grown layer. The single orientation character of the WS_2 monolayer was verified by XPD measurements in association with multiple scattering simulations.

Once the single domain character of the SL WS_2 was established, the sample was used to perform ARPES measurements as reported in Hinsche *et. al* [20], in order to study the WS_2 electronic structure. The valence band dispersion showed very sharp bands and presented previously undetected details such as moiré induced minigaps in the two spin-split branches of the valence band. Finally, the strong splitting was used to study the temperature dependence of the electron-phonon coupling strength, close to the top of the upper and the lower valence band at the **K** point of the surface Brillouin zone of SL WS_2.

4.1 Experiments and methods

Single layer WS_2 was grown at the SuperESCA beamline of Elettra [8] and characterized using XPS and XPD measurements. The atomically clean Au(111) surface was prepared similarly to what described in the previous chapter, by repeated cycles of Ar^+ sputtering at 2 keV followed by an annealing to 940 K for 10 min. The sample cleanliness was checked with XPS and no contaminants were detected. The final LEED pattern showed the spots of the herringbone reconstruction typical of the clean Au(111). Tungsten atoms were deposited from a home-built evaporator (consisting of a W filament heated through direct current) and H_2S, as source of sulfur with a nominal purity of 99.8%, was dosed through a leak valve. The W evaporator was mounted in front of the sample and H_2S was introduced in the main chamber during measurements.

We followed the real time evolution of the WS_2 layer growth by means of fast-XPS of the W $4f_{7/2}$ core level (at photon energy $h\nu = 140$ eV). After the completion of the growth, high resolution XPS (energy resolution better than 50 meV) measured at room temperature (RT) in normal emission conditions and LEED measurements were used to characterize the WS_2 monolayers. All the binding energies (BEs) are referred to Fermi level of the Au substrate. XPD measurements with photon energy corresponding to photoelectron KE $\sim$ 326 eV for tungsten and $\sim$ 397 eV for bottommost sulfur in the covalently bonded 'S-W-S' layers of WS_2 were measured in order to achieve mostly forward scattering conditions. The experimental XPD results were compared with multiple scattering simulations performed at the same electron KE, using the EDAC program package. [9] ARPES measurements were performed at the SGM-3 beamline of the synchrotron radiation facility ASTRID2 in Aarhus. [10] The energy and angular resolution were better than 30 meV and 0.2°, respectively. The sample temperature was $\sim$ 30 K during the measurements. The sample

was transferred to Aarhus in air. After inserting it into the ultrahigh vacuum system, it was annealed at 800 K for 30 minutes, in order to remove adsorbed impurities.

4.2 Growth of single layer WS_2 on Au(111)

Two procedures that exploited different growth conditions were used for the growth of single layer WS_2 on Au(111). In chapter 3, we have shown that the HTG method adopted for the growth of MoS_2/Au(111) results in high quality singly oriented MoS_2 monolayers. Consequently, the HTG method was used also to grow WS_2 on Au(111).

At the beginning of the first procedure, Growth 1, while depositing W the sample temperature was set at 873 K and the initial H_2S pressure was $1{\times}10^{-6}$ mbar. During the growth, the sample temperature varied between 823 K and 873 K. The W deposition rate, measured by a quartz micro-balance, amounted to $\sim 7.5 \times 10^{-3}$ ML/minute, where a monolayer (ML) corresponds to the surface atomic density of the Au(111) surface.

In figure 4.1 (a), the fast-XPS intensity plot is shown together with the peak fit analysis of the last W $4f_{7/2}$ core level spectrum of the fast-XPS spectral sequence. The spectrum was fitted based on the analysis of the high-resolution measurements, discussed later in this chapter. The growth of the peak (grey) at the BE (W $4f_{7/2}$ = 32.79 eV) corresponding to the basal plane component of WS_2, [2] is accompanied by the contribution from various components at lower BE. The presence of these components is consistent with the formation of incompletely sulfided species of the form WS_{2-x} ($0 < x \leq 1$), as observed for the same system in [2, 11, 12], as well as for the TPG grown MoS_2 on Au(111), described in chapter 3.

As already pointed out in the case of the growth of MoS_2, the increased mobility of the atoms at higher temperature is expected to improve the quality of the final layer. Therefore, we decided to use a higher temperature for the consequent growth. However, S desorption from the surface at higher temperature could take place, leading to W-Au alloying and defect creation (such as S vacancies) in the layer. The careful tuning of the growth parameters, in terms of H_2S pressure and W deposition rate, due to the availability of fast-XPS, allowed us to avoid the growth of the extra components observed in figure 4.1 (a) for Growth 1. The new growth (Growth 2), was performed at a constant sample temperature of 923 K, at a lower W deposition rate of $\sim 3.3 \times 10^{-3}$ ML/minute, together with a higher H_2S pressure of $5{\times}10^{-6}$ mbar that was further increased to $1{\times}10^{-5}$ mbar after the completion of about 10% of the growth and thereafter kept between $1{\times}10^{-5}$ and $2{\times}10^{-5}$ mbar. The difference between the two growth procedures can be seen from the fast-XPS intensity plots and the deconvolution of the spectrum at the end of the Growth 2 (figure 4.1 (b)), showing only the presence of the peak belonging to SL WS_2 with negligible contribution from additional components.

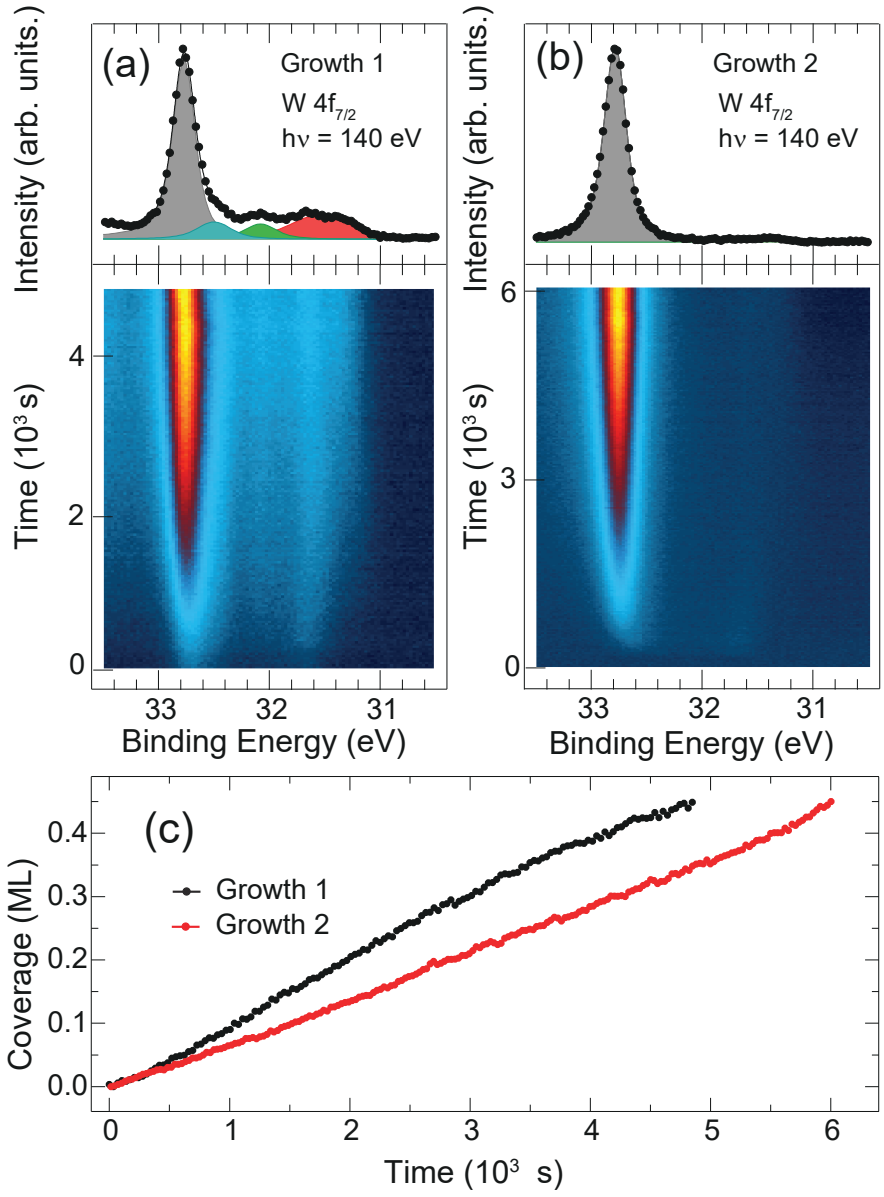

Figure 4.1: (a) and (b) W $4f_{7/2}$ fast-XPS intensity plot obtained at 140 eV photon energy for Growth 1 (T = 823 - 873 K) and Growth 2 (T = 923 k), respectively, together with the last W $4f_{7/2}$ core level spectra of the fast-XPS series, showing the spectral contributions resulting from peak fit analysis. (c) The evolution of the WS_2 coverage, proportional to the intensity of the W 4f peak (grey), as a function of deposition time.

For the two growth procedures, the coverage of WS_2, which is proportional to the intensity of the main grey component of the W 4f core level of figure 4.1, is shown as a function of time in figure 4.1 (c). The coverage of WS_2 was calculated from the decrement in the intensity of the clean surface peak of the Au $4f_{7/2}$ XPS spectra after the growth of the WS_2 layer (figure 4.2), as explained in the following section. Hereafter, a coverage of 1 ML is defined as one complete layer of WS_2 on Au(111) that corresponds to W surface density of 1.15×10^{15} atoms/cm^2, considering the lattice parameter of WS_2 of 0.315 nm. In figure 4.1 (c), it can be seen that the W 4f intensity is an almost linear function of the W deposition time for Growth 2 (red curve) throughout the deposition, up to a coverage of $\sim$ 0.45 ML. This suggests that all the deposited W atoms react and form WS_2. On the other hand, for Growth 1 (black curve), the intensity shows a deviation from the linear behavior and the slope starts to decline at a coverage of 0.25 ML. Moreover, the much higher W deposition rate for Growth 1 (more than double than that for Growth 2) is not reflected in a comparable increase of the WS_2 growth rate, as seen from the slope of the two curves in the initial stage of the growth. This is due to the formation of incompletely sulfided species right from the beginning which, as the coverage increases, prevent the formation of WS_2. Moreover, the growth of double layers cannot be excluded in this case.

In figure 4.2 (a) and (b), the high-resolution XPS spectra of Au $4f_{7/2}$ core level are shown for the clean Au(111) and after the growth of WS_2 for Growth 2, respectively. Table 4.1 presents the parameters of the fit of the peaks. The growth of SL WS_2 results in the appearance of an extra component (S_{WS_2}) and the decrement in the intensity of the clean surface peak S_{clean}. Following the same argument as in the case of MoS_2/Au(111), this new peak can be attributed to the Au surface atoms that feel the presence of the WS_2 layer on top. Indeed, Dendzik *et al.* [2] have also reported a similar behavior, although their sample showed the presence of extra peaks in the W 4f core level besides the ones belonging to WS_2.

In order to calculate the WS_2 coverage of the grown layer, we used the same strategy adopted for the MoS_2/Au(111) case of chapter 3, considering the decrement of the S_{clean} component in the Au $4f_{7/2}$ spectrum after WS_2 growth for the sample prepared with Growth 2, where only the WS_2 related XPS features are present. Using equation 3.1, we find a WS_2 coverage of 0.45 ML for Growth 2. The same WS_2 coverage was present at the end of Growth 1 as found by comparing the intensity of the grey W 4f components in figure 4.1 (a) and (b).

Figure 4.3 shows the high-resolution W 4f and S 2p core level spectra measured after the Growth 2, together with the deconvoluted spectral components resulting from peak-fit analysis. The parameters of the fits for Growth 2 are presented in table 4.2. The W 4f core level spectrum for Growth 2 (figure 4.3 (a)), presents an intense peak for the W $4f_{7/2}$ component at 32.79 eV BE, with its spin-orbit doublet at 2.14 eV higher BE. The position of this peak is in close agreement with the values reported in the literature for SL WS_2

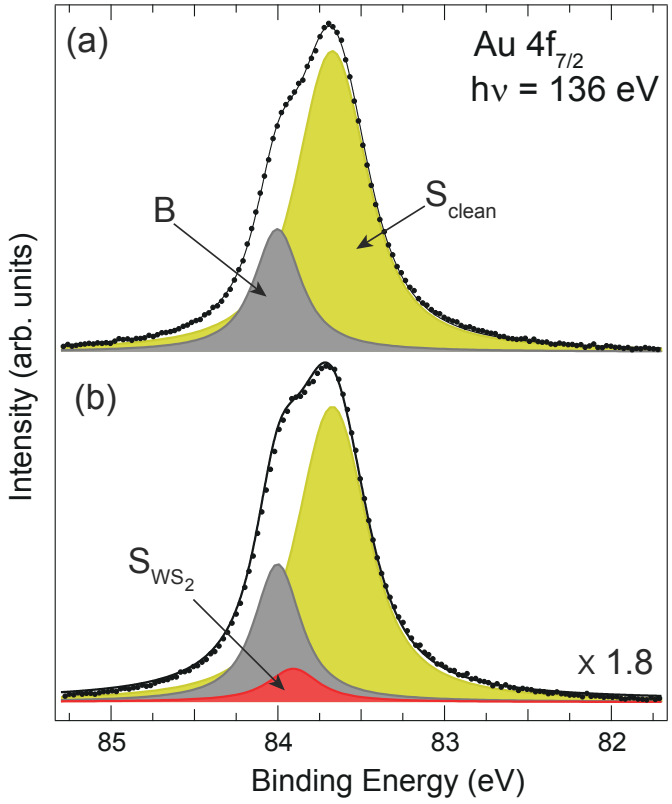

Figure 4.2: High-resolution XPS of Au $4f_{7/2}$ core level acquired at 136 eV photon energy for (a) the clean sample and (b) after Growth 2, corresponding to the WS_2 coverage of 0.45 ML, together with the spectral contributions resulting from peak fit analysis. The experimental data (dots) and the fit (line) are presented together with the spectral contributions resulting from peak fit analysis (solid fill).

Au $4f_{7/2}$ ($h\nu$=136 eV)	L(eV)	α	G(eV)	SCLS(eV)
Bulk (B)	0.31	0.02	0.09	0.0
Surface (S_{clean})	0.37	0.02	0.23	-0.33
S_{WS_2}	0.37	0.02	0.23	-0.09

Table 4.1: Line shape parameters for different components in Au $4f_{7/2}$ spectrum acquired at 136 eV photon energy. L is the Lorentzian width, α is the asymmetry parameter and G is the gaussian width.

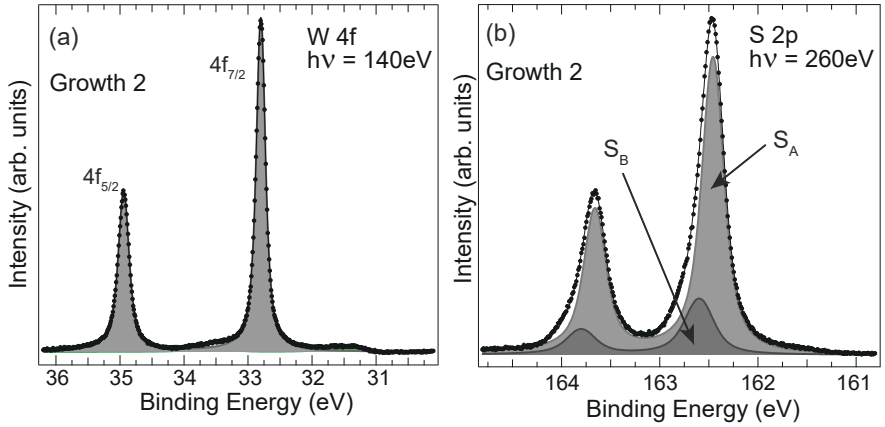

Figure 4.3: (a) and (b) show high-resolution XPS of W 4f and S 2p core levels, respectively, for Growth 2. The experimental data (dots) and the fit (line) are presented together with the spectral contributions (solid fill) resulting from peak-fit analysis.

on Au(111). [2]. Similar to the findings in the case of MoS_2 in chapter 3, the S 2p spectum (figure 4.3 (b)) presents two spin-orbit doublets S_A (grey) and S_B (black). We have shown in chapter 3 that depending upon the strength of interactions with the Au(111) surface the bottom layer S atoms present different spectral components in the S 2p core level, belonging to the strongly (shifted to higher BE) and weakly (at the same BE of top S) interacting S atoms (see figure 3.14 (e) in chapter 3). Due to the structural similarities, one can expect this to be true also for WS_2. Therefore, S_B corresponds to the strongly interacting bottom layer S atoms, while S_A includes the contribution from top layer S atoms and the weakly interaction bottom S, in the 'S-W-S' structure of WS_2. The former being significantly suppressed due to inelastic scattering from the W and S layer above, appears at 0.14 eV higher BE than S_A (S $2p_{3/2}$ at 162.45 eV). This is due to the interaction between the bottom layer S atoms and Au surface, which results also in the appearance of the core level shifted component in the Au $4f_{7/2}$ spectrum of figure 4.2 (b). It is interesting to compare the S 2p spectrum of WS_2/Au(111) with that of MoS_2/Au(111) (see figure 3.10 of chapter 3). In the latter case the S 2p BE shift of S_B with respect to S_A is 290 meV, while for the WS_2 the shift is smaller (140 meV). Moreover, the intensity ratio between the S_B and S_A for MoS_2 (0.21) is similar to that for WS_2 (0.23). Considering that the S 2p spectra have been measured at the same photon energy (260 eV), i.e. same KE, the IMFP is similar in the two cases. Therefore, a comparable intensity of the spectral component corresponding to the strongly interacting bottom layer S atoms ($S_B \sim 60\%$ of the total contribution from bottom layer S atoms, in figure 4.3 (b)) for

W 4f ($h\nu$=140 eV)	L(eV)	α	G(eV)	BE(eV)
$4f_{7/2}$	0.13	0.01	0.08	32.79
$4f_{5/2}$	0.16	0.01	0.09	34.93
S 2p ($h\nu$=260 eV)	L(eV)	α	G(eV)	BE(eV)
$2p_{3/2}$ S_A	0.18	0.03	0.15	162.45
$2p_{3/2}$ S_B	0.22	0.02	0.21	162.59
$2p_{1/2}$ S_A	0.18	0.03	0.15	163.65
$2p_{1/2}$ S_B	0.22	0.02	0.21	163.79

Table 4.2: Line shape parameters for different components for W 4f and S 2p spectra acquired at 140 eV and 260 eV photon energy, respectively for Growth 2. L is the Lorentzian width, α is the asymmetry parameter and G is the Gaussian width. The main peaks for Growth 1 have the same lineshape and BE position.

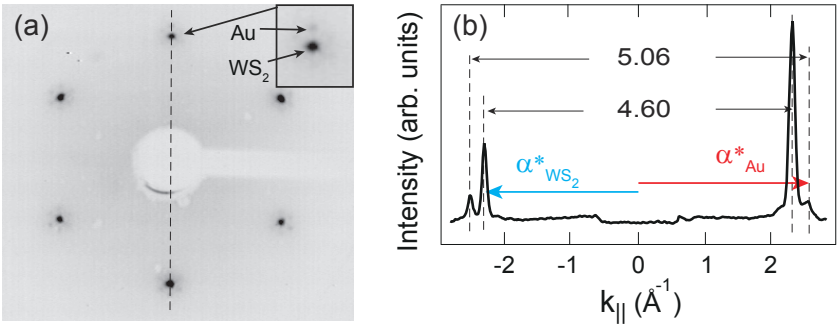

Figure 4.4: (a) LEED pattern measured at 78 eV for Growth 1. (b) Intensity line profile along the dashed line in (a), indicating the reciprocal lattice vectors corresponding to WS_2 ($\alpha^*_{WS_2}$) and Au surface (α^*_{Au}).

WS_2 and that for MoS_2 ($\sim$ 55%, in figure 3.10 of chapter 3), suggests that the interactions of WS_2 layer with the Au(111) surface are similar to that with the MoS_2 layer.

Figure 4.4 (a) shows the LEED pattern of the sample prepared by following Growth 1. The most intense spots corresponding to the reciprocal lattice of WS_2 are surrounded by moiré satellites, due to the lattice mismatch between WS_2 (lattice constant; $\alpha_{WS_2} \sim 0.315\,nm$) and the Au substrate layer ($\alpha_{Au} \sim 0.288\,nm$). The first order Au(111) diffraction spots, that can be seen in the inset, also exhibit a hexagonal pattern, though slightly bigger in dimension due to a larger reciprocal lattice vector [2, 13], and they are aligned with those of WS_2. This shows that the WS_2 lattice is aligned with the underlying Au(111) substrate. By comparing the measured reciprocal lattice vectors of WS_2 ($\alpha^*_{WS_2}$) and Au (α^*_{Au}) and using the lattice constant of WS_2 $\alpha_{WS_2} = 0.315$ nm, [14]

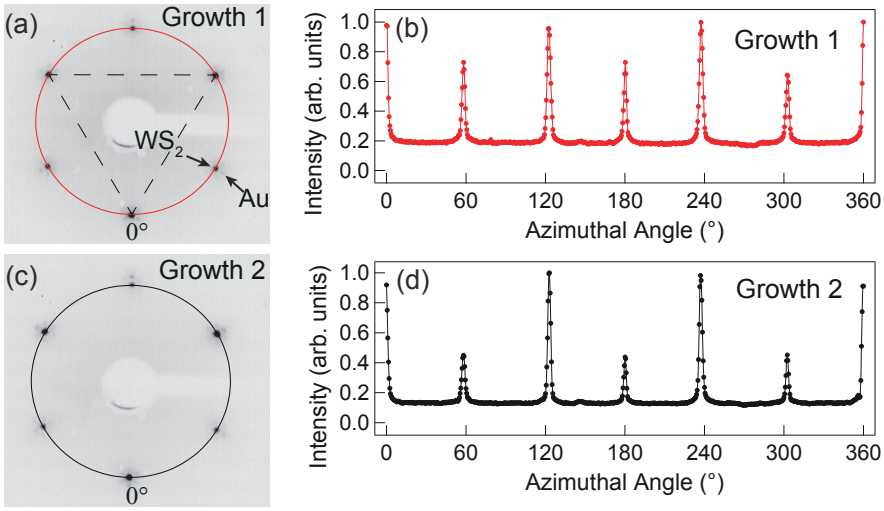

Figure 4.5: (a) and (c) show the LEED patterns acquired at 78 eV for WS_2 layer grown via Growth 1 and Growth 2, respectively. Intensity profile for the respective circular cuts (solid line) on WS_2 spots for the Growth 1 (b) and Growth 2 (d).

indicated in the intensity line profile shown in figure 4.4 (b), we obtain the moiré periodicity of 3.19±0.1 nm, in close agreement with literature. [2]. This could be compatible with the formation of a superstructure with a periodicity of 10×10-WS_2 on 11×11-Au unit cell configuration, even though the STM measurements were not performed in order to corroborate these results, as done in the case of MoS_2/Au(111) in chapter 3.

The LEED patterns of the WS_2 layers grown by following Growth 1 and Growth 2 are shown in for comparison figure 4.5 (a) and (c), respectively. The WS_2 coverage is 0.45 ML in both cases. The line profiles along the circular cuts crossing the WS_2 spots of the LEED images, displayed in figure 4.5 (b) and (d), present a different behavior for the two growth procedures. The first difference is in the intensity of the background which is almost 40% higher for the sample prepared with Growth 1 with respect to Growth 2. The higher background is likely due to the point defects such as incompletely sulfided species that are present on the surface for the Growth 1, as outlined in figure 4.1 (a), which are adsorbed in a disordered manner on the surface, thus contributing to the background intensity. The second difference is in the relative intensity of the peaks. In both cases, the behavior of the intensity reflects the three-fold symmetry of the LEED patterns, as the peaks belonging to the "triangle" of spots outlined in figure 4.5 (a) are more intense than the others. However, the ratio between the intensity of the smaller peaks and that of the larger ones,

after subtraction of the background, is 0.61 for Growth 1 and 0.38 for Growth 2. Therefore, the LEED pattern of the sample produced with Growth 2 shows a more pronounced three-fold symmetry. In analogy with the results obtained for MoS_2/Au(111) in chapter 3, we interpret the differences in the LEED patterns of WS_2 of the two growth procedures as due to a more pronounced preference for one of the two orientations of WS_2 in the case of Growth 2 than in Growth 1. This will be discussed in more detail in the following section.

4.3 Structure of SL WS_2 and single domain orientation characterization

In order to determine the structure and orientation of the WS_2 samples synthesized by the two growth methods, we performed XPD measurements and compared them with multiple scattering simulations. Figure 4.6 (c) and (d) show the W 4f XPD patterns (colored) acquired at 360 eV photon energy (corresponding photoelectron KE $\sim$ 326 eV), together with multiple scattering simulations (grey) for the sample prepared by Growth 2 and Growth 1, respectively. The simulations of the diffraction patterns were performed for the orthogonal prismatic 1H phase of WS_2 with the lattice constant $\alpha_{WS_2} =$ 3.15 Å and W-S interlayer distance of 1.57 Å, as reported in literature. [14] Due to the lack of specific adsorption configuration of WS_2 on Au(111), evident from the lattice mismatch and from the moiré pattern observed in LEED, the effect of the substrate in the simulated XPD patterns can be neglected, thus, the simulations were performed for a free standing layer of WS_2.

Figure 4.6 (a) and (b) show the W 4f XPD simulations for the two anti-parallel orientations, i.e. orientation 1 (Or1) and orientation 2 (Or2) displayed on top, presenting identical diffraction patterns but rotated by 180°. For the quantification of the contribution of the two domain orientations in the grown WS_2 layers, these simulations were mixed in different concentration and, by following the procedure explained in chapter 3 for the case of MoS_2/Au(111), the total simulated intensity was calculated by means of equation 3.2 that include different fraction of the mirror domains. The simulations were then compared with the experimental XPD patterns by means of R-factor [15], in order to optimize the fit with the experimental data. The plot of R-factor agreement for the layer grown by following Growth 2 (figure 4.6 (e)) shows a minimum (best agreement) for the simulation corresponding to Or1. Also, the added contribution from the Or2 leads to a monotonic increase in the R-factor value, indicating the worse agreement between the experiment and theory for the mixing of the two orientations. This shows that the WS_2 layer grown by Growth 2 presents just one single orientation. On the other hand, for the layer grown by Growth 1, R-factor analysis (figure 4.6 (f)) shows the coexistence of two orientations with 75% of domains analogous to Or1 and the remaining 25% to Or2. Moreover, from the analysis of LEED measurements (figure 4.5) the ratio between the intensity of peaks corresponds to a mixture of 23% of

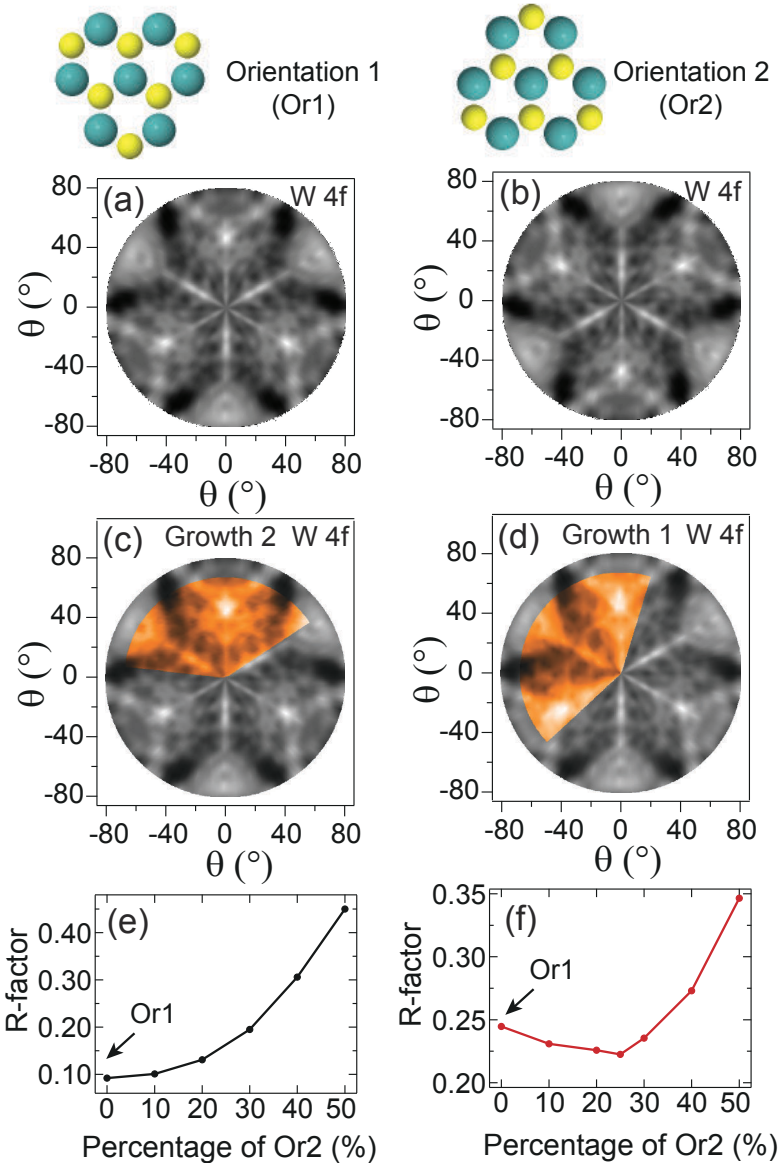

Figure 4.6: Stereographic projection of the multiple scattering simulations performed for the W 4f for (a) orientation 1 and (b) orientation 2. The two orientations are sketched on top. W 4f XPD experimental patterns (color) together with the simulations (grey) for the structure obtained with the R-factor minimization for (c) Growth 2 and (d) Growth 1. The KE is $\sim$ 326 eV. R-factor analysis for the domain orientation characterization of the SL WS_2 synthesized by (e) Growth 2 and (f) Growth 1. Ball model color code: blue (W) and yellow (S)

rotated domains for the sample prepared by Growth 1, in agreement with XPD analysis.

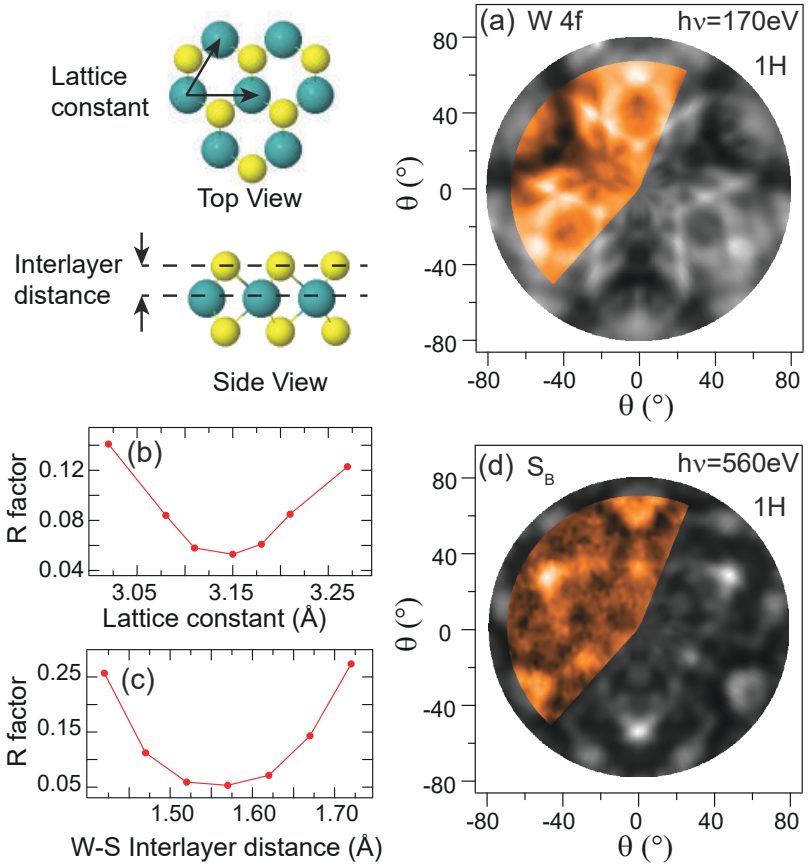

Figure 4.7: (a) W 4f XPD pattern (color) used to determine the local structure of the WS_2 layer prepared by Growth 2, together with the simulation (grey) corresponding to the best agreement based on the R-factor analysis. Ball model indicating the lattice parameter and the W-S interlayer distance for the 1H phase structure of WS_2. R-factor analysis for the determination of (b) lattice constant and (c) interlayer distance of the SL WS_2. (d) S 2p XPD spectra (color) corresponding to S_B component (KE $\sim$ 397 eV), with simulations (grey) for the bottom layer S. Ball model color code: blue (W) and yellow (S).

The characterization of the local structure of WS_2 was achieved by utilizing the single orientation character of the sample prepared by Growth 2. In order to do this, XPD measurements of the W 4f core level were performed at 170 eV photon energy (KE $\sim$ 137 eV) where both forward and backward

scattering conditions are fulfilled. The experimental XPD pattern (color), in figure 4.7 (a), was compared with the simulations performed for different structural geometry i.e. by varying the lattice constant and interlayer distance (see ball model in figure 4.7). The minimum of R-factor = 0.05 was obtained for a trigonal prismatic (1H) structural phase with the lattice parameter of 3.15±0.02 Å and W-S interlayer distance of 1.57±0.03 Å as shown in figure 4.7 (b) and (c), respectively, in very good agreement with the values reported in literature [14] and those used for domain orientation characterization earlier in this section. Thereafter, these structural parameters were used for the analysis of XPD measurements of S 2p core level for the sample prepared with Growth 2. Figure 4.7 (d) shows the XPD pattern (colored) corresponding to S_B component, measured at high KE $\sim$ 397 eV. Such an experiment is particularly well suited for the structural identification of the layer as, at the high KE of the photoelectrons, the XPD process is dominated by the forward scattering from the W and S atoms above, thus, presenting the orientation of the bottom layer with respect to the layers on top in the 'S-W-S' structure of WS_2. A clear three-fold symmetry and a very good agreement with the simulation (R-factor = 0.20) verifies the 1H structure of the WS_2 layer and confirms the assignment of the spectral component in the S 2p core level to bottom layer S atoms.

Upto this point, we have shown that SL WS_2 with single domain can be obtained by following the procedure described as Growth 2. Moreover, in order to relate the layer orientation to that of the underlying substrate, we performed XPD measurements of Au $4f_{7/2}$ core level for the clean Au(111). Figure 4.8 (a) show the XPD pattern corresponding to the Au bulk component, together with the simulation (grey) performed for a 3 layer slab of Au with emitters in all three layers emitting simultaneously. A good agreement of the three fold symmetric pattern (corresponding to the fcc (111) crystal stacking) with the simulation (R-factor = 0.32), corresponds to the orientation of the Au crystal given in figure 4.8 (b).

Figure 4.9 shows the 10×10 WS_2 superstructures on 11×11 Au unit cell that correspond to the two 180° rotated domain orientations of WS_2 in the same azimuthal alignment as that of the underlying Au(111) substrate. Clearly, due to the lattice mismatch between the WS_2 (lattice constant of 3.15 Å) and Au(111) (2.88 Å) unit cell, the lack of specific adsorption geometry of WS_2 on Au(111) can be observed in the ball model. However, in a local environment corresponding to S adsorption in *atop* position, W adsorption coincides with the fcc and *hcp* site for the two mirror orientations, as shown in the magnified regions. From these azimuthal alignment of the orientations of WS_2 to that of Au (following the LEED and XPD analysis), we can inarguably conclude that for the singly oriented WS_2 synthesized by Growth 2, the unique orientation 1 (figure 4.6) corresponds with S-W direction of $top - fcc$, as shown in figure 4.9 (a). On the other hand, for the mixed domain growth by Growth 1, apart from the 75% of domains oriented as in figure 4.9 (a), the orientation of remaining 25% domains corresponds to S-W direction of $top - hcp$ as shown

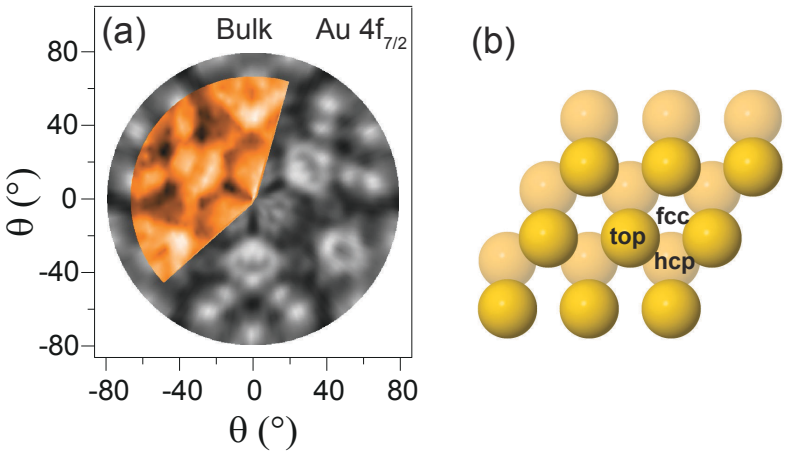

Figure 4.8: (a) XPD pattern acquired at 400 eV photon energy (KE ∼ 316 eV), showing the intensity modulation (color) of the bulk component in the Au $4f_{7/2}$ core level together with the multiple scattering simulation (grey) for the clean Au(111) sample. (b) Orientation of the Au sample derived from the comparison of the XPD experiment with the simulation.

in figure 4.9 (b). In the absence of any confirming evidence regarding the preferential adsorption site for S (as were in the case of MoS_2 [16] in chapter 3), our results are indicative of only a relative preference of orientation with respect to the Au substrate.

4.4 ARPES of single domain SL WS_2 and determination of the electron-phonon coupling strength

Once for Growth 2 the single domain character of the SL WS_2 was established, the sample was used to perform ARPES measurements, in order to study the WS_2 electronic structure. The measurements were performed at the SGM-3 beamline of ASTRID2. [10] Figure 4.10 (a) shows the valence band dispersion close to the **K** point along the **Γ**-**K** direction of the surface Brillouin zone of the WS_2 layer. Clearly, the valence band maximum (∼ 1.2 eV BE) is present at the **K** point, in close agreement with the previous experiments [2] and theoretical calculations performed for free standing SL WS_2. [17] As already discussed in the beginning of this chapter, the spin-splitting of the valence band is expected at the **K** point. Indeed, the measurements show two spin-split components at the **K** point with the lower band shifted ∼ 430 meV towards higher BE with

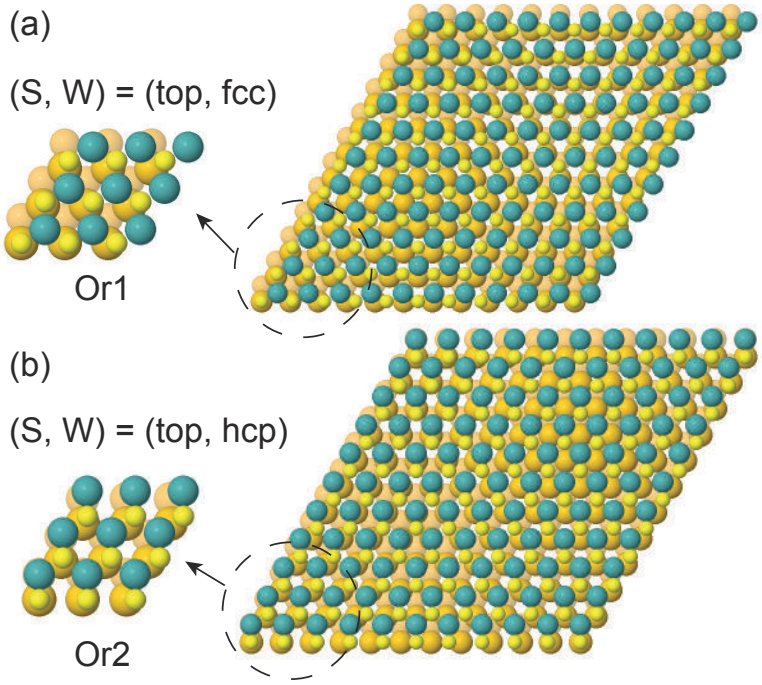

Figure 4.9: 10×10-WS_2/11×11-Au superstructure. For S adsorbed *atop* position, insets on the left show the adsorption configuration of bonding regions (a) W in *fcc* and (b) W in *hcp* sites. Ball color code: blue (W), yellow (S), orange (Au surface layer) and amber (Au second layer).

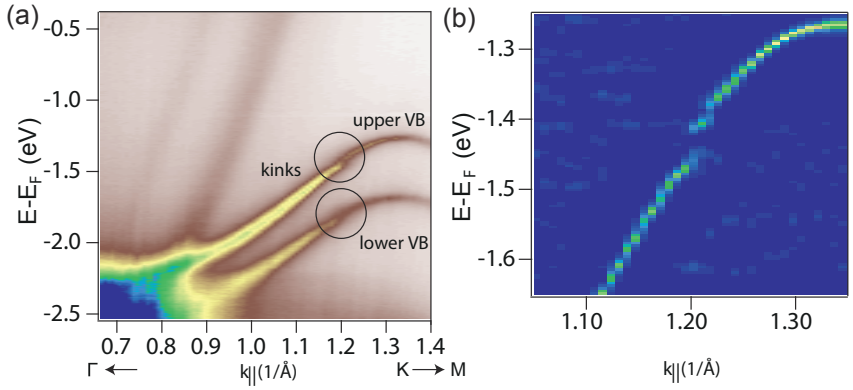

Figure 4.10: (a) Valence band dispersion along **Γ-K** direction of the surface Brillouin zone, acquired at 30 K. The positions of kinks in the WS_2 bands are marked with circles. (b) Curvature of the photoemission data presented in (a), showing the kink in the upper valence band. Adapted from ref. Hinsche *et. al* [20].

respect to the upper band, to be compared with ca. 145 meV for SL MoS_2/Au (111). [4] Similar observations were made by Dendzik *et al*. [2], though the measurements performed on the WS_2 layer produced with Growth 2 reveal much narrow linewidths of the bands. This further confirms high quality of the WS_2 layer.

The high quality of the WS_2 sample, revels some previously unexplored details. In the marked regions in figure 4.10 (a), the minigap openings at 174±14 and 124±18 meV energy below the top of the upper and lower branches of the valence band, respectively, are visible. The magnified image of the minigap in the upper band is shown in figure 4.10 (b). This is due to the superperiodic potential that develops due to the formation of moiré superstructure (the moiré pattern observed in LEED, figure 4.5) because of the lattice mismatch between the WS_2 and the Au(111) substrate, as also observed in the case of graphene on Ir(111). [18]

Another interesting feature of the valence band of SL WS_2 is the reversal of spin character for the two spin-split bands at the inequivalent valley positions i.e. for the **K** and **-K** points. This coupled with the large spin splitting and sharper bands of the WS_2 sample allowed the study of the electron phonon (el-ph) coupling for the system of states that differ only by their spin. [19] In order to determine the strength of the el-ph coupling specific to the spin-split bands, the energy distribution curves (EDCs) at the **K** point were measured by increasing the sample temperature from 30 K to 550 K. The experiments were performed within the collaboration with Prof. Philip Hofmann's group at Aarhus University, Denmark. The measured EDCs were fitted using a

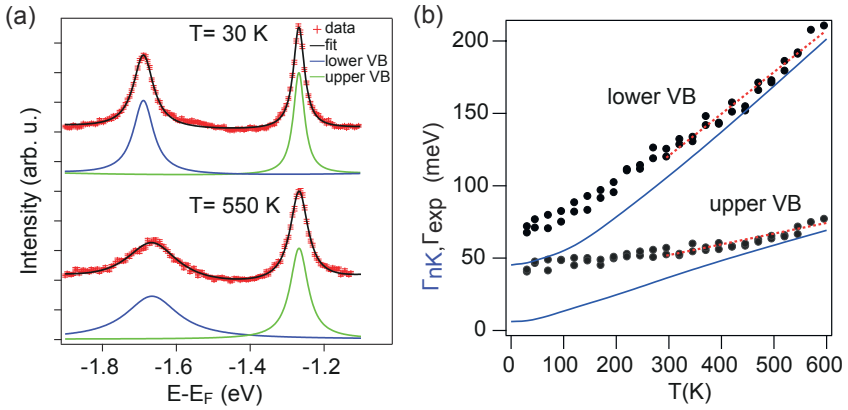

Figure 4.11: (a) Energy distribution curves (EDCs) through **K** point at low and high temperature. The markers are the data points. The resulting fit with a polynomial background and two Lorentzian peaks are also shown. (b) Temperature dependent Lorentzian linewidth of the two bands in an energy distribution curve through **K** (dots). The solid lines show the calculation for the WS_2 layer including scattering contributions from the Au(111) substrate. The dashed lines are a fit of the experimental data at high temperature (T > 300 K). Adapted from ref. Hinsche *et. al* [20].

polynomial background and two Lorentzian peaks (one for each spin-split band), as shown for the first (30 K) and the last (550 K) measurement in figure 4.11 (a). The variation in the linewidth (Γ_{exp}) determined from the peak-fit analysis is shown as a function of sample temperature in figure 4.11 (b). Clearly, the experimentally determined linewidth (dots) shows more pronounced variations for the lower band, indicating stronger el-ph coupling than for the upper band. For a more quantitative analysis, the slope of the curves in the high-temperature regime (T>300 K), calculated by applying a linear fit to the data (marked with dashed lines in figure), gives the el-ph coupling strength of ~ 0.13 and 0.52 for the upper and lower band, respectively. [20]

Although this might appear surprising, it can be explained as in the following. A simple picture of the possible contributions to the el-ph scattering process are shown in figure 4.12, through a schematic representation of the valence band of SL WS_2. The upper and lower bands at **K** are color coded according to the spin structure, which is inverted for valley at **-K**. A local maximum at Γ is situated between the upper and lower band. Let's consider now that a hole at the top of the upper band at **K** has to be filled by the transfer of crystal momentum and energy of the phonon to the electron. This can be achieved by process #1, where the electron comes from the same band very close to the top of the band and fills the hole by absorbing the energy $h\nu$ from the

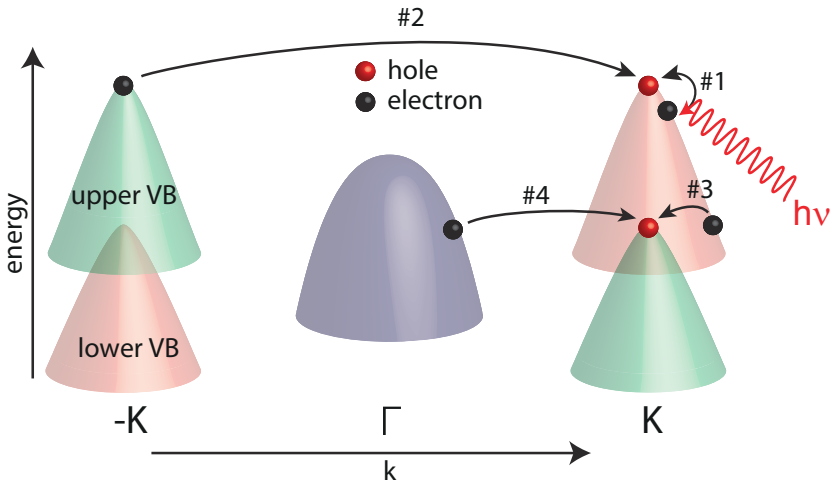

Figure 4.12: Schematic valence band for SL WS_2 with the absolute valence band (VB) maxima at **K** and **-K** and a local maximum at Γ. The VB at **K** and **-K** are spin-split with the color indicating the spin direction. The VB at Γ is spin-degenerate. El-ph scattering processes to fill holes at the top of the spin-split band at **K** are illustrated. In process #1, an electron is scattered into the hole by absorbing a phonon (red line). For the other scattering processes, the phonons are omitted for clarity. Adapted from ref. Hinsche *et. al* [20].

phonon. An electron from the top of the upper band at **-K** can also fill the hole through an elastic phonon scattering (as the energy is conserved), as shown in process #2. However, this is highly unlikely, as it would require the flipping of the spin. [21] This hole can not be filled by the electron coming from the lower band or from the band at Γ, as the respective energy difference of ca. 430 meV and 220 meV is considerably larger than the maximum phonon energy of ca. 55 meV. [22] On the other hand, a hole present at the top of the lower band can be filled by several processes such as an electron coming from the upper band but away from **K** (process #3), where the spin polarization is weakened [19]; from the band at Γ (process #4); or from the band at **-K** (not shown in figure). Therefore, it is straightforward to expect, from the picture presented here, a weak el-ph coupling for the upper band than the lower band.

For a more detailed interpretation of the process, numerical calculations were performed by Prof. Kristian Sommer Thygesen's group at the Technical University of Denmark. The electronic structure of SL WS_2 and of the unreconstructed 9 layers slab of the Au(111) substrate was calculated by first principles within density functional theory, as implemented in the QuantumESPRESSO code. [23] The phonon properties were obtained within density functional perturbation theory using the same package, while taking

into account spin-orbit coupling and other relativistic effects. The obtained electronic and vibrational properties were used to calculate the el-ph coupling within a modified version of the EPW code [24], for the SL WS_2 by including the Au(111) substrate states in the calculations. The calculated linewidths for the spin-split bands in the experimental temperature range (30 K-550 K) are shown as solid lines in figure 4.11 (b). It is evident that also the calculations predict a stronger el-ph coupling for the lower band than the upper one. As done for the experimental data, the el-ph coupling strength was determined by the linear fit to the calculated linewidth in the high-temperature regime (300 K-600 K), amounting to 0.2 and 0.58 for the upper and lower band, respectively.

The calculated el-ph coupling agrees well with the experimentally determined values, indicating its strong dependence on the branch of the spin-split valence band. The discrepancy between theory and experiment can be traced to the simplicity of the model in terms of relatively small unit cell and the unaccountability of the hybridyzation between the SL WS_2 and the Au(111) states. These results show that a longer lifetime can be expected for the holes in the upper valence band of SL WS_2, than those in the lower band, being strongly affected by the el-ph coupling. This in accordance with the strong spin-orbit splitting of the band at **K**, can be used to increase the hole density in the upper band at **K** without affecting the carrier density of the lower band or at the Γ, thus allowing to yield high hole mobilities.

4.5 Conclusions

In this chapter we have shown that, by using the HTG method adopted to grow MoS_2 on Au(111), it is possible to grow an extended SL WS_2 with unique orientation on Au(111). The HTG procedure had to be adapted in order to obtain this result, by using a lower W deposition rate and a higher temperature and H_2S pressure with respect to the growth of MoS_2. The high-resolution W 4f spectra presented only the sharp components belonging to WS_2 while the S 2p core level showed the presence of two doublets, indicating the presence of S in different chemical environments. From the analysis of the S 2p spectra it turned out that the interaction of WS_2 with the Au(111) substrate are similar to those in the case of MoS_2. The high quality of the layer was evident not only from the high resolution XPS spectra, but in particular from the LEED pattern with narrow and sharp spots and low background intensity and in the ARPES measurements where very sharp bands have been measured. The single orientation character of the WS_2 layer was verified by means of R-factor analysis of the W 4f XPD data. The grown WS_2 sample was used to measure the electron-phonon coupling strength in the spin-split valence band states at the **K** point evidencing a much larger el-ph coupling constant for the lower band with respect to the upper band.

References

[1] Elías, A. L. et al. Controlled Synthesis and Transfer of Large-Area WS_2 Sheets: From Single Layer to Few Layers. *ACS Nano* **2013**, *7*, 5235–5242.

[2] Dendzik, M.; Michiardi, M.; Sanders, C.; Bianchi, M.; Miwa, J. A.; Grønborg, S. S.; Lauritsen, J. V.; Bruix, A.; Hammer, B.; Hofmann, P. Growth and electronic structure of epitaxial single-layer WS_2 on Au(111). *Physical Review B* **2015**, *92*, 245442, 1–7.

[3] Latzke, D. W.; Zhang, W.; Suslu, A.; Chang, T.-R.; Lin, H.; Jeng, H.-T.; Tongay, S.; Wu, J.; Bansil, A.; Lanzara, A. Electronic structure, spin-orbit coupling, and interlayer interaction in bulk MoS_2 and WS_2. *Physical Review B* **2015**, *91*, 235202, 1–6.

[4] Miwa, J. A.; Ulstrup, S.; Sørensen, S. G.; Dendzik, M.; Čabo, A. G.; Bianchi, M.; Lauritsen, J. V.; Hofmann, P. Electronic Structure of Epitaxial Single-Layer MoS_2. *Physical Review Letters* **2015**, *114*, 046802, 1–5.

[5] Ovchinnikov, D.; Allain, A.; Huang, Y.-S.; Dumcenco, D.; Kis, A. Electrical Transport Properties of Single-Layer WS_2. *ACS Nano* **2014**, *8*, 8174–8181.

[6] Kormányos, A.; Burkard, G.; Gmitra, M.; Fabian, J.; Zólyomi, V.; Drummond, N. D.; Fal'ko, V. $k \cdot p$ theory for two-dimensional transition metal dichalcogenide semiconductors. *2D Materials* **2015**, *2*, 022001, 1–31.

[7] Zeng, H.; Dai, J.; Yao, W.; Xiao, D.; Cui, X. Valley polarization in MoS_2 monolayers by optical pumping. *Nature Nanotechnology* **2012**, *7*, 490–493.

[8] Abrami, A.; Barnaba, M.; Battistello, L.; Bianco, A.; Brena, B.; Cautero, G.; Chen, Q. H.; Cocco, D.; Comelli, G.; Contrino, S.; DeBona, F.; Di Fonzo, S.; Fava, C.; Finetti, P.; Furlan, P.; Galimberti, A.; Gambitta, A.; Giuressi, D.; Godnig, R.; Jark, W.; Lizzit, S.; Mazzolini, F.; Melpignano, P.; Olivi, L.; Paolucci, G.; Pugliese, R.; Qian, S. N.; Rosei, R.; Sandrin, G.; Savoia, A.; Sergo, R.; Sostero, G.; Tommasini, R.; Tudor, M.; Vivoda, D.; Wei, F. Q.; Zanini, F. Super ESCA: First beamline operating at ELETTRA. *Review of Scientific Instruments* **1995**, *66*, 1618–1620.

[9] García de Abajo, F. J.; Van Hove, M. A.; Fadley, C. S. Multiple scattering of electrons in solids and molecules: A cluster-model approach. *Physical Review B* **2001**, *63*, 075404, 1–16.

[10] Hoffmann, S. V.; Søndergaard, C.; Schultz, C.; Li, Z.; Hofmann, P. An undulator-based spherical grating monochromator beamline for angle-resolved photoemission spectroscopy. *Nuclear Instruments and Methods in Physics Research A* **2004**, *523*, 441–453.

[11] Shpak, A.; Korduban, A.; Kulikov, L.; Kryshchuk, T.; Konig, N.; Kandyba, V. XPS studies of the surface of nanocrystalline tungsten disulfide. *Journal of Electron Spectroscopy and Related Phenomena* **2010**, *181*, 234 – 238.

[12] Füchtbauer, H. G.; Tuxen, A. K.; Moses, P. G.; Topsøe, H.; Besenbacher, F.; Lauritsen, J. V. Morphology and atomic-scale structure of single-layer WS_2 nanoclusters. *Physical Chemistry Chemical Physics* **2013**, *15*, 15971–15980.

[13] Grønborg, S. S.; Ulstrup, S.; Bianchi, M.; Dendzik, M.; Sanders, C. E.; Lauritsen, J. V.; Hofmann, P.; Miwa, J. A. Synthesis of Epitaxial Single-Layer MoS_2 on Au(111). *Langmuir* **2015**, *31*, 9700–9706.

[14] Schutte, W.; Boer, J. D.; Jellinek, F. Crystal structures of tungsten disulfide and diselenide. *Journal of Solid State Chemistry* **1987**, *70*, 207 – 209.

[15] Woodruff, D. Adsorbate structure determination using photoelectron diffraction: Methods and applications. *Surface Science Reports* **2007**, *62*, 1–38.

[16] Bruix, A.; Lauritsen, J. V.; Hammer, B. Effects of particle size and edge structure on the electronic structure, spectroscopic features, and chemical properties of Au(111)-supported MoS_2 nanoparticles. *Faraday Discussions* **2016**, *188*, 323–343.

[17] Zhu, Z.; Cheng, Y.; Schwingenschlögl, U. Vacancy induced half-metallicity in half-Heusler semiconductors. *Physical Review B* **2011**, *84*, 113201, 1–4.

[18] Pletikosić, I.; Kralj, M.; Pervan, P.; Brako, R.; Coraux, J.; N'Diaye, A. T.; Busse, C.; Michely, T. Dirac Cones and Minigaps for Graphene on Ir(111). *Physical Review Letters* **2009**, *102*, 056808, 1–4.

[19] Xiao, D.; Liu, G.-B.; Feng, W.; Xu, X.; Yao, W. Coupled Spin and Valley Physics in Monolayers of MoS_2 and Other Group-VI Dichalcogenides. *Physical Review Letters* **2012**, *108*, 196802, 1–5.

[20] Hinsche, N. F.; Ngankeu, A. S.; Guilloy, K.; Mahatha, S. K.; Grubišić Čabo, A.; Bianchi, M.; Dendzik, M.; Sanders, C. E.; Miwa, J. A.; Bana, H.; Travaglia, E.; Lacovig, P.; Bignardi, L.; Larciprete, R.; Baraldi, A.; Lizzit, S., Thygesen, K. S.; Hofmann, P. Spin-dependent electron-phonon coupling in the valence band of single-layer WS_2. *Physical Review B* **2017**, *96*, 121402 (R), 1–5.

[21] Fabian, J.; Das Sarma, S. Phonon-Induced Spin Relaxation of Conduction Electrons in Aluminum. *Physical Review Letters* **1999**, *83*, 1211–1214.

[22] Molina-Sánchez, A.; Wirtz, L. Phonons in single-layer and few-layer MoS_2 and WS_2. *Physical Review B* **2011**, *84*, 155413, 1–8.

[23] Giannozzi, P. et al. QUANTUM ESPRESSO: a modular and open-source software project for quantum simulations of materials. *Journal of Physics: Condensed Matter* **2009**, *21*, 395502, 1–20.

[24] Poncé, S.; Margine, E.; Verdi, C.; Giustino, F. EPW: Electron-phonon coupling, transport and superconducting properties using maximally localized Wannier functions. *Computer Physics Communications* **2016**, *209*, 116 – 133.

CHAPTER 5

Growth of single layer MoS_2 on Ag(111): Effect of a strongly interacting substrate

The aim of the experiments described in this chapter was to explore the effects of the surface chemical composition on the growth and properties of MoS_2. Due to the strong covalent interlayer bonding resulting in the absence of dangling bonds in SL MoS_2, one can argue that the 2D dichalcogenide layer should interact with the metal substrate by means of weak van der Waals forces. The growth of SL MoS_2 on several weakly interacting substrates has been demonstrated in literature. [1–4] In chapter 3, we have shown that the epitaxial growth in presence of weak interactions, resulted in high quality single domain orientation MoS_2 monolayers on Au(111). However, the strength of these interactions may vary, depending upon the chemical composition of the underlying substrate. This would not only result in alterations of the structure, but also in the modifications of the electronic properties of the grown layer will be modified. A similar behavior has been observed in the case of graphene grown on differently interacting metal substrates. [5–8]

Indeed, theoretical calculations [9, 10] have suggested that the interactions of SL MoS_2 (although still weak van der Waals type) are significantly stronger for the MoS_2/Ag(111) interface, than on Au(111). Moreover, theoretical calculations have also predicted a much smaller (0.21 eV) Schottky barrier for MoS_2 on Ag(111), in comparison with 0.76 eV for the layer on Au(111). [10] Due to the semiconducting nature of SL MoS_2, the transport properties of the FETs, with MoS_2 as a channel material, are dominated by the Schottky barrier height (SBH) at the metal contact. In this regards, a reduction in the SBH for MoS_2/Ag(111) would result in lowering of the contact resistance, aiding to an efficient performance of the fabricated devices. [11] Furthermore, in analogy

with other 2D systems, [12–18] the increased interactions between the MoS_2 adlayer and the Ag substrate are expected to result in higher structural quality, better ordering and also extensive growth of MoS_2 domains. Such selective alterations of the intrinsic properties of 2D systems, combined with a large scale growth of high quality layers, is extremely important for the use of these 2D materials for technological applications.

In order to investigate the effect of interactions with the substrate, SL MoS_2 was grown on Ag(111), by following the already established HTG procedure that resulted in high quality MoS_2 (see chapter 3) and WS_2 monolayers (see chapter 4) on Au(111). The effects of increased adsorbate-substrate interactions on the grown layer were observed as the spectral changes in the Mo 3d and S 2p core levels, in comparison with the MoS_2 grown on Au(111) of chapter 3. The high structural quality and the long range order of the grown layer was verified by means of LEED and STM measurements that indicated a continuous growth of MoS_2 monolayer which extends over several terraces of the Ag surface. A comparison of the experimental XPD measurements with multiple scattering simulations, showed the growth of two anti-parallel domains aligned along the crystallographic axes of the substrate in equal proportions.

5.1 Experiments and methods

The growth and characterization of SL MoS_2 was performed at SuperESCA beamline of Elettra. [19] The Ag(111) crystal was cleaned by repeated cycles of Ar^+ sputtering at 1 keV, followed by annealing to 1060 K for 10 minutes. Sample cleanliness was checked by XPS that did not show any contaminants. Sharp 1×1 diffraction spots were observed in LEED, demonstrating the long range order of the surface. Molybdenum atoms were deposited on the sample from a home-built evaporator that consisted of a Mo filament (heated through direct current), mounted in front of the sample. The source of S atoms was maintained by dosing H_2S (nominal purity of 99.8%) through a leak valve.

The growth was followed by a simultaneous measurement of fast-XPS spectra of Mo 3d and S 2p core levels. High resolution XPS and LEED were measured after the deposition in order to characterize the grown sample. The energy resolution of the XPS was better than 50 meV and the BE scale was referred to the Fermi level of the Ag sample. The XPS spectra, presented in this chapter, were fitted with Doniach-Šunjić function convoluted with Gaussian and a linear background. The orientation and the structure of the grown layer was determined by XPD measurements performed at different photon energies, to tune the photelectron KE, in order to achieve forward and backward scattering conditions. XPD data were analyzed by the help of multiple scattering simulations performed using EDAC package. [20] Scanning Tunneling Microscopy (STM) measurements were performed at the CoSMoS facility at Elettra. The images were acquired at room temperature with a SPECS STM 150 Aarhus instrument. The sample was transferred through air

from the growth chamber of SuperESCA to the STM chamber of CoSMoS. The sample was subsequently annealed up to ca. 800 K for 30 min, in order to get rid of impurities adsorbed during sample transfer.

5.2 Growth of SL MoS_2 on Ag(111)

In the previous chapters, we have presented the growth of high quality MoS_2 and WS_2 monolayers on Au(111) by using the HTG method. Likewise, the HTG procedure was used to grow SL MoS_2 also on the Ag(111) substrate. Similarly to the strategy adopted in chapter 4 for the growth of WS_2 on Au(111), the careful tuning of the growth parameters was obtained by following the growth in real time by means of fast-XPS. Mo was deposited on clean Ag(111) sample kept at 823 K, in the background H_2S pressure of 3×10^{-6} mbar that was later increased to 5×10^{-6} mbar after the completion of $\sim$ 60% of the growth. The quartz microbalance was used to determine the Mo deposition rate that amounted to 9.5×10^{-3} ML/minute, where a monolayer (ML) is the surface atomic density of Au(111).

The fast-XPS measurements performed during the growth of MoS_2 and subsequent analysis is summarized in figure 5.1. The 2D intensity plot for the sequence of fast-XPS spectra of Mo 3d core level, figure 5.1 (b), shows the growth of the $3d_{5/2}$ peak centered at 229.33 eV BE. The BE of this peak is similar to that of SL MoS_2 on Au(111) described in chapter 3, although slightly higher (+0.14 eV) due to different interactions with the substrate (discussed later in this section). Therefore, this spectral component can be assigned to the basal plane of SL MoS_2 on Ag(111). The final spectrum of the fast-XPS sequence is shown in figure 5.1 (a), together with the contribution of different spectral components resulting from peak-fit analysis. The sequence of fast-XPS spectra were fitted based on the parameters determined from high-resolution XPS analysis that will be discussed in the following sections. The resulting intensity of the Mo $3d_{5/2}$ peak is shown as a function of exposure time in figure 5.1 (c). The intensity of this peak, which reflects the MoS_2 coverage, shows a behavior similar to that observed for the HTG grown MoS_2 on Au(111) substrate discussed in chapter 3. Initially, the intensity shows an almost linear behavior up to $\sim$ 25 minute deposition (indicated by the dashed line in figure 5.1 (c)), while further deposition results in a continuous decline of the growth rate up to the end of the deposition. Following the discussion for the growth trend of HTG MoS_2/Au(111) in chapter 3, this behavior can be attributed to the desorption (at high temperature) of Mo atoms impinging on the already formed MoS_2 layer. As a result, the subsequent extension of the layer is stalled, which is reflected in the slowing down of the increase in the MoS_2 related peak intensity. In addition to the main peak (grey), the Mo 3d spectrum shows the presence of another component (red) at 1.44 eV lower BE. This could be due to the formation of partially sulfided Mo-S clusters, similar to those observed for TPG MoS_2/Au(111). Although this peak appeared already

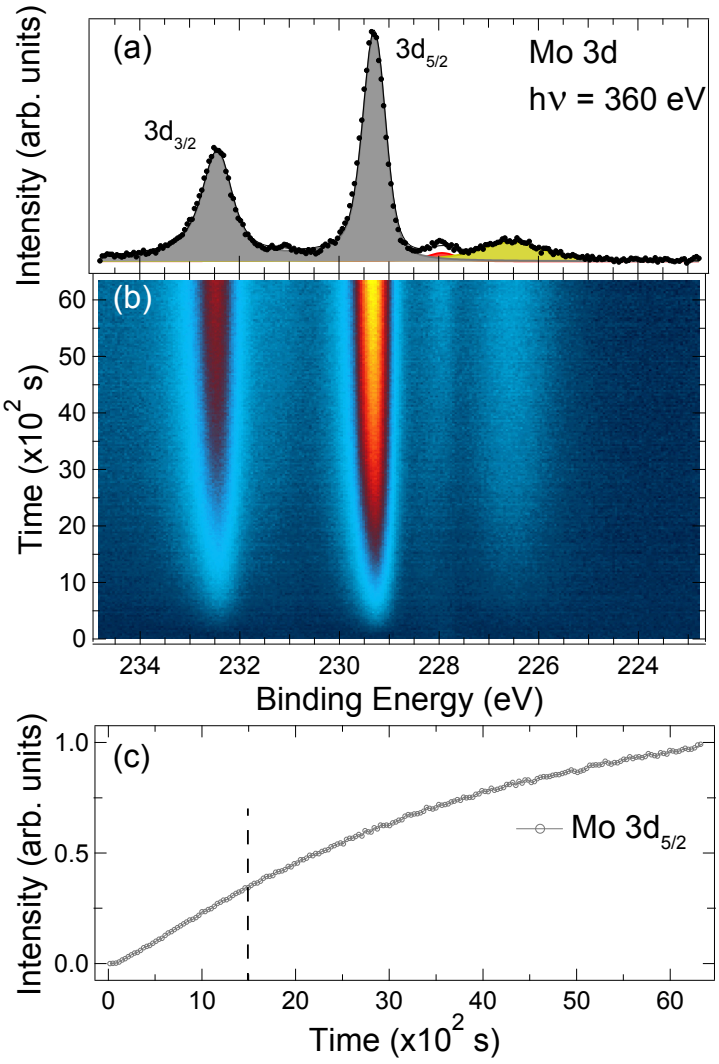

Figure 5.1: 2D intensity plot (b) for the fast-XPS sequence of spectra of Mo 3d core level at 360 eV photon energy while following the growth of SL MoS_2 on Ag(111). (a) Mo 3d core level spectrum acquired at the end of the growth, showing the spectral contributions resulting from peak fit analysis. (c) Photoemission intensity obtained from the fit of the fast-XPS spectra in (b), showing the evolution of the main peak (grey) as a function of exposure time. The final MoS_2 coverage is 0.8 ML, as explained in the text.

at the beginning, the intensity remained almost constant up to the end.

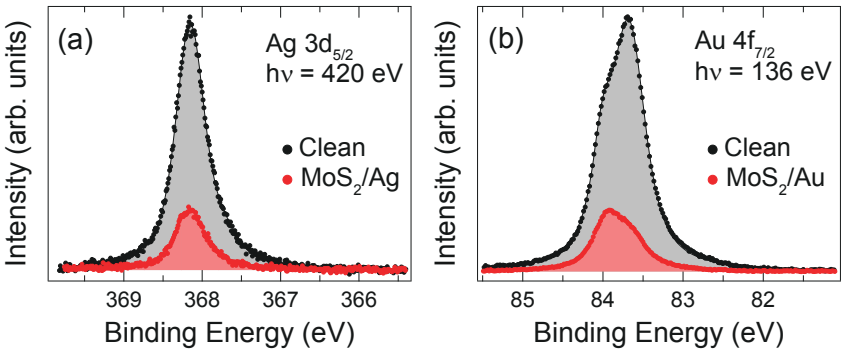

Figure 5.2: High-resolution XPS spectra of (a) Ag $3d_{5/2}$ at 420 eV and (b) Au $4f_{7/2}$ at 136 eV photon energy, before and after the growth of ca. 0.8 ML of MoS_2, respectively. The spectra were acquired at comparable photoelectron KE $\sim$ 52 eV.

Figure 5.2 (a) shows the Ag $3d_{5/2}$ spectra acquired at 420 eV photon energy, before and after the growth of SL MoS_2. For the clean Ag(111) sample, the Ag $3d_{5/2}$ peak is centered at 368.21 eV, in close agreement with the value reported for bulk component in [21], where a SCLS of 0.076±0.03 eV of the topmost layer of atoms was also reported. However, Andersen *et al.* [22] showed that the Ag $3d_{5/2}$ spectra can be fitted with just one Doniach-Šunjić line profile, corresponding to the bulk component. Therefore, since for this sample the surface peak in not visible in the Ag $3d_{5/2}$ core level, we focused our analysis for the MoS_2 coverage determination on the intensity variation of the Ag 3d spectra, rather than the spectral changes, as it was done in the case of MoS_2/Au(111). The coverage of the MoS_2 layer was determined by comparing the decrement in the total intensity of the Ag 3d spectrum ($h\nu = 420$ eV) after the growth of MoS_2, with that of the Au 4f spectrum at $h\nu = 136$ eV (figure 5.2 (b)) measured after the growth of SL MoS_2/Au(111) in chapter 3, where the coverage was measured from the decrement of the clean surface component in the Au $4f_{7/2}$ core level. In both cases, the KE of the XPS measurements was $\sim$ 52 eV. Therefore, it is reasonable to assume that the screening of the signal by the MoS_2 ad-layer should be of the same magnitude for the two substrates, owing to the fixed IMFP of the photoelectrons due to the same KE of the measurements. The calculated coverage amounted to ca. 0.8 ML, where, a monolayer (ML) represents one complete layer of MoS_2 on Ag(111) that corresponds to Mo surface density of 1.15×10^{15} atoms/cm^2 considering the MoS_2 lattice parameter of 0.315 nm.

Figure 5.3 (a) and (b) show the high-resolution Mo 3d and S 2p spectra acquired after the growth of 0.8 ML of MoS_2 on Ag(111), respectively, together

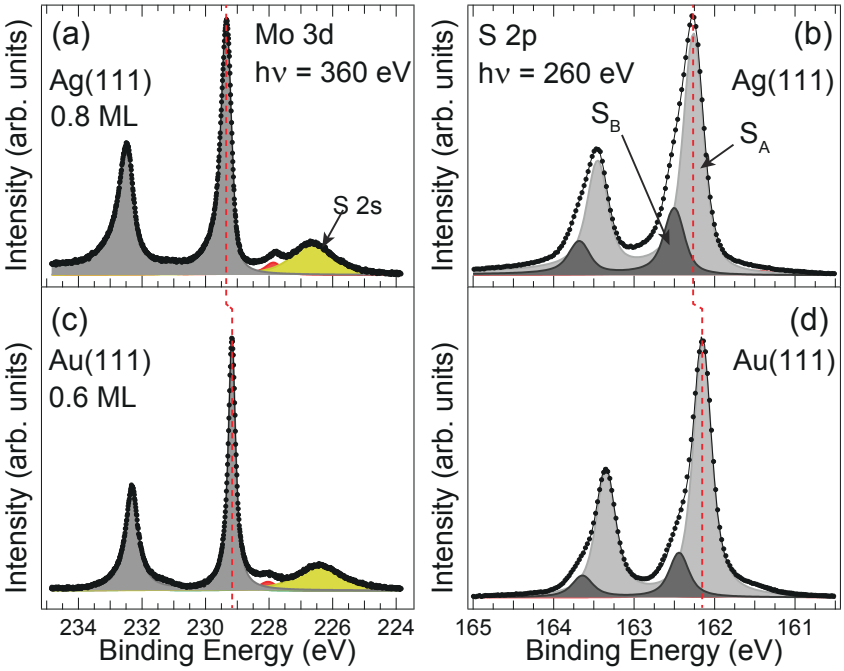

Figure 5.3: High-resolution XPS spectra for (a, c) Mo 3d (at photon energy $h\nu = 360$ eV) and (b, d) S 2p ($h\nu = 260$ eV) core levels corresponding to the SL MoS_2 grown on Ag(111) (a, b) and Au(111) (c, d) substrate. The experimental data (dots) and the best-fit (line) are presented together with the spectral contributions resulting from peak fit analysis (solid fill).

with the spectral components resulting from peak-fit analysis. The lineshape parameters used for fitting the XPS spectra are presented in table 5.1. In order to directly compare the results with MoS_2 grown on Au(111), presented in chapter 3, the corresponding Mo 3d and S 2p spectra at 0.6 ML are shown in figure 5.3 (c) and (d), respectively. For SL MoS_2 grown on both substrates, the Mo 3d spectra show an intense doublet (grey), corresponding to the Mo atoms of the basal plane of MoS_2. Similarly, the S 2p spectra show two doublets, which are related to the S atoms of the top layer plus the S atoms of the bottom layer weakly interacting with the substrate (S_A, grey) and to the strongly interacting bottom layer S atoms (S_B, black).

Apart from these inherent similarities as a result of the comparable structure of MoS_2, a more detailed analysis of the XPS spectra reveals differences that may be ascribed to the different electronic structure of the layers grown on the two substrates. As indicated by the dashed red lines in figure 5.3, the core level peaks belonging to the MoS_2 on Ag(111) show a shift of 140 meV towards

higher BE than those observed for MoS_2 on Au(111). Likewise, the main S 2p peak is shifted by 100 meV to higher BE. The observed core level shift of the spectra can be ascribed to the different work function of the two substrates with a different Fermi level pinning in the two cases. Indeed, it has been shown theoretically in [10], that the conduction band minimum (CBM) lies closer to the Fermi level for SL MoS_2 on Ag(111), than on Au(111). This consequent lowering of the valence band and increased n-type character of the MoS_2 layer on Ag(111) is reflected in the shift of the core level components towards higher BE.

In addition to the shift of the peaks, the Mo 3d core level for MoS_2/Ag(111) presents a higher asymmetry $\alpha = 0.1$, than the one observed for MoS_2/Au(111) ($\alpha = 0.05$). In the Doniach-Šunjić fitting function, the asymmetry parameter α accounts for the electron-hole pair creation in the vicinity of the Fermi level. [23, 24] Therefore, a high value of α could be ascribed to the increased density of states near the Fermi level. The measured value of $\alpha = 0.1$ for MoS_2/Ag(111), similar to the typical value observed for metallic systems, [21] indicates the presence of density of state at the Fermi level for MoS_2 layer, suggesting a semiconductor to metal transition. It is also important to highlight that the metallic behavior can also be expected from the edges of the nano-islands [25] and also from the octahedral 1T structural phase (see figure 3.1 in chapter 3) of MoS_2. [26] However, such possibilities can be neglected, as no spectral contribution is observed at the characteristic BE of the components belonging to the edges (see analysis of TPG MoS_2 in chapter 3 and ref. [25]) and 1T phase of MoS_2. [26] A similar behavior has been observed for SL WS_2 grown on Ag(111), [27] where the core level shifts and increased asymmetry of the W 4f spectra were attributed, by means of ARPES measurements and DFT calculations, to the contact induced semiconducting to metallic transition of the WS_2 monolayer.

Furthermore, the S 2p spectrum (figure 5.3 (b)) for MoS_2/Ag(111) shows a stronger signal for spectral component S_B, belonging to the bottom layer S atoms strongly interacting with the substrate, with an intensity ratio between S_B and S_A amounting to 0.27, in comparison with 0.21 for MoS_2/Au(111) (figure 5.3 (d)). S_B amounts to $\sim$ 74% (in comparison with to 55% for MoS_2/Au(111)) of the total contribution from bottom layer S atoms, while the remaining 26% of weakly interacting bottom layer S atoms contributes to the intensity of main peak S_A. The increase in the relative intensity of S_B with respect to S_A, indicates stronger interaction of the MoS_2 layer with the underlying Ag substrate. As already mentioned earlier, theoretical calculations in [9] have reported higher equilibrium BE (+0.02 eV) and shorter MoS_2-Ag(111) distance (-0.1 Å) with respect to MoS_2 on Au(111). Therefore, it can be assumed that due to the increased interactions with the Ag substrate, the bottom layer S atoms move closer to the Ag(111) than to the Au(111) surface, leading to an increased number of S atoms that feel the effect of the proximity to the Ag surface atoms. The contribution from such strongly interacting S atoms, results in an increase in the intensity of their characteristic spectral

component (S_B) in S 2p core level, observed in the XPS measurements.

Mo 3d ($h\nu$=360 eV)	L(eV)	α	G(eV)	BE(eV)
$3d_{5/2}$	0.18	0.1	0.25	229.33
$3d_{3/2}$	0.40	0.1	0.25	232.48
S 2p ($h\nu$=260 eV)	L(eV)	α	G(eV)	BE(eV)
$2p_{3/2}$ S_A	0.16	0.05	0.19	162.25
$2p_{3/2}$ S_B	0.16	0.05	0.19	162.49
$2p_{1/2}$ S_A	0.17	0.05	0.19	163.45
$2p_{1/2}$ S_B	0.17	0.05	0.19	163.69

Table 5.1: Lineshape parameters used to fit the Mo 3d and S 2p spectra of SL MoS_2 grown on Ag(111). L is the Lorentzian width, α is the asymmetry parameter and G is the Gaussian width.

5.3 Long range order and continuous growth of SL MoS_2 on Ag(111)

As already mentioned in the beginning of this chapter, stronger MoS_2/substrate interactions, observed in the XPS analysis shown above, are expected to improve the structural quality of the grown layer. Indeed, the LEED patterns (figure 5.4) obtained for 0.8 ML MoS_2 coverage, indicate towards a well ordered MoS_2 monolayer on Ag(111). Figure 5.4 (a) and (b), show the LEED patterns obtained at 117 eV and 211 eV, respectively. The observed patterns are similar to those acquired for MoS_2/Au(111) (chapter 3), where the first order diffraction spots of MoS_2 are surrounded by the characteristic moiré spots, due to the lattice mismatch between MoS_2 (lattice parameter $\alpha = 3.15$ Å) and Ag(111) unit cell ($\alpha = 2.88$ Å). More importantly, the LEED patterns obtained for the MoS_2 layer grown on Ag(111) show sharp spots with a low background intensity, indicating the presence of large domains with a low concentration of defects and other crystallographic imperfections. In addition to this, the moiré spots are aligned parallel to the principle diffraction spots, indicating that the azimuthal orientation of the MoS_2 layer is in registry with the Ag(111) surface orientation. From a more quantitative analysis, a moiré periodicity of 35.15±1 Å is obtained from the comparison between the reciprocal lattice vector of MoS_2 ($\alpha^*_{MoS_2}$) and Ag(111) (α^*_{Ag}), as shown in the intensity line profile (figure 5.4 (c)) along the indicated dashed line in figure 5.4 (a). The calculated moiré periodicity indicates the formation of a moiré superstructure consisting of 11×11 MoS_2 over 12×12 Ag(111) unit cell. Figure 5.4 (d), shows the intensity profile corresponding to the indicated red arc along the MoS_2 spots in figure 5.4 (a). In direct contradiction to the behavior observed for MoS_2/Au(111) in chapter 3, the

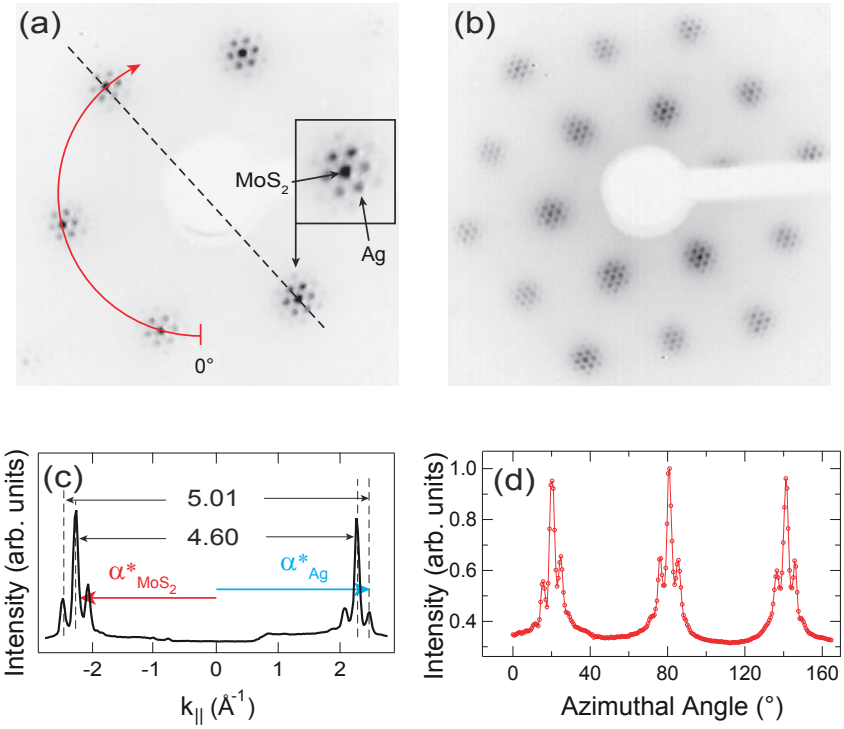

Figure 5.4: LEED patterns measured at (a) 117 eV and (b) 211 eV, showing the principle spots surrounded by moiré satellite spots for 0.8 ML coverage of SL MoS_2 on Ag(111). (c) Intensity line profile along the dashed line in (a), indicating the reciprocal lattice vectors corresponding to MoS_2 ($\alpha^*_{MoS_2}$) and Ag surface (α^*_{Ag}) unit cell. (d) Intensity profile for the circular cuts (solid red line) in (a), indicating near six-fold symmetry of the LEED pattern. The slight asymmetry of the intensity is due to a small misalignment of the sample normal with respect to the electron beam direction.

diffraction spots of MoS_2/Ag(111) show a six-fold symmetry, suggesting an equal distribution of MoS_2 mirror domains. A more detailed characterization of the domain orientation of the grown layer is discussed later in this chapter.

Further information about the structural quality and the continuity of the MoS_2 layer can be obtained from the STM measurements presented in figure 5.5. The high-resolution STM topographic image, in figure 5.5 (a), shows the top layer S atoms (small bright spots) within the hexagonally arranged bright features that indicate the formation of a moiré superstructure. From the line scan shown in figure 5.5 (d) corresponding to the marked blue line in figure 5.5 (a), eleven S atoms can be counted between the center of

adjacent moiré bright features. The distance between the S atoms amounts to 3.14±0.40 Å, in agreement with the value reported in literature for the lattice constant of MoS_2, [28, 29] with the moiré periodicity of 3.48±0.03 nm, in agreement with the 11×11 MoS_2/12×12 Ag(111) superstructure determined from LEED. The apparent out-of plane corrugation is ∼ 0.4 Å, similar to the value obtained for MoS_2/Au(111) in chapter 3.

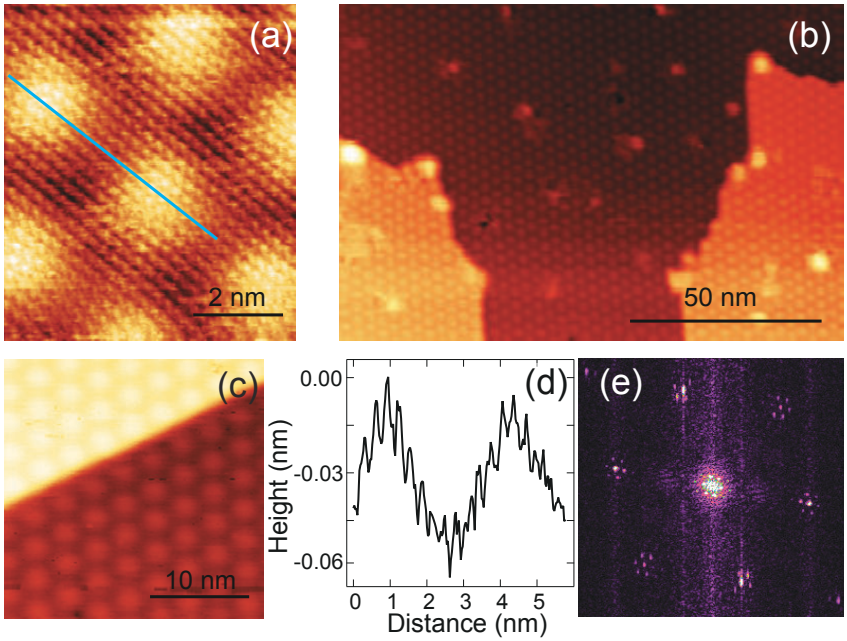

Figure 5.5: STM topographs acquired for 0.8 ML of SL MoS_2/Ag(111). (a) Atomic-resolution image showing the top layer S atoms in the moiré superstructure. (b) Large scale image showing different terraces of Ag(111) surface showing continuous coverage of MoS_2, indicated by the hexagonal moiré pattern. (c) 26 nm × 26 nm STM image showing the continuity and the extension of MoS_2 layer over the Ag(111) step-edge. (d) Line-scan along the indicated blue line on the STM image in (a) showing the moiré periodicity and the corrugation of the MoS_2 layer. (e) 2D Fast Fourier transform (FFT) of the STM image in (a). Tunneling parameters: (a) V_B = 0.039 V, I_T = 2.44 nA, (b) V_B = 1.051 V, I_T = 0.88 nA and (c) V_B = 0.221 V, I_T = 1.27 nA.

The 130 nm × 80 nm STM topograph, in figure 5.5 (b), shows several Ag terraces fully covered with the hexagonal bright features corresponding to the moiré superstructure, indicating a large scale growth of the MoS_2 layer, in agreement with the sharp LEED spots shown in figure 5.4. The randomly distributed irregular bright spots most likely related to impurities adsorbed on

the surface due to the transfer of the sample, in air, from the UHV chamber of SuperESCA to the STM chamber of CoSMoS. Another important observation can be made from the STM image acquired over a step-edge region. As shown in figure 5.5 (c), the MoS_2 layer can be seen spreading uniformly from the upper to the lower terrace of the Ag surface. This clearly suggests a continuous growth of the layer that extends over several terraces in a carpet-like fashion, without bond breaking or formation of defects, thus preserving the crystalline nature. The stimulus for such a homogeneous growth can be the stronger interactions between the MoS_2 layer and Ag surface. Effect of adsorbate-substrate interactions on large scale epitaxial growth of 2D layers have been widely asserted in literature. [12–18] Figure 5.5 (e) shows the Fourier transform of the atomic-resolution STM topograph shown in figure 5.5 (a). The moiré pattern observed in STM gives rise to the satellite spots in the FFT, that are consistent with the LEED pattern, further confirming the large scale growth of MoS_2 aligned with the Ag(111) crystallographic axis.

5.4 Local structure and domain orientation of SL MoS_2 on Ag(111)

In order to further elucidate on the LEED findings that suggest the co-existence of domains with anti-parallel orientations, XPD measurements of the Mo 3d core level were performed and compared with multiple scattering simulations, as shown in figure 5.6 (c). Analogously to the systems studied so far in previous chapters, the effect of the substrate on the diffraction pattern was neglected and the simulations were performed for the 1H phase structure of free standing MoS_2 layer, with the lattice constant of 3.15 Å and the Mo-S interlayer distance of 1.62 Å. [28, 29] The XPD simulations of the Mo 3d core level corresponding to the two 180° rotated orientations, orientation 1 (Or1) and orientation 2 (Or2) are shown in figure 5.6 (a) and (b), respectively. In order to evaluate the fraction of the two mirror domains in the grown layer, the simulated intensities were intermixed in different percentage following the equation 3.2 presented in chapter 3, and compared with the experimental Mo 3d XPD pattern (shown in color scale in figure 5.6 (c)) by means of the R-factor analysis. [30] The R-factor as a function of the percentage of Or2 in the total simulated intensity, in figure 5.6 (d), shows the best agreement between the experiment and simulations for 50% of intermixed domain orientations. This shows that the HTG grown MoS_2 on Ag(111) presents an equal concentration of 180° rotated domains, as opposed to the single orientation growth of MoS_2 on Au(111) presented in chapter 3. The presence of twin domains on Ag(111) could be ascribed to the stronger interactions with this substrate, although it could be expected that it would favor the single orientation growth. Another possibility is the higher Mo deposition rate used here, as compared to the growth of MoS_2 on Au(111). Indeed, in the case of WS_2/Au(111) (shown in chapter 4), the higher W deposition rate resulted in the coexistence of the twin WS_2 domains. Further

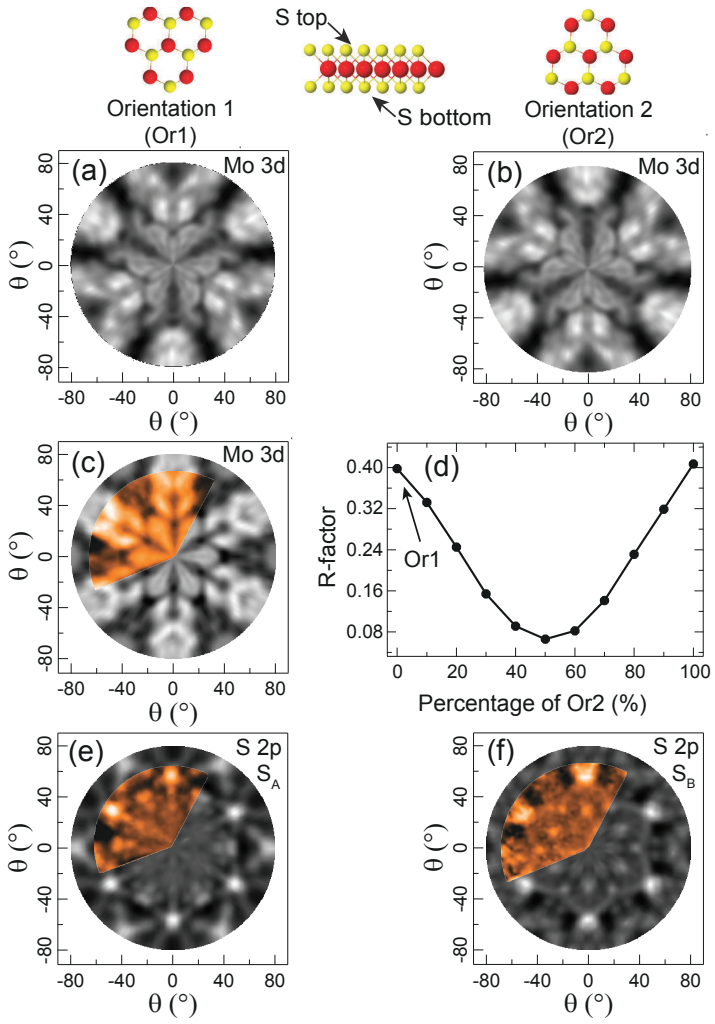

Figure 5.6: (a) and (b) show the multiple scattering simulations of Mo 3d core level performed at 130 eV KE for the two corresponding orientations (Or1 and Or2) indicated on top. (c) Experimental Mo 3d XPD pattern (color) obtained at 360 eV photon energy (corresponding photoelectron KE = 130 eV) for the grown layer together with the simulated pattern (grey) for the best matched structure based on R-factor analysis. (d) R-factor analysis for the domain orientation characterization, showing a 50-50% contribution of two mirror orientations. The S 2p XPD pattern for (e) S_A and (b) S_B components of figure 5.3 (b), acquired at 270 eV photon energy (KE = 108 eV) and 560 eV photon energy (KE = 397 eV), respectively. The experimental data (color) are presented together with the simulated patterns (grey) for (e) top layer S and (f) bottom layer S, as indicated in the ball model. Ball model color code: red (Mo) and yellow (S).

experiments and support from theoretical calculations would be important for understanding the mechanisms responsible for the observed behavior.

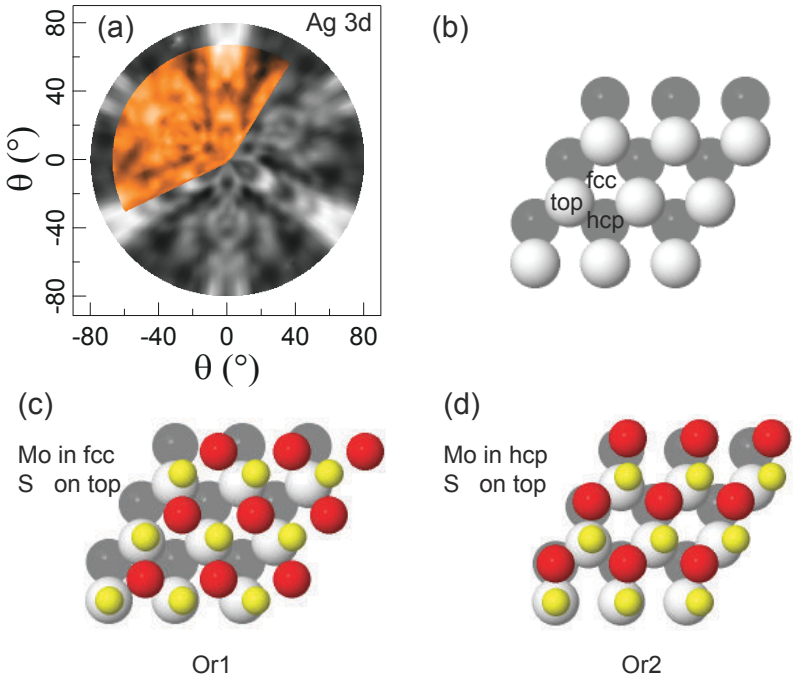

Figure 5.7: (a) XPD pattern showing the modulation function (color) of the Ag $3d_{5/2}$ core level together with the EDAC simulation (grey) for the clean Ag(111) sample. (b) The orientation of the Ag sample is derived from the comparison of the XPD experiment with the simulation. Relative orientation of the two mirror domains of SL MoS_2 on Ag(111); for S adsorbed in *atop* position, the adsorption configuration of bonding regions for (a) Or1- Mo in *fcc* and (b) Or2- Mo in *hcp* site. Ball color code: red (Mo), yellow (S), light grey (Ag surface layer) and dark grey (Ag second layer).

Figure 5.6 (e) and (f) show the S 2p XPD patterns (color) corresponding to S_A and S_B components presented in figure 5.3 (b), respectively, together with the 50-50 intermixing of simulations (grey) for Or1 and Or2, performed at the corresponding kinetic energies. In the simulation of figure 5.6 (e) for the component S_A, a contribution of 26% of bottom layer S atoms was included, because of the considerations made in the previous section. A good agreement of the experimental data with the simulations for S_A (R-factor = 0.21) and S_B (R-factor = 0.29), further confirms the 1H phase structure of the SL MoS_2. In order to determine the relative orientation of the MoS_2 layer with respect to the substrate, we performed XPD measurements on the Ag 3d core

level and compared them with multiple scattering simulations (figure 5.7 (a)) for a 3 layer slab of Ag with emitters in all three layers. A clear three-fold symmetry and a good agreement between the experiment and simulation (R-factor = 0.4), helped in the identification of the substrate orientation modeled in figure 5.7 (b). Figure 5.7 (c) and (d) show the relative arrangement of the two mirror orientations of MoS_2, determined from XPD analysis, with respect to the Ag(111) substrate. This comparison further confirms that the MoS_2 layer is aligned with the Ag(111) substrate lattice directions. Therefore, if we assume that in a specific local adsorption configuration the S atom adsorbs in *atop* position, the Mo atom can be in the fcc three-fold (figure 5.7 (c)) or *hcp* site (figure 5.7 (d)) with equal concentration because of the presence of the two 180° rotated domains.

5.5 Conclusions

In this chapter we have studied and characterized the growth of SL MoS_2 on Ag(111) that presents modifications to the electronic properties of the grown layer, mainly driven by the interactions between the ad-layer and the Ag substrate. By following an already established HTG procedure and carefully tuning the growth parameters, with the help of fast-XPS, we were able to grow a high quality MoS_2 monolayer on Ag(111). The STM analysis shows a continuous growth of the MoS_2 layer, spreading over different terraces of the Ag(111) surface and even carpeting over step-edges. The long range order of the MoS_2 layer is also reflected in the LEED measurements, that show very sharp and prominent diffraction spots with a low background intensity. In this case, the MoS_2 layer is aligned to the Ag(111) substrate with a moiré superstructure periodicity of 11×11 MoS_2/12×12 Ag(111) unit cell.

The XPD measurements show the coexistence of mirror domains in equal proportion. The Mo 3d core level presents a larger asymmetry than that measured in the case of MoS_2/Au(111). This is likely due to a semiconductor to metal transition of the MoS_2 layer as a result of the stronger interaction with the Ag(111) substrate. The degree of interaction is also evident from the S 2p core level spectrum that shows a stronger signal for the spectral component related to the strongly interacting bottom layer S atoms, that dominated over the one that corresponds to the S atoms weakly interacting with the Ag substrate.

References

[1] Wan, W.; Li, X.; Li, X.; Xu, B.; Zhan, L.; Zhao, Z.; Zhang, P.; Wu, S. Q.; Zhu, Z.-Z.; Huang, H.; Zhou, Y.; Cai, W. Interlayer coupling of a direct van der Waals epitaxial MoS_2/graphene heterostructure. *RSC Advances* **2016**, *6*, 323–330.

[2] Dumcenco, D.; Ovchinnikov, D.; Marinov, K.; Lazić, P.; Gibertini, M.; Marzari, N.; Sanchez, O. L.; Kung, Y.-C.; Krasnozhon, D.; Chen, M.-W.; Bertolazzi, S.; Gillet, P.; Fontcuberta i Morral, A.; Radenovic, A.; Kis, A. Large-Area Epitaxial Monolayer MoS_2. *ACS Nano* **2015**, *9*, 4611–4620.

[3] Sorensen, S. G.; Füchtbauer, H. G.; Tuxen, A. K.; Walton, A. S.; Lauritsen, J. V. Structure and Electronic Properties of In Situ Synthesized Single-Layer MoS_2 on a Gold Surface. *ACS Nano* **2014**, *8*, 6788–6796.

[4] Grønborg, S. S.; Ulstrup, S.; Bianchi, M.; Dendzik, M.; Sanders, C. E.; Lauritsen, J. V.; Hofmann, P.; Miwa, J. A. Synthesis of Epitaxial Single-Layer MoS_2 on Au(111). *Langmuir* **2015**, *31*, 9700–9706.

[5] Busse, C.; Lazić, P.; Djemour, R.; Coraux, J.; Gerber, T.; Atodiresei, N.; Caciuc, V.; Brako, R.; N'Diaye, A. T.; Blügel, S.; Zegenhagen, J.; Michely, T. Graphene on Ir(111): Physisorption with Chemical Modulation. *Physical Review Letters* **2011**, *107*, 036101, 1–4.

[6] Sutter, P.; Sadowski, J. T.; Sutter, E. Graphene on Pt(111): Growth and substrate interaction. *Physical Review B* **2009**, *80*, 245411, 1–10.

[7] Marchini, S.; Günther, S.; Wintterlin, J. Scanning tunneling microscopy of graphene on Ru(0001). *Physical Review B* **2007**, *76*, 075429, 1–9.

[8] Alfè, D.; Pozzo, M.; Miniussi, E.; Günther, S.; Lacovig, P.; Lizzit, S.; Larciprete, R.; Burgos, B. S.; Menteş, T. O.; Locatelli, A.; Baraldi, A. Fine tuning of graphene-metal adhesion by surface alloying. *Scientific Reports* **2013**, *3*, 2430, 1–6.

[9] Farmanbar, M.; Brocks, G. First-principles study of van der Waals interactions and lattice mismatch at MoS_2/metal interfaces. *Physical Review B* **2016**, *93*, 085304, 1–12.

[10] Zhong, H.; Quhe, R.; Wang, Y.; Ni, Z.; Ye, M.; Song, Z.; Pan, Y.; Yang, J.; Yang, L.; Lei, M.; Shi, J.; Lu, J. Interfacial Properties of Monolayer and Bilayer MoS_2 Contacts with Metals: Beyond the Energy Band Calculations. *Scientific Reports* **2016**, *6*, 21786, 1–16.

[11] Popov, I.; Seifert, G.; Tománek, D. Designing Electrical Contacts to MoS_2 Monolayers: A Computational Study. *Physical Review Letters* **2012**, *108*, 156802, 1–5.

[12] Gao, L.; Liu, Y.; Shi, R.; Ma, T.; Hu, Y.; Luo, J. Influence of interface interaction on the moiré superstructures of graphene on transition-metal substrates. *RSC Advances* **2017**, *7*, 12179–12184.

[13] Wang, B.; Bocquet, M.-L.; Marchini, S.; Gunther, S.; Wintterlin, J. Chemical origin of a graphene moiré overlayer on Ru(0001). *Physical Chemistry Chemical Physics* **2008**, *10*, 3530–3534.

[14] Martoccia, D.; Björck, M.; Schlepjütz, C. M.; Brugger, T.; Pauli, S. A.; Patterson, B. D.; Greber, T.; Willmott, P. R. Graphene on Ru(0001): a corrugated and chiral structure. *New Journal of Physics* **2010**, *12*, 043028, 1–13.

[15] Preobrajenski, A. B.; Ng, M. L.; Vinogradov, A. S.; Mårtensson, N. Controlling graphene corrugation on lattice-mismatched substrates. *Physical Review B* **2008**, *78*, 073401, 1–4.

[16] Vinogradov, N. A.; Zakharov, A. A.; Ng, M. L.; Mikkelsen, A.; Lundgren, E.; Mårtensson, N.; Preobrajenski, A. B. One-Dimensional Corrugation of the h-BN Monolayer on Fe(110). *Langmuir* **2012**, *28*, 1775–1781.

[17] Schwarz, M.; Riss, A.; Garnica, M.; Ducke, J.; Deimel, P. S.; Duncan, D. A.; Thakur, P. K.; Lee, T.-L.; Seitsonen, A. P.; Barth, J. V.; Allegretti, F.; Auwärter, W. Corrugation in the Weakly Interacting Hexagonal-BN/Cu(111) System: Structure Determination by Combining Noncontact Atomic Force Microscopy and X-ray Standing Waves. *ACS Nano* **2017**, *11*, 9151–9161.

[18] Larciprete, R.; Ulstrup, S.; Lacovig, P.; Dalmiglio, M.; Bianchi, M.; Mazzola, F.; Hornekaer, L.; Orlando, F.; Baraldi, A.; Hofmann, P.; Lizzit, S. Oxygen Switching of the Epitaxial Graphene-Metal Interaction. *ACS Nano* **2012**, *6*, 9551–9558.

[19] Abrami, A.; Barnaba, M.; Battistello, L.; Bianco, A.; Brena, B.; Cautero, G.; Chen, Q. H.; Cocco, D.; Comelli, G.; Contrino, S.; DeBona, F.; Di Fonzo, S.; Fava, C.; Finetti, P.; Furlan, P.; Galimberti, A.; Gambitta, A.; Giuressi, D.; Godnig, R.; Jark, W.; Lizzit, S.; Mazzolini, F.; Melpignano, P.; Olivi, L.; Paolucci, G.; Pugliese, R.; Qian, S. N.; Rosei, R.; Sandrin, G.; Savoia, A.; Sergo, R.; Sostero, G.; Tommasini, R.; Tudor, M.; Vivoda, D.; Wei, F. Q.; Zanini, F. Super ESCA: First beamline operating at ELETTRA. *Review of Scientific Instruments* **1995**, *66*, 1618–1620.

[20] García de Abajo, F. J.; Van Hove, M. A.; Fadley, C. S. Multiple scattering of electrons in solids and molecules: A cluster-model approach. *Physical Review B* **2001**, *63*, 075404, 1–16.

[21] Citrin, P. H.; Wertheim, G. K.; Baer, Y. Surface-atom x-ray photoemission from clean metals: Cu, Ag, and Au. *Physical Review B* **1983**, *27*, 3160–3175.

[22] Andersen, J. N.; Hennig, D.; Lundgren, E.; Methfessel, M.; Nyholm, R.; Scheffler, M. Surface core-level shifts of some 4d-metal single-crystal surfaces: Experiments and ab initio calculations. *Physical Review B* **1994**, *50*, 17525–17533.

[23] Doniach, S.; Šunjić, M. Many-Electron Singularity in X-ray Photoemission and X-ray Line Spectra from Metals. *Journal of Physical Chemistry: Solid State* **1970**, *3*, 285–291.

[24] Hüfner, S. *Photoelectron Spectroscopy*: *Principles and Applications*; Advanced Texts in Physics; Springer, 2003.

[25] Bruix, A.; Füchtbauer, H. G.; Tuxen, A. K.; Walton, A. S.; Andersen, M.; Porsgaard, S.; Besenbacher, F.; Hammer, B.; Lauritsen, J. V. In Situ Detection of Active Edge Sites in Single-Layer MoS_2 Catalysts. *ACS Nano* **2015**, *9*, 9322–9330.

[26] Kappera, R.; Voiry, D.; Yalcin, S. E.; Branch, B.; Gupta, G.; Mohite, A. D.; Chhowalla, M. Phase-engineered low-resistance contacts for ultrathin MoS_2 transistors. *Nature Materials* **2014**, *13*, 1128–1134.

[27] Dendzik, M.; Bruix, A.; Michiardi, M.; Ngankeu, A. S.; Bianchi, M.; Miwa, J. A.; Hammer, B.; Hofmann, P.; Sanders, C. E. Contact-Induced Semiconductor-to-Metal Transition in Single-Layer WS_2. *ArXiv e-prints* **2017**, *1708.02799*.

[28] Winer, W. Molybdenum disulfide as a lubricant: A review of the fundamental knowledge. *Wear* **1967**, *10*, 422 – 452.

[29] Holinski, R.; Gänsheimer, J. A study of the lubricating mechanism of molybdenum disulfide. *Wear* **1972**, *19*, 329 – 342.

[30] Woodruff, D. Adsorbate structure determination using photoelectron diffraction: Methods and applications. *Surface Science Reports* **2007**, *62*, 1–38.

[31] Dendzik, M.; Michiardi, M.; Sanders, C.; Bianchi, M.; Miwa, J. A.; Grønborg, S. S.; Lauritsen, J. V.; Bruix, A.; Hammer, B.; Hofmann, P. Growth and electronic structure of epitaxial single-layer WS_2 on Au(111). *Physical Review B* **2015**, *92*, 245442, 1–7.

CHAPTER 6

Growth of single layer MoS_2 on the anisotropic Ag(110) substrate

The ability to modify the properties of MoS_2 is highly demanding in order to extend its inclusion in a range of already existing and possible novel applications. In order to achieve the desired results, one of the most common practice is to induce structural modifications that leads to the variations in the electronic properties. Such procedures have been widely employed in the case of CVD synthesis of graphene on different *fcc* and *hcp* transition metal substrates, leading to modifications of the band structure together with morphological variations as a result of diverse interfacial interactions and substrate geometry. [1–3] In addition to that, intercalation of metal atoms [4, 5], growth of metal oxides [6] and substrate nano-patterning [7] have also been successful in inducing significant changes in the electronic properties of the grown layers. We have also demonstrated, in chapter 5, the effect of strongly interacting Ag(111) substrate that resulted in a very high quality SL MoS_2 and a possible substrate induced transition from semiconducting to metallic state. [8]

An alternative approach to modify the properties of the 2D layer is by growing it on an anisotropic substrate, i.e. with different lattice parameters along distinct crystallographic directions. This offers the possibility of variety of moiré superstructures due to the lattice mismatch between the substrate and the grown layer. Previous studies have highlighted the effect of additional periodic potential, due to the moiré superlattice, on the electronic properties of graphene and 2D h-BN grown on anisotropic substrates. [9–11] This advocates for the use of surface irregularities in order to fine tune the properties of 2D layers, motivating us to explore the effects on the structural and electronic

properties of SL MoS_2 grown on highly anisotropic Ag(110), that has a rectangular lattice as opposed to the hexagonal lattice of MoS_2. However, one of the major challenges in this case is to avoid the growth of rotated domains that might impair the properties of the grown 2D layer. In this regard, the choice of Ag(110) substrate was based on the fact that the relatively strong interfacial interactions [12] may suppress the formation of rotated domains, as evidenced for the growth of graphene and hexagonal boron nitride on strongly interacting transition metal substrates. [10, 13]

In this chapter, we demonstrate that it is possible to grow high quality SL MoS_2 on the Ag(110) substrate. Similar to the trend observed for SL MoS_2 on Ag(111), the Mo 3d XPS peak showed a high asymmetry indicating a metallic character of the layer, while the S 2p core level presented an intense component related to the strongly interacting bottom layer S atoms, suggesting stronger interactions with the underlying substrate. Moreover, the co-existence of mirror domains was verified by comparing the experimental XPD patterns with multiple scattering simulations. In addition to the long range order and high structural quality of the grown layer, the LEED and STM measurements showed the formation of a complex superstructure, observable in the form of additional moiré induced diffraction spots in LEED and striped patterns in the STM topographs. Based on the analysis of these results, we identified a structural atomic model for the MoS_2/Ag(110) interface.

6.1 Experiments and methods

The experiments presented in this chapter, including the growth and characterization of SL MoS_2, were performed at SuperESCA beamline of Elettra. [14] Prior to the growth of MoS_2, the Ag(110) crystal was cleaned by repeated cycles of Ar^+ sputtering at 1 keV, followed by annealing at 800 K for 10 minutes. Sample cleanliness was confirmed by XPS that did show any contaminants. Surface long range order was verified by LEED that presented sharp 1×1 diffraction spots corresponding to the rectangular lattice of the substrate. As for the previous cases, the Mo evaporator, mounted in front of the sample, was a Mo filament heated through direct current and H_2S was used as sulfur source.

Fast-XPS was employed for the real time monitoring of the synthesis of MoS_2. The grown layers were characterized by means of LEED and high-resolution XPS. The energy resolution was better than 50 meV and the core level spectra were normalized for the Fermi level of the Ag sample. The fit of the data was performed using Doniach-Šunjić function convoluted with Gaussian broadening and a linear background. The orientation of the MoS_2 layer was determined by XPD measurements that were compared with multiple scattering simulations performed using the EDAC package. [15] ARPES measurements were performed at the SGM-3 beamline of the synchrotron radiation facility ASTRID2 in Aarhus, [16] with the sample kept at $\sim$ 30 k. The energy and

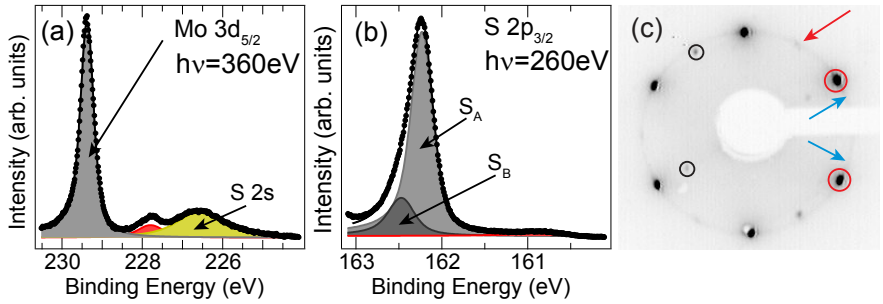

Figure 6.1: High-resolution XPS spectra of the (a) Mo $3d_{5/2}$ and (b) S $2p_{3/2}$ core levels for HTG MoS_2/Ag(110). (c) LEED pattern at 125 eV KE for $\sim$ 0.7 ML coverage of MoS_2. The principal spot corresponding to MoS_2 is indicated by the red circle, while the black circles mark the spots from Ag(110) surface. The red arrow marks the spot due to the MoS_2 domains rotated by 30° with respect to the main MoS_2 domain orientation, while the blue arrows indicate the streaks due to the randomly oriented domains.

angular resolution were better than 30 meV and 0.2°, respectively. Scanning Tunneling Microscopy (STM) measurements were performed at the CoSMoS facility at Elettra. The images were acquired at room temperature with a SPECS STM 150 Aarhus instrument. The sample was transferred through air from the chamber of SuperESCA to SGM-3 beamline and the STM chamber of CoSMoS, where it was subsequently annealed up to ca. 800 K for 30 min, in order to remove adsorbed impurities.

6.2 Growth of SL MoS_2 on Ag(110)

The HTG procedure that was successfully used to grow high quality SL MoS_2 on Au(111) (in chapter 3) and on Ag(111) (in chapter 5), was also exploited for the growth of MoS_2 on Ag(110). Mo was deposited in H_2S background pressure of 5×10^{-7} mbar on the Ag(110) sample kept at 800 K. Mo deposition rate amounted to 4.7×10^{-3} ML/minute, where a monolayer (ML) is the surface atomic density of the Au(111) surface. The coverage of MoS_2 on Ag(110) was determined by comparing the decrement of the overall intensity of the Ag 3d spectrum (after the growth of MoS_2) with that of the Ag(111) spectrum acquired at the same photon energy (i.e. same KE) after the growth of SL MoS_2 on Ag(111) presented in chapter 5. The deposition was continued up to the final MoS_2 coverage of $\sim$ 0.7 ML, with a monolayer (ML) representing one complete layer of MoS_2 on Ag(110), amounting to Mo surface density of 1.15×10^{15} atoms/cm^2 for the MoS_2 lattice parameter of 3.15 Å.

Figure 6.1 shows the high resolution XPS spectra of the Mo $3d_{5/2}$ and

the S $2p_{3/2}$ core levels, measured after the completion of the growth. The peak-fit analysis evidences the presence of the spectral components in the Mo $3d_{5/2}$ (at 229.33 eV) and S $2p_{3/2}$ (S_A at 162.27 eV and S_B at 162.51 eV) core levels at BE positions similar to those reported for SL MoS_2/Ag(111). However, the LEED pattern (figure 6.1 (c)) shows the presence of streaky features, indicated with blue arrows, symmetric to the main MoS_2 spots (red circles), indicating the formation of rotated domains of MoS_2. The diffraction spot corresponding to 30° rotated MoS_2 domains with respect to the main orientation, is indicated with the red arrow. The formation of rotated domains has also been reported in literature for graphene grown on weakly interacting transition metal substrates, [13, 17, 18] as well as on strongly interacting ones. [19, 20]

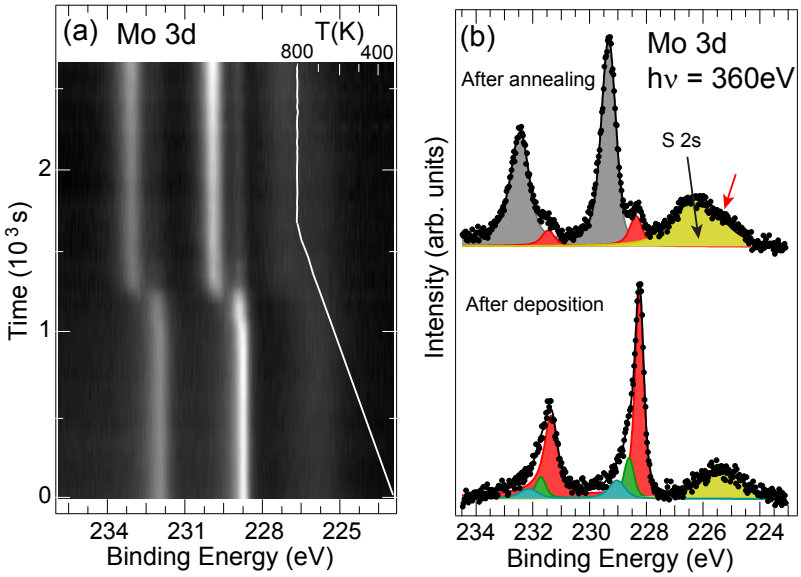

Figure 6.2: (a) 2D intensity plot of the sequence of fast-XPS spectra of the Mo 3d core level acquired while annealing the sample after the Mo deposited at RT. The annealing temperature ramp is indicated with the white solid line. (b) Mo 3d core level spectra together with the spectral contributions resulting from the peak fit analysis acquired before and after the annealing. The final MoS_2 coverage is $\sim$ 0.07 ML.

The presence of rotated domains leads to the formation of structural defects such as grain boundaries that degrade the properties of SL MoS_2. Therefore, in order to suppress the growth of rotated domains, MoS_2 was synthesized by following a stepwise growth procedure. At the beginning, the TPG method was used to grow MoS_2 up to the coverage of $\sim$ 0.07 ML. In order to do this, Mo was

deposited at RT and subsequently annealed at 800 K, both in H_2S background pressure of 5×10^{-7} mbar. Figure 6.2 (a) shows the 2D intensity plot for the sequence of fast-XPS spectra of the Mo 3d core level, acquired while annealing the pre-deposited sample up to 800 K. The behavior of the peaks is similar to the one observed for the TPG of MoS_2 on Au(111) presented in chapter 3. The Mo 3d core level spectra, in figure 6.2 (b), show the deconvoluted spectral components at the beginning and at the end of the annealing process. The spectral lineshape and the BE of the different components were determined from the analysis of the high-resolution XPS spectra presented in the following section. The Mo 3d spectrum measured at the end of the annealing process, presents an intense peak (grey) belonging to MoS_2 together with a small contribution from the incompletely sulfided Mo-S species (red). Moreover, the S 2s component in the spectrum acquired after annealing presents a small shoulder at lower BE (marked with a red arrow), indicating the presence of an extra component. This could be due to the S atoms adsorbed on the Ag(110) surface, following the dissociation of H_2S at high temperature used for the annealing, or due to the formation of nanocrystalline Ag_2S. [21]

The sample prepared with TPG should result in the formation of MoS_2 nanocrystallites as observed on the Au(111) surface. [22] Such nano-crystallites may present a preferential orientation, as it was observed for the growth of h-BN on Ir(111) using the TPG method. [23] Therefore, they can act as seeded precursors for the following growth and facilitate the expansion of the MoS_2 monolayer, while maintaining their original orientation, thus suppressing the growth of randomly oriented domains. Indeed, previous studies have demonstrated the effect of the seeded growth, by controlled nucleation of graphene grains, on the synthesis of graphene free from rotated domains and detrimental grain boundaries. [24, 25]

In order to continue the MoS_2 growth on top of the TPG grown MoS_2, further deposition was performed by following the HTG procedure, using the same growth parameters of the first HTG procedure. Figure 6.3 summarizes the XPS results of the HTG deposition. The 2D intensity plot corresponding to the fast-XPS measurements of the Mo $3d_{5/2}$ core level, figure 6.3 (a), shows that the initial peak keeps on increasing with time while maintaining the same lineshape. This can be seen in figure 6.3 (b) where the core level spectra measured at 0.25 ML (indicated by the dashed line in figure 6.3 (a)) and at the end (0.75 ML) of the deposition are presented. The deconvolution of the spectrum at the end of the growth presents a negligible contribution from the low BE peaks belonging to incompletely sulfided Mo-S species. In addition to this, the low BE shoulder in the S 2s component (green), that appeared with the TPG procedure (figure 6.2 (b)), disappears by the end of HTG. This shows that only MoS_2 is present on the surface with negligible amount of other species. From the analysis of the fast-XPS spectra, the photoemission intensity of the main peak (grey) in the Mo $3d_{5/2}$ core level, that corresponds to the coverage of MoS_2, is presented as a function of deposition time in figure 6.3 (c). The observed growth trend is similar to that of the growth of MoS_2 on Au(111) and

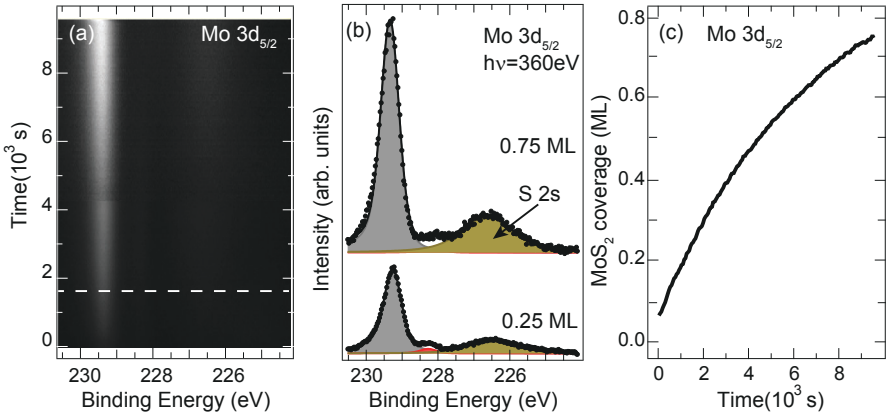

Figure 6.3: (a) 2D intensity plot of Mo $3d_{5/2}$ core level corresponding to the fast-XPS spectra acquired while following HTG on top of previously grown layer by TPG. (b) Mo $3d_{5/2}$ core level spectra together with the spectral contributions resulting from the peak fit analysis acquired at different stages of the growth. (c) Evolution of the MoS_2 coverage, proportional to the intensity of the Mo $3d_{5/2}$ peak (grey), as a function of deposition time. The final MoS_2 coverage is $\sim$ 0.75 ML.

Ag(111), showing an almost linear behavior in the beginning then slowing down continuously as the deposition continues. This behavior has been explained as due to the desorption of part of the Mo atoms that impinge on the previously formed MoS_2 layer. Most importantly, the MoS_2 layer prepared in this way (i.e. stepwise growth: TPG followed by HTG) is found to be aligned with the Ag(110) substrate with no sign of rotated domains, as discussed later in this chapter.

Figure 6.4 (a) and (b) show the Mo 3d and S 2p core level spectra, respectively, together with the spectral components resulting from the peak-fit analysis. The lineshape parameters of the fit of the XPS spectra are presented in table 6.1. Interestingly, the measured core level spectra present similarities with those reported in chapter 5 for SL MoS_2/Ag(111), in terms of lineshapes and peak positions. The Mo $3d_{5/2}$ spectrum shows an intense peak (grey) centered at 229.33 eV BE, with its spin-orbit doublet component shifted by 3.15 eV to higher BE. The BE of the main peak, as already mentioned earlier, is identical to that of MoS_2/Ag(111) shown in figure 5.3 in chapter 5. Moreover, the Mo 3d peak presents the asymmetry parameter $\alpha = 0.08$, similar to the one found for MoS_2/Ag(111) ($\alpha = 0.1$). This result was attributed to the semiconductor to metal transition of the MoS_2 layer on Ag(111) similar to the case of WS_2/Ag(111). [8]

The S 2p core level (figure 6.4 (b)) presents two spin-orbit doublets S_A

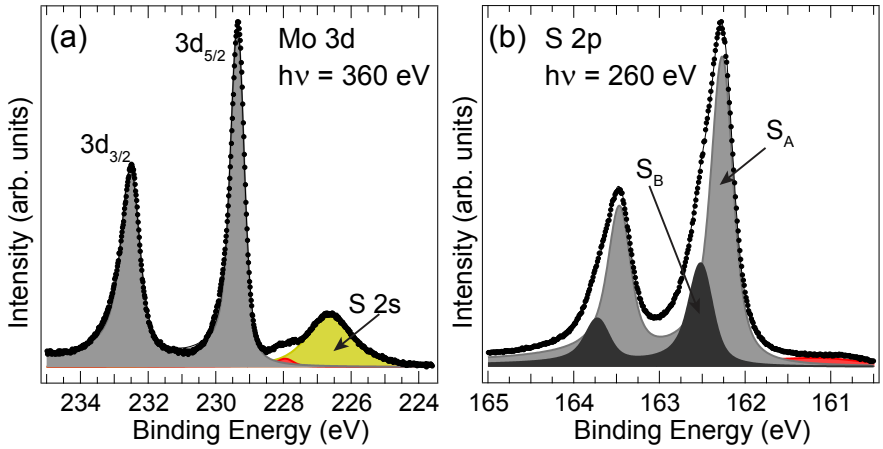

Figure 6.4: (a) and (b) high-resolution XPS of the Mo 3d and S 2p core levels, respectively, after the growth of MoS_2 on Ag(110) by following the mixed TPG and HTG procedure. The experimental data (dots) and the fit (line) are presented together with the spectral contributions (solid fill) resulting from peak-fit analysis.

Mo 3d ($h\nu$=360 eV)	L(eV)	α	G(eV)	BE(eV)
$3d_{5/2}$	0.20	0.08	0.35	229.33
$3d_{3/2}$	0.38	0.08	0.35	232.48
S 2p ($h\nu$=260 eV)	L(eV)	α	G(eV)	BE(eV)
$2p_{3/2}$ S_A	0.17	0.06	0.21	162.27
$2p_{3/2}$ S_B	0.17	0.06	0.21	162.51
$2p_{1/2}$ S_A	0.18	0.06	0.21	163.47
$2p_{1/2}$ S_B	0.18	0.06	0.21	163.71

Table 6.1: Line shape parameters for the fits of the Mo 3d and S 2p spectra acquired at 360 eV and 260 eV photon energy for 0.75 ML of SL MoS_2 grown on Ag(110). L is the Lorentzian width, α is the asymmetry parameter and G is the Gaussian width.

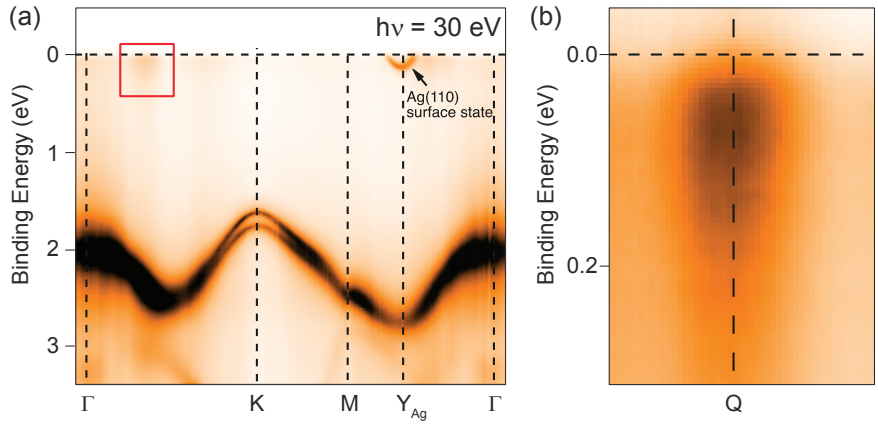

Figure 6.5: (a) Photoemission intensity along the high-symmetry directions of the MoS_2 surface Brillouin zone, acquired at 30 eV photon energy. (b) show the magnification of the region marked with red rectangle in (a), demonstrating the additional density of states at the **Q** point close to the Fermi level. In (a) the surface state of Ag substrate is also observed around the **Y** point of the surface Brillouin zone of Ag(110) crystal.

(grey) and S_B (black) with $2p_{3/2}$ components at 162.27 eV and 162.51 eV BE, respectively, in close agreement with the BE positions determined for MoS_2/Ag(111). Furthermore, the intensity ratio between S_B and S_A is found to be 0.3, in comparison with 0.27 for MoS_2/Ag(111). This suggests that the interaction of MoS_2 with the Ag(110) surface is slightly stronger than with the Ag(111) because of the increase in the population of the interacting S atoms represented by the S_B component. It has to be mentioned that the lineshape of the peaks of this mixed TPG and HTG procedure is different than that of the Mo 3d and S 2p peaks resulting from the only HTG procedure that led to the formation of rotated domains of MoS_2. Indeed, both Mo $3d_{5/2}$ and S 2p core levels of figure 6.1 are narrower than the corresponding spectra shown in figure 6.4. This is particularly evident for the S 2p core level of figure 6.4 (b) where the ratio between S_B and S_A is much larger than in figure 6.1 (b). This could be compatible with the presence of rotated domains for the HTG procedure, having weaker interaction with the Ag(110) surface than those in registry with the substrate.

In order to get further insight into the electronic structure of MoS_2, we performed ARPES measurements as shown in figure 6.5. The plot of the photoemission intensity showing the band dispersion along different high symmetry directions of the MoS_2 surface Brillouin zone can be seen in figure 6.5 (a). The spin-splitted band typical of MoS_2 is visible at the **K** point, with a spin-orbit splitting of 144 meV, similar to the one measured for MoS_2 on

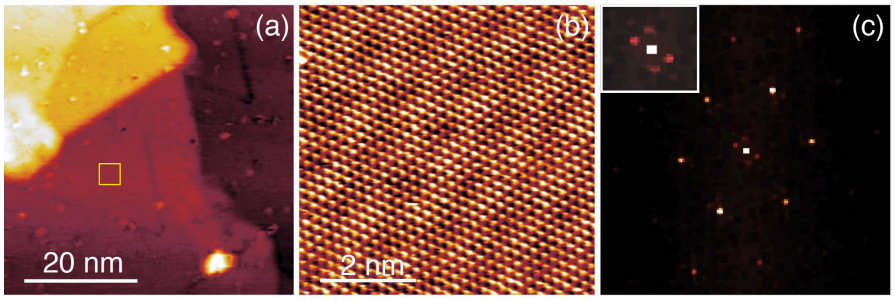

Figure 6.6: (a) Large scale STM topograph of MoS_2 on Ag(110). V_B=-1250 mV, I_T=0.06 nA. (b) Atomically resolved STM image from the region highlighted by the yellow box in (a), showing a moiré superstructure. V_B=-740 mV, I_T=1.51 nA. (c) FFT of the STM image shown in (b). The inset shows the moiré induced satellite spots in rectangular pattern around the spot corresponding to the lattice parameter of MoS_2.

Au(111). [26, 27] However, the upper band at **K** is found at 1.61 eV BE, to be compared with 1.39 eV for MoS_2 on Au(111) (see chapter 3). This shift may be ascribed to the different work function of the Ag(110) substrate with respect to the Au(111), similar to the case of MoS_2/Ag(111) discussed in chapter 5, which is reflected also in a shift of the Mo 3d and S 2p core levels to higher BE, although to a lesser extent. The absence of any additional band, due to the second layer, at the **Γ** point further confirms the single layer character of the MoS_2 sample. [27] Interestingly, the diffuse feature along the **Γ**-**K** direction (marked by the red box) indicates the presence of additional states close to the Fermi level at the **Q** point, which is further highlighted in the magnified image (figure 6.5 (b)) of the marked region in figure 6.5 (a). This is due to the hybridization of the MoS_2 electronic states with those of the underlying Ag substrate, leading to the semiconductor to metal transition of the MoS_2 layer, in agreement with the similar results obtained for WS_2/Ag(111). [8] This proves that indeed the increase of the asymmetry of the Mo 3d core level peak (grey component in figure 6.4 (a)) is caused by the presence of MoS_2 related density of states at the Fermi level due to the metallic character of the MoS_2 layer when adsorbed on the Ag surface.

6.3 STM and LEED investigation of MoS_2 on Ag(110)

STM and LEED measurements were performed in order to study the structure of the MoS_2/Ag(110) interface. In figure 6.6 (a), a large scale STM image presents the morphology of the Ag(110) surface, observable in the form of

terraces and steps. Conversely to the observation of moiré induced bright protrusions for MoS_2 on Ag(111), no indication of MoS_2 is directly visible at this scale. However, an atomically-resolved STM image (figure 6.6 (b)), acquired in the region indicated by the yellow box in figure 6.6 (a), shows the hexagonally arranged topmost layer S atoms of MoS_2, together with the appearance of a moiré superstructure. Interestingly, the moiré induced features appear to be misaligned with the rows of S atoms. These observations are more evident from the 2D FFT of this image, which represents the reciprocal space and, therefore, can be used to determine the rotations and periodicity of the moiré superstructure. As shown in figure 6.6 (c), a rectangular arrangement of satellite spots can be observed around each of the spots associated with the lattice parameter of MoS_2. These spots are rotated with respect to the MoS_2 lattice by an angle of 30° with a reciprocal space vector length that is $\frac{1}{5}^{th}$ of that of MoS_2. Such a pattern in the FFT image can be assigned to the moiré superstructure observed in figure 6.6 (b).

The results from the STM analysis are complemented by the LEED measurements shown in figure 6.7 (a). The principal spots from the MoS_2 ad-layer (red circle) are visible, together with the principal spots originating from the Ag(110) substrate (black circles). The latter can be clearly identified by a direct comparison with a LEED pattern (figure 6.7 (b)) acquired on the clean Ag(110) sample at the same KE. A near six-fold symmetry of the MoS_2 spots suggests the presence of an equal proportion of anti-parallel domain orientations of MoS_2, similar to the case of MoS_2/Ag(111). In addition to this, the MoS_2 spots are accompanied by the satellite spots arranged in the rectangular pattern (marked with the dashed blue rectangle, see inset in figure 6.7 (a)), indicating the formation of the moiré superstructure, in agreement with the FFT of the STM topographic image shown in figure 6.6 (c). Moreover, one vertex of the rectangle corresponds to the (1,1) diffraction spot of Ag(110), while the other two vertices corresponds to the $(1,\frac{1}{2})$ and $(\frac{4}{5},1)$ as displayed in figure 6.7 (a). This shows that the components of the lattice vector of the moiré superstructure are five times and two times the lattice parameters of the Ag(110) surface along the $[1\bar{1}0]$ and [001] directions, respectively. Therefore, based on the STM and LEED findings, we can sketch a model for the MoS_2/Ag(110) interface. The modeled structure is shown in figure 6.7 (d), which can be directly compared with the atomically resolved STM image of figure 6.7 (c), where the periodicity and orientation of the moiré superstructure (blue arrows) is also indicated. In order to achieve this periodicity and to match the nearest integer number of Ag atoms underneath, the MoS_2 lattice vector (red arrow) aligned along the $[1\bar{1}0]$ direction of the Ag(110) substrate has to be stretched up to 3.25 Å, indicating an expansion of ca. 3% in that direction, while the lattice vector in the other direction (green arrow) is the same (3.15 Å) of that reported in literature. [28, 29]

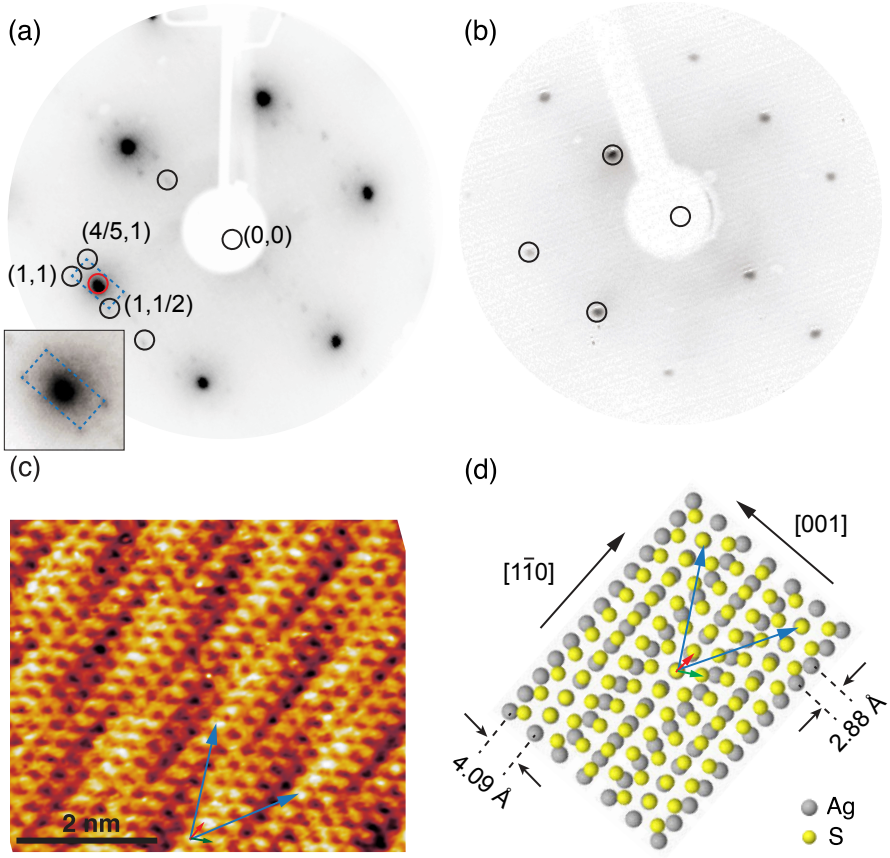

Figure 6.7: LEED patterns (a) of the MoS_2/Ag(110) sample and (b) of the clean Ag(110) substrate, both acquired at 120 eV. The diffraction spots corresponding to MoS_2 (red circle) and Ag(110) (black circles) are indicated. (c) STM atomic resolution image (V_B=1200 mV, I_T=2.05 nA) showing the MoS_2 layer and the moiré superstructure. (d) Ball model of the MoS_2/Ag(110) interface, deduced from the STM and LEED measurements. Only the first layer Ag atoms of Ag(110) and the top sulfur atoms of MoS_2 are shown for clarity. The lattice parameters of Ag(110) along the [001] and [1$\bar{1}$0] crystallographic axes are also indicated.

6.4 Local structure and domain orientation of SL MoS_2 on Ag(110)

In order to further examine the LEED findings that indicate the presence of mirror domain orientations of MoS_2, we performed XPD measurements of the

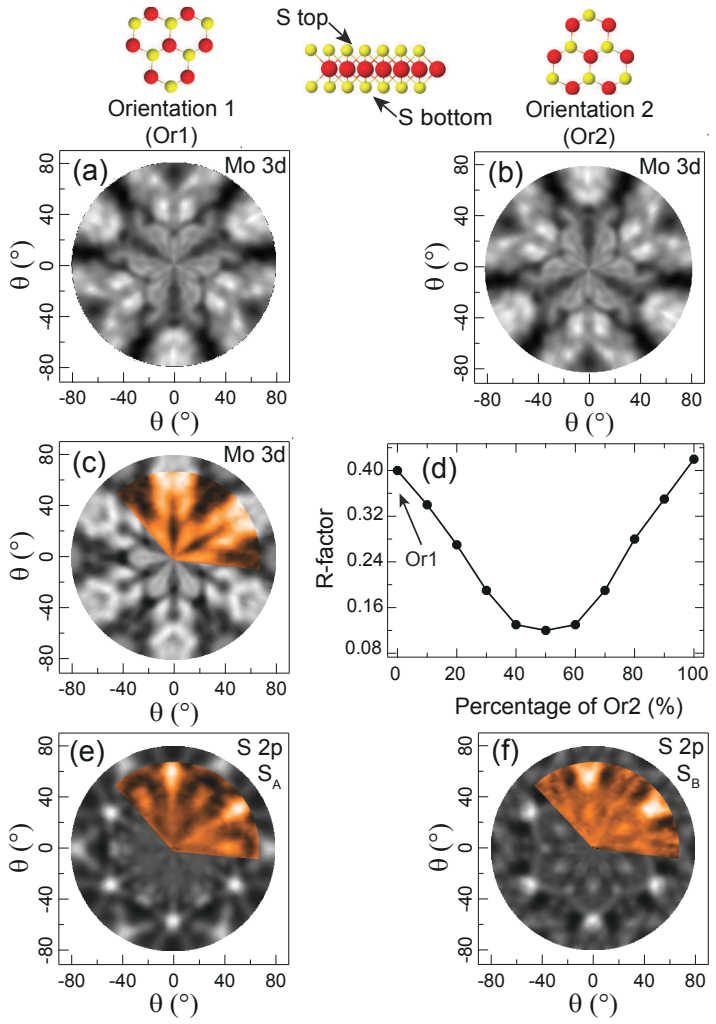

Figure 6.8: Multiple scattering simulations of Mo 3d core level performed at 130 eV KE for the two corresponding orientations (a) Or1 and (b) Or2. (c) The experimental Mo 3d XPD pattern (color) obtained at 360 eV photon energy (photoelectron KE = 130 eV) for the grown layer together with simulated pattern (grey). (d) R-factor analysis for the domain orientation characterization, presenting a 50-50 contribution of two mirror orientations. The S 2p XPD pattern for (e) S_A and (b) S_B components, acquired at 270 eV photon energy (KE = 108 eV) and 560 eV photon energy (KE = 397 eV), respectively. The experimental data (color) are presented together with the simulated patterns (grey) for (e) top layer S and (f) bottom layer S, as indicated in the ball model. Ball model color code: red (Mo) and yellow (S).

Mo 3d core level (color), figure 6.8 (c), and compared the experimental data with multiple scattering simulations (grey). As the effect of the substrate can be neglected due to the lack of specific adsorption configuration of MoS_2 layer on Ag(110), the simulations were performed for a free standing MoS_2 layer, with the thermodynamically stable 1H phase structure with lattice parameter of 3.15 Å and Mo-S interlayer distance of 1.62 Å. [28, 29] In order to quantify the relative contribution of different domain orientations in the grown layer, the simulated patterns of the Mo 3d core level (KE $\sim$ 130 eV) for the two anti-parallel orientations Or1 (figure 6.8 (a)) and Or2 (figure 6.8 (b)), were intermixed in different proportions by following equation 3.2 in chapter 3, and compared with the experimental Mo 3d XPD pattern by means of R-factor. [30] In figure 6.8 (d), the plot of the R-factor shows a minimum value, that indicates best agreement between the experimental and simulated XPD patterns, when 50% of the mirror domain orientation is intermixed in the total simulated intensity. This, verifies that the MoS_2 monolayer consists of 180° rotated domains in equal proportion, similar to the MoS_2 grown on Ag(111) in chapter 5. Moreover, the XPD measurements were performed for the S 2p core level as well using different photon energies, in order to satisfy the forward (at high KE) and backward (at low KE) scattering conditions. The XPD measurements (color) belonging to S_A (figure 6.8 (e)) and S_B components (figure 6.8 (f)) show good agreement with the simulations (grey) corresponding to the mixture of the two orientations for the top layer S (R-factor = 0.24) and bottom layer S (R-factor = 0.27), respectively.

Finally, in order to provide a compelling evidence that the MoS_2 layer is aligned with one of the two crystallographic directions of the Ag(110) substrate, as already observed in LEED, we performed XPD measurements of the Ag 3d core level. Figure 6.9 (a) shows the Ag 3d XPD pattern (color) for the clean Ag(111) substrate, i.e. before the growth of MoS_2. The pattern is two-fold symmetric, as expected from the rectangular lattice of (110) stacking of an *fcc* crystal. The simulation (grey) was performed for a 3 layer slab of Ag, at KE = 112 eV, with the atoms in all three layers emitting simultaneously. From the comparison between the simulation and the experimental XPD pattern (R-factor = 0.37), the orientation of the Ag(110) crystal was determined, as shown in figure 6.9 (b). From the orientation of the MoS_2 mirror domains (ball model for figure 6.8 (a) and (b)) and that of the Ag(110) surface shown in figure 6.9 (b), the relative arrangement of the MoS_2 ad-layer on the substrate can be obtained as shown in figure 6.9 (c) and (d). It was assumed that the MoS_2 layer adsorbs with the S atom in the *atop* position. The XPD measurements prove that the MoS_2 layer is aligned parallel to the dense packed rows along the $[1\bar{1}0]$ direction of the Ag(110) substrate, with the two equally probable orientations shown in the figure. These results are in agreement with the LEED findings in figure 6.7.

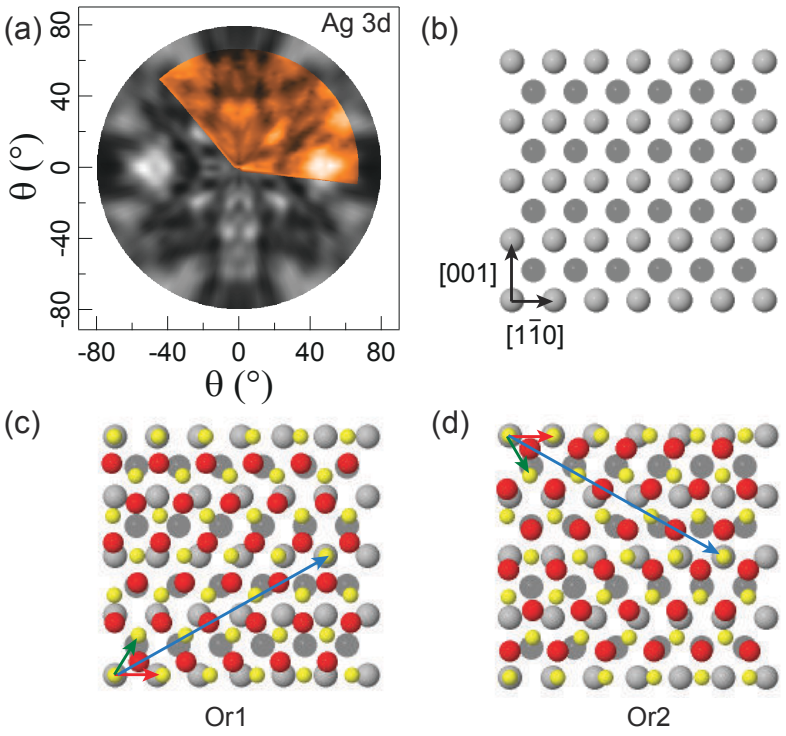

Figure 6.9: (a) XPD pattern of the Ag $3d_{5/2}$ core level (color) together with the EDAC simulation (grey) for the clean Ag(110) sample. (b) Orientation of the Ag sample obtained from the comparison of the XPD experiment with the simulation. Relative orientation of the two mirror domain orientations (c) Or1 and (d) Or2 of SL MoS_2 on Ag(110). In both the cases the MoS_2 lattice vector (red arrow) is aligned with the [1$\bar{1}$0] direction of Ag(110). Ball color code: red (Mo), yellow (S), light grey (Ag surface layer) and dark grey (Ag second layer).

6.5 Conclusions

We have shown that a well ordered MoS_2 layer can be grown on the anisotropic Ag(110) surface. In order to avoid the formation of randomly oriented domains, we developed a new growth procedure that consisted of initial seeding of MoS_2 nano-crystallites by means of TPG, followed by HTG deposition. The high-resolution XPS measurements presented a high intensity of the S 2p component belonging to the strongly interaction bottom S atoms, as well as a high asymmetry in the Mo 3d peak of the MoS_2 layer. ARPES measurements showed additional intensity near the Fermi level, at the **Q** point of surface Brillouin zone of MoS_2. These observations indicate that the MoS_2/Ag(110) is a strongly interacting system and that a semiconductor to metal transition of the MoS_2 layer could take place. The latter interpretation is confirmed by the ARPES measurements, showing the build-up of the intensity close to the Fermi level at the **Q** point of the surface Brillouin zone of MoS_2.

The MoS_2 layer presented a high structural quality, as demonstrated by the STM and LEED measurements, where the presence of a moiré superstructure was also detected. It was found that the superstructure, that appears as alternating streaks in the STM topographic images, is misaligned by 30° with respect to the MoS_2 lattice with a periodicity which is 5 times the MoS_2 lattice parameter. In order to match this periodicity with the Ag(110) substrate periodicity, the MoS_2 lattice vector has to be stretched by ca. 3% along the closed-packed rows of Ag(110). Based on these findings a ball model is also proposed for the MoS_2/Ag(110) interface. The XPD measurements showed the coexistence of mirror domains in equal proportion, and verified that the MoS_2 lattice is, indeed, aligned with the high symmetry $[1\bar{1}0]$ direction of the Ag(110) surface.

References

[1] Casarin, B.; Cian, A.; Feng, Z.; Monachino, E.; Randi, F.; Zamborlini, G.; Zonno, M.; Miniussi, E.; Lacovig, P.; Lizzit, S.; Baraldi, A. The Thinnest Carpet on the Smallest Staircase: The Growth of Graphene on Rh(533). *The Journal of Physical Chemistry C* **2014**, *118*, 6242–6250.

[2] Locatelli, A.; Wang, C.; Africh, C.; Stojić, N.; Menteş, T. O.; Comelli, G.; Binggeli, N. Temperature-Driven Reversible Rippling and Bonding of a Graphene Superlattice. *ACS Nano* **2013**, *7*, 6955–6963.

[3] Wofford, J. M.; Nie, S.; McCarty, K. F.; Bartelt, N. C.; Dubon, O. D. Graphene Islands on Cu Foils: The Interplay between Shape, Orientation, and Defects. *Nano Letters* **2010**, *10*, 4890–4896.

[4] Bianchi, M.; Rienks, E. D. L.; Lizzit, S.; Baraldi, A.; Balog, R.; Hornekær, L.; Hofmann, P. Electron-phonon coupling in potassium-doped graphene: Angle-resolved photoemission spectroscopy. *Physical Review B* **2010**, *81*, 041403, 1–4.

[5] Wong, S. L.; Huang, H.; Wang, Y.; Cao, L.; Qi, D.; Santoso, I.; Chen, W.; Wee, A. T. S. Quasi-Free-Standing Epitaxial Graphene on SiC (0001) by Fluorine Intercalation from a Molecular Source. *ACS Nano* **2011**, *5*, 7662–7668.

[6] Larciprete, R.; Ulstrup, S.; Lacovig, P.; Dalmiglio, M.; Bianchi, M.; Mazzola, F.; Hornekaer, L.; Orlando, F.; Baraldi, A.; Hofmann, P.; Lizzit, S. Oxygen Switching of the Epitaxial Graphene-Metal Interaction. *ACS Nano* **2012**, *6*, 9551–9558.

[7] Lee, J.-K.; Yamazaki, S.; Yun, H.; Park, J.; Kennedy, G. P.; Kim, G.-T.; Pietzsch, O.; Wiesendanger, R.; Lee, S.; Hong, S.; Dettlaff-Weglikowska, U.; Roth, S. Modification of Electrical Properties of Graphene by Substrate-Induced Nanomodulation. *Nano Letters* **2013**, *13*, 3494–3500.

[8] Dendzik, M.; Bruix, A.; Michiardi, M.; Ngankeu, A. S.; Bianchi, M.; Miwa, J. A.; Hammer, B.; Hofmann, P.; Sanders, C. E. Contact-Induced Semiconductor-to-Metal Transition in Single-Layer WS_2. *ArXiv e-prints* **2017**, *1708.02799*.

[9] Vinogradov, N. A.; Zakharov, A. A.; Kocevski, V.; Rusz, J.; Simonov, K. A.; Eriksson, O.; Mikkelsen, A.; Lundgren, E.; Vinogradov, A. S.; Mårtensson, N.; Preobrajenski, A. B. Formation and Structure of Graphene Waves on Fe(110). *Physical Review Letters* **2012**, *109*, 026101, 1–5.

[10] Vinogradov, N. A.; Zakharov, A. A.; Ng, M. L.; Mikkelsen, A.; Lundgren, E.; Mårtensson, N.; Preobrajenski, A. B. One-Dimensional Corrugation of the h-BN Monolayer on Fe(110). *Langmuir* **2012**, *28*, 1775–1781.

[11] Šrut, I.; Trontl, V. M.; Pervan, P.; Kralj, M. Temperature dependence of a graphene growth on a stepped iridium surface. *Carbon* **2013**, *56*, 193–200.

[12] Farmanbar, M.; Brocks, G. First-principles study of van der Waals interactions and lattice mismatch at MoS_2/metal interfaces. *Physical Review B* **2016**, *93*, 085304, 1–12.

[13] Preobrajenski, A. B.; Ng, M. L.; Vinogradov, A. S.; Mårtensson, N. Controlling graphene corrugation on lattice-mismatched substrates. *Physical Review B* **2008**, *78*, 073401,1–4.

[14] Abrami, A.; Barnaba, M.; Battistello, L.; Bianco, A.; Brena, B.; Cautero, G.; Chen, Q. H.; Cocco, D.; Comelli, G.; Contrino, S.; DeBona, F.; Di Fonzo, S.; Fava, C.; Finetti, P.; Furlan, P.; Galimberti, A.; Gambitta, A.; Giuressi, D.; Godnig, R.; Jark, W.; Lizzit, S.; Mazzolini, F.; Melpignano, P.; Olivi, L.; Paolucci, G.; Pugliese, R.; Qian, S. N.; Rosei, R.; Sandrin, G.; Savoia, A.; Sergo, R.; Sostero, G.; Tommasini, R.; Tudor, M.; Vivoda, D.; Wei, F. Q.; Zanini, F. Super ESCA: First beamline operating at ELETTRA. *Review of Scientific Instruments* **1995**, *66*, 1618–1620.

[15] García de Abajo, F. J.; Van Hove, M. A.; Fadley, C. S. Multiple scattering of electrons in solids and molecules: A cluster-model approach. *Physical Review B* **2001**, *63*, 075404, 1–16.

[16] Hoffmann, S. V.; Søndergaard, C.; Schultz, C.; Li, Z.; Hofmann, P. An undulator-based spherical grating monochromator beamline for angle-resolved photoemission spectroscopy. *Nuclear Instruments and Methods in Physics Research A* **2004**, *523*, 441–453.

[17] Enachescu, M.; Schleef, D.; Ogletree, D. F.; Salmeron, M. Integration of point-contact microscopy and atomic-force microscopy: Application to characterization of graphite/Pt(111). *Physical Review B* **1999**, *60*, 16913, 1–7.

[18] Loginova, E.; Nie, S.; Thürmer, K.; Bartelt, N. C.; McCarty, K. F. Defects of graphene on Ir(111): Rotational domains and ridges. *Physical Review B* **2009**, *80*, 085430, 1–8.

[19] Africh, C.; Cepek, C.; Patera, L. L.; Zamborlini, G.; Genoni, P.; Menteş, T. O.; Sala, A.; Locatelli, A.; Comelli, G. Switchable graphene-substrate coupling through formation/dissolution of an intercalated Ni-carbide layer. *Scientific Reports* **2016**, *6*, 19734, 1–8.

[20] Bignardi, L.; Lacovig, P.; Dalmiglio, M. M.; Orlando, F.; Ghafari, A.; Petaccia, L.; Baraldi, A.; Larciprete, R.; Lizzit, S. Key role of rotated domains in oxygen intercalation at graphene on Ni(111). *2D Materials* **2017**, *4*, 025106, 1–11.

[21] Zhang, W.; Zhang, L.; Hui, Z.; Zhang, X.; Qian, Y. Synthesis of nanocrystalline Ag_2S in aqueous solution. *Solid State Ionics* **2000**, *130*, 111 – 114.

[22] Lauritsen, J. V.; Kibsgaard, J.; Helveg, S.; Topsøe, H.; Clausen, B. S.; Lægsgaard, E.; Besenbacher, F. Size-dependent structure of MoS_2 nanocrystals. *Nature Nanotechnology* **2007**, *2*, 53–58.

[23] Orlando, F.; Lacovig, P.; Omiciuolo, L.; Apostol, N. G.; Larciprete, R.; Baraldi, A.; Lizzit, S. Epitaxial Growth of a Single-Domain Hexagonal Boron Nitride Monolayer. *ACS Nano* **2014**, *8*, 12063–12070.

[24] Yu, Q.; Jauregui, L. A.;Wu, W.; Colby, R.; Tian, J.; Su, Z.; Cao, H.; Liu, Z.; Pandey, D.; Wei, D.; Chung, T. F.; Peng, P.; Guisinger, N. P.; Stach, E. A.; Bao, J.; Pei, S.-S.; Chen,Y. P. Control and characterization of individual grains and grain boundaries in graphene grown by chemical vapour deposition. *Nature Materials* **2011**, *10*, 443–449.

[25] Lee, J.-K.; Lee, S.; Kim, Y.-I.; Kim, J.-G.; Min, B.-K.; Lee, K.-I.; Park, Y.; John, P. The seeded growth of graphene. *Scientific Reports* **2014**, *4*, 5682, 1–5.

[26] Grønborg, S. S.; Ulstrup, S.; Bianchi, M.; Dendzik, M.; Sanders, C. E.; Lauritsen, J. V.; Hofmann, P.; Miwa, J. A. Synthesis of Epitaxial Single-Layer MoS_2 on Au(111). *Langmuir* **2015**, *31*, 9700–9706.

[27] Miwa, J. A.; Ulstrup, S.; Sørensen, S. G.; Dendzik, M.; Čabo, A. G.; Bianchi, M.; Lauritsen, J. V.; Hofmann, P. Electronic Structure of Epitaxial Single-Layer MoS_2. *Physical Review Letters* **2015**, *114*, 046802, 1–5.

[28] Winer, W. Molybdenum disulfide as a lubricant: A review of the fundamental knowledge. *Wear* **1967**, *10*, 422 – 452.

[29] Holinski, R.; Gänsheimer, J. A study of the lubricating mechanism of molybdenum disulfide. *Wear* **1972**, *19*, 329 – 342.

[30] Woodruff, D. Adsorbate structure determination using photoelectron diffraction: Methods and applications. *Surface Science Reports* **2007**, *62*, 1–38.

CHAPTER 7

Si adsorption on Ir(111): Silicene synthesis or silicide formation?

Another material of the 2D family is Silicene, the silicon based analogue of graphene, consisting of a single atomic layer of Si atoms arranged in honeycomb like structure. Although already mentioned in a theoretically study by Takeda and Shiraishi [1] in 1994, silicene remained largely unexplored until re-investigated by Guzmán-Verri *et al.* in 2007, [2] also acknowledged for the nomenclature. The interest in silicene can be seen with respect to its similarities with graphene and potential applications in next generation devices. Although, silicene is shown to have a buckled structure due to weak π bonding, it presents several exotic properties such as linear band dispersion near Dirac points, [3] phase transition from topological to band insulator under strong external electric field [4] and excitonic effects in optical absorption. [5]

In addition to that, silicene has several advantages over graphene such as, a stronger spin-orbit coupling that may lead to the observation of valley polarization [6] and quantum spin Hall effect at experimentally accessible temperatures, [7] and the possibility of direct inclusion in the current Si based technology. However, unlike in the case of graphene, mechanical exfoliation can not be used to isolate a free standing silicene layer, as silicon does not have a layered phase similar to graphite. Therefore, a more sophisticate approach, consisting of epitaxial growth of silicon on metal substrates, needs to be adopted in order to achieve the desired results.

In agreement with DFT calculations, Si nano-ribbons grown on Ag(110), with hexagonal unit cell, have recently demonstrated the characteristic linear band dispersion as an evidence of sp^2 hybridized graphene-like structural arrangement. [8, 9] The subsequent demonstration of silicene growth on Ag(111)

in, [10] has fueled the attraction towards silicene growth on other metal substrates. However, Si adsorption on various transition metal substrates have reportedly resulted in the formation of binary alloys. [11] The process of Si adsorption on metal substrates is indeed complex, governed by several parameters such as temperature, Si surface density, and metal cohesive energy. Studies have shown that the interactions between Si and metal atoms results in various site-exchange processes following the adsorption of Si, leading to the incorporation of Si atoms in the surface [12–15]; formation of silicide islands [13] and the segregation of Si below the metal surface. [16]

Apart from the fact that a weakly interacting Si-metal system is crucial for maintaining the free standing-like properties of the epitaxially grown silicene on a metal surface, the growth of silicene on strongly interacting Ir(111) has been reported in [17]. The DFT calculations have shown that the presence of strong interactions leads to deformation of the layer and hybridization of its electronic states. [17, 18] Moreover, it has been well established in literature that the Si-Ir system has a strong affinity toward silicide formation. [19, 20] Ir layers deposited on Si that results in alloying as the Si-Ir bond formation is energetically more favorable and can proceed at the cost of Si-Si bond breaking. [19–21] In the presence of such contradictory evidences, a more detailed analysis of the Si/Ir interface at different adsorption conditions and post-deposition treatments, is essential to identify the factors governing the interplay between silicene growth and silicide formation on Ir(111).

In this chapter, we provide a comprehensive overview of the Si/Ir(111) interface, complementary to the scanning probe approach that has been widely used to study such systems. Adsorption of Si on Ir(111), starting from the clean metal surface up to the coverage exceeding one monolayer, was followed in real time by means of fast-XPS. The evolution of the interface, following the deposition of Si at different temperatures, was monitored by LEED and characterized with the help of high-resolution XPS measurements. We studied the transition of a well ordered superstructure, that included the contribution of Si atoms incorporated into the top Ir layer, to a disordered structure and the formation of bilayers with the increasing Si coverage. The energy barrier encountered by the Si ad-atoms to penetrate into the Ir surface was calculated with density functional theory (DFT).

In addition to that, the DFT calculated energetics of different adsorption configurations of Si ad-atoms also supported the experimentally observed spectral contributions at various Si coverages. In the following, we will discuss separately the adsorption of Si at coverage below and above 0.5 ML. Moreover, the effect of temperature on the adsorption and interface structuring was also explored by comparing the deposition of Si at high temperature (670 K), with that performed at lower temperature (300 K and 520 K) followed by annealing induced ordering of the interface.

7.1 Experiments and methods

The study of Si adsorption on Ir(111) was performed by the experiments carried out at SuperESCA beamline of Elettra. [22] The atomically clean Ir(111) surface was prepared by repeated cycles of Ar^+ sputtering at 2 keV and oxygen treatments at high temperatures, followed by a flash annealing to 1470 K in order to get rid of any residual oxygen from the surface. The sample cleanliness was checked with XPS and no contaminants were detected. The Ir $4f_{7/2}$ core level spectra showed the SCLS of -550 meV, typical of a clean Ir(111) surface. [23] Surface order was verified by means of LEED that showed sharp (1×1) diffraction spots corresponding to the (111) truncation of the fcc crystal. An electron beam evaporator, placed 60 mm in front of the Ir sample and on the side of the analyzer, was used to deposit atomic silicon. The Si deposition rate was calibrated by means of a quartz microbalance and amounted to ca. 0.022 ML/minute, where a monolayer (ML) is the surface atomic density of Ir(111) i.e. 1.57×10^{15} atoms/cm^2. The Si deposition was followed in real time by means of fast-XPS of the Ir $4f_{7/2}$ and the Si 2p core levels at 136 eV and 150 eV photon energy, respectively. The photoelectrons were collected at normal emission for the high-resolution XPS and at the emission angle of 40° for the fast-XPS measurements. The energy resolution was better than 50 meV and all the measured spectra were corrected for the Fermi level of Ir sample. The core level spectra were analyzed by fitting them with Doniach-Šunjić function convoluted with Gaussian and a linear background.

The Density Functional Theory (DFT) calculations for the energetic and dynamics of the Si atoms on Ir(111) surface, were performed by the group of Dr. Mauro Satta at CNR-ISMN, Roma, using the QuantumESPRESSO Simulation Package [24] within the Kohn-Sham implementation, with the Khon-Sham valence states expanded in a plane-wave basis set with a cutoff of 340 eV for the kinetic energy. The PBE (Perdew Burke Ernzerhof) exchange-correlation functional ultrasoft pseudopotentials was used and the self consistency of electron density was reached for a mixing factor for self-consistency of 0.7 and the energy threshold set to 10^{-5} eV. Integrations in the reciprocal space were performed using a MonkhorstPack automatically generated uniform grid of 16 k-points. The calculations were performed using the rhombohedral primitive unit cell containing 35 atoms of Ir, and one or more Si atoms, with the Ir atoms of the bottom layers fixed at their bulk values. A cell dimension corresponding to a=b=8.15 Å and a height of 25 Å was used to minimize the vertical interactions among replicated cells. Calculations for the energy barriers were performed by varying the vertical displacement of Si ad-atom on Ir surface, while the core level shifts were determined from the difference in total energy, calculated using the pseudopotentials for Ir and Si by including a hole in the core level of the atom participating in photoemission.

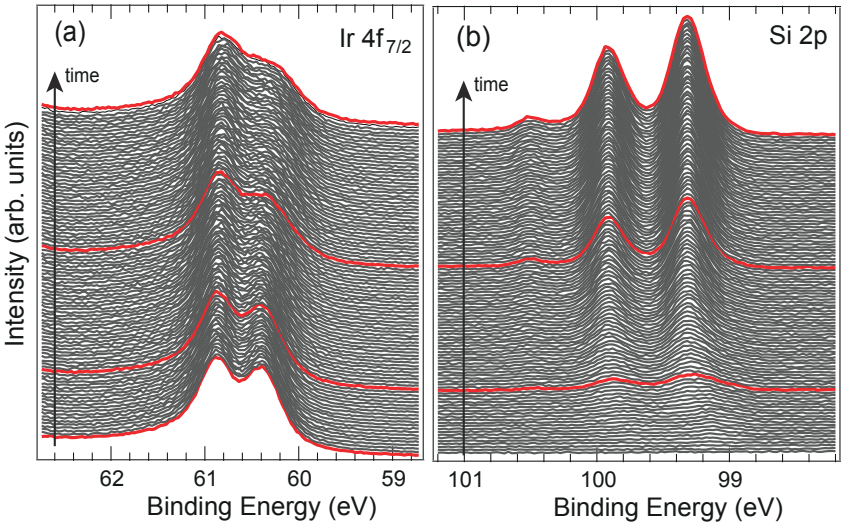

Figure 7.1: Sequences of (a) Ir $4f_{7/2}$ and (b) Si 2p spectra acquired during Si adsorption up to 0.5 ML at 670 K. The red curves mark the coverages corresponding to the high resolution spectra shown in figure 7.2 (a) and (b).

7.2 Adsorption of Si on Ir(111) up to 0.5 ML

In the first part of the experiments, Si was deposited on the clean Ir(111) surface at 670 K, up to the final coverage of 0.5 ML. The sequence of spectra acquired during the deposition are shown in figure 7.1 (a) and (b), respectively. Clearly, the appearance of intensity in the Si 2p spectra, was closely followed by spectral changes in the Ir $4f_{7/2}$ core level that continued up to the end of the deposition. The high-resolution XPS spectra of Ir $4f_{7/2}$ and Si 2p core levels were obtained at different stages of growth, marked with red curves in the fast-XPS spectra shown in figure 7.1, corresponding to the coverage of 0.1, 0.3 and 0.5 ML.

The Ir $4f_{7/2}$ core level spectra, shown in figure 7.2 (a), present two components for the clean surface (before the deposition of Si) that originate from the bulk (B at 60.35 eV BE) and the surface atoms (S at 60.90 eV) of the Ir crystal. The measured SCLS of -550 meV for the two components is in excellent agreement with the value reported in literature. [23] With the increase of the Si coverage, new components appear at 60.17 eV (Ir_A) and 60.69 eV (Ir_B) BE, that continue to grow at the expense of Ir_S peak throughout the deposition. The increase in Si coverage is complemented by the appearance of various components in the Si 2p core level spectra, presenting the spin-orbit splitting of 0.6 eV, as shown in figure 7.2 (b). For simplicity the BE of the Si 2p doublet components is marked with the BE of the $2p_{3/2}$ component and the

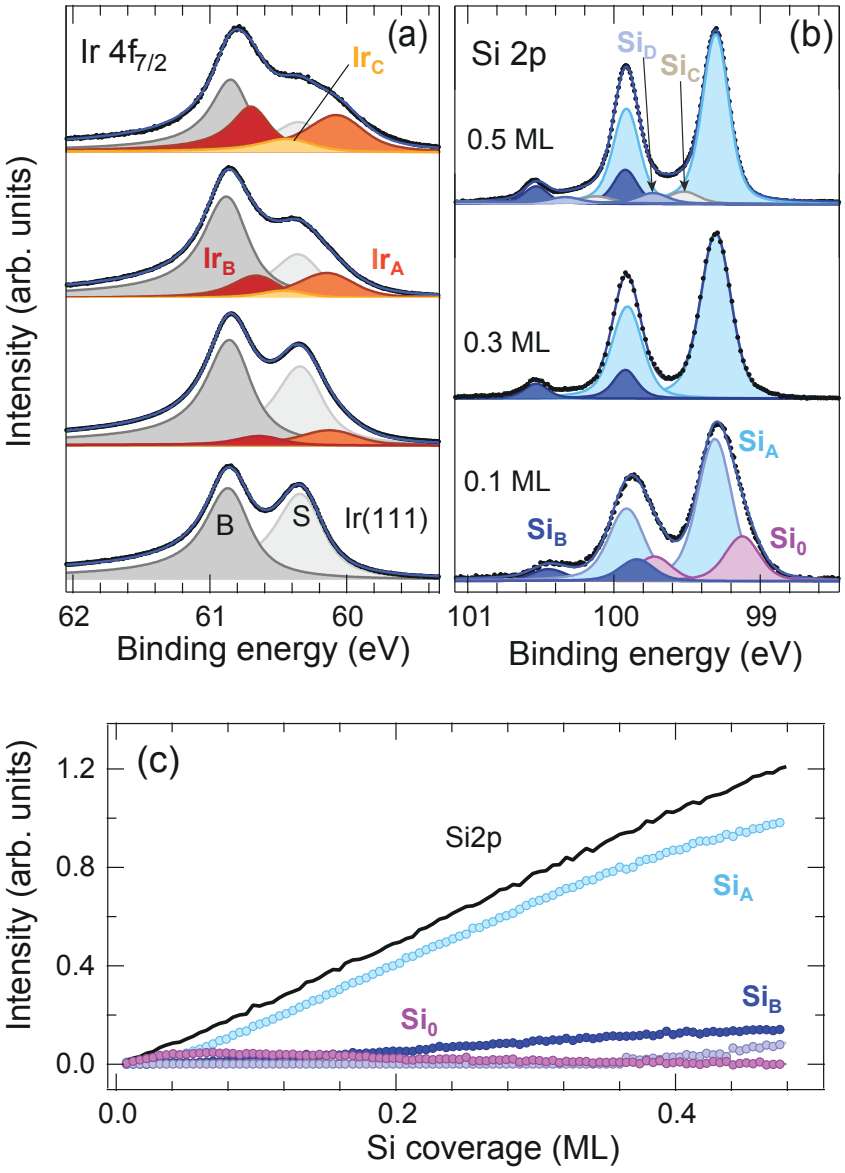

Figure 7.2: (a) Ir $4f_{7/2}$ and (b) Si 2p high resolution XPS spectra measured at selected Si coverages after adsorption of Si on Ir(111) at 670 K. The experimental curves (dots) are shown with the best fit curves (solid line) and the spectral components. (c) Intensity profile of the different components in the Si 2p core level spectra as a function of Si coverage, obtained from the fitting of the sequence of fast-XPS spectra in figure 7.1 (b). The solid black line shows the intensity of Si 2p spectrum as a whole.

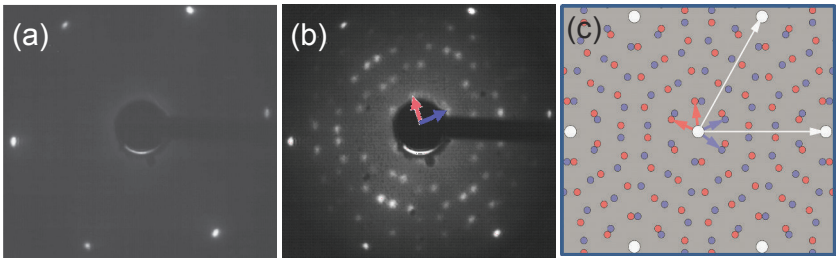

Figure 7.3: LEED patterns acquired at 58 eV (a) on the clean Ir(111) surface and (b) after the deposition of 0.4 ML of Si. In (b) the reciprocal space vectors corresponding to the $\sqrt{19} \times \sqrt{19}$ R23.4° superstructure are indicated. (c) Map of the diffraction spots in the reciprocal space for the Ir lattice (white) and the two $\sqrt{19} \times \sqrt{19}$ R23.4° domains (red and blue)

same follows in the rest of this chapter. The deconvolution of the spectrum at 0.1 ML (bottom curve) shows three spin-orbit doublet peaks at 99.17 eV (Si_O), 99.30 eV (Si_A) and 99.92 eV (Si_B). At higher coverage, i.e. 0.3 and 0.5 ML, only Si_A and Si_B components are still present, and the Si_O component disappears.

In order to understand the evolution of these components, the sequence of fast-XPS spectra (figure 7.1 (b)) were fitted by using the lineshape parameters obtained from the analysis of the high-resolution XPS (T $\sim$ 300 K), while allowing for the Gaussian broadening due to the high temperature of the fast-XPS measurements (T = 670 K). The resulting intensities (markers) of the different components appearing in the Si 2p core level are shown in figure 7.2 (c), as a function of the Si coverage. The Si_O peak is clearly the dominant peak in the initial stage of the growth, however, the intensity of this component quickly declines just after reaching a maximum at coverage $\sim$ 0.08 ML. On the other hand, the intensities of Si_A and Si_B continue to grow till the end up to the total Si coverage of 0.5 ML, while maintaining almost a constant ratio among them. Although the total intensity of the Si 2p core level (solid black line) shows a continuous growth, Si_A and Si_B deviate from the linear behavior towards the end (coverage $>$ 0.42 ML), due to the appearance of new components in the Si 2p core level. The high-resolution spectrum (figure 7.2 (b)) at 0.5 ML, shows the presence of two new peaks (Si_C and Si_D) in the Si 2p core level, complemented by the appearance of Ir_C component of the Ir $4f_{7/2}$ spectrum (top curve of figure 7.2 (a)). The nature of these components will be discussed later in this chapter. In this regards, it has to be noted that the spectral features corresponding to the initial stage of Si adsorption on Ir(111) at 670 K, are characterized by the appearance of Si_A and Si_B components of the Si 2p core level, and the Ir_A and Ir_B components of the Ir $4f_{7/2}$ core level spectra.

Structural information about the Si-Ir interface can be obtained from

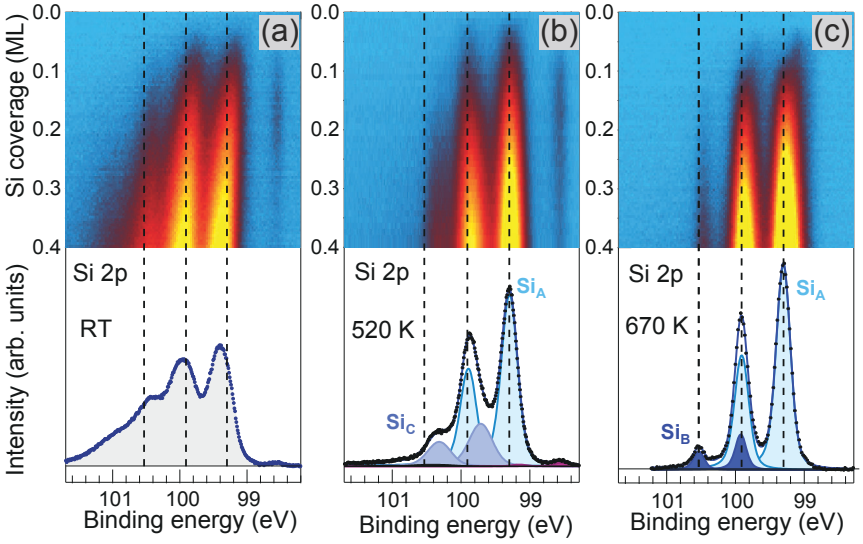

Figure 7.4: top: 2D intensity plots of the fast-XPS spectra measured during the adsorption of Si (maximum coverage 0.4 ML) on Ir(111) at (a) room temperature (RT), (b) 520 K and (c) 670 K; bottom: high resolution Si 2p spectra measured at room temperature after the Si adsorption. For (b) and (c) the best-fit curves and the spectral components are also shown. The dashed black lines mark the BE of the Si_A and Si_B doublets.

the LEED patterns shown in figure 7.3. For the clean Ir(111), the LEED pattern acquired at 58 eV shows three-fold symmetric 1×1 diffractions spots (figure 7.3 (a)). After the adsorption of 0.4 ML of Si at 670 K, the LEED pattern in figure 7.3 (b) presents new diffraction spots corresponding to the formation of $\sqrt{19} \times \sqrt{19}$ R23.4° superstructure with two equivalent domains, whose reciprocal lattice vectors are marked with colored arrows. A similar $\sqrt{19} \times \sqrt{19}$ R23.4° superstructure with rotated domains has been observed in literature for intercalated Si below graphene on Ir(111), [24] and Si adsorption on Pt(111) leading to the formation of Si_3Pt surface alloy. [16] The simulated LEED pattern (figure 7.3 (c)) for the two domains also corresponds well with the experimentally obtained pattern in figure 7.3 (b), thus, confirming the assignment of the diffraction spots to the ordered Si structure on Ir(111).

By following the deposition of Si on Ir(111) at temperature lower than for the previous growth (T < 670 K), we studied the effect of substrate temperature on the adsorption configuration of Si. Figure 7.4 (a), (b) and (c) show the fast-XPS intensity plots of Si 2p core level acquired while depositing Si upto a coverage of 0.4 ML at room temperature (T ∼ 300 K), 520 K and 670 K, respectively. The high-resolution XPS of Si 2p core level acquired at the completion of the

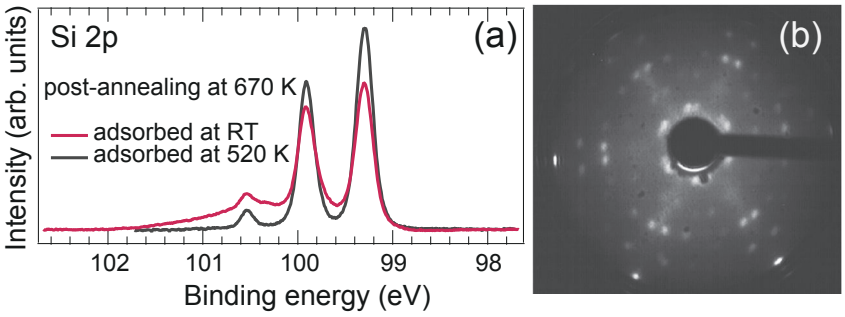

Figure 7.5: (a) Si 2p spectra measured on the Si layers adsorbed at RT and 520 K and annealed at 670 K. In both cases the similar integrated intensity of the Si 2p spectra measured before and after annealing excludes the desorption of Si from the surface. (b) $\sqrt{19} \times \sqrt{19}$ R23.4° LEED pattern measured on the Si layer adsorbed at RT and annealed at 670 K.

respective growth are shown in the bottom panel, together with the fitting and the deconvolution into different spectral components for the sample grown at 520 K and 670 K.

For the deposition performed at room temperature (RT), in figure 7.4 (a), Si adsorption proceeds with the rise in intensity in the BE of Si_A (99.30 eV; marked with the dashed line). The increasing coverage results in the overall boarding of the spectrum towards higher BE. Similarly, the deposition performed at 520 K (figure 7.4 (b)) results in the appearance of intensity at the BE of Si_A that continues to grow with the increasing coverage, together with the contribution from another component at higher BE. The peak position of the new doublet Si_C (99.75 eV) was determined from the fitting of the high-resolution spectra measured at the end of the deposition. Interestingly, the Si 2p spectra shows no contribution from the Si_B component that is observed for the deposition performed at 670 K (figure 7.4 (c)). Also, the LEED pattern for the RT and the deposition at 520 K (not shown) shows 1×1 spots of Ir(111) with no indication of a superstructure formation. Moreover, the low temperature depositions in figure 7.4 (a) and (b) evidence the presence of a weak component at ∼ 98.6 eV BE, which is not observed for the growth performed at 670 K (figure 7.4 (c)). This suggests the presence of Si atoms adsorbed at defect sites or step edges, that is avoided by the increased mobility while dosing at high temperature.

The samples prepared by dosing Si at RT and 520 K were annealed up to 670 K, in order to induce layer ordering. As a result, the Si 2p lineshape changes as shown in figure 7.5 (a), with an intense peak and a weaker component. The spectral components that appear after the post-annealing are the same Si_A and Si_B components observed for the growth performed at 670 K, shown in figure 7.2 (a) and figure 7.4 (c). These spectral changes are accompanied by

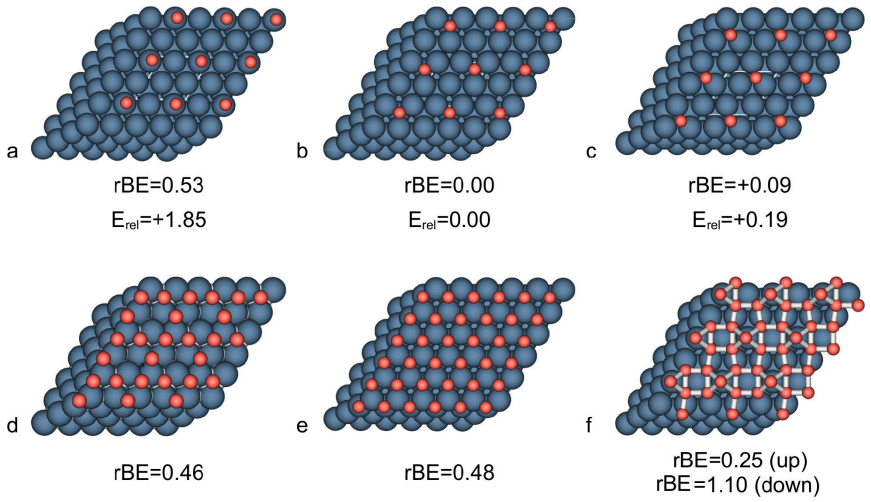

Figure 7.6: Si ad-atoms on the Ir(111) surface at the (a) *atop*, (b) *hcp* and (c) *fcc* hollow sites for a coverage of 0.25 ML; at the *hcp* sites for (d) 0.75 ML and (e) 1 ML of Si, and (f) at the second layer on top of (e). E_{rel} and rBE are the difference in adsorption energy and the relative shifts of the Si 2p BE, respectively, with respect to the values calculated for (b), which is the most stable adsorption site.

the appearance of a LEED pattern, indicating the formation of the $\sqrt{19} \times \sqrt{19}$ R23.4° superstructure (figure 7.5 (b)), similar to the one observed for the high temperature (T = 670 K) deposition (figure 7.3 (b)). However, the post-annealing of the Si deposited at RT did not result in complete ordering at the Si-Ir interface, as indicated by the residual background in the Si 2p spectrum (figure 7.5 (a)) and the broad diffraction spots with higher background in the LEED pattern (figure 7.5 (b)).

The aforementioned results indicate that irrespective of the substrate temperature, the Si atoms are predominantly adsorbed at the surface site that correspond with Si_A component in the Si 2p spectra. However, the layer ordering, that coincides with the formation of a $\sqrt{19} \times \sqrt{19}$ R23.4° superstructure in the LEED pattern, is obtained only after the annealing at 670 K, when the Si_B component develops.

DFT calculations were performed in order to identify the origin of the different components observed in the Si 2p core level. The adsorption energy E_{ads} and the BE of the Si 2p components were calculated for different adsorption configurations of Si ad-atoms on Ir(111) surface, as shown in figure 7.6. The most favorable adsorption site for an isolated Si atom is the *hcp* hollow site with the calculated E_{ads} of 7.11 eV (figure 7.6 (b)), in agreement with [25]. Hereafter, for other adsorption arrangements of Si on Ir(111), the

difference in adsorption energy E_{rel} and the relative BE shift rBE will be reported with respect to the values obtained for Si adsorbed at the *hcp* site of figure 7.6 (b). The adsorption of Si at the fcc site is slightly less stable with $E_{rel} = 0.2$ eV and presents a negligible BE shift of $rBE = 0.09$ eV, whereas the adsorption at the *atop* site is less favorable with $E_{rel} = 1.85$ eV and $rBE = 0.56$ eV. The calculations did not show any convergence for the adsorption at the bridge site. The *hcp* hollow site is the most favorable also for higher coverage of Si, although resulting in BE shifts $rBE = 0.46$ eV (at 0.75 ML) and $rBE = 0.48$ eV (at 1 ML), owing to the increased Si-Si interactions due to the reduction in the distance between neighboring Si ad-atoms. The calculations for the growth of a second layer on top of a complete monolayer of *hcp* adsorbed Si, results in the rBE of 0.25 and 1.1 eV for the top and bottom layers, respectively.

From the results of the DFT calculations we can assign the Si_A component of the Si 2p spectra, that dominates during Si adsorption at high temperature up to 0.5 ML, to the Si atoms adsorbed at the *hcp* sites, being energetically most favorable. However, due to the relatively low adsorption energy difference and a minor BE shift, the possibility of Si ad-atoms at the fcc sites can not be ruled out. Regarding the assignment of Si_B component of the Si 2p spectra, several aspects needs to be considered. First of all, the theoretical calculations rule out the possibility of adsorption at the bridge sites. The possibility of Si adsorbed at the *atop* site contributing to the Si_B component is supported by the calculated $rBE = 0.56$ eV and the experimentally determined BE separation of 0.62 eV from Si_A. However, the high E_{rel} suggests that the Si atoms adsorbed at *atop* site would diffuse to the *hcp* site at 670 K. [25] Also, the possibility of the initial formation of silicene where some of the Si atoms may occupy *atop* sites can also be ignored based on the findings of Wei *et al.* [26], showing that the Si hexagons at low coverage tend to form distorted and irregular rings that are incompatible with the LEED pattern indicating the presence of the $\sqrt{19} \times \sqrt{19}$ R23.4° superstructure.

Another possibility can be that the Si_B component is a contribution from the Si atoms that penetrates in the surface rather than from those on top of Ir(111). This issue of Si atoms occupying the sites in the top layer or even segregating below the surface, has been well addressed in literature for different Si-metal interfaces. [12, 14–16, 27] In order to verify this hypothesis, calculations were performed of the energy barrier, along the Minimum Energy Path (MEP), involved in the transition from Si adsorbed in *hcp* site to the inclusion of the Si in the Ir surface by a site-exchange procedure resulting in the ejection of Ir atom on the surface. In figure 7.7, the MEP shows a minimum for the Si atom placed 0.3 Å below the surface of Ir(111). However, for this site exchange process to take place, the energy barrier of ~ 3 eV must be overcome as shown by the MEP curve in figure 7.7. In this regard, we must consider that the energy released upon Si adsorption (7.11 eV) can be consumed by the three competing processes such as diffusion of the Si ad-atom on the surface, thermal heating of the bulk or most importantly it can be used by the Si atom to react

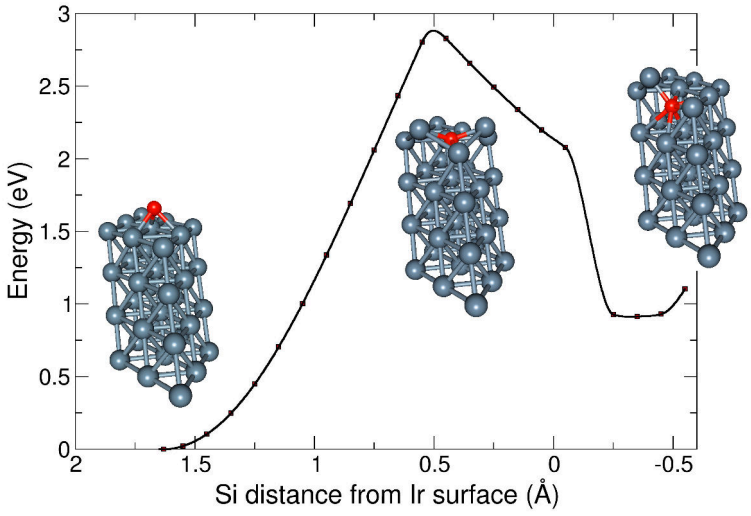

Figure 7.7: (a) Minimum energy path (MEP) calculated for the penetration of the Si atom (red) adsorbed at the *hcp* site into the Ir surface.

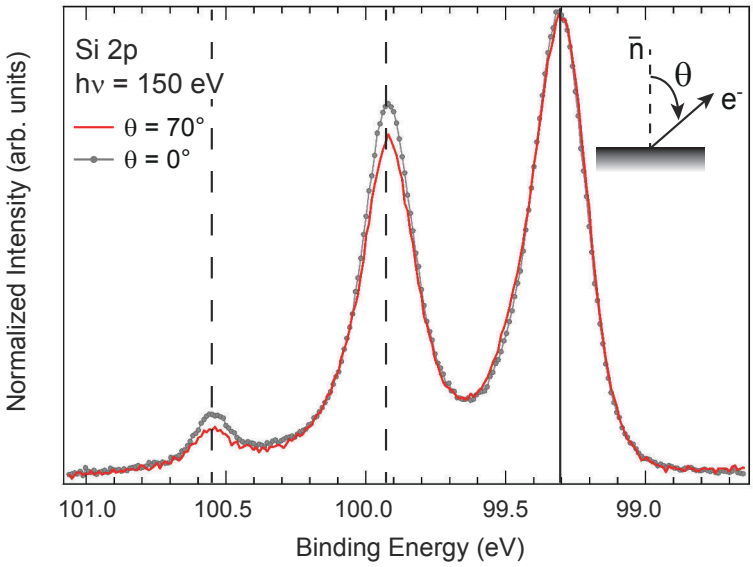

Figure 7.8: Si 2p spectra acquired 0.4 ML coverage, presenting the variations in the relative intensities of Si_B and Si_A as a function of the polar emission angles θ. The spectral intensities are normalized so that the peak maxima coincide. The BE of Si_A and Si_B are indicated by the solid and dashed lines, respectively.

with the Ir atoms present in the adsorption place. [12] For the case modeled in figure 7.7, the system has at disposal the energy released during the adsorption of Si at the *hcp* site $E_{ads} = 7.11$ eV, which is much larger than the height of the energy barrier in the MEP curve. Therefore, it is possible for a Si ad-atom to penetrate into the Ir(111) surface.

In order to further elucidate on the assignment of the Si_A and Si_B components, we measured the Si 2p core level at normal and grazing emission at a fixed photon energy as shown in figure 7.8, in order to tune the probing depth on the sample, owing to the finite IMFP of the photoelectrons at the given kinetic energy $KE \sim 50$ eV, corresponding to the photon energy $h\nu = 150$ eV used for the measurements. Clearly, the ratio Si_B/Si_A shows an increase while going from the surface sensitive (grazing emission, $\theta = 70°$) to bulk sensitive (normal emission, $\theta = 0°$) configuration. This suggests that the Si atoms contributing to the Si_B component in the Si 2p spectra lies below the atoms that contribute to the Si_A component (i.e. adsorbed at the *hcp* hollow site). Based on this assignment of the core level components of the Si 2p spectra and the trend observed while annealing the 0.4 ML of Si deposited at low temperature up to 670 K (figure 7.4 and 7.5), it is worth mentioning that the Si penetration below the Ir surface, accompanied by the observation of Si_B

component in the Si 2p spectrum, remains largely disfavored up to 520 K. On the other hand, while dosing or annealing at 670 K, significant amount of Si penetrates into the top Ir layer.

By comparing the DFT calculations with the spectroscopy data, we can conclude that for the early stage of Si adsorption (coverage $\sim$ 0.4 ML) most of the Si ad-atoms occupy the *hcp* hollow site while a small fraction (15-20%) penetrates into the Ir surface layer, although, there are no specific evidences to prove whether Si penetrates not only into the first Ir layer but also the deeper ones. The simultaneous appearance of the Si_B component and the $\sqrt{19} \times \sqrt{19}$ R23.4° LEED pattern, after annealing at 670 K of the Si layer adsorbed at lower temperature, suggests that also the Si atoms corresponding to Si_B component generate the superstructure. Concerning the Ir 4f spectra, the components appearing after Si deposition can be assigned to the corresponding peaks in Si 2p spectra. Therefore, Ir_A can be attributed to the Ir atoms bounded to the Si ad-atoms at the *hcp* site (Si_A), while the first layer Ir atoms that feel the presence of Si atoms included in the surface layer, gives rise to the Ir_B component. It is interesting to note that the apparently smaller fraction of Si atoms penetrating into the surface with respect to Si/Cu(111) and Si/Ni(111) where Cu_2Si [27] and Ni_2Si [13] alloys form, can be explained as due to the higher cohesive energy of Ir (6.94 eV/atom) than Cu (3.49 eV/atom) and Ni (4.44 eV/atom). [28]

7.3 Effect of high Si coverage on Si-Ir interface

In order to further investigate the silicene formation on Ir(111) we studied the Si-Ir interface for coverages higher than 0.5 ML. Similar to the procedure followed in the last section 7.2, Si was deposited on Ir(111) surface kept at 670 K up to the final coverage of 1.5 ML. The deposition was followed by means of fast-XPS that allowed real time monitoring of the Si 2p spectra, as shown in figure 7.9. Up to 0.5 ML coverage of Si, the spectral features are the same of those reported in the previous section. With the increase of the Si coverage above 0.5 ML, the Si 2p spectrum shifts towards higher BE with the appearance of new components, as indicated by the broad intensity distribution in the later stage of Si deposition. Figure 7.10 (a) and (b) show the high-resolution Ir $4f_{7/2}$ and Si 2p spectra acquired at the Si coverage indicated also in figure 7.9, together with the best fit curves and the deconvoluted components, while table 7.1 shows the BE positions of the different components. In order to study the evolution of the different Si 2p components, the fast-XPS sequence of spectra (figure 7.9) was fitted and the resulting intensities (markers) are shown as a function of Si coverage in figure 7.11, together with the overall intensity of the Si 2p spectrum (solid black line).

The increase of the Si coverage gives rise to the appearance of new components and to the decrease of the peaks that are present in the Si 2p spectra at low Si coverage. In particular above 0.5 ML, the intensity of Si_A

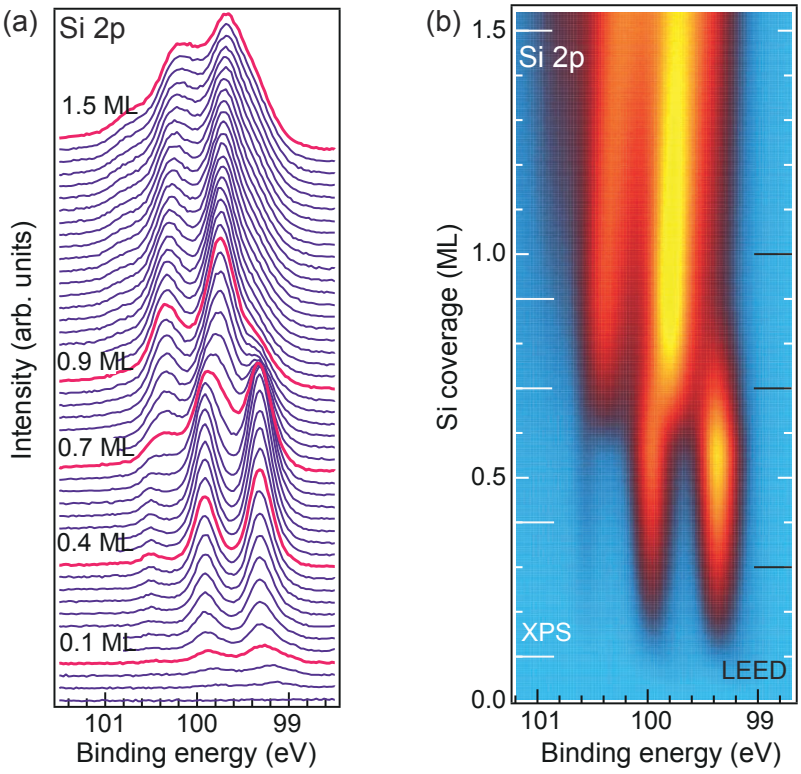

Figure 7.9: (a) Fast-XPS sequence of spectra and (b) 2D intensity plots of Si 2p core level, measured during the adsorption of Si (maximum coverage 1.5 ML) on Ir(111) at 670 K. In (b) the marked white lines on the left axis, indicate the coverage at which high-resolution XPS (in figure 7.10) were acquired, while the black lines on the right axis, correspond with the LEED measurements presented in figure 7.13.

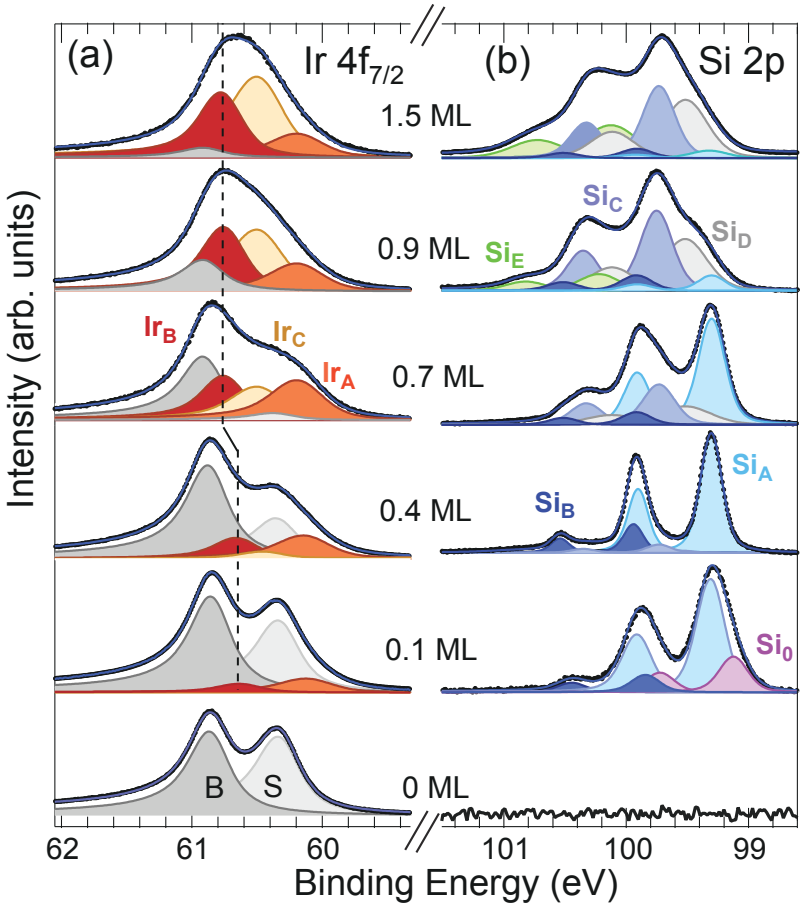

Figure 7.10: (a) Ir $4f_{7/2}$ and (b) Si 2p high resolution XPS spectra measured at the indicated Si coverages, corresponding to the white lines of figure 7.9 (b).

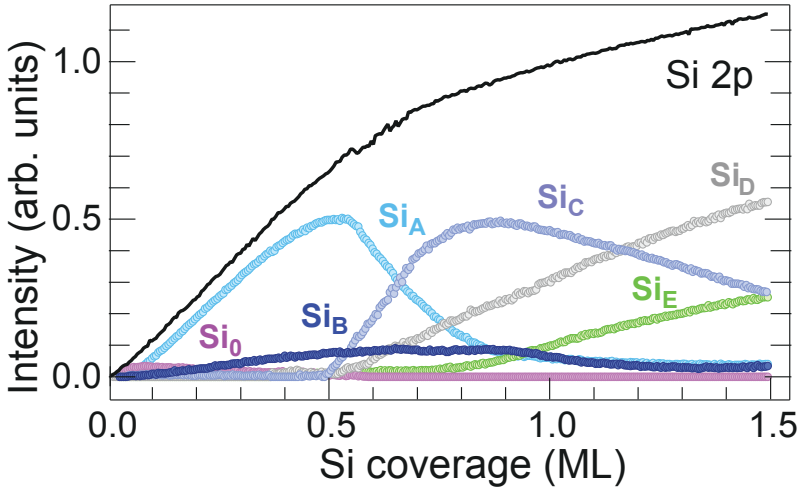

Figure 7.11: Intensity profile of the different components in the Si 2p core level spectra as a function of Si coverage, obtained from the fitting of the sequence of fast-XPS spectra in figure 7.9. The solid black line shows the intensity of Si 2p spectrum as a whole.

starts decreasing with a simultaneous appearance of Si_C (at 99.75 eV BE), that continues to grow linearly at the expenses of Si_A. The BE difference between Si_C and Si_A (0.45 eV) is in agreement with the calculated rBE ($\sim$ 0.46 eV) for the Si ad-atoms in *hcp* hollow site at coverage $\sim$ 0.75 and 1 ML (figure 7.6). As the Si_A component was assigned to the isolated Si ad-atoms in *hcp* site, it is reasonable to assume that the transfer of intensity from Si_A to Si_C is due to the increased concentration of Si ad-atoms in *hcp* sites, and the increased Si-Si interaction results in the observed core level shift. Moreover, the growth of Si_C is closely followed by the appearance of a new component Ir_C in the Ir $4f_{7/2}$ spectra at 60.49 eV BE. This suggests that the Ir surface atoms feel the presence of the increased surface density of Si ad-atoms. Therefore, Ir_A can be assigned to the Ir surface atoms bonded to more than one Si ad-atom.

Increasing the Si coverage above 0.7 ML, the intensity of Si_C starts to decline and two new components Si_D and Si_E appear in the Si 2p spectrum. Both Si_D (at 99.49 eV) and Si_E (at 100.21 eV) continue to grow, while maintaining a near constant ratio, throughout the Si deposition up to 1.5 ML. However, the Ir 4f spectrum does not present any extra component related to the new components appearing in Si 2p spectrum. Therefore, these new components should be related to Si adsorption at the second layer. Moreover, Si_D and Si_E are shifted with respect to Si_A by 0.19 eV and 1.19 eV, respectively. This corresponds to the calculated rBE for the atoms in the top (0.25 eV) and bottom layer (1.1 eV) of the Si bilayer on Ir(111), as shown in figure 7.6. The growth of the second

Ir $4f_{7/2}$	BE(eV)	Si 2p	BE(eV)	BE_{shift}
B	60.35	Si_O	99.17	-0.13
S	60.90	Si_A	99.30	0
Ir_A	60.17	Si_B	99.92	+0.62
Ir_B	60.69	Si_C	99.75	+0.45
Ir_C	60.49	Si_D	99.49	+0.19
		Si_E	100.21	+1.19

Table 7.1: Binding energy of the different components observed in the Ir $4f_{7/2}$ and Si 2p spectra, while dosing 1.5 ML of Si on Ir(111) at 670 K, as shown in figure 7.10. For each Si $2p_{3/2}$ component BE_{shift} indicates the shift with respect to the BE of Si_A.

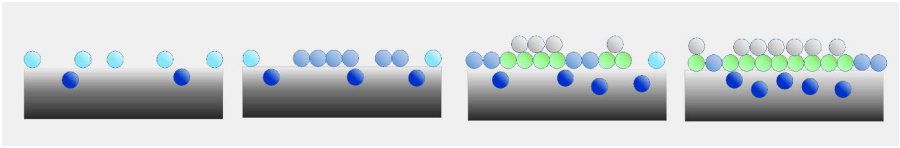

Figure 7.12: Sketch indicating the evolution of Si/Ir(111) interface. The colors of Si atoms corresponds to the spectral components of Si 2p spectra in figure 7.10 (b).

layer changes the coordination of the layer underneath, which is reflected by the presence of a core level shifted component and the transfer of intensity from Si_C to Si_E. Therefore, based on the behavior of the relative intensities and the agreement between the theoretical and the experimentally determined BEy shifts, Si_D and Si_E can be assigned to the Si atoms in the top and the bottom layer of Si bilayer that forms at high Si coverage.

The Ir $4f_{7/2}$ spectrum also shows the effects of the increasing Si coverage. As already mentioned earlier, Ir_C that appears with Si_C, belongs to the Ir surface atoms in the presence of more than one Si atom. Indeed, as the Si coverage increases from 0.5 ML to 1.5 ML, the Ir_C component continues to grow at the expenses of Ir_A, following the trend of Si_C and Si_A. Interestingly, the Ir_B component shifts to higher BE with the increase in Si coverage, as indicated by the dashed line in figure 7.10 (a). In addition to this, the intensity of Ir_B increases continuously at the expenses of Ir bulk (B). This indicates enhanced Si penetration into the Ir substrate. As a result, not only the metal surface but also the layer underneath are perturbed by the presence of Si. Based on this analysis, the subsequent stages of Si adsorption on Ir(111) are sketched in figure 7.12.

Additional information about the Si-Ir interface structure can be determined

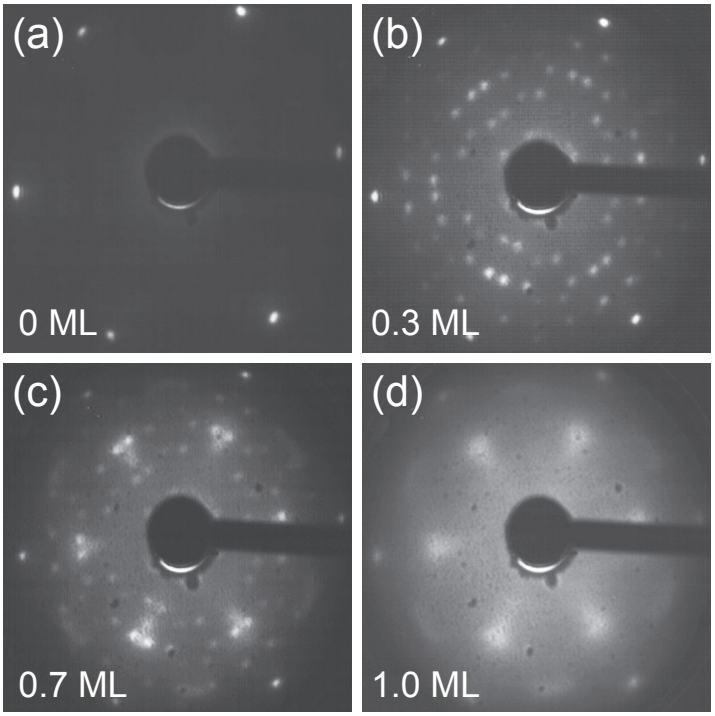

Figure 7.13: (a-d) LEED patterns obtained for the Si/Ir(111) interface at the indicated Si coverages, corresponding to the black lines on the right side of figure 7.9 (b).

from the LEED patterns acquired at different Si coverage, as shown in figure 7.13. At low coverage (0.3 ML) the $\sqrt{19}\times\sqrt{19}$ R23.4° pattern is observed as explained in previous section 7.2. At higher coverage (0.7 ML) diffused spots corresponding to the 2×2 periodicity of the Ir substrate are superimposed to the previous structure. At 1 ML coverage the LEED pattern shows only the diffused 2×2 spots with increased background. This indicates that the long range order diminishes at high Si coverage. It is also important to emphasize that we did not observe, at any coverage up to 1.5 ML, the $\sqrt{7}\times\sqrt{7}$ LEED pattern that was attributed to silicene growth on Ir(111). [17]

As it was done for the lower Si coverage, we investigated the effect of the temperature on layer ordering by post-annealing to temperatures $>$ 670 K $\sim$ 1 ML of Si deposited at lower temperature. Figure 7.14 (a) and (e) show the fast-XPS intensity plot of Si 2p spectra obtained while dosing Si at RT and 520 K, respectively. For both procedures, the high-resolution XPS spectra measured at the end of the deposition are reported in figure 7.14 (b) and (f). Following the high temperature annealing, the indication of interface ordering can be seen from the sharpening of the initially broad spectrum, as shown in the intensity plots in figure 7.14 (c) and (g). For the RT deposition, the layer ordering takes place at $\sim$ 700 K and no further spectral changes are observed while annealing to 700 K for 15 minutes. The final high-resolution XPS spectra, in figure 7.14 (d), show the presence of a dominant Si_C peak, indicating the redistribution of Si ad-atoms to the densely packed *hcp* adsorption configuration. However, the presence of residual components such as Si_A, Si_D and Si_E suggests an inhomogeneous ordering of the layer that is further confirmed by the diffuse 2×2 LEED pattern (not shown), similar to the one reported in figure 7.13 (d).

A more homogeneous redistribution of Si ad-atoms is obtained by post-annealing to 1000 K, the layer deposited at 520 K. In figure 7.14 (h), the Si 2p core level shows only the Si_C component, indicating a better ordered Si layer. However, in both cases the Si_B component is not present. This might suggest that the Si penetration into the Ir surface is largely unfavored, once the Si density exceeds a certain limit, before interface reordering.

As already mentioned earlier, it has been reported in literature that Si deposited at room temperature on Ir(111), followed by annealing to 670 K, leads to the formation of a silicene layer with a Si coverage of 0.85 ML. The proposed structure presented a $\sqrt{7}\times\sqrt{7}$ LEED pattern and according to the calculations formed a buckled layer, strongly bonded with the substrate because of strong hybridization of the electronic states. [17, 18] However, our results show that Si adsorption on Ir(111) leads to the transition from a $\sqrt{19}\times\sqrt{19}$ R23.4° to a diffuse 2×2 LEED pattern moving from low ($\sim$ 0.3 ML, see figure 7.13 (b)) to high coverage (1.5 ML, see figure 7.13 (d)). These findings together with the strong variations in Si 2p spectra with the increasing coverage (figure 7.4 (b)), which are not expected if the growth of a silicene layer would proceed in a similar manner of graphene growth on transition metal substrates, [29, 30] where the same C 1s lineshape is present from the begenning of the growth, rules out the formation of silicine layer for the experiments discussed in this

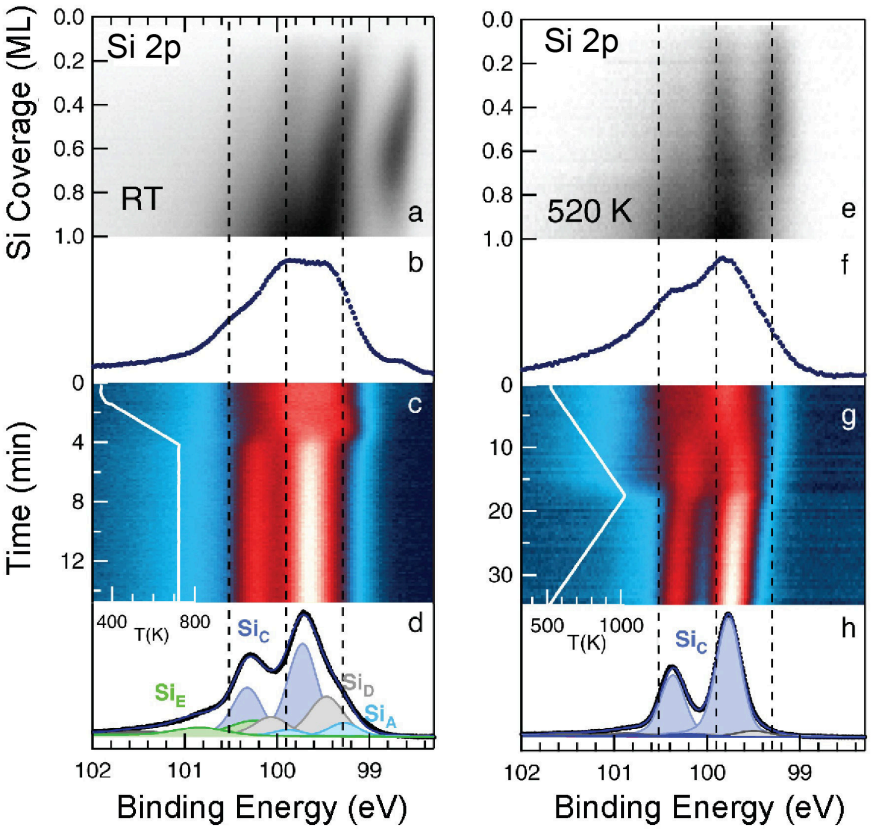

Figure 7.14: 2D intensity plots of the Si 2p spectra measured during the deposition of Si on Ir(111) (up to 1 ML) at (a) RT and (e) at 520 K; with the corresponding high resolution Si 2p spectra (b) and (f) acquired after the end of growth. (c,g) 2D intensity plots of the Si 2p spectra measured during sample annealing. Sample temperatures are plotted (white lines) as a function of the annealing time on the left side of the figures. (d,h) High resolution Si 2p spectra measured on the annealed samples, shown with the best-fit curves and the spectral components. The dashed lines mark the BE of the Si_A and Si_B doublets.

chapter.

It is worth comparing our results with those observed for the Si/Pt(111) interface. [16] Similar to our observations, Si adsorption on Pt(111) at 0.3 ML coverage resulted in a $\sqrt{19} \times \sqrt{19}$ R23.4° LEED pattern, that has been attributed to the penetration of Si ad-atoms into the Pt surface with the formation of an ordered 2D alloy consisting of Si_3Pt tetramers. The Si 2p spectrum for the Si/Pt(111) interface presented two equally intense components that were attributed to Si in *fcc* and *hcp* sites. In our case the strong intensity difference between the two spectral components Si_A and Si_B in figure 7.10 (b) suggests that the Si/Ir(111) interface cannot be reconciled with the same structure proposed for Si/Pt(111).

7.4 Conclusions

Si adsorption on Ir(111) was followed in real time by fast-XPS of Si 2p and Ir $4f_{7/2}$ spectra. Our results indicates that regardless of the growth temperature, Si adsorption starts predominantly at hollow sites. A stable $\sqrt{19} \times \sqrt{19}$ R23.4° structure appears when Si is deposited or annealed at 670 K, characterized by a simultaneous appearance of two components (Si_A and Si_B) in the Si 2p spectra. Based on the behavior of the Si 2p spectral components, observed in a wide set of experiments and on the results of DFT calculations, we conclude that together with a dominant adsorption of Si at hollows sites, a small fraction penetrates into the Ir surface layer.

We found that Si adsorption at high coverage (0.5-1.5 ML) results in the formation of a Si bilayer. In addition to this, a strong perturbation of the Ir bulk component suggests the penetration of Si atoms into the substrate. The observed behavior cannot be attributed to the formation of a silicene layer on Ir(111), but implies the instability of the Si/Ir(111) interface towards the formation of a Si-Ir alloy.

References

[1] Takeda, K.; Shiraishi, K. Theoretical possibility of stage corrugation in Si and Ge analogs of graphite. *Physical Review B* **1994**, *50*, 14916–14922.

[2] Guzmán-Verri, G. G.; Lew Yan Voon, L. C. Electronic structure of silicon-based nanostructures. *Physical Review B* **2007**, *76*, 075131, 1–10.

[3] Cahangirov, S.; Topsakal, M.; Aktürk, E.; Şahin, H.; Ciraci, S. Two- and One-Dimensional Honeycomb Structures of Silicon and Germanium. *Physical Review Letters* **2009**, *102*, 236804, 1–4.

[4] Ezawa, M. Spin-valley optical selection rule and strong circular dichroism in silicene. *Physical Review B* **2012**, *86*, 161407, 1–4.

[5] Wei, W.; Dai, Y.; Huang, B.; Jacob, T. Many-body effects in silicene, silicane, germanene and germanane. *Physical Chemistry Chemical Physics* **2013**, *15*, 8789–8794.

[6] Ezawa, M. Valley-Polarized Metals and Quantum Anomalous Hall Effect in Silicene. *Physical Review Letters* **2012**, *109*, 055502, 1–5.

[7] Liu, C.-C.; Feng, W.; Yao, Y. Quantum Spin Hall Effect in Silicene and Two-Dimensional Germanium. *Physical Review Letters* **2011**, *107*, 076802, 1–4.

[8] Sahaf, H.; Masson, L.; Léandri, C.; Aufray, B.; Lay, G. L.; Ronci, F. Formation of a one-dimensional grating at the molecular scale by self-assembly of straight silicon nanowires. *Applied Physics Letters* **2007**, *90*, 263110, 1–4.

[9] De Padova, P.; Quaresima, C.; Perfetti, P.; Olivieri, B.; Leandri, C.; Aufray, B.; Vizzini, S.; Le Lay, G. Growth of Straight, Atomically Perfect, Highly Metallic Silicon Nanowires with Chiral Asymmetry. *Nano Letters* **2008**, *8*, 271–275.

[10] Vogt, P.; De Padova, P.; Quaresima, C.; Avila, J.; Frantzeskakis, E.; Asensio, M. C.; Resta, A.; Ealet, B.; Le Lay, G. Silicene: Compelling Experimental Evidence for Graphenelike Two-Dimensional Silicon. *Physical Review Letters* **2012**, *108*, 155501, 1–5.

[11] Okamoto, H. *Journal of Phase Equilibria and Diffusion* **2011**, *32*, 391–391.

[12] Satta, M.; Colonna, S.; Flammini, R.; Cricenti, A.; Ronci, F. Silicon Reactivity at the Ag(111) Surface. *Physical Review Letters* **2015**, *115*, 026102, 1–5.

[13] Lalmi, B.; Girardeaux, C.; Portavoce, A.; Ottaviani, C.; Aufray, B.; Bernardini, J. Formation and stability of a two-dimensional nickel silicide on Ni(111): An Auger, LEED, STM, and high-resolution photoemission study. *Physical Review B* **2012**, *85*, 245306, 1–6.

[14] Enriquez, H.; Mayne, A.; Kara, A.; Vizzini, S.; Roth, S.; Lalmi, B.; Seitsonen, A. P.; Aufray, B.; Greber, T.; Belkhou, R.; Dujardin, G.; Oughaddou, H. Adsorption of silicon on Au(110): An ordered two dimensional surface alloy. *Applied Physics Letters* **2012**, *101*, 021605, 1–6.

[15] Martín-Gago, J. A.; Fasel, R.; Hayoz, J.; Agostino, R. G.; Naumovic-acute, D.; Aebi, P.; Schlapbach, L. Surface atomic structure of c(2×2)-Si on Cu(110). *Physical Review B* **1997**, *55*, 12896–12898.

[16] Švec, M.; Hapala, P.; Ondráček, M.; Merino, P.; Blanco-Rey, M.; Mutombo, P.; Vondráček, M.; Polyak, Y.; Cháb, V.; Martín Gago, J. A.; Jelínek, P. Silicene versus two-dimensional ordered silicide: Atomic and electronic structure of Si-$(\sqrt{19} \times \sqrt{19})R23.4°$/Pt(111). *Physical Review B* **2014**, *89*, 201412, 1–5.

[17] Meng, L.; Wang, Y.; Zhang, L.; Du, S.; Wu, R.; Li, L.; Zhang, Y.; Li, G.; Zhou, H.; Hofer, W. A.; Gao, H.-J. Buckled Silicene Formation on Ir(111). *Nano Letters* **2013**, *13*, 685–690.

[18] Quhe, R.; Yuan, Y.; Zheng, J.; Wang, Y.; Ni, Z.; Shi, J.; Yu, D.; Yang, J.; Lu, J. Does the Dirac Cone Exist in Silicene on Metal Substrates? *Scientific Reports* **2014**, *4*, 5476, 1–8.

[19] Demuth, V.; Strunk, H.; Wörle, D.; Kumpf, C.; Burkel, E.; Schulz, M. Formation of amorphous layers by solid-state reaction from thin Ir films on Si(100). *Applied Physics A* **1999**, *68*, 451–455.

[20] Benedictus, R.; Böttger, A.; Mittemeijer, E. J. Thermodynamic model for solid-state amorphization in binary systems at interfaces and grain boundaries. *Physical Review B* **1996**, *54*, 9109–9125.

[21] Wörle, D.; Grünleitner, H.; Demuth, V.; Kumpf, C.; Strunk, H.; Burkel, E.; Schulz, M. Amorphous and crystalline IrSi Schottky barriers on silicon. *Applied Physics A* **1998**, *66*, 629–637.

[22] Abrami, A.; Barnaba, M.; Battistello, L.; Bianco, A.; Brena, B.; Cautero, G.; Chen, Q. H.; Cocco, D.; Comelli, G.; Contrino, S.; DeBona, F.; Di Fonzo, S.; Fava, C.; Finetti, P.; Furlan, P.; Galimberti, A.; Gambitta, A.; Giuressi, D.; Godnig, R.; Jark, W.; Lizzit, S.; Mazzolini, F.; Melpignano, P.; Olivi, L.; Paolucci, G.; Pugliese, R.; Qian, S. N.; Rosei, R.; Sandrin, G.; Savoia, A.; Sergo, R.; Sostero, G.; Tommasini, R.; Tudor, M.; Vivoda, D.; Wei, F. Q.; Zanini, F. Super ESCA: First beamline operating at ELETTRA. *Review of Scientific Instruments* **1995**, *66*, 1618–1620.

[23] Bianchi, M.; Cassese, D.; Cavallin, A.; Comin, R.; Orlando, F.; Postregna, L.; Golfetto, E.; Lizzit, S.; Baraldi, A. Surface core level shifts of clean and oxygen covered Ir(111). *New Journal of Physics* **2009**, *11*, 063002, 1–18.

[24] Meng, L.; Wu, R.; Zhou, H.; Li, G.; Zhang, Y.; Li, L.; Wang, Y.; Gao, H.-J. Silicon intercalation at the interface of graphene and Ir(111). *Applied Physics Letters* **2012**, *100*, 083101, 1–5.

[25] Gao, N.; Liu, H.; Zhou, S.; Bai, Y.; Zhao, J. Interaction between Post-Graphene Group-IV Honeycomb Monolayers and Metal Substrates: Implication for Synthesis and Structure Control. *The Journal of Physical Chemistry C* **2017**, *121*, 5123–5129.

[26] Wei, W.; Dai, Y.; Huang, B.; Whangbo, M.-H.; Jacob, T. Loss of Linear Band Dispersion and Trigonal Structure in Silicene on Ir(111). *The Journal of Physical Chemistry Letters* **2015**, *6*, 1065–1070.

[27] Curson, N. J.; Bullman, H. G.; Buckland, J. R.; Allison, W. Interaction of silane with Cu(111): Surface alloy and molecular chemisorbed phases. *Physical Review B* **1997**, *55*, 10819–10829.

[28] Kittel, C. In *Introduction to Solid State Physics*, 8th ed.; Hoboken, N., Ed.; John Wiley and Sons, Inc, 2004.

[29] Alfè, D.; Pozzo, M.; Miniussi, E.; Günther, S.; Lacovig, P.; Lizzit, S.; Larciprete, R.; Burgos, B. S.; Menteş, T. O.; Locatelli, A.; Baraldi, A. Fine tuning of graphene-metal adhesion by surface alloying. *Scientific Reports* **2013**, *3*, 2430, 1–6.

[30] Grúneis, A.; Kummer, K.; Vyalikh, D. V. Dynamics of graphene growth on a metal surface: a time-dependent photoemission study. *New Journal of Physics* **2009**, *11*, 073050, 1–9.

Acknowledgments

This thesis is an outcome of the exciting journey that I took upon three years ago and the blessings of my teachers, family and friends. It is my pleasure to express my recognitions to all those who have contributed, by several means, towards the completion of this work.

I wish to express my heartfelt gratitude and sincere acknowledgment to my supervisor Alessandro Baraldi for his valuable suggestions and guidance for the sound completion of this thesis. I will always be indebted for his continuous cooperation in sorting out not only the scientific but also the bureaucratic problems that I faced during my stay in Trieste. My sincere thanks to my co-supervisor Silvano Lizzit for his continuous support and encouragement that influenced me both professionally and personally, throughout the last three years. He has enriched my knowledge with his experiences and skills that helped me in shaping this work. My sense of appreciation towards him cannot be framed in the boundaries of words. I am also indebted to the beamline scientist at SuperESCA beamline Paolo Lacovig for helping me with the analysis, introducing me to the technicalities of UHV and also for bringing me home after late night shifts during the beamtimes.

Working together with colleagues has stimulated me to finish this study as per schedule. I am delighted to write about my lab-mates Elisabetta Travaglia, Luca Bignardi, Francesco Presel, Daniel Lizzit, Davide Curcio, Dario De Angelis, Luca Omiciuolo, Naila Jabeen, Cristian Tache and Nicoletta Apostol, for their cooperation during experiments, thesis writing and for all the fun that we had together. I have experienced some of the most precious moments with them which I will never forget throughout my life. Special thanks to Elisabetta, Francesco and Luca B. for the helping hands they always extended whenever I was in need.

I would like to thank Rosanna Larciprete who not only helped me in my project but also introduced me to the CVD technique and Raman spectroscopy,

I am greatly indebted to her. My thanks to Dr. Roberto Cimino for allowing me to work in his laboratory at INFN in Frascati. My sincere thanks also go to Prof. Philip Hofmann, from the Aarhus University in Denmark, for sharing his experience and motivations that allowed us to perform some very exciting experiments. I would like to thank all the members of the collaborating group for their scientific help, support and fruitful discussions.

Thanking friends is not easy; a note of thanks seems so inadequate for them; their lovely company created memories of lifetime for me. I want to deeply acknowledge the Indian community at Trieste, in particular Manendra Pachauri, Jayashree Thatte and Vipin Rawat, for all the sustenance they have provided and above all for being there in need. I could not have thought of completing this thesis without them. Financial assistance in the form of research fellowship from EMINTE and the assistance from the coordinating team at Lund University, especially from Mr. Niklas Nannskog, is dully acknowledged. I am also grateful to Mr. Luciano Acquavita and other members of the mobility office at UNITS, and Madam Rosita Glavina of the Physics department for their support in official dealings and other assistances.

Finally, I would like to thank my father and uncle who gave me the inspiration to follow my dreams, my mother and aunt whose love and affection has always been a source of strength, my lovely sisters Meenu, Nikita, Nimisha, Srishti and Drishti who never fail to cheer me up, and my close friends Mamchand and Vineet for bearing with me for this long.

List of publications

Peer reviewed publications related to the PhD research project

1. Nicki Frank Hinsche, Arlette S. Ngankeu, Kevin Guilloy, Sanjoy K. Mahatha, Antonija Grubišić Čabo, Marco Bianchi, Maciej Dendzik, Charlotte E. Sanders, Jill A. Miwa, Harsh Bana, Elisabetta Travaglia, Paolo Lacovig, Luca Bignardi, Rosanna Larciprete, Alessandro Baraldi, Silvano Lizzit, Kristian Sommer Thygesen, and Philip Hofmann "Spin-dependent electron-phonon coupling in the valence band of single-layer WS_2" *Physical Review B* 96, 121402(R) (2017).

Submitted or in preparation manuscripts related to the PhD research project

1. Harsh Bana, Elisabetta Travaglia, Luca Bignardi, Paolo Lacovig, Charlotte E. Sanders, Maciej Dendzik, Matteo Michiardi, Marco Bianchi, Daniel Lizzit, Francesco Presel, Dario De Angelis, Nicoleta Apostol, Pranab Kumar Das, Jun Fujii, Ivana Vobornik, Rosanna Larciprete, Alessandro Baraldi, Philip Hofmann, and Silvano Lizzit "Synthesis of Single-Orientation High-Quality MoS_2 Monolayers with Complete Spin Polarization" *submitted, under review.*

2. Harsh Bana, Elisabetta Travaglia, Luca Bignardi, Paolo Lacovig, Daniel Lizzit, Charlotte E. Sanders, Maciej Dendzik, Marco Bianchi, Nicoleta Apostol, Rosanna Larciprete, Alessandro Baraldi, Philip Hofmann, and Silvano Lizzit "Synthesis of Single-Orientation High-Quality WS_2 Monolayers" *in preparation.*

3. Rosanna Larciprete, Mauro Satta, Harsh Bana, Elisabetta Travaglia, Luca Bignardi, Paolo Lacovig, Nicoleta Apostol, Alessandro Baraldi, and Silvano Lizzit "Adsorption of silicon on the Ir(111) surface" *in preparation.*

4. Elisabetta Travaglia, Harsh Bana, Luca Bignardi, Paolo Lacovig, Daniel Lizzit, Sanjoy Kr. Mahatha, Charlotte E. Sanders, Marco Bianchi, Rosanna Larciprete, Alessandro Baraldi, Philip Hofmann and Silvano Lizzit "Large area epitaxial growth of MoS_2 on Ag(111)" *in preparation.*

5. Luca Bignardi, Sanjoy Kr. Mahatha, Daniel Lizzit, Harsh Bana, Elisabetta Travaglia, Paolo Lacovig, Charlotte E. Sanders, Marco Bianchi, Rosanna Larciprete, Alessandro Baraldi, Philip Hofmann, and Silvano Lizzit "Growth of single layer MoS_2 on anisotropic Ag(110)" *in preparation.*

Other publications

1. Yujing Ma, Elisabetta Travaglia, Harsh Bana, Luca Bignardi, Paolo Lacovig, Silvano Lizzit, and Matthias Batzill "Periodic Modulation of Graphene by a 2D-FeO/Ir(111) Moiré Interlayer" *The Journal of Physical Chemistry C* 121 (5), 2762-2770 (2017).

2. Elisabetta Travaglia, Harsh Bana, Luca Bignardi, Paolo Lacovig, Daniel Lizzit, Rosanna Larciprete, Alessandro Baraldi, and Silvano Lizzit "Intercalation of oxygen under graphene on Ir(111)" *in preparation.*